Intrinsically Microporous Polymers in Heterogeneous Redoxcatalysis

Wang, Lina

Award date:
2023

Awarding institution:
University of Bath

Intrinsically Microporous Polymers in Heterogeneous Redoxcatalysis

Lina Wang

A thesis submitted for the degree of Doctor of Philosophy

University of Bath

Department of Chemistry

September 2022

Declaration of any previous submission of the work.

The material presented here for examination for the award of a higher degree by research has not been incorporated into a submission for another degree.

Candidate's signature: _ [redacted]

Declaration of authorship

I am the author of this thesis, and the work described therein was carried out by myself personally.

Candidate's signature: _ [redacted]

Abstract

Microporous composite materials have been studied for a considerable range of heterogeneous catalysis applications due to their large inner specific area and the potential of adsorbing small species into their microporous structure. Though prominent types of microporous crystalline hosts, zeolites and metal frameworks (MOFs), for example, are advantageous to many applications, they are not processable. Polymers of intrinsic microporosity (PIMs) have emerged as a new class of microporous materials which are molecularly rigid structures with poor packing and a high degree of open porosity at the nanometre scale. Characteristics of good solubility, processability (into a film by drop-casting or spin-coating), thermal and mechanical stability, and gas and ion species permeability enable PIMs to be applied in fields of electrochemistry. In this thesis, the opportunities for applications of PIMs in heterogeneous redoxcatalysis are investigated.

Redoxcatalytic reactions within microporous composites involve several interrelated processes, including diffusion and permeation of reactants and products, adsorption and desorption of active species, binding and decomposition of substances coupled with electron transfer processes, and on some occasions, involvement of non-reactive solvents. The whole reaction can be complex; however, simple redox systems based on PIM composites can be explored individually as a starting point. Examples are the binding behaviour and reactivity of ions ($Fe(CN)_6^{3-/4-}$) and molecules (catechin and quercetin) inside the PIM host. More complicated systems (H_2 and H_2O_2 generation from formic acid and O_2) are studied next. Practical nano-catalysts (Pd, bipolar Pd/Au, and PdAu mixture) immobilised in PIMs for redoxcatalysis with gases, ions, and molecules are investigated.

In this thesis, the main aims are (i) to develop an understanding of the role of PIMs as host for heterogeneous catalysts for redoxcatalysis, (ii) to explore the mechanisms of reactions occurring within PIM composites, and (iii) to optimise and extend the applications of PIMs for useful product generation (H_2 or H_2O_2 for example). The mechanism is investigated primarily with voltammetry to distinguish potential-dependent processes. Analysis methods are developed for quantification of products or species (catechin, quercetin, and H_2O_2) based on liquid chromatography coupled with mass spectrometry (LC-MS), for evaluation of O_2 generation and H_2 production based on a Clark-type sensor, and for colourimetric assay of H_2O_2 generation based on a sensor dye 3,5,3’,5’-tetramethylbenzidine (TMB). A

computational DFT simulation is carried out for verification of PIMs as an active component during redoxcatalysis.

The electrochemical and binding behaviour of redox species is investigated by immobilisation of $Fe(CN)_6^{3-/4-}$ or *ortho*-quinol molecules, catechin and quercetin, into PIM-EA-TB. The interaction between $Fe(CN)_6^{3-/4-}$ and protonated amine sites in PIM-EA-TB is proposed to be linked to the retention and relatively slow leaching process. The PIM-EA-TB with immobilised $Fe(CN)_6^{3-/4-}$ is applied for the electrocatalytic oxidation of ascorbic acid. Hydrogen bonding is suggested to be responsible for *ortho*-quinol molecules immobilisation in the PIM-EA-TB host. A thin mono-layer film with one catechin or quercetin molecule binding to each monomeric PIM-EA-TB unit configuration is electrochemically active. Either spontaneous or electrochemically triggered leaching of guest *ortho*-quinol molecules is shown to depend on the state of the films.

Palladium nano-catalysts are incorporated in PIM-EA-TB. Competing processes of H_2O_2, water, and H_2 production from formic acid and O_2 are investigated for the Pd@PIM-EA-TB catalyst. Next, gold is electrolessly deposited and attached to the Pd in PIM-EA-TB. The Pd/Au@PIM-EA-TB product gives enhanced H_2O_2 production with suppressed H_2 generation. It is suggested that Pd and Au work hand-in-hand as bipolar electrocatalysts. The Pd@PIM-EA-TB catalyst is also evaluated for formate oxidase reactivity as a nanozyme to produce H_2O_2. This, in turn, drives the TMB colour reaction in the presence of formic acid. A computational DFT simulation proves that, as an active component, PIM-EA-TB enhances both 2-electron formate oxidation and 2-electron oxygen reduction to H_2O_2 on palladium.

Furthermore, the reactivity of nano-Pd, -Au, and -PdAu mixture towards formic acid oxidation and oxygen reduction during H_2O_2 production is investigated and compared in two microporous polymer hosts (PIM-1 and PIM-EA-TB). PdAu@PIM-EA-TB shows the best reactivity towards H_2O_2 production. In contrast to PIM-1, PIM-EA-TB is proposed to directly contribute to the catalytic process with amine sites accepting protons during formate oxidation and ammonium sites donating protons for oxygen reduction.

Overall, this thesis highlights the reactivities and applications of PIMs as part of microporous composites in heterogeneous redoxcatalysis. The role of PIMs in the catalytic processes is investigated. New hypotheses are proposed for the mechanisms of the catalytic reactions studied in this thesis, and novel experimental approaches are developed to verify them.

Acknowledgements

Years of studies and experiences have made me much stronger, both academically and emotionally. If it were years ago, I would not imagine how far I would get. I was trying to use the word “achieve”, but then I realised it might be too “big” to say. I have not done much really, except get to know a brand-new country basically from trivial experience. That sounds like nothing, but it is something inconceivable to me. As a part of my life, getting a PhD degree has become less difficult with the help of many people I encountered.

“**S**ilent” love is probably the best way to describe the connection between my family and me. My family have been supporting me with their action most of the time. I am not saying that they are stingy with expressing their bonding to me. On the contrary, they probably think it is more “useful” to do something to help rather than to say. I decided to give my first thanks to my dearest mom, Jinping Wang, dad, Siyuan Wang, brother, Dechang Wang, and sister-in-law, Miaomiao Huo. Thanks to my other families, my aunt, Runling Wang, my uncle-in-law, Zhengbin Li, my little sisters, Rui Li and Nan Li. Thanks to them for their endless and generous love and for always standing behind me. I would like to send my best wishes to my two little nephews, Zhenhan Wang and Jinyu Wang. May you embrace happy lives and bright futures. I would like to deliver my appreciation to one of the most important people in my life, my grandmother, Junmei Liu, for her years of caring for me. You will never be forgotten. Furthermore, I would like to give my great appreciation to Yanshi Yu, my better half, for your support, understanding, and encouragement throughout my PhD journey. I do not know what the future holds, but I believe that our unwavering bonds will only strengthen with time.

Applying and becoming a member of the Marken group is one of the things I would never regret. I would like to give my great appreciation to my supervisor Prof. Frank Marken. Frank has this energy and enthusiasm for science that I would pursue throughout my entire life. One can see his sparkling eyes when he hears or finds something interested. There were many times when I thought there was no clue for my experiment, but when I discussed it with him, something new came out. Frank is exceptionally nice to all of us and is an amazing supervisor. Thanks to Frank for your fantastic supervision.

Next, I would like to thank everyone who has supported my work. I would like to thank Dr Philip Fletcher for spending many hours helping me take the SEM and TEM images. I would like to give thanks to Dr Shaun Reeksting for LC-MS training and helpful advice. I am grateful to members of the Marken group (Dr Elena Madrid, Dr Amelia R. Langley, Dr Budi Riza Putra, Dr Yuanzhu Zhao, Dr Bingbing Fan, Dr Yu Wang, Tianting Pang, Zhongkai Li, Akalya Karunakaran, Simon Wikeley, and Dr Maísa Beluomini) for all the inspirations you have brought to me during the group meetings and daily conversations. I would like to extend my appreciation to Tianting for taking care of me and for all the delicious meals. I am grateful to Prof. Karen Edler and Prof. Petra Cameron for your valuable suggestions on my confirmation viva. I would like to thank Dr Alberto Roldan for your support on DFT calculations.

Outstanding funding support from the China Scholarship Council and University of Bath Joint scholarship is sincerely appreciated.

Contents

Abbreviations

BET	Brunauer, Emmett and Teller (Theory)
BSE	backscattered electrons
cPIM	carbonised polymer of intrinsic microporosity
DFT	density functional theory
EA	ethanoanthracene
EC'	electrocatalysis
EDX	energy dispersive X-ray spectroscopy
FESEM	field emission scanning electron microscopy
FFT	fast Fourier transform
FSC	fast scanning calorimetry
FTO	fluorine-doped tin oxide
GCE	glassy carbon electrode
GGA	generalized gradient approximation
HOMO	highest occupied molecular orbital
HPLC	high-performance liquid chromatography
ITO	indium tin oxide
LC	liquid chromatography
LC-MS	liquid chromatography – mass spectroscopy
LUMO	lowest unoccupied molecular orbital
MOFs	metal-organic frameworks
MS	mass spectroscopy

OCP	open circuit potential
PAW	Projected Augmented Wave
PCM	polarised continuum model
PET	polyethylene terephthalate
PIMs	polymers of intrinsic microporosity
PPP	4-(3-phenyl-propyl)pyridine
PTFE	polytetrafluoroethylene
RPBE	revised functional of Perdew-Burke-Ernzerhof
SA	surface area
SAED	selected area electron diffraction
SCE	saturated calomel electrode
SE	secondary electrons
SEI	solid-electrolyte-interphase
SEM	scanning electron microscopy
S_NAr	aromatic nucleophilic substitution
STEM	scanning transmission electron microscopy
TB	Tröger's base
TEM	transmission electron microscopy
4B-TEMPO	4-benzoyloxy-2,2,6,6-tetramethylpiperidine-1-oxyl
THF	tetrahydrofuran
TMB	3,5,3',5'-Tetramethylbenzidine
TPP	tetraphenylporphyrinato
VASP	Vienna Ab initio Software Package

List of Symbols

Subscripts

a	anodic reaction at electrode
c	cathodic reaction at electrode
eq	equilibrium
F	fermi level
i	species i
O	pertaining species O in $O + ne^- \rightleftharpoons R$
ox	oxidation reaction for $O + ne^- \rightleftharpoons R$
p	peak
R	pertaining species R in $O + ne^- \rightleftharpoons R$
red	reduction reaction for $O + ne^- \rightleftharpoons R$
x	species x
0	zero distance (at electrode surface)

Greek Symbols

Symbol	Description	Typical Units
α	charge transfer coefficient	no units
γ	activity coefficient	no units
δ	diffusion layer thickness	m
η	overpotential ($E - E_{eq}$)	V
v	scan rate	mV s^{-1}
ϕ	i) electrostatic potential	V
	ii) electrode diameter	mm
Φ	flux density	mol m^{-2} s^{-1}

Roman Symbols

Symbol	Description	Typical Units
a	chemical activity	no unit
A	electrode area	cm^2
c	concentration	mol dm^{-3}
$c_i(x,t)$	concentration of species i at time t and distance x	mol dm^{-3}
D	diffusion coefficient	cm^2 s^{-1}
D_i	diffusion coefficient of species i	cm^2 s^{-1}
E	potential	V
E^0	standard potential	V
$E^{0'}$	formal standard potential	V

Symbol	Description	Typical Units
E_a	activation energy	J mol^{-1}
E_{mid}	redox potential (1/2($E_p^a + E_p^c$))	V
ΔE	potential difference / change	V
F	Faraday constant	(96485) C mol^{-1}
G	Gibbs free energy	J mol^{-1}
$G^{\ddagger}$	Gibbs free energy of activation	J mol^{-1}
G^0	Standard Gibbs free energy	J mol^{-1}
$\Delta G^{\ddagger}$	change in Gibbs free energy of activation	J mol^{-1}
i	current	A
i_0	exchange current	A
i_{total}	total current from electrolysis	A
J	flux to electrode	mol cm^{-2} s^{-1}
k	rate constant	depends on order
	i) homogeneous first order rate constant	s^{-1}
	ii) heterogeneous rate constant	m s^{-1}
n	number of transferred electrons	no units
p	pressure	atm
Q	charge	C
R	gas constant (8.31447 J K^{-1} mol^{-1})	J K^{-1} mol^{-1}
t	time	s
T	temperature	K
T_g	glass transition temperatures	K
V	volume	m^3

Symbol	Description	Typical Units
x	distance	m

List of Figures

List of Tables

Chapter 1 Introduction to Polymers of Intrinsic Microporosity (PIMs) in Electrochemistry

Contents

Chapter Abstract

Polymers of intrinsic microporosity (PIMs) have emerged as a class of glassy microporous materials with high free volume, good gas permeability, good selectivity, and excellent processibility. Unlike other crystalline or cross-linked microporous materials, PIMs display intrinsic microporosity due to their highly rigid polymer chains causing free volume elements. The rigidity in the backbone limits molecular interactions inside the polymers leading to good solubility and processibility. Free-standing films and coatings can be readily prepared by dissolving PIMs in organic solvents and casting on targeting substrates such as electrodes. Due to the microporosity and good permeability to both gases and liquids, catalysts or electrodes modified by PIMs will remain active. This results in opportunities for PIMs to be applied in electrochemistry. The selectivity of PIMs towards different species in liquids enables applications as separation membranes in ionic diodes, in corrosion protection, and in energy storage and conversion. Furthermore, metal-free or metal-containing heterocarbons obtained by carbonisation of PIMs retain microporosity and permeability.

In this chapter, an introduction to PIMs is given. The design and synthesis strategies of typical PIMs, in particular PIM-1 and PIM-EA-TB, are explained, which leads to the properties and corresponding applications. The applications of PIMs in electrochemistry, catalysis, and in photocatalysis are emphasised. Finally, the aims of the work are summarised.

Publications associated with this chapter:

Some parts/contents of this chapter have been published in:

Wang, L., Zhao, Y., Fan, B., Carta, M., Malpass-Evans, R., McKeown, N. B., & Marken, F. Polymer of intrinsic microporosity (PIM) films and membranes in electrochemical energy storage and conversion: a mini-review. *Electrochemistry Communications* **118**, 106798 (2020).

Marken, F., Wang, L., Zhao, Y., Li, Z., Amiri, M., & Imanzadeh, H. Polymers of intrinsic microporosity (PIMs) in sensing and in electroanalysis. *Current Opinion in Chemical Engineering* **35**, 100765 (2022).

1.1 Design and Synthesis of PIMs

Conventional microporous materials (such as zeolites, metal-organic frameworks or MOFs) are generally either crystalline or cross-linked structures causing poor solubility and restricted film applications. The concept of Polymers of Intrinsic Microporosity (PIMs) was proposed by Budd et al. [1] to achieve a solution-processed membrane which can be further used to make devices such as sensors [2,3], gas separators [4,5], and electrochemical systems [6,7].

The definition of PIM is a '*Polymer that is composed of a fully (or predominantly) fused-ring macromolecular chain that is fixed in a 2D or 3D random coil conformation due to sites of contortion, such as bridged bicyclic or spirocyclic units, so that they pack space inefficiently in the solid state*'. [8] The intrinsic microporosity in PIMs is generated from the rigid and contorted macromolecular chains with inefficient space packing in the solid state. [9] So the design idea is to employ non-linear and conformationally locked monomers and a polymerisation reaction providing linkage with prohibited or hindered rotation (see Figure 1.1). [9,10] There are a few polymerisation reactions proven to be efficient in preparing PIMs, particularly based on dibenzodioxane formation (e.g. PIM-1), Tröger's base formation (e.g. PIM-EA-TB), and imide formation. Here the focus is on the former two reactions.

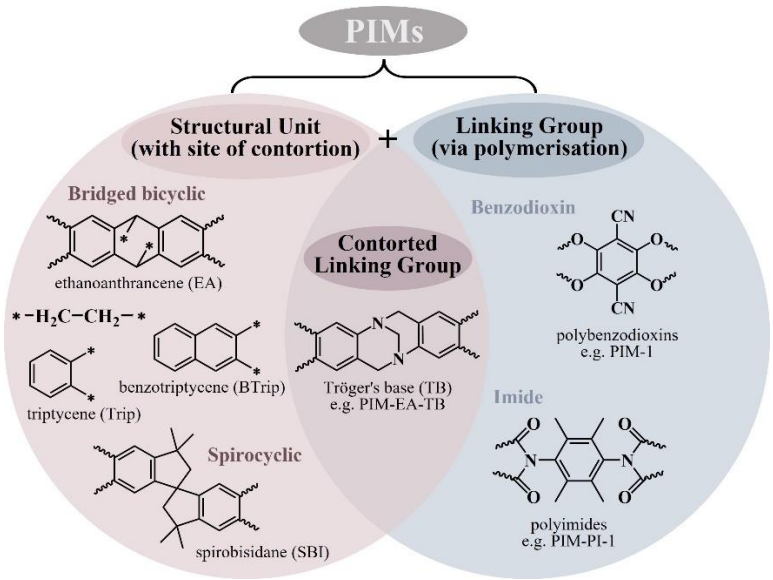

Figure 1.1 Design strategy of PIMs. The synthesis of PIMs requires both conformationally locked structural units and a polymerisation reaction that generate a linking group in which rotation is prohibited or hindered. [8,10]

Dibenzodioxane Reaction. The polymerisation using dibenzodioxane formation involves the aromatic nucleophilic substitution (S_NAr) mechanism between a biscatechol and a

tetrahalide-containing monomer. Figure 1.2A shows a typical S_NAr reaction, in which a nucleophile ($Nu^{\ominus}$) attacks an electron-poor aromatic molecule, giving the substitution of a leaving group. The first successful example based on this reaction is PIM-1 (see molecular structure in Figure 1.2B). The original method of making PIM-1 is named the "low temperature method", which is performed by the reaction between two monomers of 5,5'6,6'-tetrahydroxy-3,3,3',3'-tetramethyl-1,1'-spirobisindane, the nucleophile, and 2,3,5,6-tetrafluoroterephthalonitrile, the electron-poor aromatic molecule, at 50-60 °C for 24-72 h in the presence of potassium carbonate powder. [1] Fluorine is the leaving group due to its high electronegativity. In this reaction, the concentration of monomer is critical as cross-linking happens at high concentrations, whereas oligomers form at low concentrations. Meanwhile, a sufficiently high average molecular mass (typically $M_n > 30\times10^3$ g/mol) is needed to ensure the mechanical robustness of casting films.

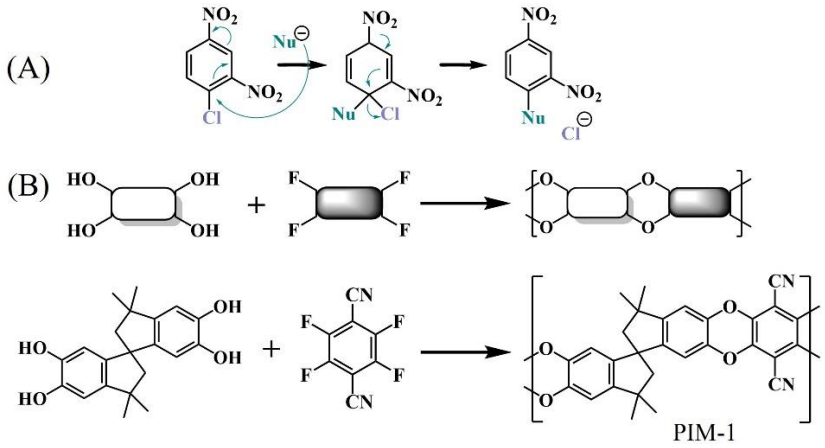

Figure 1.2 (A) An example of nucleophilic aromatic substitution (S_NAr); (B) PIMs prepared using dibenzodioxane polymerisation [9]

Tröger's Base Formation. Tröger's base (TB), also named as 2,8-dimethyl-6H,12H-5,11-ethanodibenzo[b,f][1,5]diazocine, is prepared by an electrophilic aromatic substitution mechanism. The reaction is excellent in producing six new covalent bonds by one step from an aromatic amine and formaldehyde or a formaldehyde replacement. The bridged bicyclic structure in TB provides a contorted site, which therefore makes it applicable in the synthesis of rigid PIMs. The synthesis of PIM-EA-TB relies on TB polymerisation (Figure 1.3). Generally, only one type of aromatic monomer is needed in this reaction. There are amine sites in the monomer of PIM-EA-TB (see Figure 1.3B), which can be protonated in acidic solutions. Once protonated, PIM-EA-TB attracts anions such as $PdCl_4^{2-}$, which allows metal nanoparticle formation/immobilisation in micropores by reduction reaction.

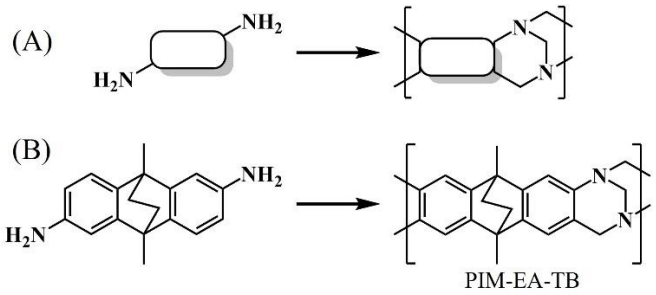

Figure 1.3 PIMs prepared using Tröger's Base polymerisation [9]

1.2 Properties of PIMs

Microporosity. The intrinsic microporosity of PIMs results from inefficient chain packing in the solid state. Taking PIM-1 (Figure 1.2 B) for example, the fused ring structure of the dibenzodioxin linkage and the spiro-centre cause the rigid and contorted chain structure and thereby generate intrinsic microporosity. With good microporosity of PIMs, comes high surface area (typically 1000 m^2 g^{-1} apparent BET surface area). The pore size and surface area of PIM-1 and PIM-EA-TB are summarised in Table 1.1.

Table 1.1 Solubility and microporosity of PIMs.

PIMs	Solubility	Surface Area (BET) (m^2/g)	Pore Size (nm)	Reference
PIM-1	$CHCl_3$, THF	760-850	0.4-0.8	[1,11,12]
PIM-EA-TB	$CHCl_3$, CH_2Cl_2	1028	1.4 (average)	[13,14]

Solubility. Solubility in common organic solvents is a key property of PIMs. The rigidity and contortion of chain structures reduce inter-chain cohesion and promote the absorption of solvent into PIMs, resulting in good solubility. [10] With intrinsic microporosity (pore size < 2 nm), PIMs provide nanochannels for liquids to coexist. [15] PIM-1 is readily soluble in common organic solvents like tetrahydrofuran and chloroform (Table 1.1). PIM-EA-TB displays good solubility in chloroform and dichloromethane (Table 1.1), likely stemming from H-bonding interaction between the tertiary amine and the solvent [10]. The good solubility of PIMs enables their processibility by casting into free-standing films through casting for further applications.

Thermal and Mechanical Properties. Generally, PIMs present thermo-oxidative stability and degrade at a temperature higher than 250 °C in air. Glass transition temperatures (T_g) of PIMs are very high and difficult to locate before thermal decomposition. However, a technique called fast scanning calorimetry (FSC) has been applied to determine the T_g where thermal decomposition of polymers was avoided by applying ultrafast heating rates. Results show that values of T_g are 663 K for PIM-EA-TB and 644 K for PIM-1, respectively. [16] Such good thermal stability of PIMs enables them to be applied over a wide range of temperatures. Notably, PIM membranes/films show good mechanical strength and robustness suited for gas permeability measurements, and gas storage and separation membranes. [14,17]

Gas Adsorption. The adsorption of nitrogen (N_2) at 77 K is typically used to detect porosity. The isotherm results provide information on apparent internal surface area and pore size distribution. [18] PIMs with highly rigid structures and large inter-chain distances tend to show significant adsorption of gases at a low relative pressure ($P/P_0 < 0.01$). According to the result of N_2 isotherms, the internal surface area (SA_{BET}) can be calculated despite PIM swelling during N_2 adsorption. [19]

Gas Permeability. The gas permeability of PIMs is generally used to assess the potential of PIMs as membranes for gas separation. [20] Gas separation performance of polymer membranes is limited by distinct trade-off relations: more permeable polymers are less selective and *vice versa*. [21] The continuous free volume elements inside PIMs acting as nanopores provide gas transport pathways. For PIMs with larger free volume elements, both smaller gas molecules (such as He and H_2) and larger ones (like N_2 and CH_4) can access their internal pores, which means high permeability yet less selectivity. [8] Furthermore, the permeability-selectivity trade-off relates significantly to the continuum of the size distribution of elements of free volume within polymers. Accordingly, tightly chain-packed polymers provide low permeability but good selectivity, whereas polymers with loose chain-packing display high permeability yet poor selectivity. Specifically, PIMs with great chain rigidity (e.g. PIM-EA-TB [22] and PIM-Trip-TB [23]) provide great selectivity resulting from the greater thermal activation energy demanded to open sufficiently large apertures or space to allow larger gas molecules to move from one free volume to another compared to that required for smaller gas molecules. [10,24,25]

1.3 Applications of PIMs in Electrochemistry

PIMs show good solubility in common organic solvents and excellent processability into films/membranes by casting. Their characteristic features, including high porosity, good permeability to both gas and liquid, and chemical stability, making them attractive for a wide range of applications such as gas storage, [26] gas and liquid separation, [5,27] gas phase sensing, [6] energy storage and conversion, [28] as well as electrochemistry [7] and catalysis [29]. These applications of PIMs in electrochemistry, catalysis and electrocatalysis will be discussed.

One of the exceptional characteristics of PIMs is that when applied on or mixed with other solid materials (electrodes or catalysts), the activities of the surface will not be diminished or blocked. The continuous free volume elements of PIMs provide paths for reagent species (gases and/or liquids) to diffuse in and products to diffuse out. Meanwhile, PIMs can create triphasic interfaces on which solids (catalysts), gases, and liquids (reagents or products) will maintain their reactivity without compromising permeability in PIMs. The common ways of applying PIMs into electrochemical systems are: (i) modifying catalysts or electrodes with a PIM coating, (ii) immobilising or absorbing reactive species into PIM films, (iii) applying self-standing PIM membranes as separation and/or permeable membranes, (iv) decorating electrodes with PIM nanoparticles, and (v) carbonising PIMs with/without immobilised species.

Molecular structures listed in Figure 1.4 will be mentioned in the following discussion of PIM applications. A summary of PIM applications in electrochemistry is presented in Table 1.2. Up to now, PIM-1 and PIM-EA-TB are of the most dominant materials applied in electrochemistry applications.

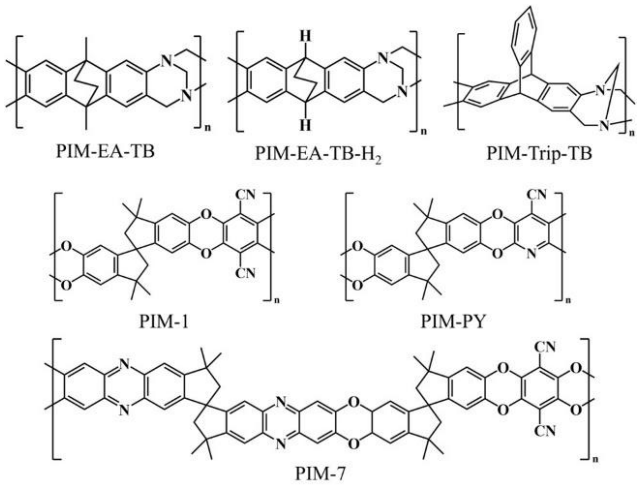

Figure 1.4 Molecular structures of selected PIMs.

Table 1.2 A summary of PIM applications in electrochemistry. Note that "GCE" stands for glassy carbon electrode. FeTPP is an abbreviation of tetraphenylporphyrinato-Fe(II). "SEI" means solid-electrolyte-interphase.

PIMs	State	Electrode Configuration	Application	Ref.
PIM-EA-TB	film	Pd lamella @ PIM-EA-TB film / GCE	Electrocatalytic oxidation of HCOOH	31
	film	FeTPP@PIM-EA-TB film / GCE	Electrocatalytic reduction of O_2 and H_2O_2	33
	film	PIM-EA-TB film / Au nanoparticles / ITO	Electrocatalytic oxidation of glucose	34
	film	Free-standing film	Ionic diode	42, 44
	film	Free-standing film	Electro-osmotic molecular pumping	48
	carbon	Pd@carbonised PIM-EA-TB	Gas redox reactions	52
PIM-1	carbon	Carbonised PIM-1	Active material in supercapacitors	51
	film	PIM-1 film on polyacrylonitrile supports	All-vanadium redox flow battery	35
	film	PIM-1 film on electrodes	Artificial SEI layers in batteries	40

PIMs	State	Electrode Configuration	Application	Ref.
PIM-1	nanoparticles	PIM-PY nanoparticles on Pt or GCE electrode	Enhancing O_2 and H_2 binding and thus their electrocatalytic reactivity	63
	film	Pt@g-C_3N_4/PIM-1 coating	Photocatalytic H_2 generation in the presence of quencher	64
	film	Pt@g-C_3N_4/PIM-1 coating on a Clark probe	Photocatalytic H_2 production and O_2 consumption	66
	Film or particles	g-C_3N_4@PIM-1	Photocatalytic H_2O_2 production	67
PIM-EA-TB-H_2	carbon	Pt@carbonised PIM-EA-TB-H_2	Selective oxidation of H_2	53
PIM-Trip-TB	membrane	Free-standing membrane	Enhancement of membrane gas selectivity	23
PIM-PY	nanoparticles	PIM-PY nanoparticles on Pt or GCE electrode	Enhancing O_2 and H_2 binding and thus their electrocatalytic reactivity	63
PIM-7	film	Pd@PIM-7	Electrocatalytic H_2 evolution and HCOOH oxidation	62

Electrochemical Methods Based on PIM-modified Electrodes. Electrode modification by PIMs is readily achieved by drop-casting or spin-coating a thin layer of film from a PIM solution onto an electrode (different cases of PIM components electrodes are shown in Figure 1.5). The PIM solution could be pure PIM or PIM incorporated with other reactive species. The electrode could be bare (glassy carbon electrode, Pt electrode, graphene electrode, or any other types of conducting substrates like indium tin oxide (ITO) or fluorine-doped tin oxide (FTO)), or an electrode with pre-deposited active materials on the surface. Generally, PIMs act as a scaffold providing robust porosity for reactions to happen, but also preventing the formation of macroscopic gas bubbles and promoting the surface reactivity

when gas evolution is involved in the electrochemical reaction. [30] The developments of PIM applications in electrochemistry over recent years are summarised in Figure 1.6.

One of the remarkable features of PIMs is the versatility of their synthesis, making it possible to introduce different functional groups into the structure. [9] Taking PIM-EA-TB for example, there are tertiary amines in the polymer backbone, which allows protonation to happen, leading to further binding with anions (e.g. $PdCl_4^{2-}$) [31]. PIM-EA-TB films can also incorporate/absorb redox active species like indigo carmine to complement the intrinsic cation charge in the polymer structure (Figure 1.5A). [31] Both species mentioned here display redox reactivity when tested under electrochemical conditions immersed in an electrolyte.

Apart from providing permeability towards small species, PIMs are also used to immobilise large guest molecules. PIM-EA-TB was reported to form an organo-gel (Figure 1.5B) with an organic water-immiscible phase called 4-(3-phenyl-propyl)pyridine (PPP). [32] An example redox active metal complex tetraphenylporphyrinato-Mn(III)Cl (MnTPP) was embedded in the organo-gel phase and showed cyclic voltammetry responses for the Mn(II/III) redox reaction. The mechanism of this process was explained as a combination of electron transfer (electrode | organo-gel) and anion transfer (electrolyte | organo-gel). In this case, PIM-EA-TB acts as a scaffold to stabilise the organo-gel / aqueous electrolyte phase boundary.

For species soluble in chloroform or THF, it is readily conceivable to immobilise them into PIMs by co-deposition of a mixed solution of PIMs and species (Figure 1.5C). The encapsulation of tetraphenylporphyrinato-Fe(II) or FeTPP into PIM-EA-TB film was achieved by drop-casting the same chloroform solution (containing FeTPP and PIM-EA-TB) onto a glassy carbon electrode. [33] The resulting film was electrochemically active and investigated to detect O_2 and H_2O_2.

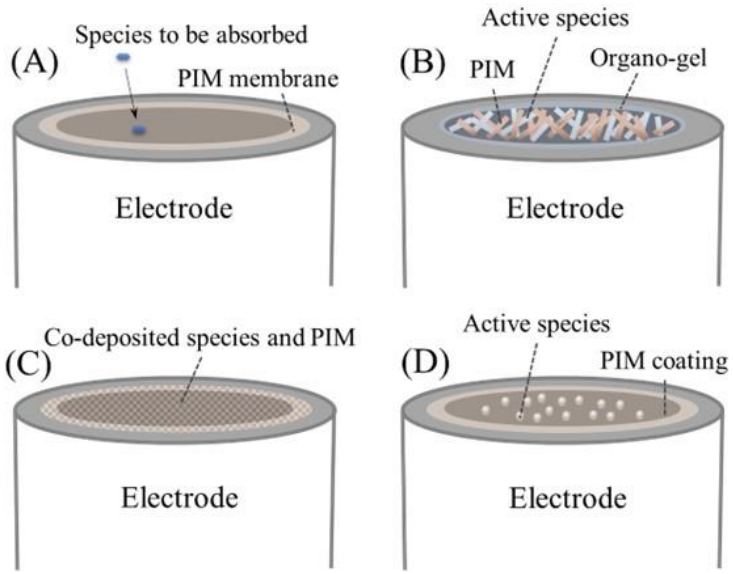

Figure 1.5 Different ways to apply PIMs membrane and active species onto electrodes. (A) Applying pure PIMs membrane onto an electrode, and then absorbing species from solutions; (B) Mixing PIMs and active species (not soluble in chloroform or THF) with another organo-solvent to form an organo-gel; (C) Dissolving PIMs and active species into the same solvent (chloroform or THF) and then co-depositing the mixture onto electrodes; (D) Depositing active species on electrodes followed by PIM coating over the surface.

In addition to encapsulating different electroactive materials into PIMs by absorbing, mixing, and co-depositing, it is possible to directly apply a thin PIM film over the surface of catalysts (Figure 1.5D). This can protect and enhance the properties of the catalyst. Gold nanoparticles were electrodeposited on an ITO electrode, followed by coating a thin layer of PIM-EA-TB. [34] The PIM coating not only enhanced the reactivity of Au nanoparticles towards glucose catalytic oxidation, but prevented the poisoning from proteins in the solution, probably because of size selectivity.

Electrochemical Methods Based on PIMs-Membranes. The facile production of free-standing PIM membranes makes it feasible to study ion transport inside the polymer as well as applications of PIMs in batteries, and in energy conversion. For adapting PIM membranes to different applications, methods are used to produce robust macro-sized (several cm^2 or even larger) or smaller sized (a few μm^2) films. In the former, spin-coating PIM solution on a smooth solid substrate, followed by evaporation, lifting, and transferring onto another substrate will give a uniform film with controllable thickness and area. Alternatively, for the

latter, inert substrates (for example, polyethylene terephthalate, or PET film) with laser drilled micro-holes can be used to define the effective area of PIM membranes.

Excellent processibility, permeability and selectivity to species in liquids have been essential for PIMs to be applied in energy storage and conversion. PIMs have been shown to have high proton/vanadium selectivity for all-vanadium redox flow battery system (PIM-1 [35]), high polysulfide-blocking ability for lithium-sulfur flow battery systems (cross-linked PIM-1 [36]), and self-healing anti-corrosion ability for the protection of aluminium alloy (PIM-1 [37]). Moreover, PIMs can suppress copper colloidal corrosion (PIM-EA-TB [38]), act as an artificial solid-electrolyte-interphase (SEI) layer in batteries to avoid dendrimer growth (PIM-DMBP-TB [39], PIM-1 [40]), and stabilise catalysts in fuel cells (PIM-EA-TB [41]).

When applied to a PET film with micro-holes, PIM-EA-TB films were demonstrated to act as an ionic diode and tested by a four-electrode voltammetry experiment. [42] Protonation of the polyamine happens at approximately pH < 4, which is responsible for the ability of PIM-EA-TB to switch from neutral anion/cation-conducting to protonated anion-conducting behaviour. PIM-EA-TB asymmetrically deposited onto PET micro-holes was shown to exhibit ionic rectification behaviour leading to potential applications in water desalination. [43] Further studies indicate PIM-EA-TB with pH-induced reversal of ionic diode polarity, [44] and anion uptake and transport effects [45]. Other types of ionic diodes were developed by Putra *et al.* [46] by creating heterojunctions between PIM-EA-TB and Nafion polymer. The heterojunction diode was proposed to be sensitive to perchlorate and potassium ions as a sensor. [47]

Molecular transport through PIM membranes is also of great interest in terms of better understanding of the structure inside PIMs, accumulation and removal of pollutants, or water molecules transport during electroosmosis. Electro-osmotic molecular pumping phenomena through PIM-EA-TB membranes were investigated by Li *et al.* [48]. The binding and accumulation of caffeic acid into PIM-EA-TB microchannels caused modulation of the ionic current. A voltage-driven caffeic acid pump was proposed. Furthermore, the electroosmotic transport of water through PIM-EA-TB was observed coupled to chloride anion transport. [49]

Electrochemical Methods Based on carbonised PIMs. PIMs are carbonised (cPIM) without loss of the microporosity structure during vacuum thermolysis, resulting in electrically conducting porous heterocarbons (nitrogen retaining from functional groups of

the PIM structure). One of the carbon products from PIM-EA-TB at 500 °C showed pH-dependent capacitance – higher capacitance in acidic solution probably undergoing redox-driven proton insertion and expulsion. [50] Another microporous caron powder produced from PIM-EA-TB-H_2 exhibited pH-dependent capacitance switching over a wide pH range after being immersed into aqueous $HClO_4$. [50] Moreover, a hierarchical porous carbon based on PIM-1 was produced by Jeon *et al.* [51] to be applied as active material in supercapacitors showing long-term cycling stability.

Composites of metal and cPIM (or metal@cPIM) can be produced by pre-impregnating a metal precursor into PIMs followed by the carbonisation process. Based on this routine, Pd@cPIM was prepared by Liong *et al.* [52] by immobilising $PdCl_4^{2-}$ into PIM-EA-TB and vacuum carbonisation. Liquid and gas can bind simultaneously to Pd@cPIM, creating triphasic conditions, giving rise to selectivity towards gas redox reactions, particularly H_2 oxidation or O_2 reduction.

By embedding $PtCl_6^{2-}$ into PIM-EA-TB-H_2, Pt nanoparticles within heterocarbon (or Pt@cPIM) were produced by Adamik *et al.* [53] after carbonisation at 700 °C. Pt@cPIM has been demonstrated to be reactive towards H_2 oxidation instead of bigger molecules in methanol oxidation or in oxygen reduction. Direct formation of H_2O_2 was observed with this catalyst in the presence of O_2 and H_2.

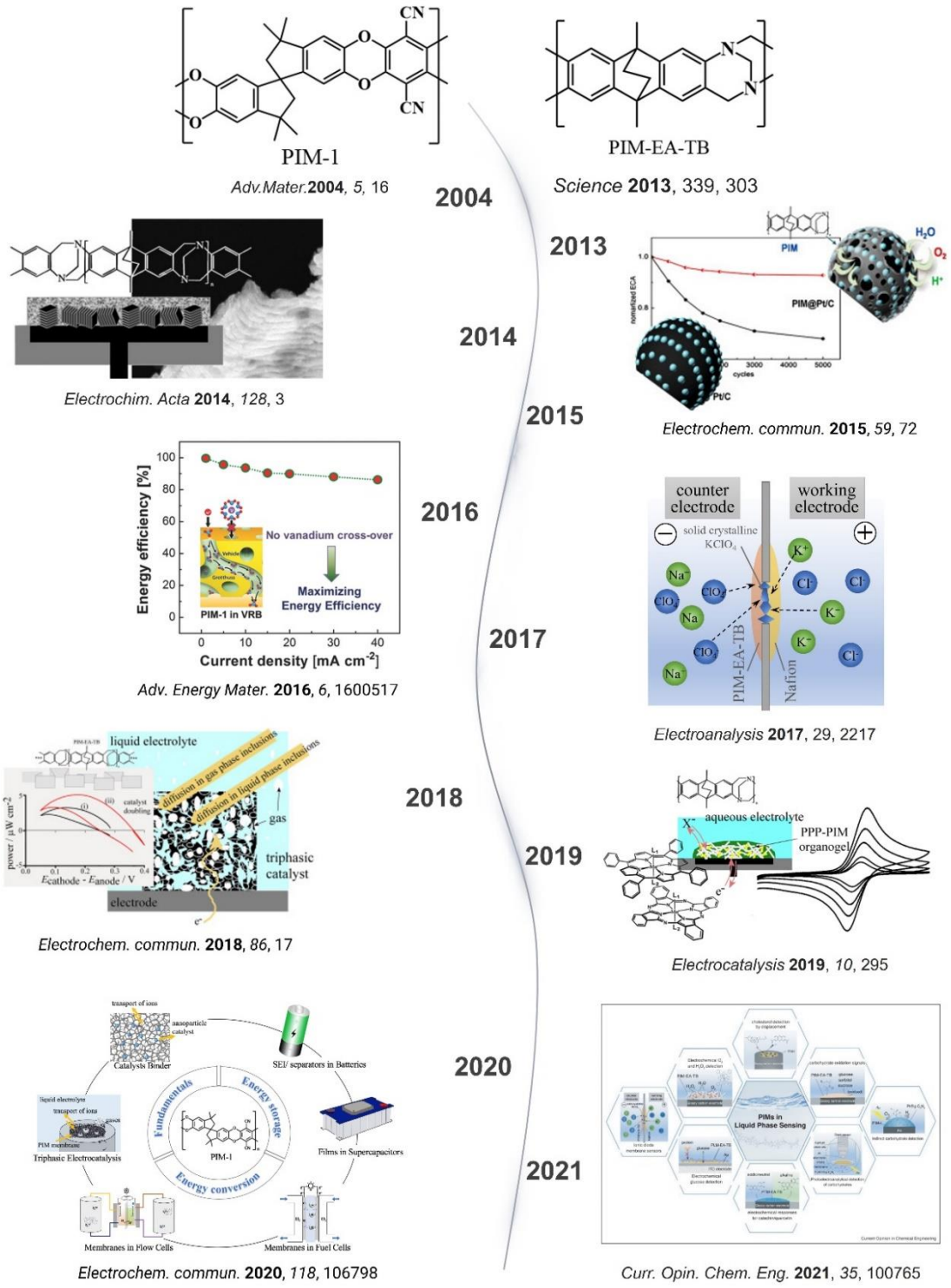

Figure 1.6 Developments of applications of PIMs in electrochemistry and electrocatalysis

1.4 Applications of PIMs in Catalysis and in Photocatalysis

PIM materials, as inert microporous hosts, are employed to incorporate catalysts or photocatalysts in electrochemical processes. Rigid microporosity in PIMs provides access to

active surface sites and sometimes induces reactions in a confined environment, thus catalytically enhancing the reaction rate. [29] PIMs and modified PIMs in the form of both nanoparticles and films have been used for catalysis applications for C-C bond formation, CO_2 conversion and cyclisations, and oxidation reactions. [54] In this introduction, the focus is on applications of PIMs in catalysis and photocatalysis are focused on and elaborated in detail.

Applications of PIMs in Catalysis. PIMs have been applied to aid catalytic oxidation of aliphatic/aromatic alcohols and carbohydrates. The immobilisation of 4-benzoyloxy-2,2,6,6-tetramethylpiperidine-1-oxyl (4B-TEMPO) into PIM-EA-TB by co-deposition was reported to produce films with catalytic reactivity towards oxidation of alcohols in alkaline condition [55] and towards oxidation of glucose, sorbitol, and sucrose [56].

PIMs can create triphasic conditions beneficially affecting the interfacial reaction and the permeability to both gas and liquid. Metal nanoparticles were demonstrated to be embedded in PIMs to resist poisoning, [57] detrimental loss, and corrosion [58]. Silver nanoparticles coated with PIM-EA-TB were shown to be electrocatalytically active towards two-electron reduction of nitrate to nitrite. [59] The PIM-EA-TB polymer coating provided mechanical protection and prevents loss and dislodgement of silver catalyst. Platinum, as a fuel cell anode catalyst, was shown to be stabilised by PIM-EA-TB coating for three different fuel cell anode reactions: methanol oxidation, ethanol oxidation, and formic acid oxidation. [60] PIM-EA-TB was reported to produce conducting platinum nanoparticle networks which could be beneficial in electrocatalysis and sensing. [61] Furthermore, the catalytic reactivity of palladium towards hydrogen evolution and formic acid oxidation was enhanced by applying a PIM-7 coating. [62]

PIMs have also seen employed in the form of nanoparticles. Both PIM-1 and PIM-PY nanoparticles were produced by an anti-solvent precipitation method. [63] Typically, a PIM chloroform solution being dropped into vigorously stirred absolute alcohol solutions like isopropanol or ethanol is a way to produce PIM nanoparticles. PIM nanoparticles can be separated from the alcohol suspension by a high-speed centrifuge. Voltammetry results suggest hydrogen and oxygen binding to PIM nanoparticles on the electrode surface. Gas storage and binding induce electrocatalytic reactivity for oxygen reduction and for hydrogen oxidation.

Applications of PIMs in Photocatalysis. PIMs have been applied to help immobilising photocatalysts. Graphitic carbon nitride (g-C_3N_4) with photo-deposited platinum nanoparticles, Pt@g-C_3N_4, has been reported to generate hydrogen under light in the presence of hole quenchers. [64] When coated with PIM-1, a higher photocurrent of Pt@g-C_3N_4 from hydrogen production was observed. Better performance with PIM-1 was proposed due to triphasic conditions created by the microporous film of PIM-1. Further work based on Pt@g-C_3N_4 with PIM-1 coating has been reported for the indirect detection of carbohydrates. [65] Sugars or carbohydrates were applied as hole quenchers during the photo-generation of hydrogen. A connection between potentiometry signal, hydrogen generation, and hole quencher (carbohydrates) monitoring was established. PIM-1 in this case made it facile to attach catalysts on a thin palladium membrane by simply suspension (Pt@g-C_3N_4 catalysts mixed in PIM-1 chloroform solution) casting. Moreover, with the aid of a Clark sensor, hydrogen production and oxygen consumption have been detected for Pt@g-C_3N_4 with PIM-1 coatings in the presence of hole quenchers with different molecular sizes. [66] PIM-1 was shown to have distinct size selectivity over quencher species, resulting in high reactivity when the quencher was small and flexible (*e.g.* gluconic acid) instead of big and rigid (*e.g.* raffinose). Recent work by Zhao *et al.* [67] proved that the absorption of quencher (Triton X-100) into PIM-1 host environment has enhanced the photochemical production of hydrogen peroxide on g-C_3N_4.

Studies show that PIMs themselves can be photocatalysts for pollutant degradation, detoxification of chemical warfare agent simulants, or for hydrogen production. Functional PIMs with zwitterionic and D–π–A structures produced by Tang and co-workers [68] exhibited visible-light-driven catalytic activity for the degradation of organic dyes in the absence of sacrificial components or metal co-catalysts. In this PIM structure, phenyl rings link tertiary amines (electron donors, D) to the neighbouring quaternized ammonium (electron acceptors, A). The visible-light absorption and intramolecular charge-carrier separation/migration are boosted by the D–π–A structures. On another study it was demonstrated that porphyrin-based PIMs can degrade a mustard-gas simulant under light. [69] Linear conjugated PIMs were synthesised and tested as photocatalysts for hydrogen production from water. [70] Porous and wettable conjugated PIMs were permeable to water, thus showing high performance without the need for added photocatalysts.

Overall, PIMs prove to be versatile as hosts for catalysts. This work will contribute to developing new combination of catalysts and PIM hosts for catalytic reactions involving H_2 and H_2O_2 production.

1.5 Project Aims

The work presented in this thesis aims to explore the potential applications of PIMs for biomass conversion with embedded heterogeneous redoxcatalysts. Biomass comprises all biological materials, including living or recently living organisms which can be used for the generation of different forms of energy (*e.g.* heat, electrical, and chemical energy) and useful material products [71] such as gaseous fuels (*e.g.* hydrogen), and industrial bleaching agents (*e.g.* hydrogen peroxide). As an abundant and renewable energy source, biomass has been considered one of the most promising alternatives to fossil fuels. Most biomass molecules are very hard to break up and therefore in this study formic acid is employed as a model case for biomass conversion. Formic acid or formate is a simple product which can be yielded from model biomass materials like glucose, starch, and cellulose. Formic acid is attractive as a sustainable hydrogen source when carrying out fundamental and primary studies.

The aims of this thesis are:

- To develop an understanding of the role of PIMs as hosts for heterogeneous catalysis for redoxcatalysis.
- To develop new experimental tools and to explore the mechanisms of reactions occurring within PIM composites.
- To optimise and extend the applications of PIMs for useful product formation (H_2 or H_2O_2 from biomass).

1.6 References

1 Budd, P. M., Elabas, E. S., Ghanem, B. S., Makhseed, S., McKeown, N. B., Msayib, K. J., Tattershall, C. E. & Wang, D. Solution-processed, organophilic membrane derived from a polymer of intrinsic microporosity. *Advanced Materials* **16**, 456-459 (2004).

2 Wang, Y., McKeown, N. B., Msayib, K. J., Turnbull, G. A. & Samuel, I. D. Laser chemosensor with rapid responsivity and inherent memory based on a polymer of intrinsic microporosity. *Sensors* **11**, 2478-2487 (2011).

3 Rakow, N. A., Wendland, M. S., Trend, J. E., Poirier, R. J., Paolucci, D. M., Maki, S. P., Lyons, C. S. & Swierczek, M. J. Visual indicator for trace organic volatiles. *Langmuir* **26**, 3767-3770 (2010).

4 Budd, P. M., McKeown, N. B., Ghanem, B. S., Msayib, K. J., Fritsch, D., Starannikova, L., Belov, N., Sanfirova, O., Yampolskii, Y. & Shantarovich, V. Gas permeation parameters and other physicochemical properties of a polymer of intrinsic microporosity: Polybenzodioxane PIM-1. *Journal of Membrane Science* **325**, 851-860 (2008).

5 Lee, W. H., Seong, J. G., Hu, X. & Lee, Y. M. Recent progress in microporous polymers from thermally rearranged polymers and polymers of intrinsic microporosity for membrane gas separation: pushing performance limits and revisiting trade-off lines. *Journal of Polymer Science* **58**, 2450-2466 (2020).

6 Marken, F., Wang, L., Zhao, Y., Li, Z., Amiri, M., & Imanzadeh, H. Polymers of intrinsic microporosity (PIMs) in sensing and in electroanalysis. *Current Opinion in Chemical Engineering* **35**, 100765 (2022).

7 Madrid, E. & McKeown, N. B. Innovative methods in electrochemistry based on polymers of intrinsic microporosity. *Current Opinion in Electrochemistry* **10**, 61-66 (2018).

8 McKeown, N. B. Polymers of intrinsic microporosity (PIMs). *Polymer* **202**, 122736 (2020).

9 McKeown, N. B. The synthesis of polymers of intrinsic microporosity (PIMs). *Science China Chemistry* **60**, 1023-1032 (2017).

10 McKeown, N. B. The structure-property relationships of Polymers of Intrinsic Microporosity (PIMs). *Current Opinion in Chemical Engineering* **36**, 100785 (2022).

11 Budd, P. M., Ghanem, B. S., Makhseed, S., McKeown, N. B., Msayib, K. J., & Tattershall, C. E. Polymers of intrinsic microporosity (PIMs): robust, solution-processable, organic nanoporous materials. *Chemical Communications*, 230-231 (2004).

12 Du, N., Song, J., Robertson, G. P., Pinnau, I. & Guiver, M. D. Linear high molecular weight ladder polymer via fast polycondensation of 5, 5′, 6, 6′-tetrahydroxy-3, 3, 3′, 3′-tetramethylspirobisindane with 1, 4-dicyanotetrafluorobenzene. *Macromolecular Rapid Communications* **29**, 783-788 (2008).

13 Carta, M., Malpass-Evans, R., Croad, M., Rogan, Y., Lee, M., Rose, I., & McKeown, N. B. The synthesis of microporous polymers using Tröger's base formation. *Polymer Chemistry* **5**, 5267-5272 (2014).

14 Carta, M., Malpass-Evans, R., Croad, M., Rogan, Y., Jansen, J. C., Bernardo, P., Bazzarelli, F. & McKeown, N. B. An efficient polymer molecular sieve for membrane gas separations. *Science* **339**, 303-307 (2013).

15 Marken, F., Carta, M. & McKeown, N. B. Polymers of intrinsic microporosity in the design of electrochemical multicomponent and multiphase interfaces. *Analytical Chemistry* **93**,1213-1220 (2021)

16 Yin, H., Yang, B., Chua, Y. Z., Szymoniak, P., Carta, M., Malpass-Evans, R., McKeown, N. B., Harrison, W. J., Budd, P. M., Schick, C., Böhning, M. & Schönhals, A. Effect of backbone rigidity on the glass transition of polymers of intrinsic microporosity probed by fast scanning calorimetry. *ACS Macro letters* **8**, 1022-1028 (2019).

17 Polak-Kraśna, K., Dawson, R., Holyfield, L. T., Bowen, C. R., Burrows, A. D., & Mays, T. J. Mechanical characterisation of polymer of intrinsic microporosity PIM-1 for hydrogen storage applications. *Journal of Materials Science* **52**, 3862-3875 (2017).

18 Thommes, M., Kaneko, K., Neimark, A. V., Olivier, J. P., Rodriguez-Reinoso, F., Rouquerol, J., & Sing, K. S. Physisorption of gases, with special reference to the evaluation of surface area and pore size distribution (IUPAC Technical Report). *Pure and Applied Chemistry* **87**, 1051-1069 (2015).

19 Minelli, M., Paul, D. R. & Sarti, G. C. On the interpretation of cryogenic sorption isotherms in glassy polymers. *Journal of Membrane Science* **540**, 229-242 (2017).

20 Wang, Y., Ma, X., Ghanem, B. S., Alghunaimi, F., Pinnau, I., & Han, Y. Polymers of intrinsic microporosity for energy-intensive membrane-based gas separations. *Materials Today Nano* **3**, 69-95 (2018).

21 Freeman, B. D. Basis of permeability/selectivity tradeoff relations in polymeric gas separation membranes. *Macromolecules* **32**, 375-380 (1999).

22 Williams, R., Burt, L. A., Esposito, E., Jansen, J. C., Tocci, E., Rizzuto, C., Lanč, M., Carta, M. & McKeown, N. B. A highly rigid and gas selective methanopentacene-based polymer of intrinsic microporosity derived from Tröger's base polymerization. *Journal of Materials Chemistry A* **6**, 5661-5667 (2018).

23 Carta, M., Croad, M., Malpass-Evans, R., Jansen, J. C., Bernardo, P., Clarizia, G., Friess, K., Lanč, M. & McKeown, N. B. Triptycene induced enhancement of membrane gas selectivity for microporous Tröger's base polymers. *Advanced Materials* **26**, 3526-3531 (2014).

24 Fuoco, A., Comesaña-Gándara, B., Longo, M., Esposito, E., Monteleone, M., Rose, I., Bezzu., C. G., Carta, M., McKeown, N. B. & Jansen, J. C. Temperature dependence of gas permeation and diffusion in triptycene-based ultrapermeable polymers of intrinsic microporosity. *ACS Applied Materials & Interfaces* **10**, 36475-36482 (2018).

25 Fuoco, A., Rizzuto, C., Tocci, E., Monteleone, M., Esposito, E., Budd, P. M., Carta, M., Comesaña-Gándara, B., McKeown, N. B. & Jansen, J. C. The origin of size-selective gas transport through polymers of intrinsic microporosity. *Journal of Materials Chemistry A* **7**, 20121-20126 (2019).

26 Ramimoghadam, D., Gray, E. M. & Webb, C. Review of polymers of intrinsic microporosity for hydrogen storage applications. *International Journal of Hydrogen Energy* **41**, 16944-16965 (2016).

27 Ye, H., Zhang, C., Huo, C., Zhao, B., Zhou, Y., Wu, Y., & Shi, S. Advances in the Application of Polymers of Intrinsic Microporosity in Liquid Separation and Purification: Membrane Separation and Adsorption Separation. *Polymer Reviews* **61**, 239-279 (2021).

28 Wang, L., Zhao, Y., Fan, B., Carta, M., Malpass-Evans, R., McKeown, N. B., & Marken, F. Polymer of intrinsic microporosity (PIM) films and membranes in electrochemical energy storage and conversion: a mini-review. *Electrochemistry Communications* **118**, 106798 (2020).

29 Antonangelo, A. R., Hawkins, N. & Carta, M. Polymers of intrinsic microporosity (PIMs) for catalysis: a perspective. *Current Opinion in Chemical Engineering* **35**, 100766 (2022).

30 Marken, F., Madrid, E., Zhao, Y., Carta, M. & McKeown, N. B. Polymers of intrinsic microporosity in triphasic electrochemistry: perspectives. *ChemElectroChem* **6**, 4332-4342 (2019).

31 Xia, F., Pan, M., Mu, S., Malpass-Evans, R., Carta, M., McKeown, N. B., Attard, G. A., Brew, A., Morgan, D. J. & Marken, F. Polymers of intrinsic microporosity in electrocatalysis: Novel pore rigidity effects and lamella palladium growth. *Electrochimica Acta* **128**, 3-9 (2014).

32 Ganesan, V., Madrid, E., Malpass-Evans, R., Carta, M., McKeown, N. B., & Marken, F. Biphasic Voltammetry and Spectroelectrochemistry in Polymer of Intrinsic Microporosity−4-(3-Phenylpropyl)-Pyridine Organogel/Aqueous Electrolyte Systems: Reactivity of MnPc Versus MnTPP. *Electrocatalysis* **10**, 295-304 (2019).

33 Rong, Y., Malpass-Evans, R., Carta, M., McKeown, N. B., Attard, G. A., & Marken, F. High density heterogenisation of molecular electrocatalysts in a rigid intrinsically microporous polymer host. *Electrochemistry Communications* **46**, 26-29 (2014).

34 Rong, Y., Malpass-Evans, R., Carta, M., McKeown, N. B., Attard, G. A., & Marken, F. Intrinsically porous polymer protects catalytic gold particles for enzymeless glucose oxidation. *Electroanalysis* **26**, 904-909 (2014).

35 Chae, I. S., Luo, T., Moon, G. H., Ogieglo, W., Kang, Y. S., & Wessling, M. Ultra-high proton/vanadium selectivity for hydrophobic polymer membranes with intrinsic nanopores for redox flow battery. *Advanced Energy Materials* **6**, 1600517 (2016).

36 Doris, S. E., Ward, A. L., Frischmann, P. D., Li, L. & Helms, B. A. Understanding and controlling the chemical evolution and polysulfide-blocking ability of lithium-sulfur battery membranes cast from polymers of intrinsic microporosity. *Journal of Materials Chemistry A* **4**, 16946-16952 (2016).

37 Li, Z., Qin, B., Zhang, X., Wang, K., Wei, Y., & Ji, Y. Self-healing anti-corrosion coatings based on polymers of intrinsic microporosity for the protection of aluminum alloy. *RSC Advances* **5**, 104451-104457 (2015).

38 Langley, A. R., Carta, M., Malpass-Evans, R., McKeown, N. B., Dawes, J. H., Murphy, E., & Marken, F. Linking the Cu (II/I) potential to the onset of dynamic phenomena at corroding copper microelectrodes immersed in aqueous 0.5 M NaCl. *Electrochimica Acta* **260**, 348-357 (2018).

39 Qi, L., Shang, L., Wu, K., Qu, L., Pei, H., Li, W., Zhang, L., Wu, Z., Zhou, H., McKeown, N. B., Zhang, W. & Yang, Z. An interfacial layer based on polymers of intrinsic microporosity to suppress dendrite growth on Li metal anodes. *Chemistry–A European Journal* **25**, 12052-12057 (2019).

40 Ma, L., Fu, C., Li, L., Mayilvahanan, K. S., Watkins, T., Perdue, B. R., Zavadil, W. R. & Helms, B. A. Nanoporous polymer films with a high cation transference number stabilize lithium metal anodes in light-weight batteries for electrified transportation. *Nano Letters* **19**, 1387-1394 (2019).

41 He, D., Rong, Y., Carta, M., Malpass-Evans, R., McKeown, N. B., & Marken, F. Fuel cell anode catalyst performance can be stabilized with a molecularly rigid film of polymers of intrinsic microporosity (PIM). *RSC Advances* **6**, 9315-9319 (2016).

42 Madrid, E., Rong, Y., Carta, M., McKeown, N. B., Malpass-Evans, R., Attard, G. A., Clarke, T. J., Taylor, S. H., Long. Y.-T. & Marken, F. Metastable Ionic Diodes Derived from an Amine-Based Polymer of Intrinsic Microporosity. *Angewandte Chemie* **126**, 10927-10930 (2014).

43 Madrid, E., Cottis, P., Rong, Y., Rogers, A. T., Stone, J. M., Malpass-Evans, R., Carta, M., McKeown, N. B. & Marken, F. Water desalination concept using an ionic rectifier based on a polymer of intrinsic microporosity (PIM). *Journal of Materials Chemistry A* **3**, 15849-15853 (2015).

44 Rong, Y., Song, Q., Mathwig, K., Madrid, E., He, D., Niemann, R. G., Cameron, P. J., Dale, S. E.C., Bending, S., Carta, M., Malpass-Evans, R., McKeown, N. B. & Marken, F. pH-induced reversal of ionic diode polarity in 300 nm thin membranes based on a polymer of intrinsic microporosity. *Electrochemistry Communications* **69**, 41-45 (2016).

45 Rong, Y., Kolodziej, A., Madrid, E., Carta, M., Malpass-Evans, R., McKeown, N. B., & Marken, F. Polymers of intrinsic microporosity in electrochemistry: Anion uptake and transport effects in thin film electrodes and in free-standing ionic diode membranes. *Journal of Electroanalytical Chemistry* **779**, 241-249 (2016).

46 Putra, B. R., Aaronson, B. D., Madrid, E., Mathwig, K., Carta, M., Malpass-Evans, R., McKeown, N. B. & Marken, F. Ionic Diode Characteristics at a Polymer of Intrinsic Microporosity (PIM) | Nafion "Heterojunction" Deposit on a Microhole Poly (ethylene-terephthalate) Substrate. *Electroanalysis* **29**, 2217-2223 (2017).

47 Putra, B. R., Carta, M., Malpass-Evans, R., McKeown, N. B. & Marken, F. Potassium cation induced ionic diode blocking for a polymer of intrinsic microporosity | nafion "heterojunction" on a microhole substrate. *Electrochimica Acta* **258**, 807-813 (2017).

48 Li, Z., Wang, L., Malpass-Evans, R., Carta, M., McKeown, N. B., Mathwig, K., Fletcher, P. J. & Marken, F. Ionic Diode and Molecular Pump Phenomena Associated with Caffeic Acid Accumulated into an Intrinsically Microporous Polyamine (PIM-EA-TB). *ChemElectroChem* **8**, 2044-2051 (2021).

49 Li, Z., Malpass-Evans, R., McKeown, N. B., Carta, M., Mathwig, K., Lowe, J. P., & Marken, F. Effective electroosmotic transport of water in an intrinsically microporous polyamine (PIM-EA-TB). *Electrochemistry Communications* **130**, 107110 (2021).

50 Rong, Y., He, D., Sanchez-Fernandez, A., Evans, C., Edler, K. J., Malpass-Evans, R., Carta, M., McKeown, N. B., Clarke, T. J., Taylor, S. H., Wain, A. J., Mitchels, J. M. & Marken, F. Intrinsically microporous polymer retains porosity in vacuum thermolysis to electroactive heterocarbon. *Langmuir* **31**, 12300-12306 (2015).

51 Jeon, J. W., Han, J. H., Kim, S. K., Kim, D. G., Kim, Y. S., Suh, D. H., Hong, Y. T., Kim, T. H., & Kim, B. G. Intrinsically microporous polymer-based hierarchical nanostructuring of electrodes via nonsolvent-induced phase separation for high-performance supercapacitors. *Journal of Materials Chemistry A* **6**, 8909-8915 (2018).

52 Leong, S. X., Carta, M., Malpass-Evans, R., McKeown, N. B., Madrid, E., & Marken, F. One-step preparation of microporous Pd@cPIM composite catalyst film for triphasic electrocatalysis. *Electrochemistry Communications* **86**, 17-20 (2018).

53 Adamik, R. K., Hernández-Ibáñez, N., Iniesta, J., Edwards, J. K., Howe, A. G., Armstrong, R. D., Taylor, S. H., Roldan, A., Rong, Y., Malpass-Evans, R., Carta, M., McKeown, N. B., He, D. & Marken, F. Platinum nanoparticle inclusion into a carbonized polymer of intrinsic microporosity: electrochemical characteristics of a catalyst for electroless hydrogen peroxide production. *Nanomaterials* **8**, 542 (2018).

54 Antonangelo, A. R., Hawkins, N. & Carta, M. Polymers of intrinsic microporosity (PIMs) for catalysis: a perspective. *Current Opinion in Chemical Engineering* **35**, 100766 (2022).

55 Ahn, S. D., Kolodziej, A., Malpass-Evans, R., Carta, M., McKeown, N. B., Bull, S. D., Buchard, A. & Marken, F. Polymer of intrinsic microporosity induces host-guest substrate selectivity in heterogeneous 4-benzoyloxy-TEMPO–catalysed alcohol oxidations. *Electrocatalysis* **7**, 70-78 (2016).

56 Kolodziej, A., Ahn, S. D., Carta, M., Malpass-Evans, R., McKeown, N. B., Chapman, R. S., Bull, S. D. & Marken, F. Electrocatalytic carbohydrate oxidation with 4-benzoyloxy-TEMPO heterogenised in a polymer of intrinsic microporosity. *Electrochimica Acta* **160**, 195-201 (2015).

57 Rong, Y., Malpass-Evans, R., Carta, M., McKeown, N. B., Attard, G. A., & Marken, F. Intrinsically porous polymer protects catalytic gold particles for enzymeless glucose oxidation. *Electroanalysis* **26**, 904-909 (2014).

58 He, D., Rong, Y., Kou, Z., Mu, S., Peng, T., Malpass-Evans, R., Carta, M., McKeown, N. B. & Marken, F. Intrinsically microporous polymer slows down fuel cell catalyst corrosion. *Electrochemistry Communications* **59**, 72-76 (2015).

59 He, D., Rauwel, E., Malpass-Evans, R., Carta, M., McKeown, N. B., Gorle, D. B., Kulandainathan, M. A. & Marken, F. (2017). Redox reactivity at silver

microparticle−glassy carbon contacts under a coating of polymer of intrinsic microporosity (PIM). *Journal of Solid State Electrochemistry* **21**, 2141-2146 (2017).

60 He, D., Rong, Y., Carta, M., Malpass-Evans, R., McKeown, N. B., & Marken, F. Fuel cell anode catalyst performance can be stabilized with a molecularly rigid film of polymers of intrinsic microporosity (PIM). *RSC Advances* **6**, 9315-9319 (2016).

61 He, D., He, D. S., Yang, J., Low, Z. X., Malpass-Evans, R., Carta, M., McKeown, N. B. & Marken, F. Molecularly rigid microporous polyamine captures and stabilizes conducting platinum nanoparticle networks. *ACS Applied Materials & Interfaces* **8**, 22425-22430 (2016).

62 Mahajan, A., Bhattacharya, S. K., Rochat, S., Burrows, A. D., Fletcher, P. J., Rong, Y., Dalton, A. B., McKeown, N. B. & Marken, F. Polymer of intrinsic microporosity (PIM-7) coating affects triphasic palladium electrocatalysis. ChemElectroChem **6**, 4307-4317 (2019).

63 Madrid, E., Lowe, J. P., Msayib, K. J., McKeown, N. B., Song, Q., Attard, G. A., Düren, T. & Marken, F. Triphasic nature of polymers of intrinsic microporosity induces storage and catalysis effects in hydrogen and oxygen reactivity at electrode surfaces. *ChemElectroChem* **6**, 252-259 (2019).

64 Zhao, Y., Al Abass, N. A., Malpass-Evans, R., Carta, M., Mckeown, N. B., Madrid, E., Fletcher, P. J. & Marken, F. Photoelectrochemistry of immobilised Pt@g-C_3N_4 mediated by hydrogen and enhanced by a polymer of intrinsic microporosity PIM-1. *Electrochemistry Communications* **103**, 1-6 (2019).

65 Zhao, Y., Dobson, J., Harabajiu, C., Madrid, E., Kanyanee, T., Lyall, C., Reeksting, S., Carta, M., McKeown, N. B., Torrente-Murciano, L., Black, K. & Marken, F. Indirect photo-electrochemical detection of carbohydrates with Pt@g-C_3N_4 immobilised into a polymer of intrinsic microporosity (PIM-1) and attached to a palladium hydrogen capture membrane. *Bioelectrochemistry* **134**, 107499 (2020).

66 Zhao, Y., Malpass-Evans, R., Carta, M., McKeown, N. B., Fletcher, P. J., Kociok-Köhn, G., Lednitzky, D. & Marken, F. Size-Selective photoelectrochemical reactions in microporous environments: Clark probe investigation of Pt@g-C_3N_4 embedded into intrinsically microporous polymer (PIM-1). *ChemElectroChem* **8**, 3499-3505 (2021).

67 Zhao, Y., Wang, L., Malpass-Evans, R., McKeown, N. B., Carta, M., Lowe, J. P., Lyall, C. L., Castaing, R., Fletcher, P. J., Kociok-Köhn, G., Wenk, J., Guo, Z. & Marken, F. Effects of g-C_3N_4 heterogenization into intrinsically microporous polymers on the photocatalytic generation of hydrogen peroxide. *ACS Applied Materials & Interfaces* **14**, 19938-48 (2022).

68 Tang, Q., Gong, J., Zhao, Q. Efficient organic pollutant degradation under visible-light using functional polymers of intrinsic microporosity. *Catalysis Science & Technology* **9**, 5383-5393 (2019).

69 Choi, H. M., Kim, Y. J., Choi, E. T., Lee, T. Y., & Lee, S. J. Use of porphyrin-containing polymers of intrinsic microporosity as selective photocatalysts for oxidative detoxification of chemical warfare agent simulant. *Journal of Porphyrins and Phthalocyanines* **26**, 340-347 (2022).

70 Bai, Y., Wilbraham, L., Gao, H., Clowes, R., Yang, H., Zwijnenburg, M. A., Cooper, A. I. & Sprick, R. S. Photocatalytic polymers of intrinsic microporosity for hydrogen production from water. *Journal of Materials Chemistry A* **9**, 19958-19964 (2021).

71 Baskar, C., Baskar, S. & Dhillon, R. S. Biomass conversion: The interface of biotechnology, chemistry and materials science. *Springer Science & Business Media* (2012).

Chapter 2 Introduction to Electrochemical and Material Characterisation Methods

Contents

Chapter Abstract

In this chapter, fundamental concepts behind electrochemical processes are introduced, including basic electrochemistry concepts and electrochemical methods. Thermodynamics and electrode kinetics are discussed with regard to two principal expressions, the Nernst equation and the Butler-Volmer equation. Mass transport in solution and in membranes are and explained. Electrochemical methods including potential step chronoamperometry, cyclic voltammetry, and Clark probe chronoamperometry are introduced. Finally, the material characterisation methods used in the studies in this thesis are briefly presented.

2.1 Basic Electrochemistry

Electrochemistry is concerned with the interrelation of chemical effects caused by the passage of an electric current and the production of electrical energy by chemical reactions. It is essential to understand the fundamental principles of electrochemistry since they apply to all the electrochemical fields encompassing different phenomena (from electrophoresis to corrosion), devices (electroanalytical sensors, batteries, supercapacitors, and fuel cells), and technologies (the electroplating of metals).

Of particular importance are the processes and factors that affect the transport of charge across the interface between an electronic conductor (an electrode) and an ionic conductor (an electrolyte). Many variables affect the electrochemical behaviour comprising electrode variables (material, surface area, and surface condition), mass transfer variables (mode of mass transfer, surface concentrations, and adsorption), solution variables (bulk concentration of electroactive species, and solvent), and electrical variables (potential and current).

The electrode reaction, often referred to as electrolysis, happens when the electrons are forced in/or out of the electrode. An overall electrode reaction, $O + ne^- \rightleftarrows R$, consists of a series of steps causing the conversion of dissolved species, O, to a reduced form, R (Figure 2.1). The electrode reaction rate is generally controlled by:

i) Rates of mass transfer (of O from the bulk solution to the electrode surface).
ii) Rates of chemical reactions.
iii) Rates of electron transfer at the electrode surface.
iv) Other reactions such as adsorption and desorption.

The magnitude of the reaction is defined by one or more slowest steps named rate-determining steps. The rate constants of electron transfer at the electrode surface depend on the potential. Later in this chapter, the factors of thermodynamics, electrode kinetics, and mass transport will be discussed in more detail.

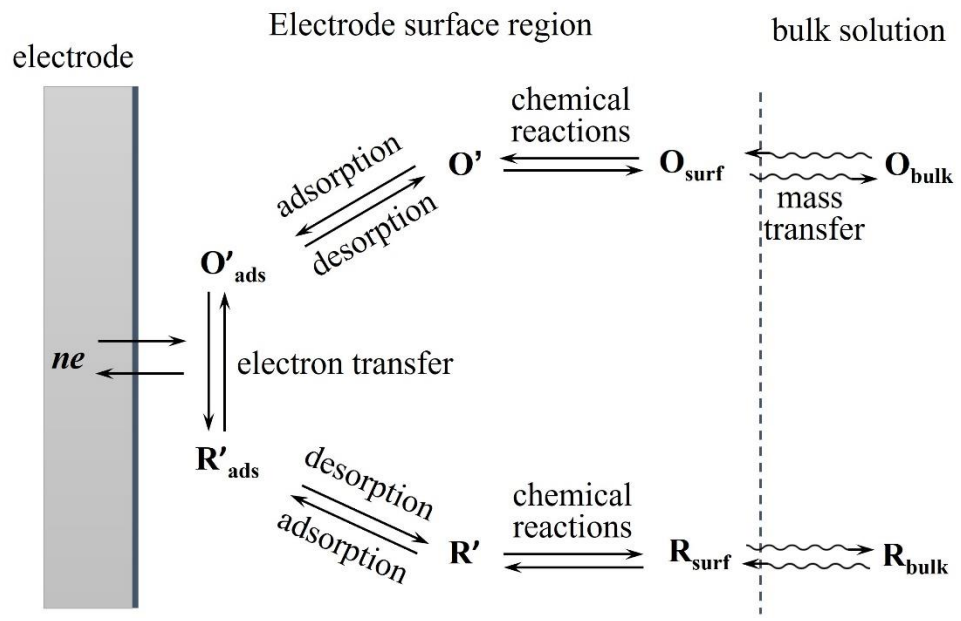

Figure 2.1 Pathway of a general electrode reaction simplified to five steps: 1) transport of reactant O to the electrode surface region, 2) adsorption of O to the electrode surface, 3) transfer of electrons to reactant O, giving product R, 4) desorption of R, and 5) mass transport of R away from the electrode surface to the bulk solution.

2.1.1 Thermodynamics

The key to driving an electrode reaction is the imposition of an external potential. The unit of potential is volt (V = Joule (J) / Coulomb (C)), the energy required to move charge (Q). The application of a potential to an electrode therefore alters the energy of the electrons within a metal electrode. The energy of the electrons can be raised by driving the electrode to more negative potentials generally achieved by connecting a power supply to the electrode. Flow of electrons from electrode to solution happens when their energy is higher than the lowest unoccupied molecular orbital (LUMO) of the analyte, inducing a reduction current [1] (Figure 2.2A). Similarly, under a positive potential bias, the electron energy is lowered below the highest occupied molecular orbital (HOMO) of the solute, favouring the oxidation of the species at the electrode surface (Figure 2.2B). The critical potentials at which these processes occur are correlated to the standard potential (E^0, as given in the electrochemistry theories defined at standard pressure and standard state at a given temperature).

In electrochemistry, the linkage between electrode potential, or rather the equilibrium potential (E_{eq}), and the concentrations of reactants in the electrode reaction:

$$O + ne^- \rightleftarrows R \tag{2.1}$$

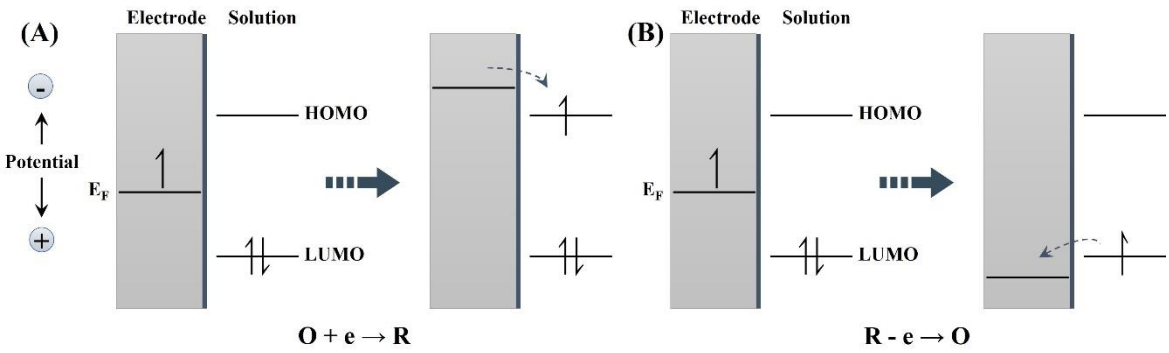

Figure 2.2 Illustration of reduction and oxidation process of a species in solution. (A) Negative potential bias raising the Fermi level (E_F) of the electrode, resulting in the reduction of the analyte; (B) E_F of the electrode being lowered by positive potential bias, favouring the oxidation of the analyte.

is described by the Nernst equation [2]:

$$E_{eq} = E^0 + \frac{RT}{nF} \ln \frac{a_O}{a_R} \tag{2.2}$$

Here E_{eq} is the equilibrium potential of the electrode reaction system, E^0 is the standard potential of the reaction couple, R is the universal gas constant (8.31447 J K^{-1} mol^{-1}), T is the temperature (K), n is the number of electrons transferred per molecule or ion, F is the Faraday constant (96485 C mol^{-1}), and a is the activity of the oxidised/reduced species (a_O/a_R). This means that the potential established at the electrode under equilibrium conditions is given by the standard potential (a natural characteristic) and activity ratio (an experimental condition) of the reactants.

The Nernst equation is only applicable to reversible systems at equilibrium. The concept of equilibrium refers to a process of being able to move in either of two opposite directions from the equilibrium position. It can be reached when an appropriate electrode is immersed in a solution in which fast electron transfer occurs between the species and the electrode. When a thermodynamic equilibrium is established, the oxidation rate of reduced species and the reduction rate of oxidised species are the same; therefore, zero current is obtained.

It is generally inconvenient to deal with activities in evaluations of electrode reactions because of unknown activity coefficients (γ). Therefore, the quantity of formal potential ($E^{0'}$)

is introduced into the Nernst equation. The formal potential manifests the link between the standard potential and activity coefficients.

At equilibrium the concentration of redox reactants at the electrode is equal to the concentration in bulk. For a given species x with concentration [x], the activity is:

$$a_x = \gamma_x[x] \tag{2.3}$$

Substituting the equation 2.3 into the Nernst equation (equation 2.2) yields

$$E_{eq} = E^0 + \frac{RT}{nF}\ln\frac{\gamma_O[O]_{bulk}}{\gamma_R[R]_{bulk}} \tag{2.4}$$

which is

$$E_{eq} = E^{0'} + \frac{RT}{nF}\ln\frac{[O]_{bulk}}{[R]_{bulk}} \tag{2.5}$$

where

$$E^{0'} = E^0 + \frac{RT}{nF}\ln\frac{\gamma_O}{\gamma_R} \tag{2.6}$$

Here, $[x]_{bulk}$ is the concentration of species x in the bulk solution, whereas γ_x stands for the activity coefficient. Note that $E^{0'}$ varies from medium to medium since the activity coefficients are affected by ionic strength. Formal potentials are experimentally measured so that they contain factors related to ion interactions.

The thermodynamic characteristics depicted above predict the possibility of the electrode reactions. Whether the reactions occur depends on the rate or kinetics of the electron transfer.

2.1.2 Electrode kinetics

The rate of electron transfer. The electrode kinetics can be governed by the applied potential for a given electrode process. Quantitative rationalisation of the heterogeneous rate constant for the electron transfer is essential to give an accurate description of an electrode reaction.

For a general reaction at the electrode

$$O(aq) + e^{-}(m) \underset{k_{ox}}{\overset{k_{red}}{\rightleftharpoons}} R(aq) \qquad (2.7)$$

the two reactants in an aqueous solution (O and R) are interconverted by a single electron transfer reaction. Here, k_{red} and k_{ox} represent the first-order rate constants for the reductive and oxidative electron transfer reactions.

The reduction (cathodic) and oxidation (anodic) currents i_{red} (Equation 2.8) and i_{ox} (Equation 2.9) of reaction 2.7 can be predicted by

$$i_{red} = -FAk_{red}[O]_0 \qquad (2.8)$$

$$i_{ox} = FAk_{ox}[R]_0 \qquad (2.9)$$

where $k_{red}[O]_0$ and $k_{ox}[R]_0$ are the respective fluxes of reactants to the electrode surface. The net current (i) for the overall reaction is

$$i = i_{red} + i_{ox} \qquad (2.10)$$

thus

$$i = FA(k_{ox}[R]_0 - k_{red}[O]_0) \qquad (2.11)$$

The transition state model in Figure 2.3 is used to describe chemical kinetics and to establish the influence of the applied potential on the rate constants. Figure 2.3 depicts the reaction as occurring via a path that contains a transition state. The reactants [O(aq)+e$^-$(m)] need to overcome an energy barrier to become product R(aq) [3].

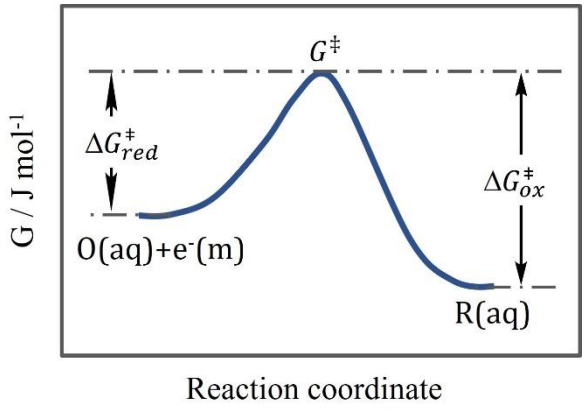

Figure 2.3 Free energy plot for a one-electron reduction of species O(aq) to product R(aq), illustrating the free energy change of activation of reduction $\Delta G^{\ddagger}_{red}$ and oxidation $\Delta G^{\ddagger}_{ox}$ Reactions. $G^{\ddagger}$ is the free energy of the transition state.

The rate of the reduction reaction (k_{red}) can be predicted by the transition state theory as

$$k_{red} = Aexp\left(\frac{-\Delta G_{red}^{\ddagger}}{RT}\right) \tag{2.12}$$

Where $\Delta G_{red}^{\ddagger}$ is the free energy of activation, and *A* is a "frequency factor" accounting for the collision of the reactant with the electrode surface and the tunnelling probability.

For the Reaction 2.7, the activation energy for the reductive reaction under fixed temperature and pressure is given by

$$\Delta G_{red}^{\ddagger} = G^{\ddagger} - G_{ox} \tag{2.13}$$

which is simply the free energy change between the reactant O and the transition state ($G^{\ddagger}$). Whilst the oxidative free energy is the difference between the free energy of R and the transition state

$$\Delta G_{ox}^{\ddagger} = G^{\ddagger} - G_{red} \tag{2.14}$$

The effect of potential. If the potential of the one-electron transfer reaction (Equation 2.7) is changed from its equilibrium potential (E_{eq}) to a new value *E*, the relative free energy of the electron resident on the electrode changes by

$$\Delta G = -nF\left(E - E_{eq}\right) = -F\eta \tag{2.15}$$

in which the overpotential η is the deviation of *E* from E_{eq} being a driving force of the current.

Accordingly, the overall free Gibbs free energy for the reactants (O + e^-) G_{ox} can be given by the standard Gibbs free energy of the reactants G_{ox}^{0} and a function of overpotential (Equation 2.16). Meanwhile, the free Gibbs free energy for the products stays the same (Equation 2.17) because no electron is included in the products.

$$G_{ox} = G_{ox}^{0} + (-F\eta) \tag{2.16}$$

$$G_{red} = G_{red}^{0} \tag{2.17}$$

Additionally, the free energy of the transition state $G^{\ddagger}$ is also altered by the overpotential:

$$G^{\ddagger} = G^{0\ddagger} + (-(1-\alpha)F\eta) \tag{2.18}$$

Here, the parameter α denotes the transfer coefficient reflecting the sensitivity of the transition state to the overpotential. The value of α ranges from zero to unity, depending on the shape of the intersection region. Typically, α is found to be close to 0.5 for many reactions.

A simplified model shown in Figure 2.4 is typically used to demonstrate a linear relationship between the free energy change and the imposed overpotential. Then, the activation energies for reduction and oxidation will follow

$$\Delta G_{red}^{\ddagger} = \Delta G_{red}^{0\ddagger} + \alpha F\eta \tag{2.19}$$

and

$$\Delta G_{ox}^{\ddagger} = \Delta G_{ox}^{0\ddagger} - (1-\alpha)F\eta \tag{2.20}$$

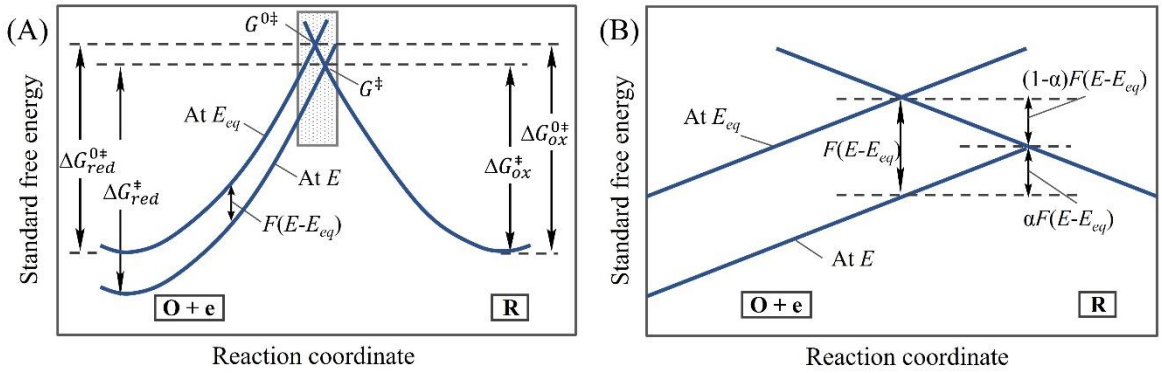

Figure 2.4 Effects of applied potential on the standard free energies of activation for reduction and oxidation. Application of overpotential alters the free energies of the reactants and the transition state, and the activation energies vary accordingly. (B) is a magnification of the intersection region of (A).

It is desirable to show that the rate constants depend on the overpotential for experimental purposes. Substituting Equation 2.19 into the expression for the reduction rate constant (Equation 2.12) gives

$$k_{red} = Aexp\left(\frac{-\Delta G_{red}^{0\ddagger}}{RT}\right)\exp\left(\frac{-\alpha F\eta}{RT}\right) \tag{2.21}$$

Similarly, the oxidation rate constant is expressed as

$$k_{ox} = Aexp\left(\frac{-\Delta G_{ox}^{0\ddagger}}{RT}\right)\exp\left(\frac{(1-\alpha)F\eta}{RT}\right) \tag{2.22}$$

If η-independent constants of k_{red}^{0} and k_{ox}^{0} are introduced in the above two expressions (Equations 2.21 and 2.22), the rate constants can be simplified as

$$k_{red} = k_{red}^{0}\exp\left(\frac{-\alpha F\eta}{RT}\right) \tag{2.23}$$

$$k_{ox} = k_{ox}^{0}\exp\left(\frac{(1-\alpha)F\eta}{RT}\right) \tag{2.24}$$

where

$$k_{red}^{0} = Aexp\left(\frac{-\Delta G_{red}^{0\ddagger}}{RT}\right) \tag{2.25}$$

$$k_{ox}^{0} = Aexp\left(\frac{-\Delta G_{ox}^{0\ddagger}}{RT}\right) \tag{2.26}$$

These results show that rate constants for the electron transfer steps are proportional to the exponential of the overpotential. Therefore, the rate of electrode reactions is variable on the magnitude of applied potential.

The Butler-Volmer equation. By substituting Equations 2.26 and 2.27 into Equation 2.11, the final relationship for the net current (i) to the overpotential (η) and transfer coefficient (α) is formulated:

$$i = i_0\left(\frac{[R]_0}{[R]_{bulk}}\exp\left\{\frac{(1-\alpha)F\eta}{RT}\right\} - \frac{[O]_0}{[O]_{bulk}}\exp\left\{\frac{-\alpha F\eta}{RT}\right\}\right) \tag{2.27}$$

where i_0 is the standard exchange current:

$$i_0 = FAk^0[R]_{bulk}^{\alpha}[O]_{bulk}^{1-\alpha} \tag{2.28}$$

which can be considered as a scaling factor. In the expression of i_0 (Equation 2.28), the standard rate constant denoted k^0 means a measure of the kinetic facility of a redox couple. It is from a particular case when the interface between the electrode and the solution is at

equilibrium at which $[O]_0 = [R]_0$ in the solution and no current flows. According to Equation 2.11, a deduction of $k_{red} = k_{ox}$ can be made, which is the definition of k^0.

Equation 2.28 is the complete current-potential relationship, being known as the Butler-Volmer formulation (see Butler [4] and Volmer [5]). This relation is significant in almost every occasion, taking heterogeneous kinetic into account. It can be simplified to

$$i = i_0 \left(\exp\left\{ \frac{(1-\alpha)F\eta}{RT} \right\} - \exp\left\{ \frac{-\alpha F\eta}{RT} \right\} \right) \tag{2.29}$$

when the solution is well stirred and thus the surface concentrations equal the bulk values.

2.1.3 Mass Transport

Other processes like mass transport (as shown in Figure 2.1) may contribute to the overall electrode reaction other than the kinetics of electron transfer. Particularly, the reaction could be affected or even dominated by the rate of reactants or products being brought to or from the electrode surface since electrons can only tunnel a few Ångstrom at most. Specifically, the current flowing during an electrolytic reaction can be controlled by the rate constant and the surface concentration of material (see Equations 2.8 and 2.9). If the rate constant is so large that the reactants on the electrode surface are consumed instantaneously, then the current will be controlled by the speed of fresh material reaching the interface from bulk (*i.e.* mass transport).

The following forms of mass transport are significant: diffusion, convection, and migration.

Diffusion. Diffusion is the movement of species along a concentration gradient which occurs in all solutions. It arises from uneven local concentrations driven by entropic forces (*i.e.* maximises entropy by smoothing out inhomogeneities of reactants). The current that flows from an electrochemical reaction is proportional to the concentration of reactants on the surface (see Equation 2.8). So, it is vital to understand the concentration of reactant [O] (taking reduction reaction as an example) as a function of distance from the electrode. Such a relationship is described first by Fick [6] by considering the simple case of linear diffusion to a planar surface (Figure 2.5). The mathematical expression

$$J_O = -D_O \frac{\partial [O]}{\partial x} \tag{2.30}$$

relates the diffusional flux J_O (the number of moles of O diffusing through a unit area per second) to the diffusion coefficient D_O and the concentration gradient $\partial[O]/\partial x$. Equation 2.30 is Fick's first law of diffusion. The negative sign indicates material moving down a concentration gradient.

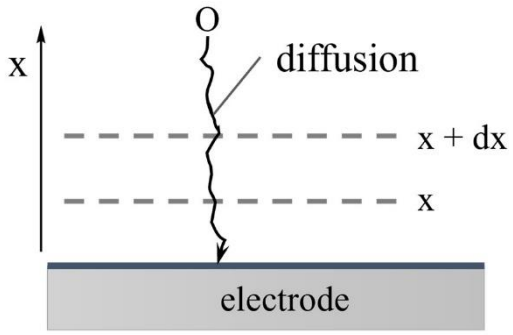

Figure 2.5 Diffusion of reactant O to a large planar surface from the bulk solution.

In practice, one needs to know how the concentration of material changes with respect to time (t) as a reaction progresses.

$$\frac{\partial [O]}{\partial t} = D_0 \left(\frac{\partial^2 [O]}{\partial x^2} \right) \tag{2.31}$$

Equation 2.31 is Fick's second law. It enables the prediction of the variation of concentration of electroactive species as a function of time. Diffusion is considered the most significant mass transport process for many electrochemical processes.

Convection. Convection is the transport of species resulting from the mechanical force acting on a solution. The force can be pumping, gas bubbling through a solution, stirring, or even gravity.

There are two distinguished types of convection. The first termed natural convection is present in any solution. It is caused by thermal gradients and/or density differences in the solution. The natural convection acts unpredictably to mix the solution in a random manner.

The second one entitled forced convection is usually introduced deliberately in the solution to drown out the effect of the natural convection influence. It is achieved by external forces such as stirring and typically several orders of magnitude greater than natural convection. Introduction of forced convection into a solution in a well-defined and quantitative way ensures reproducibility of experiments (*e.g.* rotating disk electrode).

Migration. Migration is an electrostatic effect on charged species existing in the electrode/solution interface region resulting from applying an external potential to the electrode. Any charged species near the interface region will either be attracted or repelled from the electrode surface. Migration is difficult to quantify because of ion solvation shell and diffuse layer interactions in solution, making interpretation of experimental data complicated.

In practice, chemically and electrochemically inert background electrolyte (*e.g.* KCl) is added to the solution in high concentrations. The purpose is to eliminate the reactants from being exposed to migration effects. By introducing a large quantity of the electrolyte (typically around or more than 0.1 M) relative to the reactants, the electrolysis reaction is not significantly affected by the small charge change of migration. Adding background electrolyte has other benefits: increasing the solution conductivity and helping the passage of current through the solution; controlling the thickness of the electric double-layer and thus the potential drops on the electrode surface, and making the ionic strength of the solution effectively constant.

2.1.4 Membrane Transport

Polymers of intrinsic microporosity (PIMs) are known to be processed into membranes by simply drop-casting or spin-coating. PIMs have good permeability towards gas and ions and high free volumes stemming from their extremely stiff backbone. Here, an overview is given of permeation of different species through membranes in terms of applications of PIMs in electrochemistry.

Transport models in membranes. There are two different models to describe the mechanisms of permeation as shown in Figure 2.6. The first one is called solution-diffusion model (Figure 2.6A), in which species dissolve in the membrane and then diffuse through

the membrane from the high concentration to the low concentration region. The separation of species is due to the difference in their solubility and mobility in the membrane material. The other one is the pore-flow model (Figure 2.6B), in which permeants transport through pores of the membrane driven by pressure. The permeants are separated caused by the filtration effect from some of the pores in the membrane.

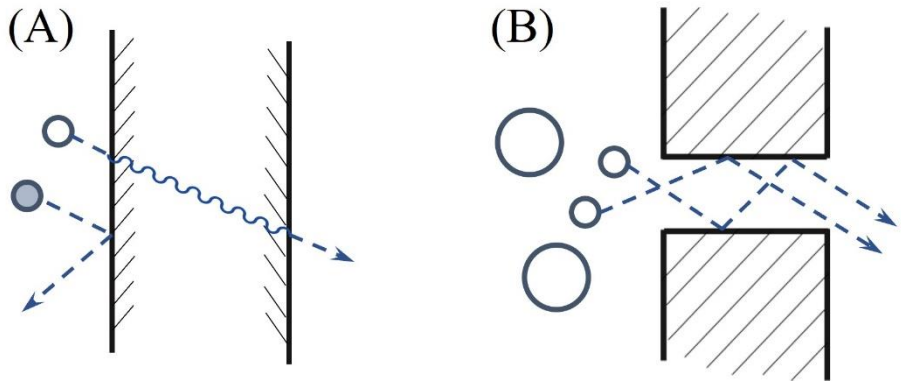

Figure 2.6 Two models of molecular transport through membranes. (A) Solution-diffusion model achieved by differences in the solubility and mobility of permeants dissolved in the membrane. (B) Pore-flow model based on molecular filtration in microporous membranes.

The solution-diffusion model follows Fick's theory as explained earlier (Section 2.1.3 Mass transport, Diffusion). Once dissolved in the membrane medium, permeants tend to transfer down a concentration gradient following Fick's first law of diffusion (Equation 2.30). The equation is duplicated here for a legible purpose:

$$J_i = -D_i \frac{\partial c_i}{\partial x} \tag{2.32}$$

where J_i is the transfer rate of matter i, and $\partial c_i/\partial x$ is the concentration gradient of i. Since the solution-diffusion process is inherently slow, the membrane used in experiments is normally very thin, and the concentration gradient inside the membrane is significant in order to get effective fluxes.

The basis of the pore-flow model is pressure-driven convective flow, which can be covered by Darcy's law [7]

$$J_i = K' c_i \frac{\partial p}{\partial x} \tag{2.33}$$

in which $\partial p/\partial x$ is the pressure gradient, K' is a coefficient related to the characteristic of the membrane, and c_i is the concentration of i in the membrane.

The criteria for distinguishing between the solution-diffusion and pore-flow sit in the relative size and the permanence of the pores inside the membrane. For the membranes with tiny free volume elements (pores) caused by the thermal motion of the polymer chains, the transport of permeants is best described by the solution-diffusion model. The pores change on the time scale of matter motion in the membrane. Reverse osmosis and gas separation membranes are classified as solution-diffusion transport models as illustrated in Figure 2.7. For membranes with relatively large and fixed pores which do not change on the time scale of permeants traversing the membrane, the pore-flow mechanism is the best way to explain the transport of species. Typical examples of the pore-flow mechanism include microfiltration and ultrafiltration membranes (Figure 2.7). The transition between the above two models lies in the group of membranes with pore sizes in the range of 5-10 Å [7]. PIMs with semi-permanent cavities fall into this transition category (see Figure 2.7).

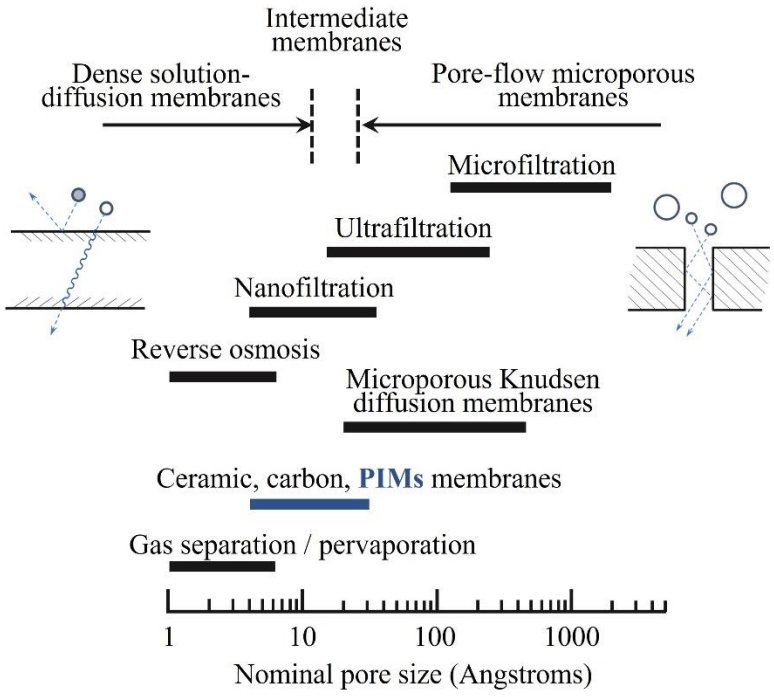

Figure 2.7 Schematic illustration of categories of the separation membranes and their related theoretical models with respect to the pore size. [7]

Diffusive transport theory in membranes. The foundation of studying heterogeneous electrocatalysis in PIMs is understanding how species transfer through membranes. The actual transport of material from solution to electrode surface through membranes can be complex because of the diversity of membrane properties, solutes, electrolytes, and solvents. A simplified diffusion model (Figure 2.8) is discussed here in terms of comprehension. Some assumptions are made: i) one-dimensional transport process from solution to electrode surface across the membrane; ii) the membrane is chemically inert and porous; iii) the solution is well-mixed, so there is no need to consider mass transport in solution; iv) the volume of the solution is massive compared to the membrane volume, and v) the solute to be transported is neutral.

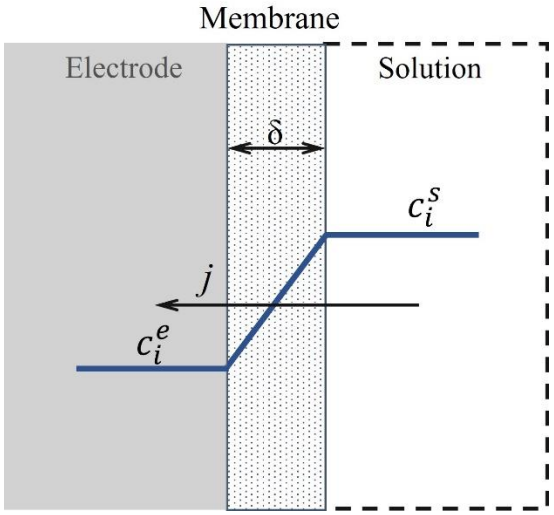

Figure 2.8 Illustration of the transport of a neutral species i from solution to the electrode surface across an inert, porous membrane.

The species exists only in solution initially as represented in Figure 2.8. The flux density of the species i across the membrane can be given by the mass balance [8]

$$J = -\frac{V^s}{A}\frac{dc_i^s}{dt} \tag{2.34}$$

in which V^s is the volume of the solution, c_i^s is the species concentration in solution, A is the membrane area, and t is time.

Meanwhile, the flux density follows Fick's first relation (Equation 2.32) along distance. Integration of Equation 2.32 over the membrane gives

$$J = -D_i \frac{c_i^e - c_i^s}{\delta} \tag{2.35}$$

where D_i is the diffusion coefficient of i in the membrane, c_i^e is the concentration of i on the electrode surface, and δ is the thickness of the membrane. Normally, the electron transfer process is faster than the diffusive transport [9], so the species that reach the electrode will be converted into products immediately.

2.2 Electrochemical Measurement Methods

2.2.1 Three-electrode System

In most electrochemical experiments, a three-electrode configuration is used as illustrated in Figure 2.9. The essential elements contained in an electrochemical cell are electrodes, a solvent, a background electrolyte, and the reactant. The electrode of interest, named working electrode, is where the target reaction happens. During a redox reaction, the external potential is exerted between the working electrode and the reference electrode (such as a saturated calomel electrode, or SCE, with known potential). At the same time, current flows between the working electrode and a counter electrode such as a platinum wire or any other inert, conducting, and convenient one.

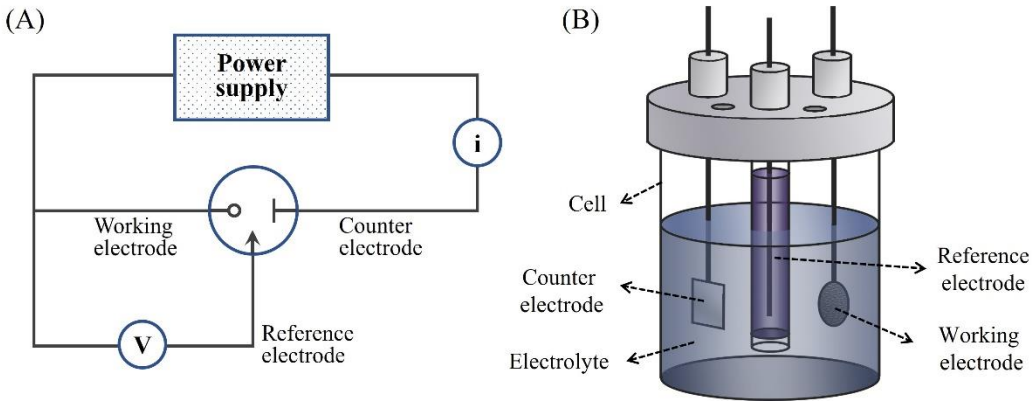

Figure 2.9 The configuration (A) and a schematic diagram (B) of a three-electrode system.

2.2.2 Potential Step Chronoamperometry

In a basic potential step experiment, the potential E_1 (as shown in Figure 2.10A) is generally set to a value where no reaction happens. Then the potential E_2 is switched to a region in which a faradaic process occurs. The resulting current *i* is monitored as a function of time. Instantaneously following the step of the potential, a large current is detected followed by a steady drop with time (Figure 2.10B). The concentration of the reactant on the electrode surface is sufficient before the potential step. However, once the reaction happens, the reactant is consumed immediately and needs to be transferred from bulk to the electrode surface via diffusion (in stagnant conditions).

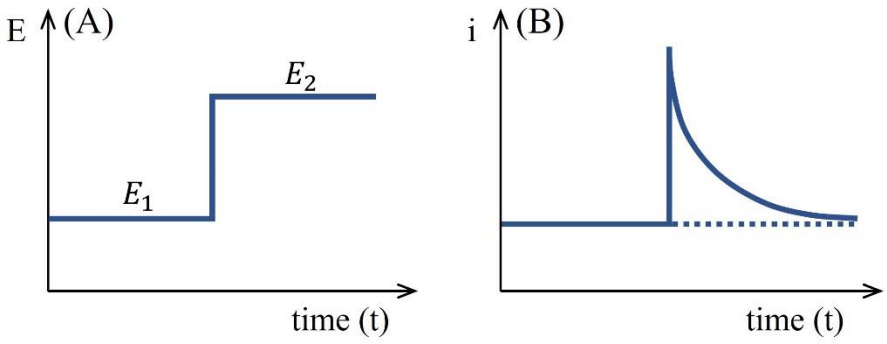

Figure 2.10 (A) Waveform of applied potential in a potential step experiment. (B) The current response against time.

As noted previously, the magnitude of current is controlled by the rate of reactant diffusion, which is dependent on the concentration gradient. The concentration gradient drops as the reaction happens (*i.e.* time) as depicted in Figure 2.11. Thus, the current response drops over time. Further quantification of the relation between current *i* (taking reduction as an example) and reaction time *t* can be achieved by substituting $i = nFAk_{red}[O]$ (Equation 2.8) to Fick's second law (Equation 2.31), which gives the Cottrell equation [10,11]

$$|i| = \frac{nFA[O]D^{\frac{1}{2}}}{\pi^{\frac{1}{2}}t^{\frac{1}{2}}} \tag{2.36}$$

Note here [O] is the bulk concentration of reactant O, and *n* is the number of electrons transferred per reaction. This relation suggests that the diffusion coefficient *D* can be measured by potential step tests.

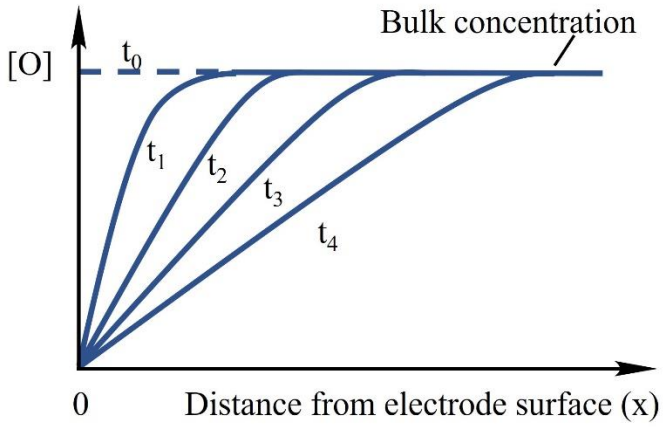

Figure 2.11 Concentration profiles of reactant O versus distance for various times after the potential stepped to E_2. ($t_0 < t_1 < t_2 < t_3 < t_4$)

2.2.3 Cyclic Voltammetry

Cyclic voltammetry is always the first technique carried out in electroanalytical investigation as it provides informative and quick results. In a cyclic voltammetry experiment, the potential is controlled and swept at a constant rate from E_1 where no reaction happens, to E_2 which is positive (or negative) enough for oxidation (or a reduction) to occur, and then swept back to E_1 (see Figure 2.12A).

Initially, no current flows because the applied potential is not positive enough to induce electron transfer (Figure 2.12B). When the potential is swept more positive, the current starts to pass and rises approximately exponentially with time (electrode kinetic control, see Equation 2.27). Note that the potential is swept at a constant rate so that the potential axis can be considered the time axis. Then the current rise becomes slower before a maximum (i_p^{ox}) is reached. The slower current rise can be rationalised by the current being dependent on not only the rate constant (k_{ox}) but the concentration of reactant [R] on the electrode surface. The reactant near the electrode is consumed with time, slowing the current increase. By the point of E_p^{ox} the concentration [R] is depleted from the surface. Once the peak current is reached, the current becomes diffusion-controlled since fresh reactant needs to get to the electrode by diffusional transport from the bulk. The current decrease in this area follows the Cottrell equation (Equation 2.36). Similar rules can be applied when the potential is swept back to E_1 and reduction happens.

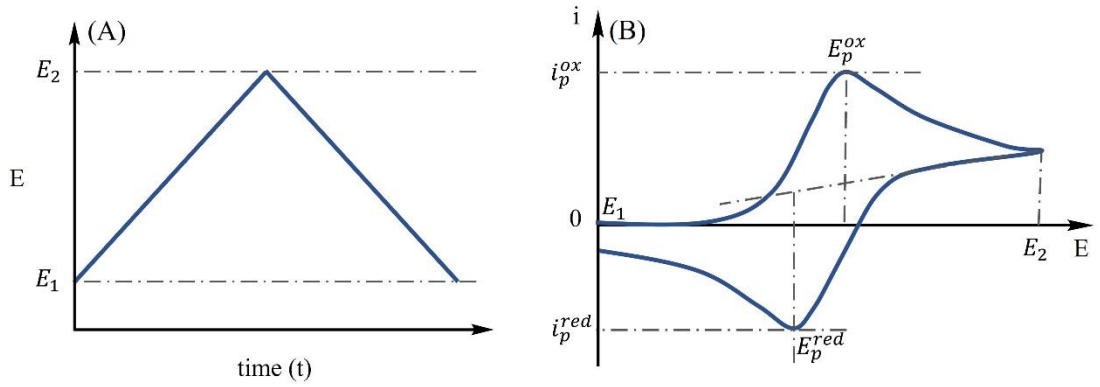

Figure 2.12 (A) Profile of the applied potential as a function of time in a cyclic voltammetry experiment. (B) Cyclic voltammogram for a reversible electron transfer reaction.

Scan rate effect. There are specific characteristics of cyclic voltammograms of fully reversible electrode reaction: i) the locations of current peaks are independent of scan rate as shown in Figure 2.13; ii) the potential difference between two current peaks ($E_p^{ox} - E_p^{red}$) equals 59/*n* mV; iii) the magnitude of the peak currents is the same ($|i_p^{ox}| = |i_p^{red}|$) which is proportional to the square root of the scan rate ($\sqrt{\nu}$) as described in the Randles-Ševčík equation [12,13]

$$i_p = 0.446 n^{\frac{3}{2}} F^{\frac{3}{2}} A c \left(\frac{\nu D}{RT}\right)^{\frac{1}{2}} \tag{2.37}$$

where i_p is the peak current (A), *n* is the number of electrons transferred per molecule in the redox reaction, *F* is Faraday constant (C mol^{-1}), *A* is electrode area (cm^2), *c* is the concentration of reactant (mol cm^{-3}), ν is scan rate (V s^{-1}), *D* is diffusion coefficient (cm^2 s^{-1}), *R* is gas constant (J K^{-1} mol^{-1}), and *T* is the absolute temperature (K). This equation relates the current response to scan rate, concentration, and diffusional properties of the species in solution. The determination of the diffusion coefficient of electroactive species can be achieved by measuring current.

The dependence of the current response of cyclic voltammograms on potential scan rates is illustrated in Figure 2.13. As predicted by the Randles-Ševčík equation, the peak current i_p increases with potential scan rate. According to Fick's first law (Equation 2.30), the flux reflects the concentration gradient of the reactant near the electrode. If the potential scan rate is high, relatively less time is taken to deplete the reactant near the electrode, resulting in a

steeper concentration gradient. Thus, a faster scan rate gives a larger flux, which means a higher peak current.

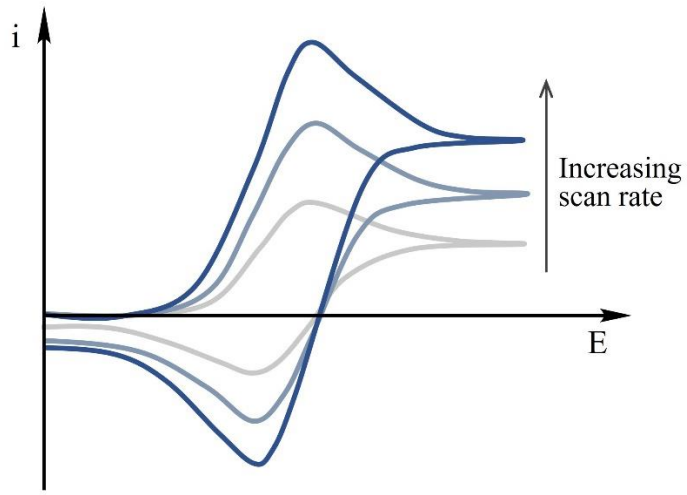

Figure 2.13 Cyclic voltammograms for a reversible electron transfer reaction with different potential scan rates.

Electrocatalysis (EC') mechanism. Cyclic voltammetry is also applied in enzyme processes and in electrocatalysis. In general, the electrocatalytic reaction is denoted as EC', where E stands for a heterogeneous electron transfer at the electrode, C represents a homogeneous chemical reaction, and the prime (') labels a catalytic process. The EC' mechanism can be summarised as

$$R \rightleftharpoons O + e^- \tag{2.38}$$

$$O + Y \xrightarrow{k_{EC'}} R + Products \tag{2.39}$$

The catalysis happens as the product of the electron reaction, O, reacts with a substrate species Y in solution (Reaction 2.39). This process consumes O and gives the starting material R (the catalytic cycle), which can then be oxidised again to O at the electrode. Meanwhile, Y is converted to products. The overall resulting voltammograms are shown in Figure 2.14 for differing quantities of substrate Y. The oxidation peak current increases with the concentration of Y.

The second-order chemical rate equations of Reaction 2.39 contribute to the concentration gradients for R and O:

$$\frac{\partial[R]}{\partial t} = D_R \frac{\partial^2[R]}{\partial x^2} + k_{EC'}[O][Y] \tag{2.40}$$

$$\frac{\partial[O]}{\partial t} = D_O \frac{\partial^2[O]}{\partial x^2} - k_{EC'}[O][Y] \tag{2.41}$$

This cyclic voltammetry technique is commonly used to determine electrocatalysis and enzyme catalysis for bio-sensor applications.

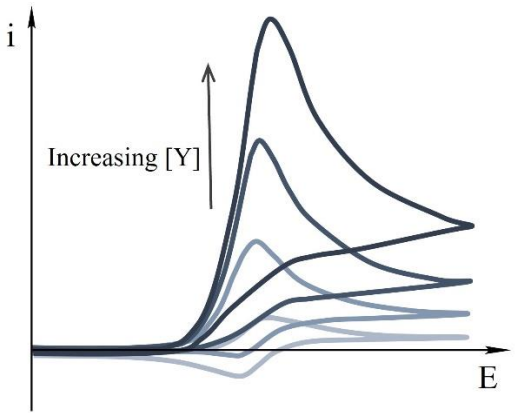

Figure 2.14 Cyclic voltammograms for electrocatalytic EC' process. The oxidation peak current increases with the concentration of substrate Y.

2.2.4 Clark Probe Chronoamperometry

The Clark oxygen electrode was invented by Clark in 1962 [14] for the detection of ambient oxygen. Various commercial Clark products are being applied in blood oxygen monitoring. Only recently, the application of the Clark probe has been extended in the detection of hydrogen *in situ* [15] by immobilising a catalyst on a gas-permeable Teflon (polytetrafluoroethylene, or PTFE) membrane. As depicted in Figure 2.15, the Clark probe is essentially an electrochemical cell enclosed in a Teflon-equipped cap. Gases like oxygen (or hydrogen) permeate through the membrane and diffuse to the platinum (Pt) electrode surface, being reduced (or oxidised) under externally applied potential. The reduction of oxygen (or oxidation of hydrogen) gives current responses recorded by a potentiostat.

The electrochemical cell in the Clark probe consists of a Pt electrode as the working electrode, a silver/silver chloride (Ag/AgCl) electrode as the reference and counter electrode, and concentrated potassium chloride (KCl) as the electrolyte. In oxygen detection, a relatively negative potential is applied to reduce oxygen to water. Positive potential is used

in hydrogen monitoring to get an oxidation current response. Currents are usually recorded as a function of time (chronoamperometry). The magnitude of the current shows the flux of gases produced by a catalyst.

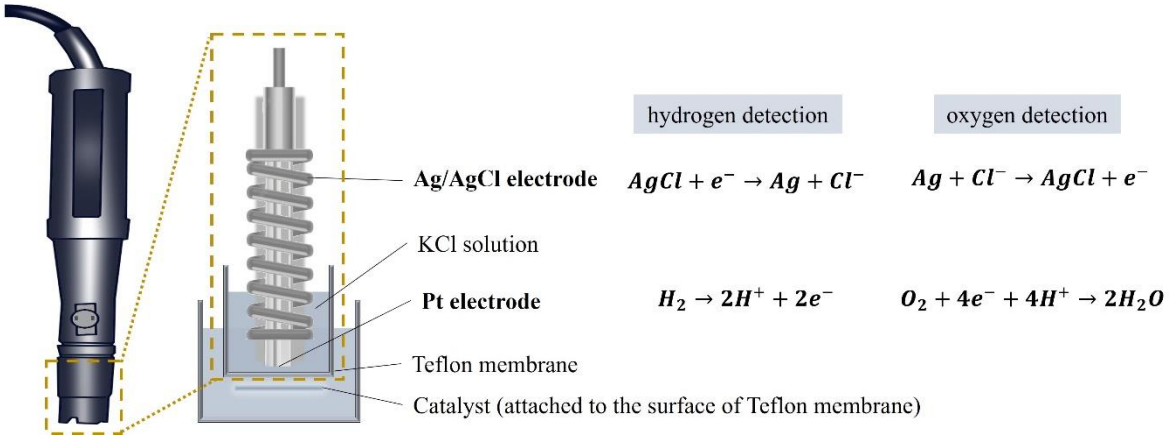

Figure 2.15 Schematic representation and the working principle of a Clark probe in hydrogen and oxygen detection. The catalyst is attached to a gas-permeable polytetrafluoroethylene (PTFE, or Teflon) membrane cap. Gases diffuse through the membrane, being oxidised or reduced on the Pt electrode under different applied potentials.

2.3 Materials and Analytical Characterisation Methods

2.3.1 Scanning Electron Microscopy (SEM)

Electron microscopy is a powerful and valuable tool to obtain high-resolution images with applications in biomedical research, forensics, and other technologies. An electron microscope works by accelerating an electron stream in a high-vacuum chamber towards a sample. For scanning electron microscopy (SEM), the high-energy electron stream is focused using electromagnetic lenses, as illustrated in Figure 2.16A. The interaction between an electron beam and sample induces various signals containing surface information, including secondary electrons (SE), backscattered electrons (BSE), and characteristic X-rays [16,17]. The signal of SE is ejected from valance or conduction bands of samples under irradiation by the high-energy electrons. It is generally detected in SEM measurements because of the high yield. The magnification of SEM is up to two million times. Samples to be examined by an SEM are commonly dispersed on a conductive substrate like carbon tape to avoid sample charging and so to get a high-resolution image.

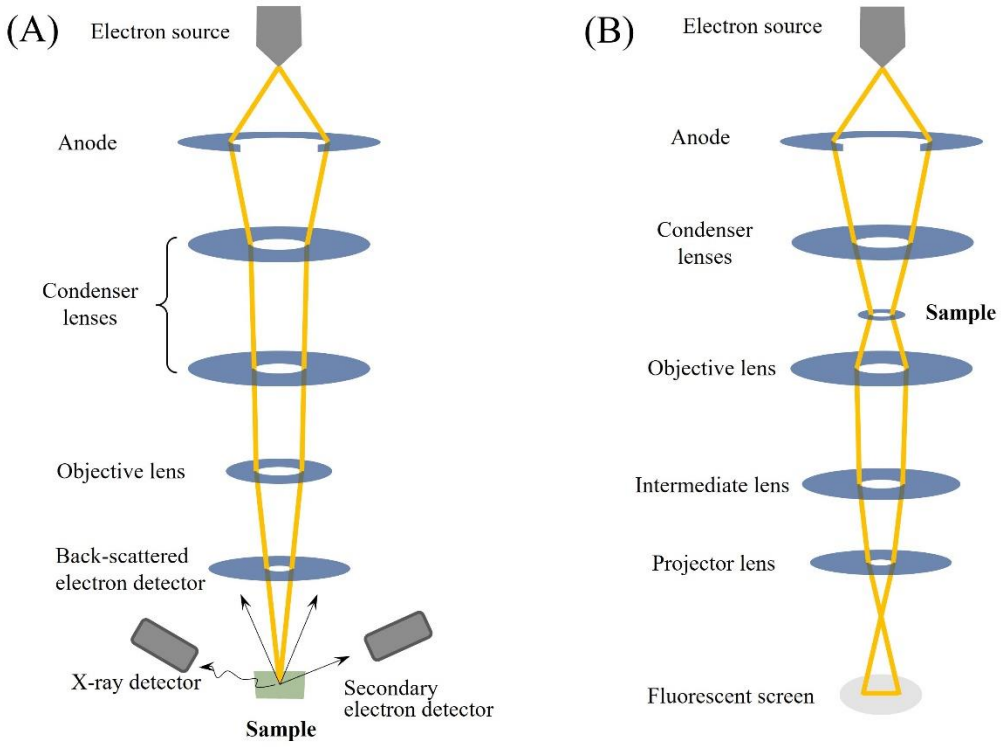

Figure 2.16 Schematic view of (A) scanning electron microscope (SEM) and (B) transmission electron microscope (TEM).

2.3.2 Transmission Electron Microscopy (TEM)

In addition to the surface morphology of samples, more details, including composition and crystal structure, are required in the sciences. Transmission electron microscopy (TEM) is a technology detecting electron transmitted through a sample (Figure 2.16B). Samples must be thin enough (typically less than 150 nm thick) so that electrons can penetrate them and arrive at the fluorescent screen or a detector. TEM has the potential to magnify an image 10-50 million times. Atomic-level details [18] can be provided. The differences between SEM and TEM are summarised in Table 2.1.

Table 2.1 Differences between SEM and TEM.

	Electron stream	Image taken	Resolution	Sample	Magnification
SEM	fine, focused	topographical	lower	thin/thick	2,000,000 times
TEM	broad	internal	higher	ultrathin	50,000,000 times

2.3.3 Energy Dispersive X-Ray Spectroscopy (EDX)

Energy dispersive X-ray spectroscopy (EDX) is used to identify the elemental composition of samples. EDX systems are usually attached to SEM or TEM instruments where the sample location of interest can be identified. After the interaction of samples with an incident electron beam, internal electrons will escape from these atoms [19]. As a result, the atoms will be in the excited state. There will be different ways, including Auger electrons and X-rays, to release the excess energy for the atoms to return to the ground state. The EDX technique utilises the X-ray signal to identify the elements and their concentrations. [20] Figure 2.17 shows the mechanism of the characteristic X-ray generation. With appropriate energy, the electron from the inner shell (for example, the K shell) can be ejected to form a photoelectron, and the electrons from outer shell orbitals will replace and fill the hole. The energy difference between the outer and inner shells creates the characteristic X-ray. For a specific element, the energy of a characteristic X-ray is fixed, which allows the fundamental elemental identification by EDX.

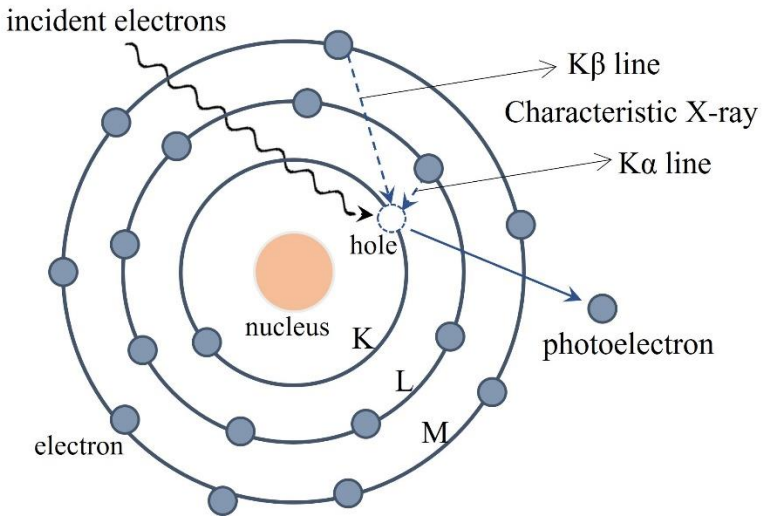

Figure 2.17 Diagram representing the mechanism of characteristic X-ray generation.

2.3.4 Liquid chromatography-mass spectrometry (LC-MS)

Liquid chromatography (LC) is a technique used to separate and identify the components of a mixture of chemicals and purify a chemical product. Each type of chromatography comprises a stationary phase and a mobile phase (liquid in LC). The substances in the

mixture separate and emerge at different times from the column because of their different ability to mix with the mobile phase or stick to the stationary phase. High-performance liquid chromatography (HPLC) is a sophisticated version of LC that can separate components with similar properties [21]. The use of fine particles in HPLC enhances the surface area of the stationary phase resulting in high separation efficiency. The fact that HPLC is performed at room temperature makes it applicable to analysing and investigating drugs and heating-sensitive biological molecules like proteins.

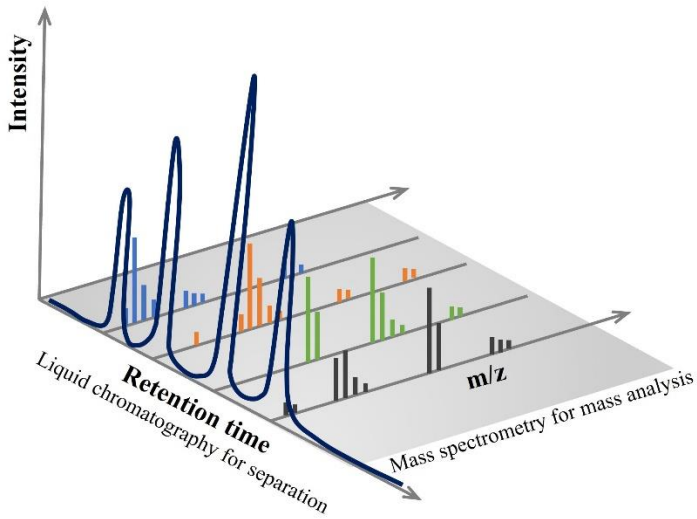

Figure 2.18 Schematic illustration of liquid chromatography-mass spectrometry (LC-MS) technique. It combines the physical separation function of LC and the mass identification capability of MS.

Mass spectrometry (MS) has been developed to separate atoms and molecules according to their mass-to-charge ratio (*m/z*) [22]. Samples from the inlet system are ionised by bombardment with electrons or by other methods. Then, the mass analyser separates ions by magnetic field or time of flight. Mass spectra are obtained after ions are captured by an ion detector. Data can be used to analyse the possible molecular structure of the material.

Liquid chromatography in conjunction with mass spectrometry (LC-MS) makes a powerful technology for separating and quantifying complex mixtures [23]. Samples are injected and separated one by one from the LC system. The chemicals from the LC column are ionised and separated in the MS analyser. Consequently, there is a separate mass spectrum for each component in the mixture (as illustrated in Figure 2.18).

2.4 References

1 Bard, A. J., Faulkner, L. R. & White, H. S. *Electrochemical methods: fundamentals and applications*. (John Wiley & Sons, 2022).

2 Nernst, W. On the electromotive forces which are aroused by magnetism in metal plates through which a stream of heat flows. *Annals of Physics* **267**, 760-789 (1887).

3 Fisher, A. C. *Electrode dynamics*. Vol. 1 (Oxford: Oxford University Press, 1996).

4 Butler, J. A. V. Studies in heterogeneous equilibria. Part III. A kinetic theory of reversible oxidation potentials at inert electrodes. *Transactions of the Faraday Society* **19**, 734-739 (1924).

5 Erdey-Grúz, T. & Volmer, M. Zur theorie der wasserstoff überspannung. *Zeitschrift für physikalische Chemie* **150**, 203-213 (1930).

6 Fick, A. V. On liquid diffusion. *The London, Edinburgh, and Dublin Philosophical Magazine and Journal of Science* **10**, 30-39 (1855).

7 Strathmann, H. *Membrane Technology and Applications, Richard W. Baker, John Wiley & Sons, Ltd., UK* (2004).

8 Kontturi, K. K., Murtomäki, L. & Manzanares, J. A. *Ionic transport processes: in electrochemistry and membrane science*. (Oxford University Press, 2008).

9 Brett, C. & Oliveira Brett, A. M. *Electrochemistry: principles, methods, and applications*. No. 544.6 BRE (1993).

10 Cottrell, F. G. Residual current in galvanic polarization, regarded as a diffusion problem. *Zeitschrift für Physikalische Chemie* **42**, 385-431 (1903).

11 Cottrell, F. G. Application of the Cottrell equation to chronoamperometry. *Zeitschrift für Physikalische Chemie* **42**, 385 (1902).

12 Randles, J. E. A cathode ray polarograph. Part II.—The current-voltage curves. *Transactions of the Faraday Society* **44**, 327-338 (1948).

13 Ševčík, A. Oscillographic polarography with periodical triangular voltage. *Collection of Czechoslovak Chemical Communications* **13**, 349-377 (1948).

14 Clark Jr, L. C. & Lyons, C. Electrode systems for continuous monitoring in cardiovascular surgery. *Annals of the New York Academy of sciences* **102**, 29-45 (1962).

15 Zhao, Y., Malpass-Evans, R., Carta, M., McKeown, N. B., Fletcher, P. J., Kociok-Köhn, G., Lednitzky, D. & Marken, F. Size-Selective Photoelectrochemical reactions in microporous environments: Clark probe investigation of Pt@g-C_3N_4 embedded into intrinsically microporous polymer (PIM-1). *ChemElectroChem* **8**, 3499-3505 (2021).

16 Amelinckx, S., Van Dyck, D., Van Landuyt, J. & van Tendeloo, G. *Electron microscopy: principles and fundamentals*. (John Wiley & Sons, 2008).

17 Goldstein, G., Newbury, D., Echlin, P., Joy, D., Romig, A., Lyman, C., Lifshin, E., Sawyer, L. & Lifshin, E. *Scanning Electron Microscopy and X-Ray Microanalysis*. New York: Plenum Press. (1981).

18 Kannan, M. Transmission electron microscope−Principle, components and applications. *A textbook on fundamentals and applications of nanotechnology* 93-102 (2018).

19 Abd Mutalib, M., Rahman, M., Othman, M., Ismail, A. & Jaafar, J. Scanning electron microscopy (SEM) and energy-dispersive X-ray (EDX) spectroscopy. In *Membrane Characterization* 161-179 (Elsevier, 2017).

20 Bell, D. & Garratt-Reed, A. *Energy dispersive X-ray analysis in the electron microscope*. Vol. 49 (Garland Science, 2003).

21 Akash, M. S. H. & Rehman, K. in *Essentials of pharmaceutical analysis* 175-184 (Springer, 2020).

22 De Hoffmann, E. & Stroobant, V. *Mass spectrometry: principles and applications*. (John Wiley & Sons, 2007).

23 Pitt, J. J. Principles and applications of liquid chromatography-mass spectrometry in clinical biochemistry. *The Clinical Biochemist Reviews* **30**, 19 (2009).

Chapter 3 The Immobilisation and Reactivity of $Fe(CN)_6^{3-/4-}$ in an Intrinsically Microporous Polyamine (PIM-EA-TB)

Contents

Chapter Abstract

The heterogeneous redoxcatalysis based on polymers of intrinsic microporosity (PIMs) incorporates several steps, such as immobilisation of ions or molecules, electron transfer at the electrode surface, and release of products. In this chapter, ferrocyanide ($Fe(CN)_6^{4-}$) and ferricyanide ($Fe(CN)_6^{3-}$) embedded into PIM-EA-TB are investigated as a model system, revealing the redox reactivity of anions in PIMs. Uptake, transport, and retention of $Fe(CN)_6^{4/3-}$ are strongly pH dependent relating to protonation of PIM-EA-TB ($pK_A \approx 4$). Both $Fe(CN)_6^{4-}$ and $Fe(CN)_6^{3-}$ can be immobilised in PIM-EA-TB and form redox-active films, but the interaction between $Fe(CN)_6^{4-}$ and the host appears to be stronger presumably through bridging protons. Loss of $Fe(CN)_6^{3-/4-}$ into aqueous solution becomes significant only at pH > 9 and is probably linked to hydroxide anions directly entering the micropores of PIMs to annihilate the protons. The interaction between $Fe(CN)_6^{3-/4-}$ and protons inside the PIM structure is proposed to be responsible for the retention and relatively slow leaching processes. Electrocatalytic oxidation of ascorbic acid is achieved by the immobilised $Fe(CN)_6^{3-/4-}$ film.

Graphical Abstract

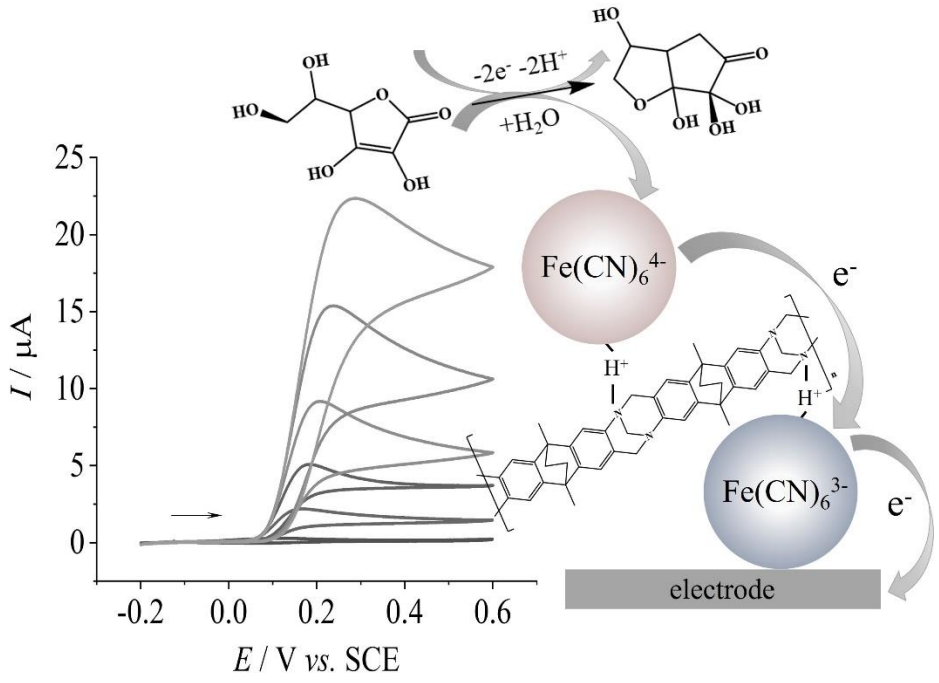

Publications associated with this chapter

Wang, L., Malpass-Evans, R., Carta, M., McKeown, N. B., & Marken, F. The immobilisation and reactivity of $Fe(CN)_6^{3-/4-}$ in an intrinsically microporous polyamine (PIM-EA-TB). *Journal of Solid State Electrochemistry*, **24**, 2797-2806 (2020).

Credit Statement

The candidate developed the immobilisation method of $Fe(CN)_6^{3-/4-}$ into PIM-EA-TB, and carried out the electrochemical experiments, data curation, and interpretation of the results. Neil B. McKeown provided the PIM-EA-TB material. Richard Malpass-Evans, Mariolino Carta, and Neil B. McKeown gave valuable input to the paper draft. Frank Marken supervised the candidate, helped with the experimental idea, gave critical comments on the data interpretation, figures and draft, and helped with reviewing and editing.

Special Acknowledgements

Special thanks to Prof. Neil McKeown and his research group from the University of Edinburgh who provide the PIM-EA-TB material. Thanks to Dr Philip Fletcher for the microscopic images collection.

3.1 Introduction

Ferrocyanide, $Fe(CN)_6^{4-}$, is a well-studied Fe(II) complex for its reversible oxidation to ferricyanide, $Fe(CN)_6^{3-}$ (see Equation 3.1), as a redox mediator and homogeneous one-electron electrocatalyst. Both $Fe(CN)_6^{4-}$ and $Fe(CN)_6^{3-}$ have been extensively employed in fundamental studies such as the investigation of metal ligand bonding [1], electro-organic transformations [2], thermoelectrochemical devices [3], redox buffer in biological studies [4], and electroanalytical determination of ascorbate [5], nitrite [6], and hydrogen sulphide [7,8]. The oxidation potential of $Fe(CN)_6^{4-}$ is adjustable and dependent on solvent [9,10] and cations [11,12], resulting in the application of this redox couple as a versatile and tunable redox mediator [13]. Ferrocyanide has also been employed as a heterogeneous or polymer-embedded catalyst for sulphide [14] and nitrite [15] detection.

$$Fe(CN)_6^{3-} + e^- \rightleftarrows Fe(CN)_6^{4-} \tag{3.1}$$

Ferrocyanide is known to form a variety of inorganic coordination materials [16], such as solid-state Prussian blue analogues [17] and related coordinate polymers [18]. Recently, the concept of "organic Prussian blues" [19] has been proposed to be associated with the formation of $Fe(CN)_6^{4-}$ with organic ammonium cations. In this chapter, an amine-containing polymer of intrinsic microporosity (PIM) with a rigid microporous structure is studied as a host for the $Fe(CN)_6^{3-/4-}$ redox mediator.

Here, the PIM-EA-TB ("EA" = ethanoanthracene and "TB" = Tröger base [20], see molecular structure in Figure 3.1) is employed as the host material. There are tertiary amine sites in the "free volume elements" of the PIM-EA-TB structure, allowing anion to be bound after protonation. In practice, it was proved that hydrophobic alcohols could partition into heterogenized redox PIM-EA-TB film [21], and small hydrophobic anions like perchlorate permeate through PIM-EA-TB [22]. The hydrophobicity of PIM-EA-TB can be complemented by ionic interaction and hydrogen bonding with multiple-charged ferrocyanide/ferricyanide as demonstrated in this chapter.

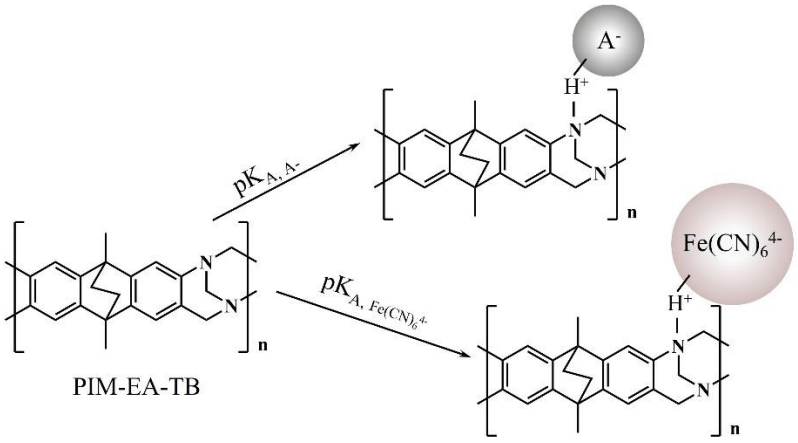

Figure 3.1 Schematic illustration of the molecular structure of PIM-EA-TB and protonation associated with anion binding taking $Fe(CN)_6^{4-}$ as an example.

There are two different categories of ferrocyanide or ferricyanide analogue contained hybrid. The first one is organic materials binding with $Fe(CN)_6^{3-/4-}$, for example, imidazolium-based polycationic polymer bound with ferricyanide [23]. The other type is hybrid materials containing organic components and Prussian blue-type components. Different methods of hybrid architectures are reported, one of which is layer-by-layer structures for a hybrid polymer-Prussian blue film [24] applied in sensor films [25]. The ferricyanide or ferrocyanide analogue contained hybrid materials have been used in electrochromic electrodes/devices [26] and films [27,28]. Polymer-Prussian blue hybrid materials with 2D structures have been fabricated [18]. A 3D bridged structured and tetra-alkylammonium cations incorporated Prussian blue analogue has been reported [29].

Here, PIM-EA-TB is studied as a microporous film/coating on glassy carbon electrode surfaces. The amines in the polymer structure are demonstrated to experience protonation and binding towards $Fe(CN)_6^{3-/4-}$ ions from the solution. The pK_A for protonation of PIM-EA-TB has been assessed to be approximate 4 for hydrophilic anions [30]. The ionic diameters of $Fe(CN)_6^{4-}$ and $Fe(CN)_6^{3-}$ are 450 pm and 440 pm, respectively [31]. These multiple-charged anions probably carry cations like H^+ and K^+ to further increase their sizes when transferred through intrinsic micropores (1-2 nm in diameter) of PIM-EA-TB [32]. It is shown that the pK_A of PIM-EA-TB shifts by approximately five units towards alkaline condition after binding of $Fe(CN)_6^{3-/4-}$. This behaviour is partly connected to the first protonation equilibrium for $Fe(CN)_6^{3-/4-}$ with $pK_{A,Fe(CN)_6^{4-}} = 4.2$ and $pK_{A,Fe(CN)_6^{3-}} < 1$ at room temperature [33,34]. Consequently, a novel film electrode based on $Fe(CN)_6^{3-/4-}$ immobilised PIM-EA-TB with catalytic characteristics is provided.

3.2 Experimental

3.2.1 Reagents

Potassium ferrocyanide or potassium hexacyanoferrate(II) ($K_4Fe(CN)_6$, 98.5–102.0%), potassium ferricyanide or potassium hexacyanoferrate(III) ($K_3Fe(CN)_6$, > 99.0%), potassium chloride (KCl, 99.0–100.5%), hydrochloric acid (HCl, 37%), chloroform (≥ 99.8%), potassium hydroxide (KOH, ≥ 85%) and L-ascorbic acid (≥ 99%) were products of Sigma Aldrich. PIM-EA-TB was synthesised following the literature method [20]. Aqueous solutions were prepared with ultra-pure water of resistivity not less than 18.2 MΩ cm (at 20 °C) taken from a Thermo Scientific water purification system.

3.2.2 Instrumentation

Electrochemical experiments are controlled by a Metrohm μAutolab II potentiostat. A three-electrode system was employed in which a 3 mm diameter glassy carbon electrode was the working electrode, a platinum wire as the counter electrode, and a KCl-saturated calomel electrode (SCE, Radiometer REF401) as the reference electrode. The pHs of the 0.1 M KCl solutions were adjusted by adding 1 M HCl or 1 M KOH solution monitored by a pH meter (Jenway 3505). The thickness of the PIM-EA-TB film on the electrode was measured by the cross-section morphology imaged by a field emission scanning electron microscope (JEOL JSM-6301F FESEM).

3.2.3 Procedures

A solution of 1 mg mL^{-1} PIM-EA-TB in chloroform was prepared by dissolving the polymer powder into chloroform. A typical amount of 2 μL was drop-casted on a glassy carbon electrode to form a polymer coating. The chloroform solvent was readily evaporated, and a uniform film with an estimated thickness of 1-2 μm can be obtained (see Figure 3.2). Then, the electrode with PIM coating was immersed in $Fe(CN)_6^{4-}$ or $Fe(CN)_6^{3-}$ dissolved HCl aqueous solution to perform protonation and immobilisation for typically 12 h at 4 °C in the dark and in a refrigerator. Finally, the electrode was removed from the solution and rinsed with water. The SEM images for PIM-EA-TB films before and after immersion into solutions were essentially identical. In the investigation of the PIM-EA-TB loading effect on the reactivity of the redox film, a larger amount of PIM-EA-TB was deposited by

repeating 2 µL of solution deposition instead of drop-casting the large amount directly on the electrode.

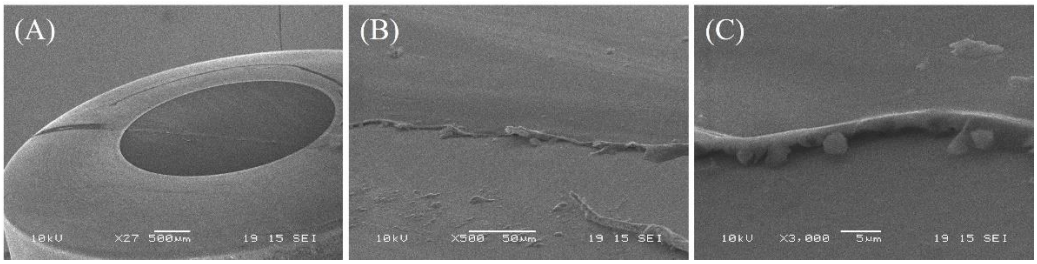

Figure 3.2 Field emission scanning electron microscopy (FESEM) images for (A) a 3 mm diameter glassy carbon disk electrode partially covered with PIM-EA-TB coating; (B) a closer look at the polymer film edge; and (C) a higher magnification image of the film edge.

3.3 Results and Discussion

3.3.1 Concentration Effects on Binding and Reactivity of $Fe(CN)_6^{3-/4-}$ in PIM-EA-TB

Preliminary experiments were carried out by coating PIM-EA-TB film on a 3 mm diameter glassy carbon disk electrode. Typically, 2 µL of 1mg mL^{-1} PIM-EA-TB solution in chloroform was drop-casted, giving a 2 µg deposit on an electrode. Given a PIM-EA-TB monomer molecular weight of 300 g mol^{-1} corresponding to 6 nmol of the monomeric unit, an assumed density of 1 g cm^{-3}, an average thickness of 0.3 µm is speculated. The hydrochloric acid ensures protonation of PIM-EA-TB and accordingly drives the binding of $Fe(CN)_6^{4-}$ at 4 °C in the dark. A similar immobilisation process performed at room temperature under light gives Prussian blue-incorporated PIM instead.

Figure 3.3 shows the photographs of the blue-green coloured (Prussian blue precursor containing) solution of 1 mM $K_4Fe(CN)_6$ in 1 mM HCl after 24 h at room temperature under light (A) and the pristine solution after 24 h at 4 °C in the dark (B). Cyclic voltammetry results for these two types of electrodes prepared after rinsing with water followed by transferred into aqueous 0.1 M KCl in 1M HCl are depicted in Figures 3.3C and D. The $Fe(CN)_6^{4-}$-embedded PIM-EA-TB obtained at 4 °C shows well-defined highly reversible redox voltammetric responses (see Figure 3.3D). The cyclic voltammetry results of freshly made electrodes are reproducible with a ±10% error. However, there are some subtle factors that affect the current response, which will be discussed later. Lower peak currents and considerable peak shape distortion (see Figure 3.3C) are observed for the coating obtained

from an ambient condition in the light, probably resulting from the existence of Prussian blue fragment or $Fe(CN)_6^{4-}$ decomposition products formed in acidic solutions [35] in the microporous structure of PIM-EA-TB.

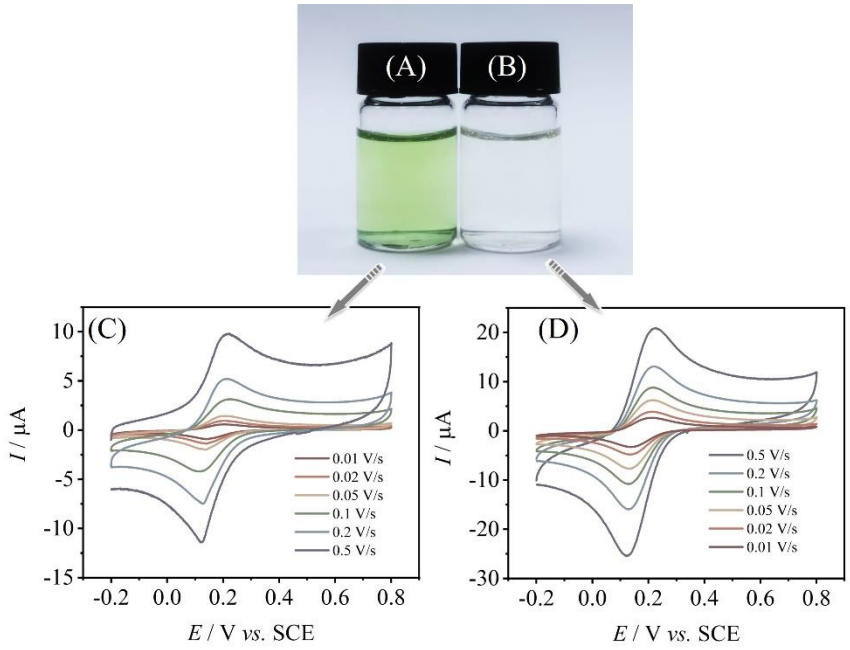

Figure 3.3 Effect of temperature and light during immobilisation. (A) Photograph of 1 mM $K_4Fe(CN)_6$ in 1 mM HCl stored in 24 h ambient light and room temperature. (B) The same solution left for 24 h at 4 °C. (C) Cyclic voltammograms (at scan rates of 10, 20, 50, 100, 200, and 500 mV s^{-1}) for a 3 mm diameter glassy carbon electrode coated with 2 μg PIM-EA-TB after 12 h immersion in 1 mM $K_4Fe(CN)_6$ in 1 mM HCl at room temperature under light. (D) As in (C) but for a sample kept at 4 °C for 12 h in the dark.

The cyclic voltammograms here are for thin films immobilised on the electrode surface and therefore not directly comparable to the voltammetric response obtained from the bare electrode immersed in $Fe(CN)_6^{3-/4-}$ solution. However, of interest is to compare the midpoint potentials. Cyclic voltammetric results at a scan rate of 10 mV s^{-1} in Figure 3.3D indicate an oxidation peak at 0.214 V *vs.* SCE and a reduction peak at 0.135 V *vs.* SCE. Thus the midpoint potential is $E_{mid} = ½ (E_{p,ox} + E_{p,red}) = 0.175$ V *vs.* SCE. The corresponding midpoint potential of a bare electrode tested in 2 mM $Fe(CN)_6^{4-}$ and 2 mM $Fe(CN)_6^{3-}$ dissolved in aqueous 0.1 M KCl is $E_{mid} = 0.193$ V *vs.* SCE. The minor negative shift of midpoint potential in the presence of PIM-EA-TB may suggest a slightly stronger binding to $Fe(CN)_6^{3-}$ compared to that for $Fe(CN)_6^{4-}$. However, other factors like polymer | electrolyte interface may also cause the potential shift.

In the following investigations, immobilisation of $Fe(CN)_6^{4-}$ or $Fe(CN)_6^{3-}$ is carried out always at 4 °C in the dark to get reproducible and reversible current responses. The electrode is then rinsed with water and transferred into an electrolyte of 1 mM HCl in 0.1 M KCl solution. Figure 3.4A shows cyclic voltammograms (at a scan rate of 0.1 V s^{-1}) of $Fe(CN)_6^{4-}$-immobilised PIM-EA-TB obtained from different solutions containing 0.01, 0.1, and 1 mM of $Fe(CN)_6^{4-}$. The voltammograms from all conditions are stable over at least 10 cyclic cycles, implying successful and strong binding between $Fe(CN)_6^{4-}$ and PIM-EA-TB.

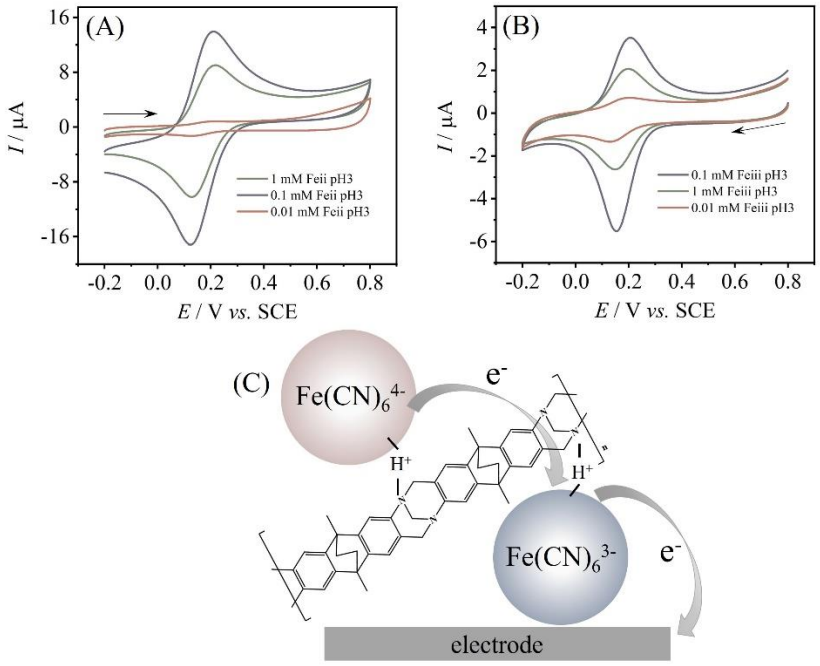

Figure 3.4 Effect of $Fe(CN)_6^{4-}$ or $Fe(CN)_6^{3-}$ concentration during immobilisation. (A) Cyclic voltammograms (first cycle; scan rate 0.1 Vs^{-1}) for a 3 mm diameter glassy carbon electrode coated with 2 µg PIM-EA-TB after 12 h immersion in 0.01, 0.1, and 1 mM $K_4Fe(CN)_6$ in 1 mM HCl (electrolyte: 0.1 M KCl containing 1 mM HCl). (B) As in (A), but for immobilisation in 0.01, 0.1, and 1 mM $K_3Fe(CN)_6$ in 1 mM HCl. (C) Schematic drawing of the proposed electron pathway during electron hopping.

When evaluating the concentration of $Fe(CN)_6^{4-}$ effect during the immobilisation process, a significant increase in current response was observed from 0.01 mM to 0.1 mM $Fe(CN)_6^{4-}$. However, for a higher concentration of 1 mM $Fe(CN)_6^{4-}$, the voltammetric peak current decreases surprisingly. An even more dramatic decrease was observed for the electrode obtained from 10 mM $Fe(CN)_6^{4-}$ (not shown), where the current response is as low as that obtained from 0.01 mM $Fe(CN)_6^{4-}$. The results indicate that increasing the amount of

$Fe(CN)_6^{4-}$ in the immobilisation solution cause detriment to the reactivity of the redox coating. Leaving the immobilisation process for 5 days results in complete loss of signal. These findings are consistent with $Fe(CN)_6^{4-}$ acting as a base with its $pK_A \approx 4.2$ [33,34]. The presence of the base leads to a lower degree of PIM-EA-TB protonation, and thus fewer $Fe(CN)_6^{4-}$ anions are bound. No current response is observed when attempting immobilisation of $Fe(CN)_6^{4-}$ in the neutral condition, which agrees with the low permeation of $Fe(CN)_6^{4-}$ through PIM-EA-TB reported in a redox flow battery system [36].

The immobilisation of $Fe(CN)_6^{3-}$ into PIM-EA-TB has also proved efficient, as well-defined reversible voltammograms are obtained in the concentration range from 0.01 to 1 mM ferricyanide. The voltammetry stays almost the same after several cycles. When testing the concentration effect of $Fe(CN)_6^{3-}$ during immobilisation, a similar trend in voltammogram response is observed, as shown in Figure 3.4B. A maximum current signal is obtained for 0.1 mM $Fe(CN)_6^{3-}$ immobilisation concentration. Again, a similar reason described for $Fe(CN)_6^{4-}$ case can be assumed to rationalise the concentration effect of $Fe(CN)_6^{3-}$ during immobilisation, although the lower pK_A of $Fe(CN)_6^{3-}$ may lead to less direct competition for protons. Cyclic voltammograms for $Fe(CN)_6^{3-}$-immobilised coating appears to be more symmetric (a lower peak-to-peak separation) with slightly lower currents, possibly revealing more limited thin film charge transport.

A presumed electron pathway of $Fe(CN)_6^{4-/3-}$-immobilised PIM-EA-TB during redox reaction is proposed (see Figure 3.4C). The electrons hop from one active binding site to another during redox processes, followed by the fast electron transfer step on the electrode.

The effect of scan rate on the voltammetric currents is studied in the following experiments for immobilisation of 0.1 mM $Fe(CN)_6^{4-}$ (Figure 3.5A) and for immobilisation of 0.1 mM $Fe(CN)_6^{3-}$ (Figure 3.5C). Both electrodes are tested in 0.1 M KCl containing 1 mM HCl. For the case of $Fe(CN)_6^{4-}$ immobilisation, a well-defined voltammetric signal with a peak-to-peak separation of typically 70 mV is shown. A double-logarithmic plot of oxidation peak current versus scan rate (Figure 3.5B) generates a gradient close to 0.5, revealing diffusion of charges within the microporous PIM-EA-TB host probably through electron hopping (similar to the processes for immobilised proteins [37]). At the slowest scan rate, 10 mV s^{-1}, the charge under the reduction peak is about 0.6 nmol. Given that the PIM-EA-TB deposit on the electrode is 2 µg (i.e. 6.7 nmol with a PIM-EA-TB monomer molecular weight of 300 g mol-1), approximately 10% of the monomer units are redox active. Since several monomer

units may be required for binding each multi-valent anion, a considerable part of the film must be active. These results demonstrate that a substantial fraction of the binding sites (protonated amines) in the PIM-EA-TB deposit is occupied by $Fe(CN)_6^{4-/3-}$ species.

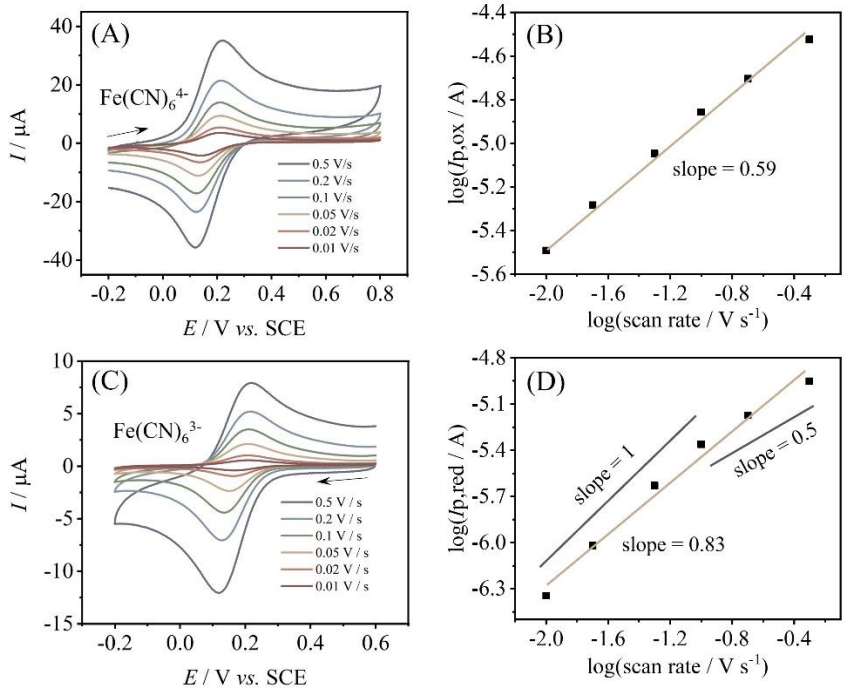

Figure 3.5 Effect of scan rate during voltammetry. (A) Cyclic voltammograms (first cycle; scan rates 10, 20, 50, 100, 200, and 500 mV s^{-1}) for a 3 mm diameter glassy carbon electrode coated with 2 µg PIM-EA-TB (after 12 h immersion in 0.1 mM $K_4Fe(CN)_6$ in 1 mM HCl at 4 °C) (electrolyte: 0.1 KCl containing 1 mM HCl). (B) A double-logarithmic plot of anodic peak current versus scan rate. (C) As in (A), but for $K_3Fe(CN)_6$. (D) A double-logarithmic plot of reduction peak current versus scan rate.

The oxidation of $Fe(CN)_6^{4-}$ has to be accompanied by either a proton expulsion or a K+ ejection from the PIM-EA-TB host to keep bulk charge neutral. For the case of $Fe(CN)_6^{3-}$ immobilisation, a similar principle would propose that the reduction of Fe(III) to Fe(II) is accompanied by cation uptake from the solution. Voltammetry in Figure 3.5C displays lower peak currents and narrower peak-to-peak separation compared to $Fe(CN)_6^{4-}$ case, implying a different type of behaviour of immobilised $Fe(CN)_6^{3-}$. The double-logarithmic plot of reduction peak current versus scan rate in Figure 3.5D produces a slope close to 1.0 at slower scan rates, signifying the thin layer reactivity of the redox active film. It appears that $Fe(CN)_6^{3-}$ is less effectively bound to PIM-EA-TB, which may be caused by its small pK_A (of less than 1), hence leading to a different type of electrochemical

activity. Although, there is another possible inference that the release of protons associated with oxidation of $Fe(CN)_6^{4-}$ is faster than the K^+ uptake during $Fe(CN)_6^{3-}$ reduction process (see Equations 3.2 and 3.3).

$$Fe(CN)_6^{4-}(PIM) + H^+(PIM) \rightleftarrows Fe(CN)_6^{3-}(PIM) + H^+(aq) + e^- \qquad (3.2)$$

$$Fe(CN)_6^{3-}(PIM) + K^+(aq) + e^- \rightleftarrows Fe(CN)_6^{4-}(PIM) + K^+(PIM) \qquad (3.3)$$

Next, the effect of PIM-EA-TB loading is examined. Cyclic voltammograms for different polymer loading after 1 mM $K_4Fe(CN)_6$ immobilisation process are shown in Figure 3.6A. Stable current responses are demonstrated in all cases. The current responses increase with PIM-EA-TB loading from 2 to 4 to 6 µg. More polymer deposit (8 µg) causes a drop in the peaks. The replicate experiments are carried out more than 3 times for each investigation so that an isolated possibility can be eliminated. Note here that the high PIM loading is achieved by repeating a few times of 2 µg deposits. The decrease in current with high loading of PIM-EA-TB is likely related to slow uptake of $Fe(CN)_6^{4-}$. Understanding the current-polymer thickness relationship is limited, and more work will be required to unravel ion mobility in PIMs. A coating of 2 µg is appropriate and used in the following experiments.

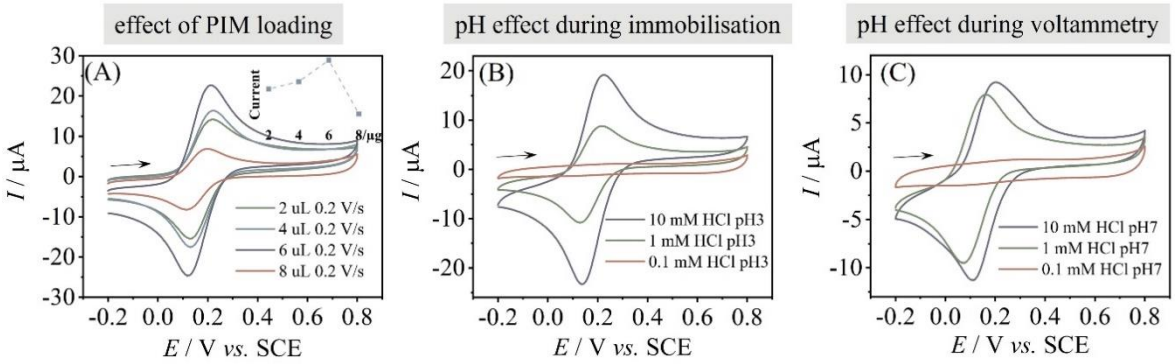

Figure 3.6 (A) **Effect of PIM-EA-TB loading.** Cyclic voltammograms (first cycle; scan rate 200 mV s^{-1}; electrolyte: 0.1 M KCl containing 1 mM HCl) for a 3 mm diameter glassy carbon electrode coated with 2, 4, 6, and 8 µg PIM-EA-TB after immersion for 12 h in 1 mM $K_4Fe(CN)_6$/1 mM HCl. (inset: plot of oxidation peak current versus PIM loading) (B) **Effect of pH during immobilisation.** Cyclic voltammograms (scan rate 100 mV s^{-1}; electrolyte: 0.1 M KCl containing 1 mM HCl) for a glassy carbon electrode coated with 2 µg PIM-EA-TB after immersion for 12 h at 4 °C in 1 mM $K_4Fe(CN)_6$ in 0.1, 1, and 10 mM HCl. (C) **Effect of pH during voltammetry.** As in (B) but immersed in 0.1 M KCl without HCl.

The effect of HCl concentration in the deposition solution on $Fe(CN)_6^{4-}$ immobilisation is depicted in Figure 3.6B. A high concentration of 10 mM HCl evidently increases the voltammetric current response, while 0.1 mM HCl concentration during immobilisation is too low. From a reported pH-dependent conductivity data [30], the protonation degree of PIM-EA-TB gradually increased when the pH of the solution went from 4 to a more acidic condition. The gradual change of protonation degree leads to swelling and more effective uptake of $Fe(CN)_6^{4-}$ in a more acidic solution, which is consistent with the results presented here. The enhanced protonation of PIM-EA-TB (immobilised in 10 mM HCl) appears to be retained when the electrode is transferred to the electrolyte with 1 mM HCl (see Figure 3.6B voltammetric data). Nevertheless, the current response observed here does not necessarily reveal the total amount of anions bound in the polymer because of the re-equilibrium after immersion of the electrode to a different condition. The re-equilibrium phenomenon can be reflected by changing the pH of the electrolyte during the cyclic voltammetry.

3.3.2 pH Effects on the Binding and Reactivity of $Fe(CN)_6^{3-/4-}$ in PIM-EA-TB

Apart from the pH effect during immobilisation of $Fe(CN)_6^{4-}$, it is essential to inspect the pH effect of the solution when carrying out the voltammetric experiments. The aim is to reveal the behaviour of the redox film in solutions with different acidity. Surprisingly, the protonation of PIM-EA-TB is not reversed when immersed in solutions with pH higher than 4, and $Fe(CN)_6^{4-}$ ions stay bound in the host structure. Cyclic voltammograms of the $Fe(CN)_6^{4-}$-immobilised films tested in 0.1 M KCl (pH ≈ 7) are shown in Figure 3.6C. Stable current responses over at least 10 cycles are obtained, consistent with data observed in pH 3 electrolyte (in Figure 3.6B). Voltammetric data for $Fe(CN)_6^{4-}$ immobilised in 1 mM HCl solution are stable. The stable voltammetric signal indicates that $Fe(CN)_6^{4-}$ binding into PIM-EA-TB remains tight even in a neutral condition. Even though some leaching out of $Fe(CN)_6^{4-}$ happens in the case of the sample immobilised from 10 mM HCl. There are two possible ways to explain the immobilisation effect. One is that the $Fe(CN)_6^{4-}$ multi-charged anion could interact with K^+ to form a second shell and become bulky leading to steric retention. Alternatively, most likely, the protonation of PIM-EA-TB retains even at a neutral solution because it requires hydroxide anions to enter the micropores to combine with the protons [21]. Therefore, the apparent $Fe(CN)_6^{4-}$ binding with PIM-EA-TB happens and remains in the absence of hydroxide, which results in a higher pK_A value of the polymer. A

systematic investigation is critical to provide further and complementary information about the $Fe(CN)_6^{4-}$ binding by changing the pH of the electrolyte during cyclic voltammetry.

The immobilisation of $Fe(CN)_6^{4-}$ in PIM-EA-TB is strongly dependent on the pH of the absorbing solution as described above, and the uptake of $Fe(CN)_6^{4-}$ can only be ensured at pH $\leq$ 3. Similarly, the redox voltammetric cycling performance of $Fe(CN)_6^{4-}$-embedded PIM-EA-TB should be affected by the pH of the electrolyte. Specifically, the cycling properties of the redox film could be changed in an alkaline condition which is of practical importance since hydroxide ions could destroy the protonation of the host and therefore cause a release of $Fe(CN)_6^{4-}$ into the solution. When $Fe(CN)_6^{3-}$-loaded PIM-EA-TB coating was tested in 0.1 M KCl solution, the resulting cyclic voltammograms are dependent on the solution pH. Figure 3.7A shows the overlayed data obtained at different pHs (pH of electrolytes adjusted by HCl or KOH). When cycled at pH 3, the voltammetric response gives a peak current of approximate 5.5 µA and a midpoint potential of E_{mid} = 0.18 V *vs.* SCE. A slight loss of voltammetric signal appears when going to pH 5, 7, or 9. The midpoint potential shifts to E_{mid} = 0.09 V *vs.* SCE and remains pH-independent. The midpoint potential altering towards a negative direction from pH 3 to pH 5 could be interpreted by proton expulsion during oxidation (each redox reaction being cycled for 4 times) as described in Equation 3.2. Then the relatively fixed midpoint potential from pH 5 to pH 9 is consistent with a process related to K^+ (see Equation 3.3).

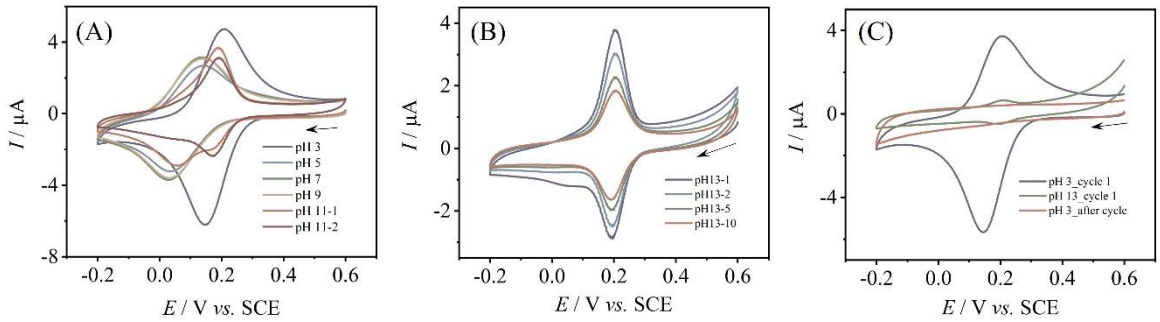

Figure 3.7 Systematic investigation of pH effect during voltammetry. (A) Cyclic voltammograms (first cycle; scan rate 100 mV s^{-1}) for 2 µg PIM-EA-TB on a glassy carbon electrode (immersed into 0.1 mM $K_3Fe(CN)_6$ and 1 mM HCl for 12 h at 4 °C) tested in aqueous 0.1 M KCl at pH 3, 5, 7, 9, 11 first cycle, and 11 second cycle. (B) As in (A), but for pH 13 cycle 1, cycle 2, cycle 5, and cycle 10. (C) As before, showing an initial experiment at pH 3, followed by an experiment at pH 13, then followed by an experiment at pH 3.

When testing the electrode in more alkaline solutions, the peak responses with E_{mid} = 0.09 V *vs.* SCE disappears, and a more symmetric small peak response with E_{mid} = 0.20 V *vs.* SCE appears (see data at pH 11 for first and second cycles in Figure 3.7A). The emerged peak current response decays over several potential cycles at pH 13 (see Figure 3.7B). These phenomena can be explained based on the hypothesis that only at pH > 9 does deprotonation of the PIM-EA-TB/H^+/$Fe(CN)_6^{4-}$ film happen, and then the resulting K^+-incorporated $Fe(CN)_6^{4-}$ complex then slowly diffuses out in alkaline condition from the PIM host to the solution. Following the results above, the apparent pK_A for deprotonation of PIM-EA-TB/H^+/$Fe(CN)_6^{4-}$ is at pH ≈ 9. More fundamentally, it means that a considerable amount of hydroxide is needed to cause deprotonation and leaching out of $Fe(CN)_6^{3-/4-}$. After cycled in solution at pH 13, the current response of the same electrode at pH 3 is indeed lost, as evidenced in Figure 3.7C.

3.3.3 Electrocatalysis with PIM-EA-TB/$Fe(CN)_6^{3-/4-}$-coated Electrodes

Heterogeneous catalysis behaviour could be studied with the $Fe(CN)_6^{3-/4-}$-immobilised PIM-EA-TB film on an electrode. Ferrocyanide and ferricyanide redox couple has been investigated as homogeneous catalysts when dissolved in solutions, such as in the detection of ascorbic acid [38] or hydrogen sulphide [7]. Here, the "organic/polymeric Prussian blue" based on PIM-EA-TB/$Fe(CN)_6^{3-/4-}$ is explored for electrocatalytic oxidation of ascorbic acid. Equation 3.4 shows the oxidation reaction of ascorbic acid, which experiences two-electron oxidation followed by a rapid hydration process [39-41].

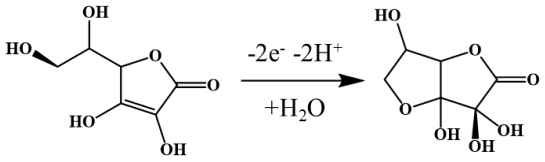

(3.4)

Figure 3.8 depicts the voltammetric data of PIM-EA-TB/$Fe(CN)_6^{3-/4-}$ film for the electrocatalytic oxidation of ascorbic acid in an aqueous 0.1 M KCl solution. The comparison of Figure 3.8A and Figure 3.8B gives the effect of immobilisation conditions (difference in $Fe(CN)_6^{4-}$ concentration during immobilisation). When the immobilisation happens in 1 mM $Fe(CN)_6^{4-}$, the amount of $Fe(CN)_6^{4-}$ absorbed in PIM-EA-TB is lower compared to that of using 0.1 mM $Fe(CN)_6^{4-}$. Thus, the electrocatalytic currents are higher in Figure 3.8B, which agrees with more catalysts and/or faster charge diffusion.

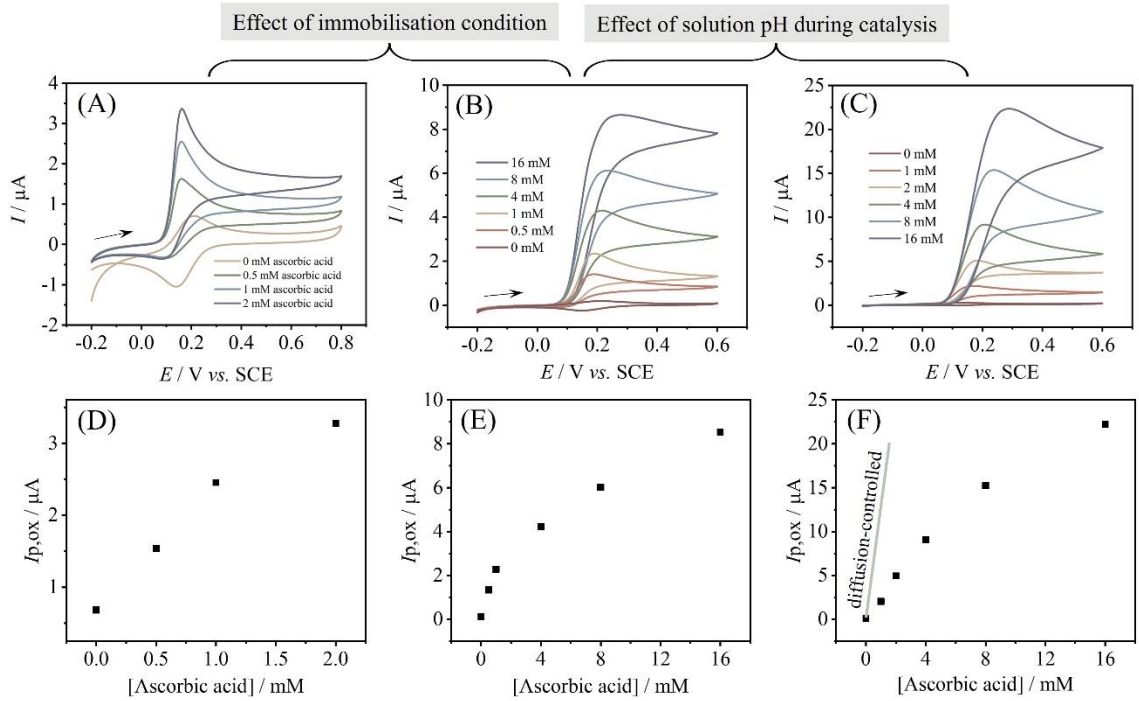

Figure 3.8 Electrocatalytic performance of PIM-EA-TB/$Fe(CN)_6^{4-}$ redox film. (A) Cyclic voltammograms (first cycle; scan rate 5 mV s^{-1}) for a 3 mm diameter glassy carbon electrode with 2 μg PIM-EA-TB (immersed into **1 mM $K_4Fe(CN)_6$** and 1 mM HCl aqueous solution at 4 °C for 12 h) in 0.1 M KCl with 1 mM HCl in the presence of 0.0, 0.5, 1.0, and 2.0 mM ascorbic acid. (B) As in (A), but kept in **0.1 mM $K_4Fe(CN)_6$** in 1 mM HCl at 4 °C for 12 h and measured in **0.1 M KCl with 1 mM HCl** in the presence of 0.0, 0.5, 1, 4, 8, and 16 mM ascorbic acid. (C) As in (B), but kept in 0.1 mM $K_4Fe(CN)_6$ in 1 mM HCl at 4 °C for 12 h and measured in **0.1 M KCl without 1 mM HCl** in the presence of 0, 1, 2, 4, 8, and 16 mM ascorbic acid. (D, E, and F) Plots of anodic peak current versus ascorbic acid concentration from (A), (B) and (C), respectively.

Next, the effect of the solution pH during electrocatalysis is explored. Figure 3.8C is recorded with the same PIM-EA-TB/$Fe(CN)_6^{4-}$ catalytic film as used in Figure 3.8B, but the ascorbic acid is dissolved in 0.1 M KCl without any HCl. The oxidation of ascorbic acid does produce localise acid (Equation 3.4), but the absence of additional protons from the electrolyte seems to increase the catalytic reaction rate.

The reaction extent of ascorbic acid oxidation can be predicted approximately by the Randles–Ševčík relation (see Equation 3.5 [42,43]). Based on this equation, the peak current for ascorbic oxidation, I_p, is correlated to the number of electrons transferred, $n = 2$; the Faraday constant, F; the electrode area, A; the ascorbic acid concentration, c; the potential scan rate, v; the diffusion coefficient of ascorbic acid, D; the gas constant, R and the temperature, T.

According to a previous study, the diffusion coefficient of ascorbic acid in aqueous solution is $D = 0.69 \times 10^{-9}$ m^2 s^{-1} [44].

$$I_p = 0.446 n^{\frac{3}{2}} F^{\frac{3}{2}} A c \sqrt{\frac{\nu D}{RT}} \tag{3.5}$$

This equation is only used to give an estimation for the current response. The actual condition can be complex due to chemical irreversibility affecting the peak current. Nevertheless, an approximate line can be previsedd, as shown in Figure 3.8F. This line provides the predicted current for the diffusion-controlled oxidation of ascorbic acid, which is significantly higher than the experimentally recorded data. The experimental process is presumably limited by either the charge hopping in the host, or the catalytic reaction rate (such as diffusion of ascorbic acid) in the redox film, or both. Further investigation needs to be done on the porosity effects on the catalytic process.

3.4 Conclusions

The preliminary study in this chapter presents the possibility of immobilising redox anions of $Fe(CN)_6^{3-/4-}$ into a microporous PIM-EA-TB host. The protonation of PIM-EA-TB associated with permeation and immobilisation of $Fe(CN)_6^{3-/4-}$ results in a redox-active film deposit. The nanochannels in the polymer provide space for ion transport and diffusion of substrates such as ascorbic acid, thus making it possible for an electrocatalytic reaction to happen. To summarise,

(i) Protonation of PIM-EA-TB at pH ≤ 3 at 4 °C over 12 h leads to an efficient immobilisation of $Fe(CN)_6^{3-/4-}$. A higher concentration of acid results in an increased amount of $Fe(CN)_6^{3-/4-}$ inside the polymer, but the binding between ions and the host structure will be destroyed in an alkaline solution at pH > 9.

(ii) When considering the permeation and transport of anions like $Fe(CN)_6^{4-}$ through microporous materials, counter ions (such as H^+ and K^+) should be considered as they can affect the rate constants.

(iii) During the immobilisation process, $Fe(CN)_6^{4-}$ acts as a base and therefore competes for protons. Thus, a higher concentration of $Fe(CN)_6^{4-}$ is unfavourable to immobilisation.

(iv) Immobilised $Fe(CN)_6^{4-}$ remains redox reactivity, which can be readily and reversibly converted into $Fe(CN)_6^{3-}$ during potential cycling. The cyclic voltammograms show diffusion-typed behaviour probably resulting from electron hopping diffusion inside the PIM-EA-TB structure.

(v) Electrocatalytic oxidation of ascorbic acid is demonstrated for PIM-EA-TB/$Fe(CN)_6^{4-}$ film. The amount of $Fe(CN)_6^{4-}$ immobilised in the film strongly affects the catalytic rates, which could be related to the rate of charge transport through the film or the diffusion ability of ascorbic acid into the nanochannels.

Work presented in this chapter gives an example of immobilisation and reactivity of ions in one of the typical PIMs. It can be seen as a first step in exploring more complicated cases of species immobilisation in PIMs. The data are incomplete in terms of models to explain the diffusion inside the polymer, the kinetic aspects, and applications of these redox systems.

In the future, other possible redox guest species can be explored to study the mechanisms of the immobilisation process and extend the applications of these hybrid films. Modifications of the molecular structures of PIM-EA-TB could also be employed to tune the properties of the redox films.

3.5 References

1 Hocking, R. K., Wasinger, E. C., de Groot, F. M., Hodgson, K. O., Hedman, B., & Solomon, E. I. Fe L-edge XAS studies of $K_4[Fe(CN)_6]$ and $K_3[Fe(CN)_6]$: a direct probe of back-bonding. *Journal of the American Chemical Society* **128**, 10442-10451 (2006).

2 Nematollahi, D. & Varmaghani, F. Paired electrochemical synthesis of new organosulfone derivatives. *Electrochimica Acta* **53**, 3350-3355 (2008).

3 Buckingham, M. A., Marken, F., Aldous, L. The thermoelectrochemistry of the aqueous iron (ii)/iron (iii) redox couple: significance of the anion and pH in thermogalvanic thermal-to-electrical energy conversion. *Sustainable Energy & Fuels* **2**, 2717-2726 (2018).

4 O'Reilly, J. E. Oxidation-reduction potential of the ferro-ferricyanide system in buffer solutions. *Biochimica et Biophysica Acta (BBA)-Bioenergetics* **292**, 509-515 (1973).

5 Zhang, H., Li, J., Wang, K., Du, X. & Li, Q. A simple and sensitive assay for ascorbate using potassium ferricyanide as spectroscopic probe reagent. *Analytical Biochemistry* **388**, 40-46 (2009).

6 Almeida Junior, P. L., Mendes, C. H., Lima, I. A., Belian, M. F., Oliveira, S. C., Brett, C. M., & Nascimento, V. B. Ferricyanide Confined in a Protonated Amine-Functionalized Silica Film on Gold: Application to Electrocatalytic Sensing of Nitrite Ions. *Analytical Letters* **51**, 496-511 (2018).

7 Jeroschewski, P., Steuckart, C. & Kühl, M. An amperometric microsensor for the determination of H_2S in aquatic environments. *Analytical Chemistry* **68**, 4351-4357 (1996).

8 Lawrence, N. S., Thompson, M., Prado, C., Jiang, L., Jones, T. G., & Compton, R. G. Amperometric detection of sulfide at a boron doped diamond electrode: The electrocatalytic reaction of sulfide with ferricyanide in aqueous solution. *Electroanalysis: An International Journal Devoted to Fundamental and Practical Aspects of Electroanalysis* **14**, 499-504 (2002).

9 Gritzner, G., Danksagmüller, K., Gutmann, V. Outer-sphere coordination effects on the redox behaviour of the $Fe(CN)_6^{3-}/Fe(CN)_6^{4-}$ couple in non-aqueous solvents. *Journal of Electroanalytical Chemistry and Interfacial Electrochemistry* **72**, 177-185 (1976).

10 McNicholas, B. J., Grubbs, R. H., Winkler, J. R., Gray, H. B. & Despagnet-Ayoub, E. Tuning the formal potential of ferrocyanide over a 2.1 V range. *Chemical science* **10**, 3623-3626 (2019).

11 Buckingham, M. A., Hammoud, S., Li, H., Beale, C. J., Sengel, J. T., & Aldous, L. A fundamental study of the thermoelectrochemistry of ferricyanide/ferrocyanide: cation, concentration, ratio, and heterogeneous and homogeneous electrocatalysis effects in thermogalvanic cells. *Sustainable Energy & Fuels* **4**, 3388-3399 (2020).

12 Peter, L., Dürr, W., Bindra, P., Gerischer, H. The influence of alkali metal cations on the rate of the $Fe(CN)_6^{4-}/Fe(CN)_6^{3-}$ electrode process. *Journal of Electroanalytical Chemistry and Interfacial Electrochemistry* **71**, 31-50 (1976).

13 Cheah, M. H. & Chernev, P. Electrochemical oxidation of ferricyanide. *Scientific Reports* **11**, 1-7 (2021).

14 Chang, J. L., Wei, G. T., Chen, T. Y. & Zen, J. M. Highly stable polymeric ionic liquid modified electrode to immobilize ferricyanide for electroanalysis of sulfide. *Electroanalysis* **25**, 845-849 (2013).

15 Jones, T. R., Hernandez-Aldave, S., Kaspar, R. B., Letterio, M. P., Yan, Y., & Bertoncello, P. Tris (2, 4, 6-trimethoxyphenyl) polysulfone-methylene quaternary phosphonium chloride (TPQPCl) ionomer chemically modified electrodes: An electroanalytical study towards sensing applications. *Electrochimica Acta* **311**, 160-169 (2019).

16 Itaya, K., Uchida, I. & Neff, V. D. Electrochemistry of polynuclear transition metal cyanides: Prussian blue and its analogues. *Accounts of Chemical Research* **19**, 162-168 (1986).

17 Azhar, A., Li, Y., Cai, Z., Zakaria, M. B., Masud, M. K., Hossain, M. S. A., Kim, J., Zhang, W., Na, J., Yamauchi, Y. & Hu, M. Nanoarchitectonics: a new materials horizon for prussian blue and its analogues. *Bulletin of the Chemical Society of Japan* **92**, 875-904 (2019).

18 Alexandrov, E. V., Virovets, A. V., Blatov, V. A. & Peresypkina, E. V. Topological motifs in cyanometallates: from building units to three-periodic frameworks. *Chemical Reviews* **115**, 12286-12319 (2015).

19 Cvrtila, I., Stilinovic, V. New tricks by old anions: hydrogen bonded hexacyanoferrous anionic networks. *Crystal Growth & Design* **17**, 6793-6800 (2017).

20 Carta, M., Malpass-Evans, R., Croad, M., Rogan, Y., Jansen, J. C., Bernardo, P., Bazzarelli, F. & McKeown, N. B. An efficient polymer molecular sieve for membrane gas separations. *Science* **339**, 303-307 (2013).

21 Kolodziej, A., Ahn, S. D., Carta, M., Malpass-Evans, R., McKeown, N. B., Chapman, R. S., Bull, S. D. & Marken, F. Electrocatalytic carbohydrate oxidation with 4-benzoyloxy-TEMPO heterogenised in a polymer of intrinsic microporosity. *Electrochimica Acta* **160**, 195-201 (2015).

22 Rong, Y., Kolodziej, A., Madrid, E., Carta, M., Malpass-Evans, R., McKeown, N. B., & Marken, F. Polymers of intrinsic microporosity in electrochemistry: Anion uptake and transport effects in thin film electrodes and in free-standing ionic diode membranes. *Journal of Electroanalytical Chemistry* **779**, 241-249 (2016).

23 Zhuang, X., Wang, D., Lin, Y., Yang, L., Yu, P., Jiang, W., & Mao, L. Strong interaction between imidazolium-based polycationic polymer and ferricyanide: Toward redox potential regulation for selective in vivo electrochemical measurements. *Analytical Chemistry* **84**, 1900-1906 (2012).

24 Gómez-Romero, P., Ayyad, O., Suárez-Guevara, J. & Muñoz-Rojas, D. Hybrid organic-inorganic materials: from child's play to energy applications. *Journal of Solid State Electrochemistry* **14**, 1939-1945 (2010).

25 Zhao, W., Xu, J. J., Shi, C. G., & Chen, H. Y. Multilayer membranes via layer-by-layer deposition of organic polymer protected Prussian blue nanoparticles and glucose oxidase for glucose biosensing. *Langmuir* **21**, 9630-9634 (2005).

26 Chaudhary, A., Pathak, D. K., Tanwar, M., Sagdeo, P. R. & Kumar, R. Prussian blue-viologen inorganic-organic hybrid blend for improved electrochromic performance. *ACS Applied Electronic Materials* **1**, 892-899 (2019).

27 Tieke, B. Coordinative supramolecular assembly of electrochromic thin films. *Current opinion in colloid & interface science* **16**, 499-507 (2011).

28 DeLongchamp, D. M. & Hammond, P. T. High-contrast electrochromism and controllable dissolution of assembled Prussian blue/polymer nanocomposites. *Advanced Functional Materials* **14**, 224-232 (2004).

29 Lapidus, S. H., Graham, A. G., Kareis, C. M., Hawkins, C. G., Stephens, P. W., & Miller, J. S. Anomalous Stoichiometry, 3-D Bridged triangular/pentagonal layered structured artificial antiferromagnet for the Prussian blue analogue $A_3Mn^{II}_5(CN)_{13}$ (A = NMe_4, $NEtMe_3$). A Cation Adaptive Structure. *Journal of the American Chemical Society* **141**, 911-921 (2018).

30 Madrid, E., Rong, Y., Carta, M., McKeown, N. B., Malpass-Evans, R., Attard, G. A., Clarke, T. J., Taylor, S. H., Long. Y.-T. & Marken, F. Metastable ionic diodes derived from an amine-based polymer of intrinsic microporosity. *Angewandte Chemie* **126**, 10927-10930 (2014).

31 Marcus, Y. Ion Properties; Marcus Dekker. *Inc, New York* (1997).

32 Rong, Y., He, D., Sanchez-Fernandez, A., Evans, C., Edler, K. J., Malpass-Evans, R., Carta, M., McKeown, N. B., Clarke, T. J., Taylor, S. H., Wain, A. J., Mitchels, J. M. & Marken, F. Intrinsically microporous polymer retains porosity in vacuum thermolysis to electroactive heterocarbon. *Langmuir* **31**, 12300-12306 (2015).

33 Jordan, J. & Ewing, G. J. The protonation of hexacyanoferrates. *Inorganic Chemistry* **1**, 587-591 (1962).

34 Sutter, J. R. & Spencer, W. An equilibrium and kinetic study of the methylene blue-ferrocyanide reaction in acid medium. *Journal of Physical Chemistry* **94**, 4116-4119 (1990).

35 Koncki, R. & Wolfbeis, O. S. Composite films of Prussian blue and N-substituted polypyrroles: fabrication and application to optical determination of pH. *Analytical chemistry* **70**, 2544-2550 (1998).

36 Tan, R., Wang, A., Malpass-Evans, R., Williams, R., Zhao, E. W., Liu, T., Ye, C., Zhou, X., Darwich, B. P., Fan, Z., Turcani, L., Jackson, E., Chen, L., Chong, S. Y., Li, T., Jelfs, K. E., Cooper, A. I., Brandon, N. P., Grey, C. P., McKeown, N. B. & Song, Q. Hydrophilic microporous membranes for selective ion separation and flow-battery energy storage. *Nature Materials* **19**, 195-202 (2020).

37 McKenzie, K. J. & Marken, F. Accumulation and reactivity of the redox protein cytochrome c in mesoporous films of TiO_2 phytate. *Langmuir* **19**, 4327-4331 (2003).

38 Thangamuthu, R., Wu, Y. C. & Chen, S. M. Selective detection of ascorbic acid using octacyanomolybdate-doped-glutaraldehyde-cross-linked poly-l-lysine film modified glassy carbon electrode. *Electroanalysis: An International Journal Devoted to Fundamental and Practical Aspects of Electroanalysis* **21**, 165-171 (2009).

39 Perone, S. & Kretlow, W. Application of controlled potential techniques to study of rapid succeeding chemical reaction coupled to electro-oxidation of ascorbic acid. *Analytical Chemistry* **38**, 1760-1763 (1966).

40 Lechien, A., Valenta, P., Nürnberg, H. W. & Patriarche, G. Determination of ascorbic acid by differential pulse voltammetry. *Fresenius' Zeitschrift für analytische Chemie* **311**, 105-108 (1982).

41 Hian, L. C., Grehan, K. J., Compton, R. G., Foord, J. S. & Marken, F. Influence of thin film properties on the electrochemical performance of diamond electrodes. *Diamond and Related Materials* **12**, 590-595 (2003).

42 Randles, J. E. A cathode ray polarograph. Part II. – The current-voltage curves. *Transactions of the Faraday Society* **44**, 327-338 (1948).

43 Ševčík, A. Oscillographic polarography with periodical triangular voltage. *Collection of Czechoslovak Chemical Communications* **13**, 349-377 (1948).

44 Motshakeri, M., Travas-Sejdic, J., Phillips, A. R. & Kilmartin, P. A. Rapid electroanalysis of uric acid and ascorbic acid using a poly (3, 4-ethylenedioxythiophene)-modified sensor with application to milk. *Electrochimica Acta* **265**, 184-193 (2018).

Chapter 4 Catechin or Quercetin Guests in an Intrinsically Microporous Polyamine (PIM-EA-TB) Host: Accumulation, Reactivity, and Release

Contents

Chapter Abstract

Electrocatalytic reactions usually contain molecularly involved processes such as redox molecular couples. For heterogeneous reactions, the diffusion and reactivity of redox molecules are of great interest. In this chapter, an intrinsically microporous polyamine (PIM-EA-TB) with typical micropore sizes of 0.5 nm to 1.5 nm has been explored as a host for binding redox guest molecules like catechin and quercetin. The guest species interact with tertiary amine sites in PIM-EA-TB *via* hydrogen bonding. Cyclic voltammetric results propose apparent Langmuirian binding constants for catechin of 550 (± 50) × 10^3 M^{-1} at pH 2 when PIM-EA-TB is protonated and 130 (± 13) × 10^3 M^{-1} at pH 6 when PIM-EA-TB is not protonated. The binding capacity is typically one guest molecule binding to each monomer of PIM-EA-TB. Although higher loading can be achieved by host/guest co-deposition from tetrahydrofuran solution, excess guest molecules will be released into the solution after a few potential cycles. The bound *ortho*-quinol molecules show 2-electron 2-proton redox conversion to the corresponding quinones in a thin mono-layer PIM-EA-TB film close to the electrode surface. Release of guest species happens depending on the amount of loading and the type of guests, either spontaneously or under electrochemical stimuli.

Graphical Abstract

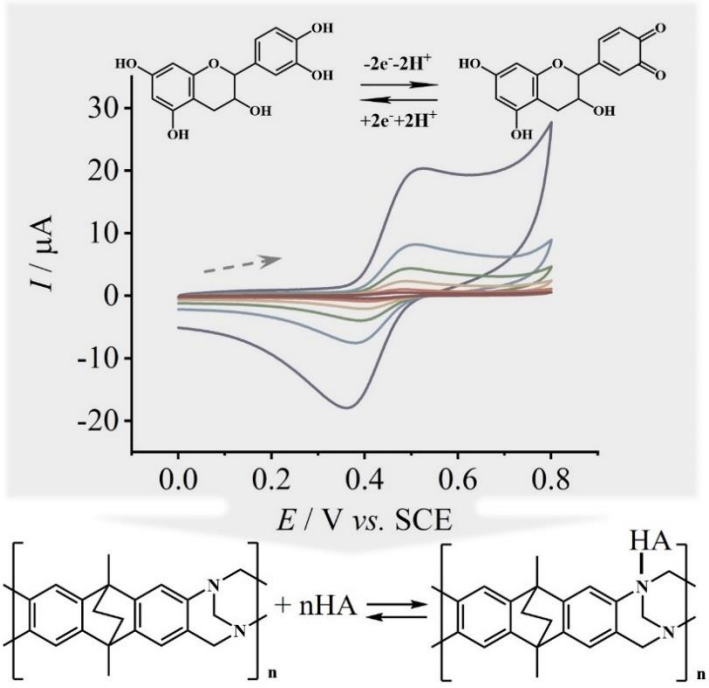

Publications associated with this chapter

Wang, L., Malpass-Evans, R., Carta, M., McKeown, N. B., Reeksting, S. B., & Marken, F. Catechin or quercetin guests in an intrinsically microporous polyamine (PIM-EA-TB) host: accumulation, reactivity, and release. *RSC Advances*, **11**, 27432-27442 (2021).

Credit Statement

The candidate developed the immobilisation methods of catechin/quercetin into PIM-EA-TB, and performed the electrochemical experiments, quantification of catechin and quercetin based on LC-MS, data curation, and interpretation of the results. Neil B. McKeown provided the PIM-EA-TB material. Shaun B. Reeksting explained and trained the candidate to use LC-MS Agilent Walk-up equipment and the data processing software Qual B 07.00 and Quant 10.0. Richard Malpass-Evans, Mariolino Carta, Neil B. McKeown, and Shaun B. Reeksting gave valuable comments to the draft. Frank Marken supervised the candidate, guided the completion of the idea, gave critical and important suggestions to this work, and helped with the reviewing and editing of the original draft.

Special Acknowledgements

I would like to thank Prof. Neil McKeown and his research group from the University of Edinburgh for providing PIM-EA-TB used in this study. Thanks to Dr Philip Fletcher for his help in taking SEM images presented in this chapter.

4.1 Introduction

Binding and release of guest species in microporous materials are of great interest in selective capture of specific species from wastewater [1], in the analysis of porous permeable membranes [2], and in controlled release of drugs in medical applications [3]. The hydrogen bonding between a guest and a microporous host enhances the host-guest interactions and induces the pH-dependent accumulation and release processes [4]. One of the prototypical polymers of intrinsic microporosity (PIMs), PIM-EA-TB (see molecular structure in Figure 4.1), is considered as a host to allow spontaneous and efficient accumulation and release of herbal drugs.

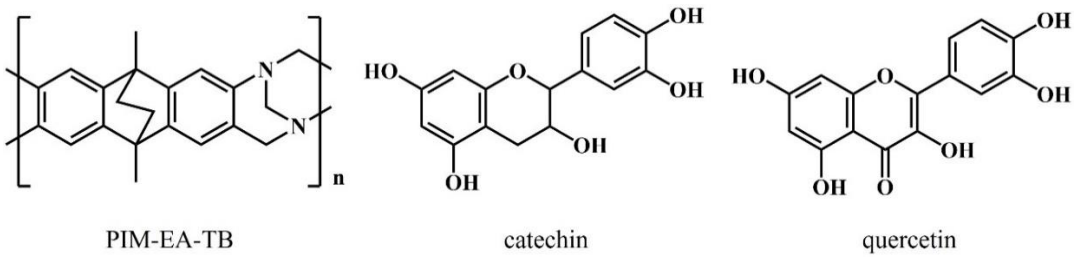

Figure 4.1 Molecular structures for PIM-EA-TB (monomeric unit m.w. 300 g mol^{-1}), the flavanol catechin (m.w. 290 g mol^{-1}), and the flavonol quercetin (m.w. 304 g mol^{-1}).

PIM-EA-TB has a typical molecular weight of 70 kDa, a Brunauer–Emmett–Teller (BET analysis of nitrogen adsorption [5]) surface area of 1000 m^2 g^{-1}, and pore sizes dominantly ranging from 0.5 nm to 1.5 nm. The presence of tertiary amine functional groups in PIM-EA-TB provide sites for protonation (at pH ≈ 4) in aqueous solution [6]. Hydrogen bonding has been reported to play an essential role in accumulating guest species like caffeic acid [7] in PIM-EA-TB at pH > 4. For weakly acidic guest species, hydrogen bonding is likely to enhance the host-guest interactions and therefore contribute to the rate of transport processes in PIM-EA-TB structure.

Catechin (see molecular structure in Figure 4.1), as an *ortho*-quinol, is a natural flavanol component in herbal teas [8,9] and wine [10]. The electrochemical properties of catechin[11] have been investigated as an antioxidant [12] and a superoxide radical quencher [13]. Electrochemically deposited catechin film on a glassy carbon electrode was studied toward electrocatalytical oxidation of hydrazine [14]. The first deprotonation of catechin happens at $pK_A = 8.7$ [15].

Quercetin (see molecular structure in Figure 4.1), another *ortho*-quinol, has similar redox-chemical reactivity as catechin, but is less soluble in water. Quercetin shows a slightly acidic first deprotonation at $pK_A \approx 7.1$ [16]. Electrochemistry of quercetin has been studied [17,18], and the electrochemical detection of quercetin based on carbon materials has been reported [19]. As a member of flavonoids, quercetin has been proved to have anti-cancer activity in vitro and in vivo [20]. The antioxidant characteristic of quercetin could be linked to medical applications [21]. The binding of quercetin into microporous metal-organic framework ZIF-90 [22] or chitosan [23], and the release of quercetin from natural hydrogels [24] have been reported. However, quercetin shows low stability when physical and chemical condition changes, such as temperature [25,26], pH [27,28], presence of metal ions [26], and oxygen [29,30]. Efforts have been put into improving stability and absorption of quercetin[31,32].

In this chapter, catechin and quercetin are investigated as guest molecules to bind into host PIM-EA-TB. The accumulation and reactivity are studied by voltammetric experiments. The binding of catechin or quercetin from aqueous solutions is revealed to reach a limit with the molar ratio of 1:1 (catechin or quercetin: PIM-EA-TB monomeric unit). Similar deposits with higher loading can be achieved by co-deposition from host and guest mixed tetrahydrofuran (THF) solution. Effects of catechin or quercetin loading and pH on binding and release are explored.

4.2 Experimental

4.2.1 Reagents

Catechin (≥98%, HPLC), quercetin (≥95%, HPLC), carbon (glassy, spherical powder, 2–12 μm, 99.5% trace metals basis), chloroform (≥99.8%), and phosphoric acid (H_3PO_4, 85 wt%) were products of Sigma Aldrich. Sodium hydroxide (NaOH, ≥97%) and tetrahydrofuran (THF, ≥99.8%) were purchased from Fisher Chemical. The synthesis of PIM-EA-TB followed the literature method.[5] Ethanol absolute from VWR Chemicals is used in the pre-dissolution of quercetin for quantification experiments. Ultra-pure water (resistivity 18.2 MΩ cm at 20 °C) from a Thermo Scientific water purification system was employed to prepare aqueous solutions.

4.2.2 Instrumentation

Electrochemistry data were recorded by a potentiostat (Metrohm μAutolab II). Electrochemical experiments were carried out with a three-electrode configuration, in which a 3 mm diameter glassy carbon disk electrode was the working electrode, a Pt wire as the counter electrode, and a KCl-saturated calomel electrode (SCE, Radiometer REF 401) was the reference electrode. Phosphate buffer solutions with different pHs were prepared with phosphoric acid solution adjusted by solid sodium hydroxide and monitored with a pH meter (Jenway 3505). The catechin and quercetin was determined by liquid chromatography-mass spectroscopy (LC-MS) technique employing an Agilent 6545 Accurate-Mass Q-TOF LC/MS system. Scanning electron microscopy (SEM) images were captured with JEOL JSM-6301F FESEM equipment.

4.2.3 Catechin Immobilisation into PIM-EA-TB by Aqueous Solution Uptake

PIM-EA-TB was dissolved in chloroform to make a 1 mg mL^{-1} stock solution. The first immobilisation method was immersing PIM-EA-TB film into catechin aqueous solutions for a specific time. Typically, a film of deposit was prepared by drop-casting 2 μL of 1 mg mL^{-1} PIM-EA-TB chloroform solution on a 3 mm diameter glassy carbon disk electrode. The uptake of catechin happened gradually by immersing the electrode in catechin-containing phosphate buffer (0.1 M) solutions and left overnight (12 h) at 4 °C in a refrigerator. Then the electrode was rinsed with water and electrochemically assessed in 0.1 M phosphate buffer electrolyte solution.

4.2.4 Catechin and Quercetin Immobilisation into PIM-EA-TB by Codeposition of THF Solutions

PIM-EA-TB, catechin, and quercetin solutions in THF were prepared by dissolution. PIM-EA-TB solution (1 mg mL^{-1}) was mixed with catechin or quercetin solution (with concentrations of 0.1 or 1 or 10 mg mL^{-1}) in a volume ratio of 1:1. Typically, 4 μL of the mixed solution was coated on a 3 mm diameter glassy carbon disk electrode, evaporated in ambient, and electrochemically tested in 0.1 M phosphate buffer electrolyte. To increase the surface area and thereby enhance the voltammetric currents for catechin-immobilised PIM-EA-TB deposit, carbon microspheres were introduced in some experiments. A THF solution of 180 mg mL^{-1} carbon spheres with 7.5 mg mL^{-1} PIM-EA-TB was prepared. Then an amount of 2 μL of the solution was deposited onto a glassy carbon electrode. The immobilisation was carried out in a refrigerator with 5 μM catechin in 0.1 M phosphate

buffer solution (pH 2) buffer for 12 h. The same procedure of catechin immobilisation was performed without carbon spheres to show the effect of surface area on the voltammetric response.

4.2.5 Catechin and Quercetin Release Quantification

The catechin or quercetin-immobilised PIM-EA-TB deposits in this section were acquired from the co-deposition method from THF solutions. Chronoamperometry was performed at different applied potentials of 0.0/−1.5/−2.0/−2.5/−3.0/−3.5 V *vs.* SCE for 5 min in 10 mM phosphate buffer solution (pH 7). The applied potential caused alkaline conditions to develop inside PIM-EA-TB to accelerate the release process. After chronoamperometry, the electrolyte solutions were analysed by liquid chromatography coupled with mass spectroscopy (LC-MS) using an Agilent QTOF 6545 walk-up system. Calibration curves (Figure 4.2) for catechin and quercetin were processed in Qual B 07.00 and Quant 10.0 software to quantify catechin and quercetin release. Note that the response values proportional to concentrations here are the integration of the compound chromatograms.

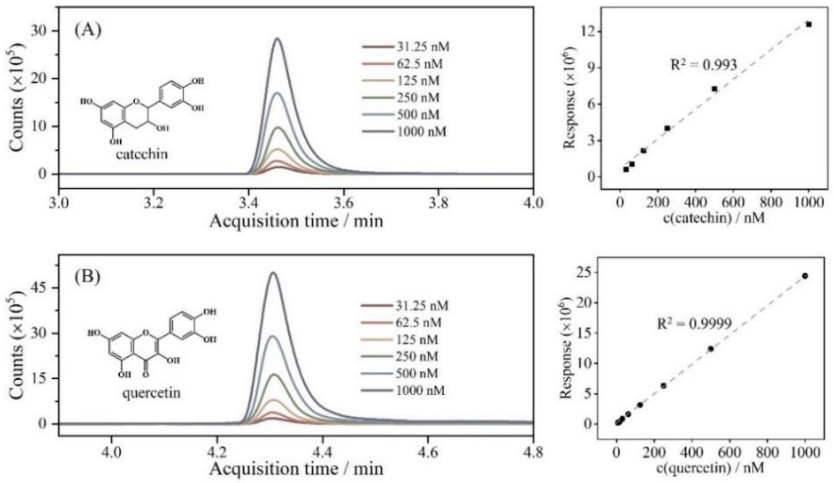

Figure 4.2 Quantification of catechin and quercetin. Compound chromatograms and calibration curves of catechin (A) and quercetin (B) from the liquid chromatography-mass spectroscopy (LC-MS) technique. Response values are areas under chromatogram curves.

4.3 Results and Discussion

4.3.1 Catechin Immobilisation by Absorption into PIM-EA-TB

When a typical amount of 2 μg PIM-EA-TB was deposited on a 3 mm diameter glassy carbon electrode, the film thickness was about 0.3 μm on average, assuming a density of

approximate 1 g cm^{-3}. The coated electrode was then immersed in 0.1 mM catechin in 0.1 M phosphate buffer at pH 2 for 12 h in a fridge. After rinsing with water, the electrode was electrochemically evaluated in 0.1 M phosphate buffer electrolyte at pH 2. Cyclic voltammograms at different potential scan rates are shown in Figures 4.3A and B. Well-defined redox shape of voltammetric data is observed with a midpoint potential $E_{mid} = ½(E_{p, ox} + E_{p, red}) = 0.46$ V *vs.* SCE. The voltammetric results agree with the reported *ortho*-quinol to *ortho*-quinone 2-electron 2-proton process for catechin [33] (Equation 4.1).

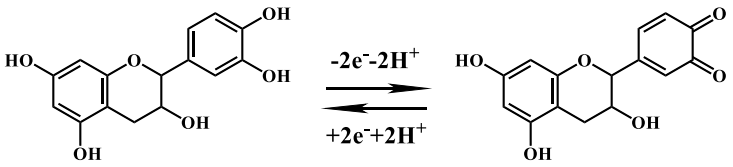

(4.1)

A double-logarithmic plot of anodic peak current against scan rate (Figure 4.3C) generates a linear relationship with a slope of close to 1.0, demonstrating an immobilised redox thin-layer behaviour without significant effects from diffusion on the peak current. The redox signal of the deposit is stable after a series of voltammetric experiments (see Figure 4.3D).

Given the linear relationship between the peak currents scale and scan rate, it is of interest to assess the charge under the oxidation peak current. The charge is approximately $Q_p = 3$ μC, corresponding to an amount of 10^{13} catechin molecules or 10^{13} PIM-EA-TB monomers, assuming the hydrogen binding (amine sites in PIM-EA-TB structure binding to hydroxide groups of catechin molecules) capacity of one molecule to one monomer unit. Therefore, the active film volume is about 4.5×10^{-9} cm^3 or an average thickness of 0.65 nm (on a 3 mm diameter electrode), presuming an approximate PIM-EA-TB density of 1 g cm^{-3}. The electrochemically active amount of the film demonstrates that only a mono-layer of catechin molecules (within tunnel distance to the electrode, see Figure 4.3F) is engaged in the redox reactions without significant propagation of charges into the bulk polymer film. It is unlikely that the transport of catechin molecules happens on the time scale of the voltammetric detection due to the rigid backbone of the host. Hydrogen bonds between catechin molecules and tertiary amines stay intact during redox tests, although there is probably a local pH change in the film.

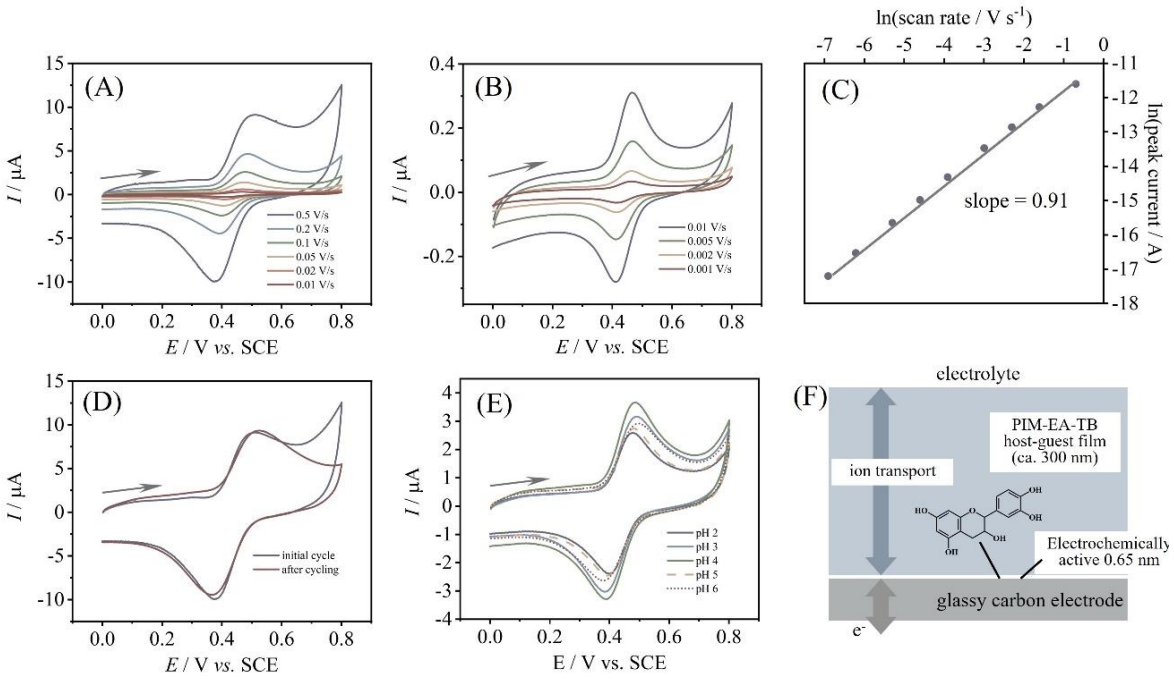

Figure 4.3 Electrochemical results of catechin-immobilised PIM-EA-TB film by absorption from aqueous solution. (A) Cyclic voltammograms (3 mm diameter glassy carbon electrode; scan rate 0.5, 0.2, 0.1, 0.05, 0.02, and 0.01 V s^{-1}) for a catechin-immobilised PIM-EA-TB film (immobilisation in 0.1 mM catechin in 0.1 M phosphate buffer at pH 2 for 12 h) tested in electrolyte of 0.1 M phosphate buffer pH 2. (B) As in (A), for scan rates 0.01, 0.005, 0.002, and 0.001 V s^{-1}. (C) A double-logarithmic plot of anodic peak current *versus* scan rate. (D) As in (A) for the initial and final potential cycles (scan rate of 0.5 V s^{-1}). (E) As in (A), comparing the effect of pH during immobilisation (scan rate 0.1 V s^{-1}). (F) Schematic drawing of the thin layer redox process.

The effect of pH during the catechin immobilisation process on the voltammetric response was investigated. Figure 4.3E shows the cyclic voltammograms of PIM-EA-TB film immobilised from catechin solution at pH 2, 3, 4, 5, and 6 and tested in electrolyte at pH 2. Note here that there is more than one redox process in the cyclic voltammograms of catechin. But in this case, the applied potential range was restricted to avoid the irreversible or electrode fouling process. The variation of the current responses is surprisingly minor. More than three times in each experiment are replicated to avoid random variation. A slight increase in peak current at pH 4 is observed, which could be tentatively explained by the higher mobility of catechin molecules in the channels of partially protonated PIM-EA-TB host. More formally, equations can be expressed to show the processes during catechin immobilisation at different pH ranges. The protonation of PIM-EA-TB in an aqueous phosphate buffer solution can be suggested as Equation 4.2. The equilibrium constant $K_A \approx 10\,000\ M^{-1}$ is associated with an approximate pK_A of 4 under these conditions. [34]

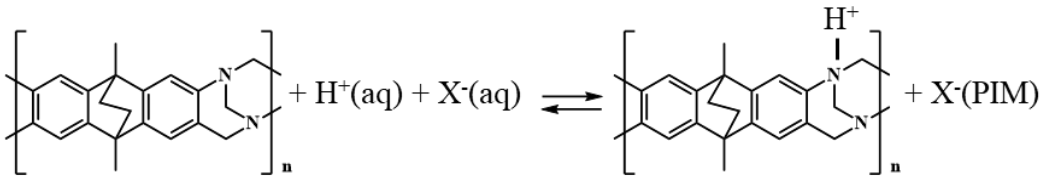

(4.2)

When immersing PIM-EA-TB in a solution with pH > 4, the tertiary amines inside the polymer are predominantly neutral, which show the ability to bind to protons from weakly acidic guest species. With a $pK_A \approx 8.7$, catechin can bind to the host through hydrogen bonding (see Equation 4.3).

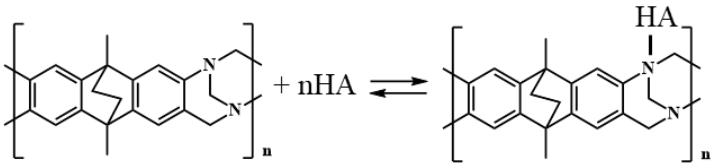

(4.3)

In a solution with pH < 4, the tertiary amines in PIM-EA-TB are predominantly protonated. Therefore, the catechin binding process could be demonstrated as an exchange reaction in which the aqueous acid is liberated, as shown in Equation 4.4.

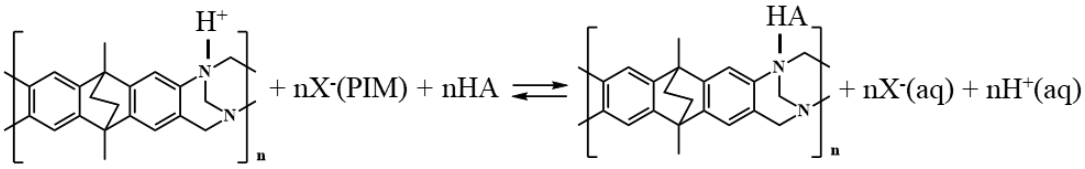

(4.4)

To better understand the immobilisation process, the apparent binding constant for catechin can be extracted from binding curves. Binding curves here are based on the electrochemically active catechin content immobilised in PIM-EA-TB (proportional to the voltammetric peak currents) as a function of catechin concentration in solution during the immobilisation process. Figure 4.4 presents data for the effect of catechin concentration on binding into PIM-EA-TB at pH = 2 (when protonation happens) and at pH = 6 (when no protonation happens). The peak currents increase with catechin concentration in solution during the immobilisation process for both cases under experimental conditions here. Binding constants are estimated from voltammetric currents plotted and fitted with a Langmurian model (Figure 4.4B and D). The binding constant at pH 2 is approximately 550 (±50) × 10^3 M^{-1}, slightly higher than that at pH 6, 130 (±13) × 10^3 M^{-1}. Even though the fitting plots are not perfect, the binding of catechin is likely to be dominated by the hydrogen bonding interaction.

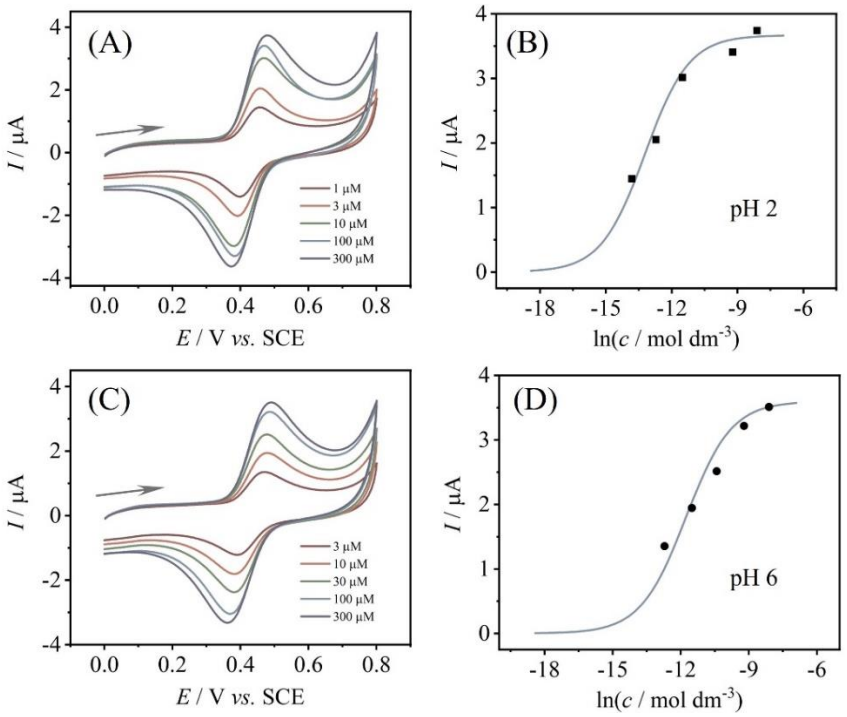

Fig. 4.4 Determination of apparent binding constants of catechin in PIM-EA-TB. (A) Cyclic voltammograms (3 mm diameter glassy carbon electrode; first cycle, scan rate 0.1 V s^{-1}) for catechin-bound PIM-EA-TB film (immobilisation in 0.001, 0.003, 0.01, 0.1, and 0.3 mM catechin in 0.1 M phosphate buffer pH 2 for 12 h) and immersed into 0.1 M phosphate buffer pH 2. (B) Plot of peak current *versus* logarithm of catechin concentration. (C) As in (A), but immobilisation in 0.003, 0.01, 0.03, 0.1, and 0.3 mM catechin in 0.1 M phosphate buffer pH 6 for 12 h. (D) Plot of peak current *versus* logarithm of catechin concentration.

Next, the binding behaviour of catechin-immobilised PIM-EA-TB was studied by varying the pH of the electrolyte. A well-defined Nernstian shift as a function of pH value is observed (Figure 4.5A and grey squared points in E). Gradual loss of catechin signal happens when pH value alters from 2 to 13. A dramatic loss of signal emerges for pH > 9. Figure 4.5B contrasts the binding behaviours from pH 2 to pH 13, then back to pH 2. The catechin signal evidently disappears in the alkaline solution. At pH 13, the deprotonation of PIM-EA-TB film takes place, and thereby binding of catechin is inhibited. The behaviours of catechin-immobilised PIM-EA-TB film under neutral (water) and alkaline (pH 13 buffer solution) conditions are qualitatively contrasted and photographed in Figure 4.5F. The colour change in alkaline solution is consistent with the reported colour of catechin [35].

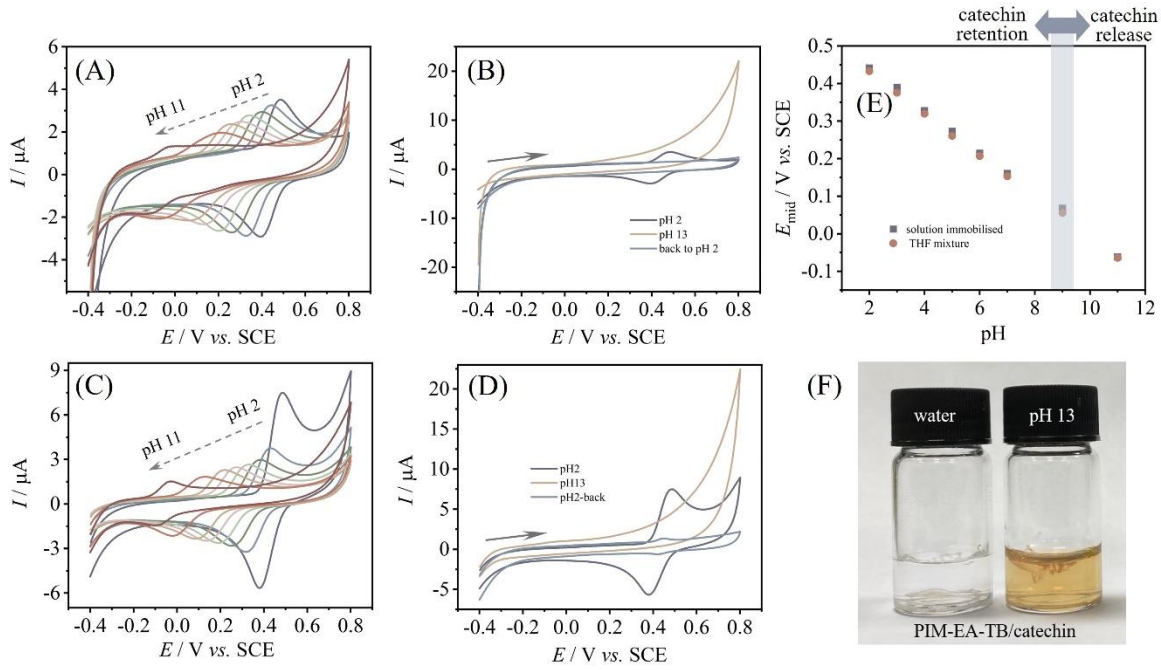

Figure 4.5 pH effects during voltammetry on catechin-immobilised PIM-EA-TB by absorbing or co-deposition method. (A) Cyclic voltammograms (3 mm diameter glassy carbon electrode; scan rate 0.1 V s^{-1}) for catechin bound into a PIM-EA-TB film and immersed into 0.1 M phosphate buffer at different pH values (pH = 2, 3, 4, 5, 6, 7, 9, and 11). (B) As in (A), but comparing pH 2, then pH 13, then back to pH 2. (C) Cyclic voltammograms (3 mm diameter glassy carbon electrode; scan rate 0.1 V s^{-1}) for catechin co-deposited into a PIM-EA-TB film and immersed into 0.1 M phosphate buffer at different pH values. (D) As in (C), but comparing pH 2, then pH 13, then back to pH 2. (E) A plot of midpoint potential $E_{mid} = ½(E_{p,ox} + E_{p,red})$ *versus* pH. (F) Photograph showing the PIM-EA-TB/catechin 1 : 1 film in a glass vial exposed to water and 0.1 M phosphate buffer pH 13.

As a result of only a very thin layer (mono-layer in this case) of the film being electrochemically active, the voltammetric currents remain low. One of the options to increase the currents is to introduce a higher surface area. Carbon microspheres of typically 2 to 12 µm (see SEM images in Figures 4.6E and F) are employed here and directly co-deposited with PIM-EA-TB chloroform solution. Since 360 µg carbon was mixed and co-deposited with 15 µg PIM-EA-TB, an approximate 24 times higher surface area is obtained (assuming an average of 6 µm diameter spheres). The electrochemical redox results of catechin-absorbed PIM-EA-TB with carbon spheres (after binding from 5 µM catechin solution) are shown in Figures 4.6A and B. The oxidative peak current is approximate 2 µA at a scan rate of 0.01 V s^{-1}. For comparison, a current of 0.2 µA was obtained for the PIM-EA-TB on a flat electrode without carbon spheres immobilised from 100 µM catechin (Figure 4.3B). The redox currents are significantly enhanced with the presence of carbon

spheres. A corresponding higher capacitive background current is consistent with a higher surface area created by carbon microspheres (Figure 4.6D).

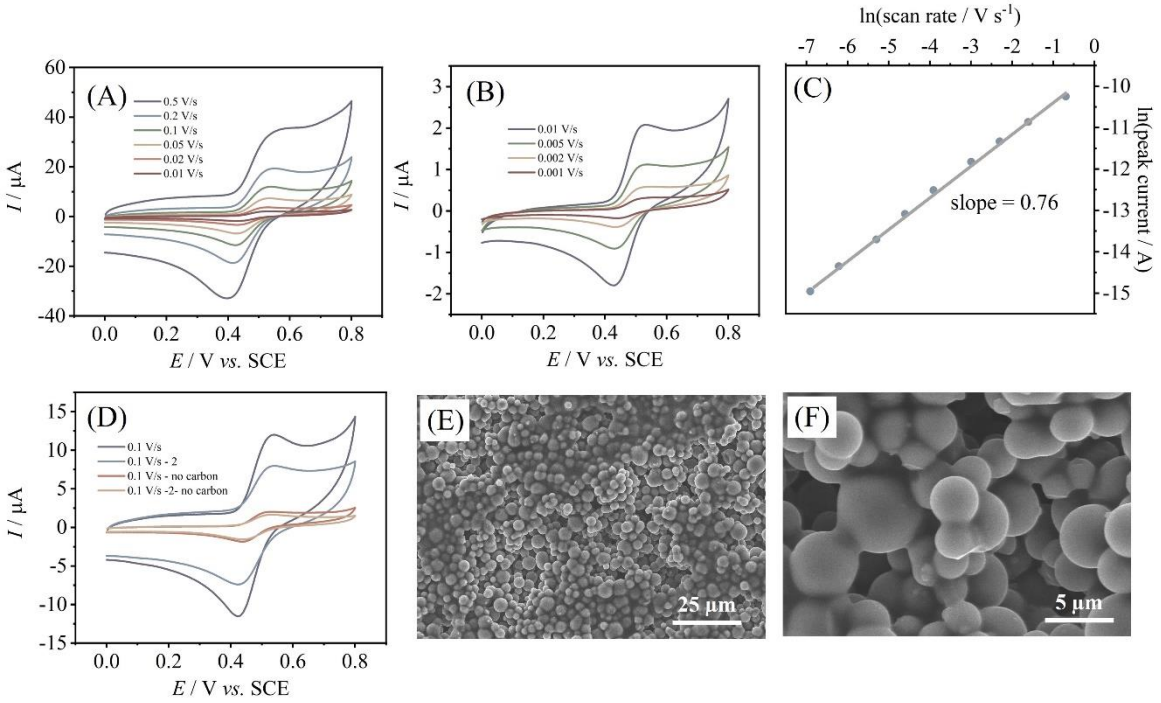

Figure 4.6 Enhancement of surface area and thereby redox current response of catechin-absorbed PIM-EA-TB. (A) Cyclic voltammograms (3 mm diameter glassy carbon electrode with 0.36 mg carbon microspheres and 15 µg PIM-EA-TB; scan rate 0.5, 0.2, 0.1, 0.05, 0.02, and 0.01 V s^{-1}) for catechin bound into a PIM-EA-TB film (immobilisation in 0.005 mM catechin in 0.1 M phosphate buffer pH 2 for 12 h) and immersed into 0.1 M phosphate buffer pH 2. (B) As in (A), for scan rates 0.01, 0.005, 0.002, and 0.001 V s^{-1}. (C) A double-logarithmic plot of anodic peak current *versus* scan rate. (D) As in (A), for the first and second potential cycles and comparison to data obtained without carbon microspheres for the first and second potential cycles (scan rate 0.1 V s^{-1}). (E and F) Scanning electron micrographs (SEM) of carbon microsphere/PIM-EA-TB deposits.

4.3.2 Catechin Immobilisation by Co-deposition with PIM-EA-TB

The catechin immobilisation in PIM-EA-TB by solution uptake method takes a long time (about 12 h). Therefore, other strategies to immobilise species like catechin into PIM-EA-TB need to be explored in terms of efficiency. PIM-EA-TB is highly processable and soluble in tetrahydrofuran (THF). So, it is feasible to dissolve PIM-EA-TB and catechin together in THF and deposit the solution onto the glassy carbon electrode.

Figure 4.7 presents voltammetric results for 2 μg catechin co-deposited with 2 μg PIM-EA-TB. Given the molecular weights of the PIM-EA-TB monomer (300 g mol^{-1}) and catechin (290.3 g mol^{-1}), the molar ratio of these two components is about 1 to 1, leading to effective hydrogen bonding. Voltammetric results in Figures 4.7A and B are very similar to those in Figures 4.3A and B. These results verify the formation of 1 : 1 PIM-EA-TB monomer repeat unit : catechin molecule during catechin absorption from solution. The oxidation peak current scale linearly related to scan rate shown in Figure 4.7C is consistent with the result in Figure 4.3C. Only a very thin layer of the film at the electrode surface is electrochemically active, as illustrated in Figure 4.7F. Accordingly, the implication is that the same type of catechin-immobilised PIM-EA-TB film can be fabricated by the aqueous solution-absorbing method or by the co-deposition method.

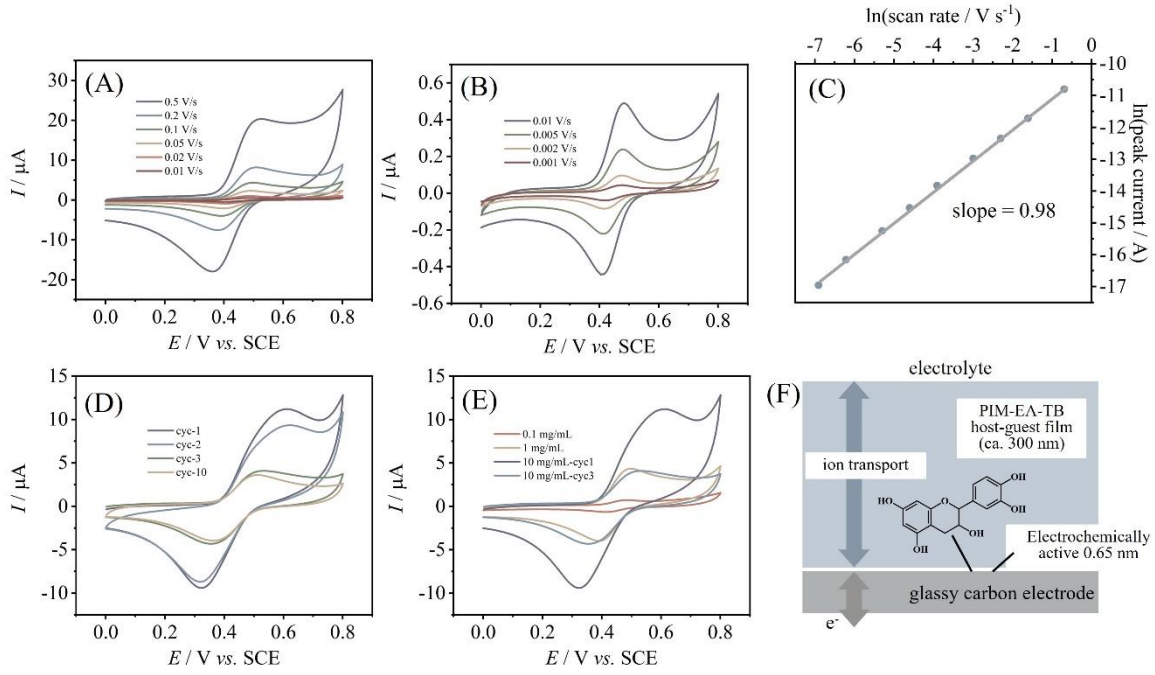

Figure 4.7 Electrochemical results for catechin-immobilised PIM-EA-TB by codeposition method. (A) Cyclic voltammograms (3 mm diameter glassy carbon electrode; scan rate 0.5, 0.2, 0.1, 0.05, 0.02, and 0.01 V s^{-1}) for catechin co-deposited with PIM-EA-TB into a film (2 μg catechin with 2 μg PIM-EA-TB) and immersed into 0.1 M phosphate buffer pH 2. (B) As in (A), for scan rates 0.01, 0.005, 0.002, and 0.001 V s^{-1}. (C) Double-logarithmic plot of anodic peak current *versus* scan rate. (D) As in (A), for 20 μg catechin with 2 μg PIM-EA-TB showing potential cycles 1, 2, 3, and 10 (scan rate 0.1 V s^{-1}). (E) As in (A), comparing (i) 20 μg catechin/2 μg PIM-EA-TB cycle 1, 20 μg catechin/2 μg PIM-EA-TB cycle 3, 2 μg catechin/2 μg PIM-EA-TB cycle 1, and 0.2 μg catechin/2 μg PIM-EA-TB cycle 1 (scan rate 0.1 V s^{-1}). (F) Schematic illustrating the thin layer redox process.

High loading of catechin can be achieved by making catechin content higher in the mixed THF solution. Figure 4.7D shows the voltammetric results for the case of 1 : 10 polymer repeat unit : catechin ratio. The initial catechin oxidation current appears to be higher, but drastically drops to the value observed for 1 : 1 polymer repeat unit : catechin film. Consequently, excess catechin molecules leach out rapidly, leaving only the bound catechin in the microporous host. Figure 4.7E displays comparison data of different loading of catechin in PIM-EA-TB. The lower loading for 1 : 0.1 host monomer : catechin case shows a considerable lower yet stable current response. The effect of electrolyte pH during electrochemical tests for catechin co-deposited in 1 : 1 ratio (Figure 4.5C and D) is very similar to the solution-absorbing method (Figure 4.5A and B).

4.3.3 Quercetin Immobilisation by Co-deposition with PIM-EA-TB

The aqueous solubility of quercetin is lower [36] compared to that of catechin. Thereby, experiments for absorption into PIM-EA-TB from aqueous solutions have not been carried out. Electrochemical investigation of quercetin immobilisation by co-deposition with PIM-EA-TB has been achieved. Figure 4.8A and B present redox peaks for quercetin in PIM-EA-TB film (1 : 1 polymer monomer : quercetin) tested in phosphate buffer electrolyte at pH 2. Oxidation and back-reduction of quercetin (see Equation 4.5) undergo the 2-electron 2-proton mechanism with a midpoint potential of $E_{mid} = ½(E_{p,\,ox} + E_{p,\,red}) = 0.42$ V *vs.* SCE, consistent with the values reported [17,18]. The redox signal is stable after several potential scans, suggesting that the instability of quercetin is inhibited by the PIM-EA-TB host. The oxidation peak current scale shows a linear relationship to scan rate with a slope of 1.0, consistent with a thin film of redox-active molecules close to the electrode surface. The charge under cyclic voltammograms is similar to that discovered for the catechin case. Thus, a similar redox-active film containing quercetin within tunnelling distance (see Figure 4.8F) can be presumed.

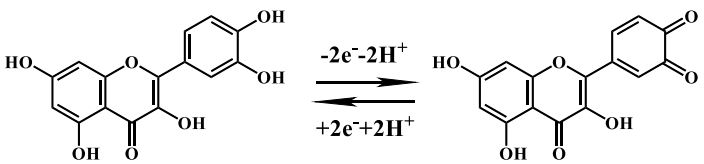

(4.5)

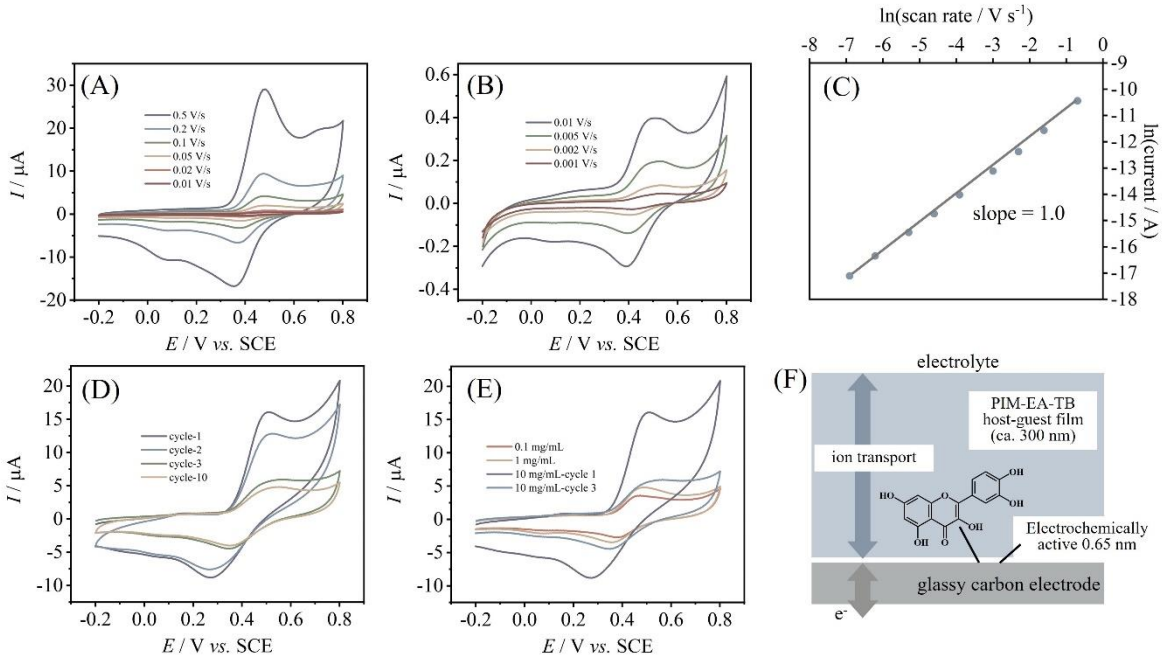

Figure 4.8 Electrochemical behaviours of quercetin-immobilised PIM-EA-TB by co-deposition method. (A) Cyclic voltammograms (3 mm diameter glassy carbon electrode; scan rate 0.5, 0.2, 0.1, 0.05, 0.02, and 0.01 V s^{-1}) for quercetin co-deposited with PIM-EA-TB into a film (2 µg quercetin with 2 µg PIM-EA-TB) and immersed into 0.1 M phosphate buffer pH 2. (B) As in (A), for scan rates 0.01, 0.005, 0.002, and 0.001 V s^{-1}. (C) Double-logarithmic plot of anodic peak current *versus* scan rate. (D) As in (A), for 20 µg quercetin with 2 µg PIM-EA-TB showing potential cycles 1, 2, 3, and 10 (scan rate 0.1 V s^{-1}). (E) As in A, comparing 20 µg quercetin/2 µg PIM-EA-TB cycle 1, 20 µg quercetin/2 µg PIM-EA-TB cycle 3, 2 µg quercetin/2 µg PIM-EA-TB cycle 1, and 0.2 µg quercetin/2 µg PIM-EA-TB cycle 1 (scan rate 0.1 V s^{-1}). (F) Schematic illustrating the thin layer redox process.

Secondary redox peaks that appeared at higher scan rates (see Figure 4.8A) could be related to localised pH differences in the microchannels of PIM-EA-TB, or could be linked to subsequent oxidation steps consistent with previous report [18]. Figure 4.8D and E represent that excess quercetin can leach out from the host (for the case of 1 : 10 host polymer repeat unit : quercetin), similar to the case of catechin. The redox current responses remain stable after 10 potential cycles, yet the signal becomes consistent with that observed for the 1 : 1 host polymer repeat unit : quercetin film deposit.

The effect of solution pH during voltammetric experiments has been studied for the quercetin-immobilised film (see Figure 4.9A). A clear Nernstian shift of midpoint potential occurs when the solution pH changes from 2 to 7 (Figure 4.9C), similar to the case of catechin. In more alkaline conditions, leaching of quercetin is proposed. Figure 4.9B contrasts voltammetric data from pH 2, then pH 13, and then back to pH 2. The signal for

quercetin is indeed lost after being exposed to alkaline solutions. The photograph in Figure 4.9D indicates the difference between quercetin-immobilised PIM-EA-TB in water and phosphate buffer of pH 13. Furthermore, the characteristic yellow colour in alkaline conditions confirms the loss of quercetin from the film.

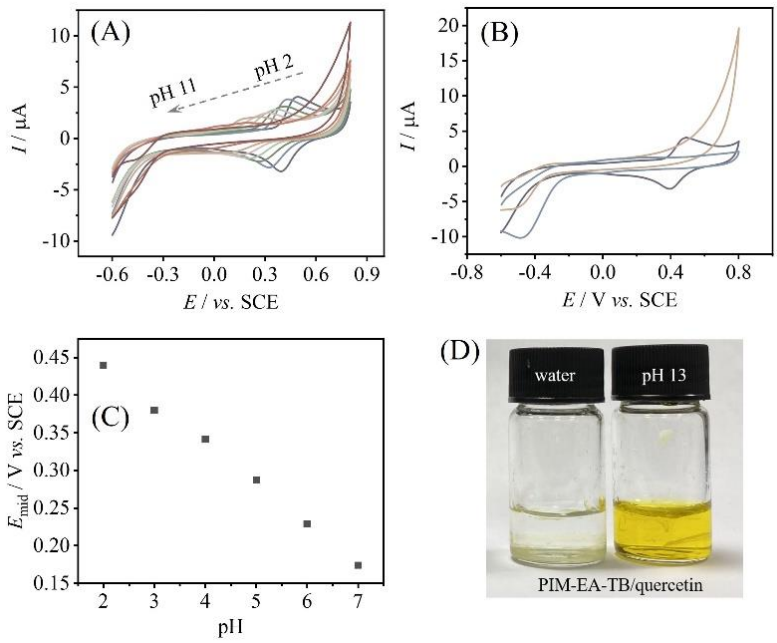

Figure 4.9 pH effects during voltammetry on catechin-immobilised PIM-EA-TB by absorbing or co-deposition method. (A) Cyclic voltammograms (3 mm diameter glassy carbon electrode; scan rate 0.1 V s^{-1}) for quercetin co-deposited into a PIM-EA-TB film and immersed into 0.1 M phosphate buffer at different pH values (pH = 2, 3, 4, 5, 6, 7, 9, and 11). (B) As in (A), but comparing pH 2, then pH 13, then back to pH 2. (C) A plot of midpoint potential E_{mid} = ½($E_{p,ox}$ + $E_{p,red}$) *versus* pH. (D) Photograph showing the PIM-EA-TB/quercetin 1 : 1 film in a glass vial exposed to water and 0.1 M phosphate buffer pH 13.

4.3.4 Catechin and Quercetin Immobilisation by Codeposition with PIM-EA-TB Followed by Electrochemically Driven Release

The release of guest species from the PIM-EA-TB host can be observed as a gradual loss of voltammetric signal. Further quantification studies were carried out by liquid chromatography coupled with mass spectroscopy (LC-MS) technique. The release of catechin or quercetin from PIM-EA-TB film into aqueous solutions was monitored in diffusion-controlled (non-electrochemical) conditions and electrochemical-controlled (by imposing negative potential) settings. Hydrogen bubbles on the electrode surface were generated while applying negative potentials, though no delamination of the thin PIM-EA-

TB film from the electrode surface was observed. Catechin or quercetin will rapidly air oxidise in extremely alkaline conditions and undergo a multitude of reactions in the LC-MS. It is ideal to show the degradation products from the LC-MS results. But when performing the MS detection, a mode of specific compound discovery was applied, and only the target compounds were highlighted and analysed. It would be important to show the actual release of catechin and quercetin from a drug delivery perspective in the future.

The release of water-soluble catechin is observed to be slightly faster when compared to less water-soluble quercetin. Figure 4.10A shows the release of catechin from 10 : 1 guest : host film into 10 mM phosphate buffer (pH 7). The loss of catechin in solution is significant even without interference from external voltage. More than half amount of catechin is released within 5 minutes (green line in Figure 4.10A). The applied potential enhances the release process by driving out the remaining catechin bound in the polymer host. The applied negative potential was imposed to locally create alkaline conditions at the electrode surface. Some remaining catechin is likely to be trapped in the host outside the electrode area.

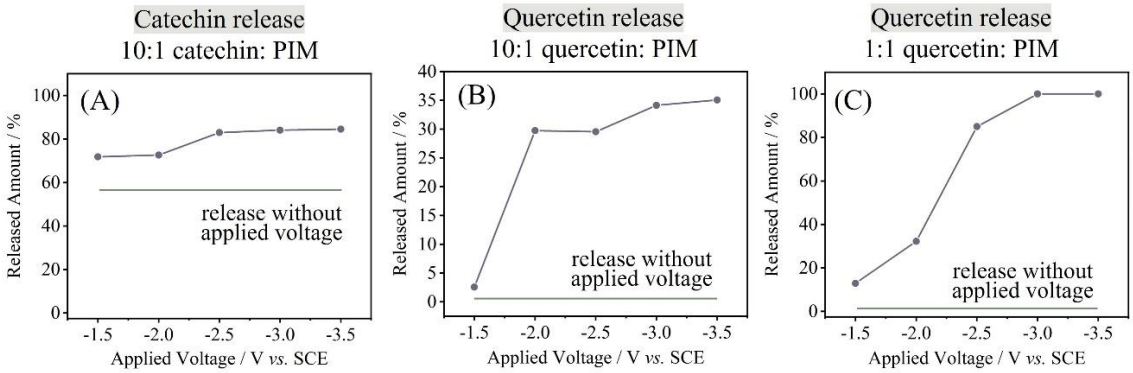

Figure 4.10 Release of catechin or quercetin from PIM-EA-TB. LC-MS data for the spontaneous and electrochemically driven release of catechin (A) and quercetin (B and C). Green line: data without electrochemical stimulation but for the same reaction time. Grey line: release data obtained with electrochemical stimulation. Each applied potential is kept for 5 min in 10 mM phosphate buffer solution at pH 7.

For the case of quercetin, the spontaneous or diffusion-driven loss is less dramatic. Only less than 5% of quercetin is released within 10 minutes (green line in Figure 4.10B) for the 10 : 1 quercetin : PIM-EA-TB deposit. A negative voltage was then applied to drive the release of quercetin. Data in Figure 4.10 indicates that a potential of -2 V *vs.* SCE is effective in the release process, and an amount of about 30% quercetin is driven out from the host. It seems

that most quercetin stays in the film, but it could also be because of the low solubility of quercetin impeding detection. Figure 4.10C presents data for 1 : 1 quercetin : host monomer case, and close to complete loss of quercetin is observed at potentials more negative than -2.5 V *vs.* SCE. Therefore, effective electrochemical release of quercetin can be possible, but the slow diffusion-driven release is always the case based on the experiments here.

4.4 Conclusions

Studies in this chapter demonstrate that catechin and quercetin can effectively bind to microporous PIM-EA-TB probably through hydrogen bonding to tertiary amine functional groups. Catechin binding can be achieved by absorbing from an aqueous solution and co-deposition method with PIM-EA-TB to give films with the same electrochemical properties, whereas quercetin binding is only performed by co-deposition. Accumulation of catechin happens in acidic and neutral conditions irrespective of PIM-EA-TB protonation. Electrochemical-driven release for both catechin and quercetin is proven to be effective. The main observation can be summarised as follows:

i) Microporous PIM-EA-TB provides conditions for the accumulation of catechin or quercetin species to form electrochemically redox film. The electrochemical reactions occur in a very thin layer close to the electrode surface.

ii) Highly chemically reversible voltammetric peaks demonstrate no polymerisation or coupling of radical intermediates during the processes. The reason could be that the mobility of guest species is limited in the microporous host structure.

iii) Accumulation of catechin has been proven effective in both acidic (pH = 2, protonated PIM-EA-TB) and neutral (pH = 6, non-protonated PIM-EA-TB) conditions with similar binding constants. Formation of 1 : 1 host polymer repeat unit : guest deposits are observed, likely attributed to hydrogen bonding.

iv) Higher loading of catechin or quercetin in PIM-EA-TB can be achieved by the co-deposition method. However, excess guest species are readily released into the electrolyte solution to result in a film with a ratio of 1 : 1 host polymer repeat unit : guest.

v) The spontaneous release of catechin into aqueous solutions is probably observed due to high water solubility. The electrochemical stimulus of catechin and

quercetin release is effective by applying negative potentials to locally create alkaline conditions.

Rigid polymer hosts with functional groups could provide environments for accumulation and release of guest species. The guest molecules studied here display limited mobilities in PIM-EA-TB due to their relatively large molecular sizes. Although the work presented in this chapter will not be able to represent electrochemical behaviours of all the molecules with different sizes, functional groups, and shapes, it could be a preliminary step for the development of similar investigations of molecules involved host-guest systems.

4.5 References

1 Xie, W., Cui, D., Zhang, S.-R., Xu, Y.-H. & Jiang, D.-L. Iodine capture in porous organic polymers and metal–organic frameworks materials. *Materials Horizons* **6**, 1571-1595 (2019).

2 Johnson, R., Cooks, R. G., Allen, T., Cisper, M. & Hemberger, P. Membrane introduction mass spectrometry: trends and applications. *Mass Spectrometry Reviews* **19**, 1-37 (2000).

3 Devine, A., Hegarty, C., Casimero, C., Molyneaux, R. L., Smith, R. B., Cardosi, M. F., & Davis, J. Electrochemically initiated release: exploring new modalities for controlled drug release. *Journal of Electroanalytical Chemistry* **872**, 113926 (2020).

4 Liu, K., Kang, Y., Wang, Z. & Zhang, X. 25th anniversary article: Reversible and adaptive functional supramolecular materials:"Noncovalent interaction" matters. *Advanced Materials* **25**, 5530-5548 (2013).

5 Carta, M., Malpass-Evans, R., Croad, M., Rogan, Y., Jansen, J. C., Bernardo, P., Bazzarelli, F. & McKeown, N. B. An efficient polymer molecular sieve for membrane gas separations. *Science* **339**, 303-307 (2013).

6 Madrid, E., Rong, Y., Carta, M., McKeown, N. B., Malpass-Evans, R., Attard, G. A., Clarke, T. J., Taylor, S. H., Long, Y. & Marken, F. Metastable Ionic Diodes Derived from an Amine-Based Polymer of Intrinsic Microporosity. *Angewandte Chemie* **126**, 10927-10930 (2014).

7 Li, Z., Wang, L., Malpass-Evans, R., Carta, M., McKeown, N. B., Mathwig, K., Fletcher, P. J. & Marken, F. Ionic Diode and Molecular Pump Phenomena Associated with Caffeic Acid Accumulated into an Intrinsically Microporous Polyamine (PIM-EA-TB). *ChemElectroChem* **8**, 2044-2051 (2021).

8 Dalluge, J. J. & Nelson, B. C. Determination of tea catechins. *Journal of Chromatography A* **881**, 411-424 (2000).

9 Sano, M., Tabata, M., Suzuki, M., Degawa, M., Miyase, T., & Maeda-Yamamoto, M. Simultaneous determination of twelve tea catechins by high-performance liquid chromatography with electrochemical detection. *Analyst* **126**, 816-820 (2001).

10 Castaignède, V., Durliat, H. & Comtat, M. Amperometric and potentiometric determination of catechin as model of polyphenols in wines. *Analytical Letters* **36**, 1707-1720 (2003).

11 Janeiro, P. & Brett, A. M. O. Catechin electrochemical oxidation mechanisms. *Analytica Chimica Acta* **518**, 109-115 (2004).

12 Šeruga, M., Novak, I. & Jakobek, L. Determination of polyphenols content and antioxidant activity of some red wines by differential pulse voltammetry, HPLC and spectrophotometric methods. *Food Chemistry* **124**, 1208-1216 (2011).

13 Nakayama, T. & Uno, B. Importance of proton-coupled electron transfer from natural phenolic compounds in superoxide scavenging. *Chemical and Pharmaceutical Bulletin* **63**, 967-973 (2015).

14 Zare, H. R. & Habibirad, A. M. Electrochemistry and electrocatalytic activity of catechin film on a glassy carbon electrode toward the oxidation of hydrazine. *Journal of Solid State Electrochemistry* **10**, 348-359 (2006).

15 Muzolf, M., Szymusiak, H., Gliszczyńska-Świgło, A., Rietjens, I. M., & Tyrakowska, B. E. pH-dependent radical scavenging capacity of green tea catechins. *Journal of Agricultural and Food Chemistry* **56**, 816-823 (2008).

16 Herrero-Martínez, J. M., Sanmartin, M., Rosés, M., Bosch, E. & Ràfols, C. Determination of dissociation constants of flavonoids by capillary electrophoresis. *Electrophoresis* **26**, 1886-1895 (2005).

17 Hendrickson, H. P., Kaufman, A. D., Lunte, C. E. Electrochemistry of catechol-containing flavonoids. *Journal of Pharmaceutical and Biomedical Analysis* **12**, 325-334 (1994).

18 Brett, A. M. O., & Ghica, M. E. Electrochemical oxidation of quercetin. *Electroanalysis: An International Journal Devoted to Fundamental and Practical Aspects of Electroanalysis* **15**, 1745-1750 (2003).

19 Hu, J. & Zhang, Z. Application of electrochemical sensors based on carbon nanomaterials for detection of flavonoids. *Nanomaterials* **10**, 2020 (2020).

20 Oh, S. J., Kim, O., Lee, J. S., Kim, J. A., Kim, M. R., Choi, H. S., Shim, J., Kang, K. W. & Kim, Y. C. Inhibition of angiogenesis by quercetin in tamoxifen-resistant breast cancer cells. *Food and Chemical Toxicology* **48**, 3227-3234 (2010).

21 Zhang, M., Swarts, S. G., Yin, L., Liu, C., Tian, Y., Cao, Y., Swarts, M., Yang, S., Zhang, S. B., Zhang, K., Ju, S., Olek Jr, D. J., Schwartz, L., Keng, P.C., Howell, R., Zhang, L., & Okunieff, P. Antioxidant properties of quercetin. *Oxygen Transport to Tissue XXXII* Springer, Boston, MA 283-289 (2011).

22 Xu, X., Nan, D., Yang, H., Pan, S., Liu, H., & Hu, X. Quercetin@ZIF-90 as a novel antioxidant for label-free colorimetric ATP sensing at neutral pH. *Sensors and Actuators B: Chemical* **304**, 127324 (2020).

23 Mu, Y., Wu, G., Su, C., Dong, Y., Zhang, K., Li, J., Sun, X., Li, Y., Chen, X., & Feng, C. pH-sensitive amphiphilic chitosan-quercetin conjugate for intracellular delivery of doxorubicin enhancement. *Carbohydrate Polymers* **223**, 115072 (2019).

24 Hemmati, K., Masoumi, A. & Ghaemy, M. pH responsive tragacanth gum and poly (methyl methacrylate-co-maleic anhydride)-g-poly (caprolactone) conetwork microgel for in vitro quercetin release. *Polymer* **59**, 49-56 (2015).

25 Moon, Y. J., Wang, L., DiCenzo, R., & Morris, M. E. Quercetin pharmacokinetics in humans. *Biopharmaceutics & Drug Disposition* **29**, 205-217 (2008).

26 Wang, W., Sun, C., Mao, L., Ma, P., Liu, F., Yang, J., & Gao, Y. The biological activities, chemical stability, metabolism and delivery systems of quercetin: A review. *Trends in Food Science & Technology* **56**, 21-38 (2016).

27 Papouchado, L., Petrie, G. & Adams, R. Anodic oxidation pathways of phenolic compounds. *Journal of Electroanalytical Chemistry and Interfacial Electrochemistry* **38**, 389-395 (1972).

28 Ryan, M. D., Yueh, A. & Chen, W. Y. The electrochemical oxidation of substituted catechols. *Journal of the Electrochemical Society* **127**, 1489 (1980).

29 Zheng, Y., Haworth, I. S., Zuo, Z., Chow, M. S. & Chow, A. H. Physicochemical and structural characterization of quercetin-β-cyclodextrin complexes. *Journal of Pharmaceutical Sciences* **94**, 1079-1089 (2005).

30 Ramešová, Š., Sokolová, R., Degano, I., Bulíčková, J., Žabka, J., & Gál, M. On the stability of the bioactive flavonoids quercetin and luteolin under oxygen-free conditions. *Analytical and Bioanalytical Chemistry* **402**, 975-982 (2012).

31 Wang, Q., Wei, H., Deng, C., Xie, C., Huang, M., & Zheng, F. Improving stability and accessibility of quercetin in olive oil-in-soy protein isolate/pectin stabilized O/W emulsion. *Foods* **9**, 123 (2020).

32 de Carli, C., Moraes-Lovison, M. & Pinho, S. C. Production, physicochemical stability of quercetin-loaded nanoemulsions and evaluation of antioxidant activity in spreadable chicken pâtés. *LWT* **98**, 154-161 (2018).

33 Janeiro, P. & Brett, A. M. O. Catechin electrochemical oxidation mechanisms. *Analytica Chimica Acta* **518**, 109-115 (2004).

34 Rong, Y., Kolodziej, A., Madrid, E., Carta, M., Malpass-Evans, R., McKeown, N. B., & Marken, F. Polymers of intrinsic microporosity in electrochemistry: Anion uptake and transport effects in thin film electrodes and in free-standing ionic diode membranes. *Journal of Electroanalytical Chemistry* **779**, 241-249 (2016).

35 Yang, M. J., Hung, Y. A., Wong, T. W., Lee, N. Y., Yuann, J. M. P., Huang, S. T., Wu, C. Y., Chen, I. Z., & Liang, J. Y. Effects of blue-light-induced free radical formation from catechin hydrate on the inactivation of Acinetobacter baumannii, including a carbapenem-resistant strain. *Molecules* **23**, 1631 (2018).

36 Riva, A., Ronchi, M., Petrangolini, G., Bosisio, S., & Allegrini, P. Improved oral absorption of quercetin from quercetin phytosome®, a new delivery system based on food grade lecithin. *European Journal of Drug Metabolism and Pharmacokinetics* **44**, 169-177 (2019).

Chapter 5 Hydrogen Peroxide Versus Hydrogen Generation at Bipolar Pd/Au Nano-catalysts Grown into an Intrinsically Microporous Polyamine (PIM-EA-TB)

Contents

Chapter Abstract

Nano-palladium is embedded in the intrinsically microporous polyamine (PIM-EA-TB) by accumulating $PdCl_4^{2-}$ into the polymer host structure, followed by borohydride reduction. The palladium with a typical 3.2 ± 0.2 nm diameter size acts as a nano-catalyst, driving the spontaneous reaction between formic acid and oxygen to competingly yield hydrogen peroxide (at low formic acid concentrations in the air), water, and hydrogen (at higher formic acid concentration or under argon). Next, a spontaneous electroless gold deposition process is applied to attach gold (with a typical size of 10 to 35 nm diameter) to the palladium in PIM-EA-TB. The Pd/Au@PIM-EA-TB product gives an order of magnitude increased hydrogen peroxide yield even at higher concentrations of formic acid with suppressed hydrogen production. Pd and Au work hand-in-hand as bipolar electrocatalysts. A Clark probe is employed to evaluate the catalyst efficiency by monitoring the rates of oxygen removal and hydrogen evolution. An indirect method based on liquid chromatography - mass spectroscopy is developed to assess and quantify hydrogen peroxide production. The Pd/Au@PIM-EA-TB catalyst is effective and can be easily recovered and reused for hydrogen peroxide production.

Graphical Abstract

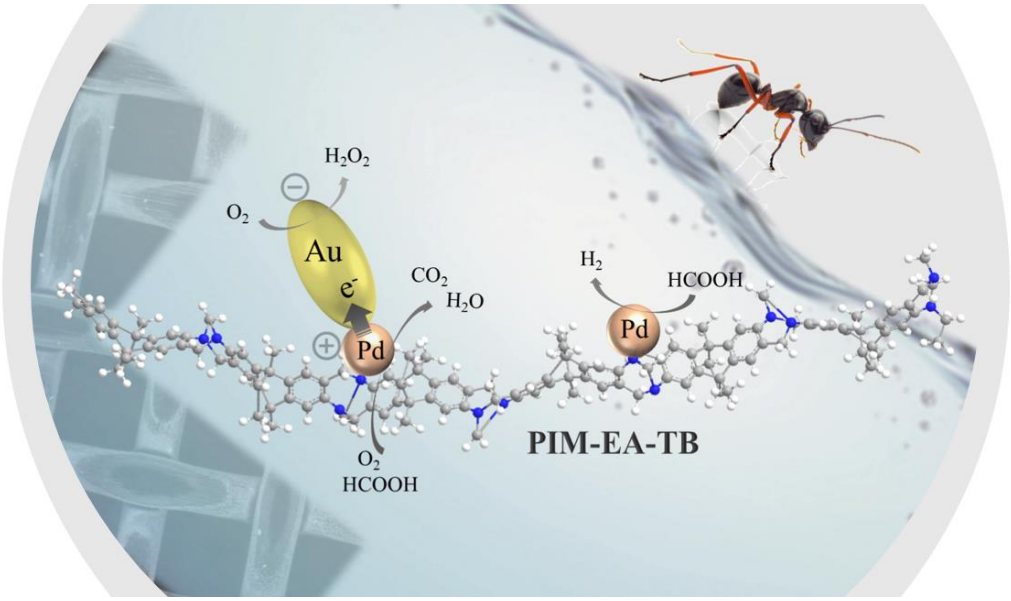

Publications associated with this chapter

Wang, L., Carta, M., Malpass-Evans, R., McKeown, N. B., Fletcher, P. J., Lednitzky, D., & Marken, F. Hydrogen Peroxide Versus Hydrogen Generation at Bipolar Pd/Au Nano-catalysts Grown into an Intrinsically Microporous Polyamine (PIM-EA-TB). *Electrocatalysis*, **12**, 771-784 (2021).

Credit Statement

The candidate developed the immobilisation method of palladium into PIM-EA-TB, gold electroless deposition method, and hydrogen peroxide quantification method based on LC-MS. The candidate performed the electrochemical experiments based on a Clark probe, quantification of hydrogen peroxide, data curation, and interpretation of the results. Neil B McKeown provided the PIM-EA-TB material. Philip J Fletcher and Diana Lednitzky performed the TEM and SEM characterisation. Mariolino Carta, Richard Malpass-Evans, Neil B McKeown, Philip J Fletcher, and Diana Lednitzky gave valuable comments and input to the draft. Frank Marken supervised the candidate, helped with the idea, gave constructive guidance to this work, and helped with reviewing and editing the original draft.

Special Acknowledgements

I acknowledge Prof. Neil McKeown and his research group from the University of Edinburgh for synthesising PIM-EA-TB material. Thanks to Dr Philip Fletcher for SEM, EDX, and TEM characterisation of the samples listed in this chapter.

5.1 Introduction

Microporous polymers act commonly as host materials for immobilisation of catalysts since they provide restricted channels for reagent access, high accessible catalyst surface area, the possibility to recover and reuse the catalyst, and enhanced catalyst efficiency, for example, for palladium catalysts [1]. Palladium has been reported for various applications in catalysis of C-C coupling chemistry [2], N-alkylation [3], hydrogenation of unsaturated olefins [4], hydrogen generation from formic acid [5], electrocatalysis [6], and H_2O_2 production [7,8]. Palladium-containing composites like Pd-Au catalyst have been applied for "green" H_2O_2 production [9], the selective methane conversion to methanol [10], and alcohol oxidation [11,12]. Immobilisation of Pd nanoparticles into microporous hosts leads to enhanced catalytic reactivity when the permeation of reactants into the host-guest structure is adequate, and the catalyst is not blocked by the immobilisation process. Palladium has been embedded in the polymer of intrinsic microporosity PIM-1 for catalytic reduction of nitroaromatics [13]. The PIM-1 host provided selectivity towards reactants with good permeation, and the guest Pd remained catalytically active. In this chapter, palladium is immobilised in the polymer of intrinsic microporosity PIM-EA-TB (see molecular structure in Figure 5.1).

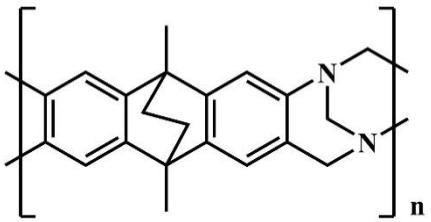

PIM-EA-TB

Figure 5.1 Molecular structure of PIM-EA-TB.

Hydrogen peroxide has been proved to be a practical component applied in disinfection [14], biomass breakdown [15,16], pollution treatment [17,18], healthcare [19], bleaching [20,21], and further chemical preparation [22]. Direct hydrogen peroxide generation from oxygen can be achieved, but the efficiency is always a challenge because of the difficulty in control of over-reduction or disproportionation of H_2O_2 into H_2O and O_2. Electrochemical H_2O_2 synthesis by oxygen reduction reaction over single atom catalysts is in progress [23]. Although photocatalysts are successfully introduced to drive the reduction of O_2 to H_2O_2 [24], other dark chemical processes

linked to ambient oxygen and reducing agents (HCOOH[25] or glucose[26]) are reported to be efficient.

In this chapter, the immobilisation of a Pd nano-catalyst and the heterogenisation of a Pd/Au catalyst into microporous PIM-EA-TB are studied. The Pd nanoparticles of a typical size of 3.2 nm are readily prepared by the accumulation of $PdCl_4^{2-}$ into PIM-EA-TB host and subsequent borohydride reduction. The resulting Pd catalysts are active towards hydrogen evolution from formic acid benefiting from the unblocked catalyst surface and adequate access of formic acid to the microstructure of the host polymer. Both hydrogen generation and oxygen consumption are evaluated in situ with a Clark probe [27]. Catalytic processes driven by Pd catalyst could be tentatively suggested as oxygen consumption (see Equations 5.1 and 5.2) and hydrogen production (Equation 5.3).

$$Process\ 1: HCOOH + O_2 \rightleftarrows CO_2 + H_2O_2 \tag{5.1}$$

$$Process\ 2: HCOOH + H_2O_2 \rightleftarrows CO_2 + 2H_2O \tag{5.2}$$

$$Process\ 3: HCOOH \rightleftarrows CO_2 + H_2 \tag{5.3}$$

Spontaneous electroless deposition of gold attached to the Pd nanoparticles creates a heterogeneous Pd/Au catalyst which shows an enhanced rate of hydrogen peroxide production by order of magnitude. The competing reactions, the bipolar nature of the Pd/Au catalyst, and the function of PIM-EA-TB are explored.

5.2 Experimental

5.2.1 Reagents

Hydrogen chloride (HCl, ACS reagent, 37%), palladium(II) chloride ($PdCl_2$, 99%), sodium borohydride ($NaBH_4$, powder, 98%), potassium gold (III) chloride ($KAuCl_4$, 98%), phosphoric acid (H_3PO_4, 85 wt.% solution, ACS Reagent), formic acid (HCOOH, 96%, ACS Reagent), sodium carbonate (Na_2CO_3, powder, $\geq$ 99.5%, ACS Reagent), and p-nitrophenylboronic acid ($\geq$ 95.0%) were products from Sigma-Aldrich. Hydrogen peroxide (H_2O_2, ACS Reagent, 30 wt.% in H_2O) and dimethyl sulfoxide (DMSO, for HPLC, $\geq$ 99.7%) were purchased from Honeywell. Sodium bicarbonate ($NaHCO_3$, $\geq$ 99.7%) and sodium hydroxide (NaOH, pellets, laboratory reagent grade) were obtained from Fluka. Jovitec universal pH test paper (pH full range 1-14) was employed to monitor the pH value of

solutions in the H_2O_2 determination experiments. PIM-EA-TB was synthesised following the reported method [28]. Nylon mesh with 75 µm diameter was purchased from Amazon.com (therpin reusable Nylon fine mesh food strainer bag).

5.2.2 Instrumentation

Clark-type polarographic dissolved oxygen probe (HI76407) and corresponding electrolyte fill solution (HI7041S) were purchased from Hanna Instruments Ltd. A thin tissue layer (Whatman Schleicher & Schuell 105 lens cleaning tissue) was employed to introduce a space between the platinum electrode and the Teflon membrane. Ultra-pure water (resistivity not less than 18.2 MΩ cm at 20 °C) from the Thermo Scientific water purification system was used to make aqueous solutions. The pH of buffer solutions was monitored by a pH meter (Jenway 3505). Morphologies of materials were imaged by a scanning electron microscope (SEM, Hitachi SU3900) and a transmission electron microscope (TEM, JEOL JEM-2100PLUS). Elemental mapping was performed with an energy dispersive X-ray analyser (170 mm^2 Ultim Max EDX) attached to the SEM equipment. Electrochemical experiments were controlled and recorded with a potentiostat (Metrohm microAutolab II). The quantification of H_2O_2 was achieved using a liquid chromatography-mass spectroscopy (LC-MS) technique with an Agilent 6545 Accurate-Mass Q-TOF LC/MS walk-up system.

5.2.3 Formation of Pd@PIM-EA-TB

A Nylon mesh substrate was introduced to study the catalytic activity of catalysts. A disk of 8 mm diameter Nylon mesh was coated with approximate 20 µg PIM-EA-TB film by drop-casting chloroform solution. Then the coated disk was immersed in 5 mM $PdCl_4^{2-}$ in 1 M HCl for 1 h for protonation of PIM-EA-TB and absorbing the $PdCl_4^{2-}$ anion into the microporous polymer host. The characteristic colour of yellow [29] is visible after the absorbing process. Next, the disk was immersed in a fresh 5 mg mL^{-1} $NaBH_4$ aqueous solution for 20 h to carry out the reduction process in a refrigerator (4 °C). The colour of the disk changed to dark after reduction (see Figure 5.2).

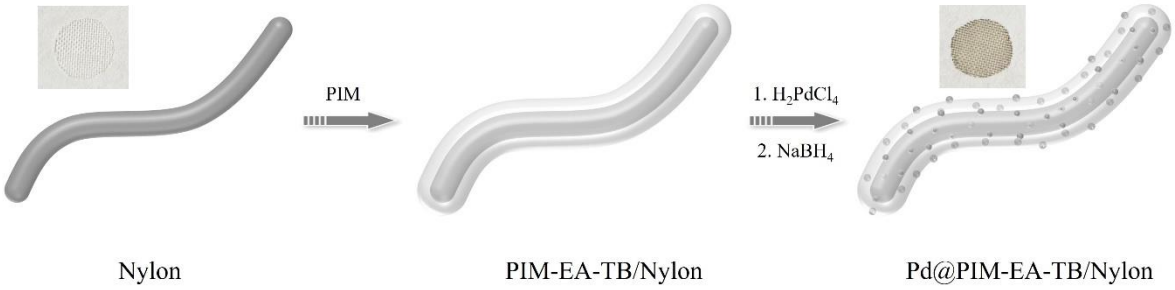

Figure 5.2 Schematic illustration of a Nylon mesh substrate that is coated with PIM-EA-TB and then exposed to $PdCl_4^{2-}$ followed by rinsing with water and reduction by $NaBH_4$ to produce Pd nanoparticles immobilised in PIM-E-ATB host (evidenced by dark colour).

The morphology and elemental distribution of the resulting Pd@PIM-EA-TB coated Nylon mesh were evaluated by scanning electron microscopy (SEM) and energy-dispersive X-ray spectroscopy (EDX). White regions in Figure 5.3A are consistent with regions of more Pd metal deposits accumulated (Figure 5.3C) owing to a higher polymer loading. PIM-EA-TB deposit appears to be higher at Nylon thread intersections caused by capillary forces during evaporation of the deposition solution. Palladium is observed as uniformly sized nanoparticles embedded in PIM-EA-TB.

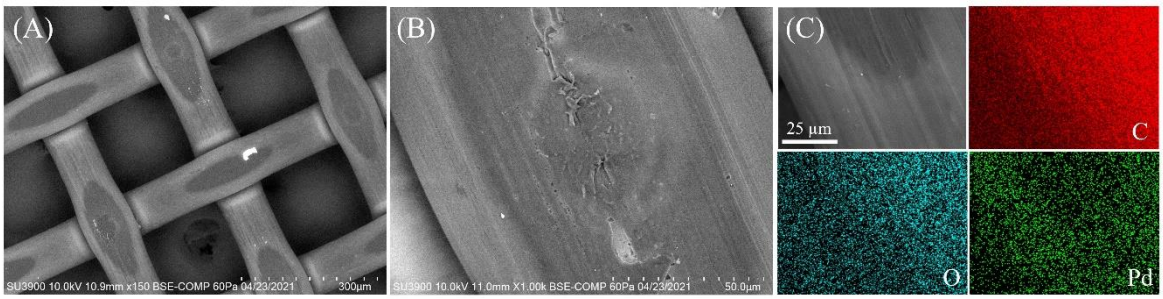

Figure 5.3 Scanning electron microscopy (SEM) images (A, B) and energy-dispersive X-ray spectroscopy (EDX) elemental mapping analysis (C) for Pd@PIM-EA-TB coated Nylon mesh.

Samples of Pd@PIM-EA-TB were ultrasonicated in isopropanol to separate the polymer from the Nylon substrate. Then the suspension was deposited onto transmission electron microscopy (TEM) grids to examine the distribution and sizes of Pd nanoparticles. Figure 5.4 presents typical results for Pd-immobilised PIM-EA-TB. Particle size analysis indicates a 3.2 ± 0.2 nm diameter of Pd.

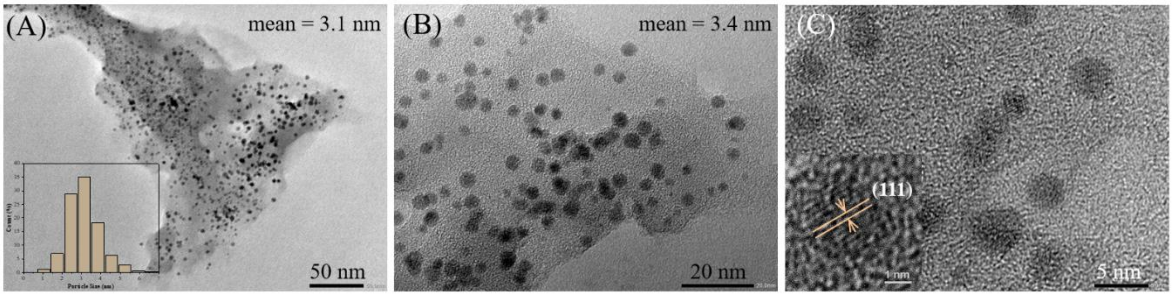

Figure 5.4 Transmission electron microscopy (TEM) images for Pd@PIM-EA-TB. (A) Pd nanoparticles with a mean size of 3.2 ± 0.2 nm evenly distributed in PIM-EA-TB (inset: size distribution of Pd nanoparticles). (B) Higher magnification image with a mean Pd particle size of 3.4 nm. (C) High-resolution image showing the (111) crystal facet of Pd.

5.2.4 Formation of Nano-PdAu@PIM-EA-TB

The spontaneous gold electroless deposition on palladium is coupled with oxygen evolution from water driven by the high Au^{3+}/Au standard potential of +1.257 V vs. SCE [30,31]. Gold deposition can be readily completed by immersion of the Pd@PIM-EA-TB coated Nylon disks into 5 mM $KAuCl_4$ in 10 mM phosphate buffer solution (at pH 7 for 20 h). The presence of gold is verified by SEM images and EDX mapping results in Figure 5.5. Gold grows in the region where palladium plays the role of nucleation site.

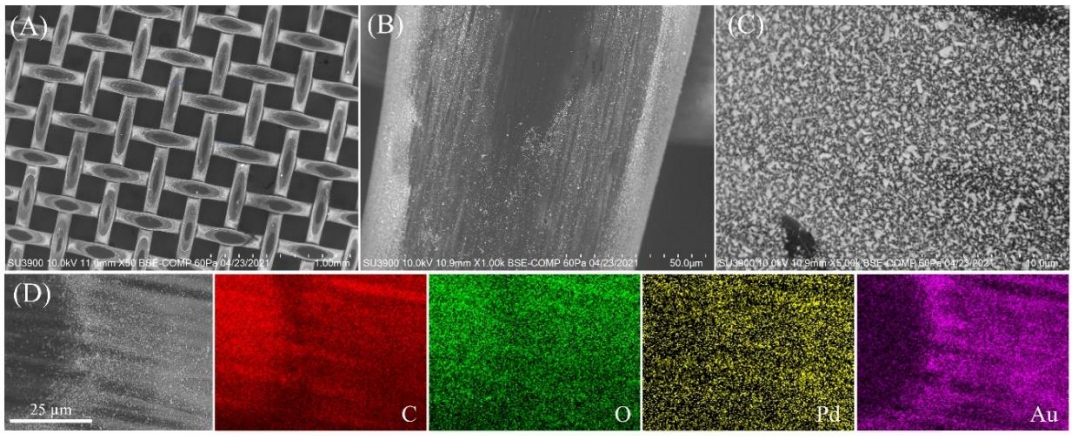

Figure 5.5 SEM images with different magnifications (A-C) and EDX elemental mapping analysis (D) for Pd/Au@PIM-EA-TB coated nylon mesh.

Samples of Pd/Au@PIM-EA-TB were investigated in TEM to obtain more detailed information about gold deposition. Figure 5.6 reveals a region where gold dominates over palladium. Gold samples are typically grown into bigger aggregates. Phase analysis of the

selected area electron diffraction (SAED) pattern in Figure 5.6B and d-spacing of 0.239 nm in Figure 5.6D verify the presence of crystalline gold.

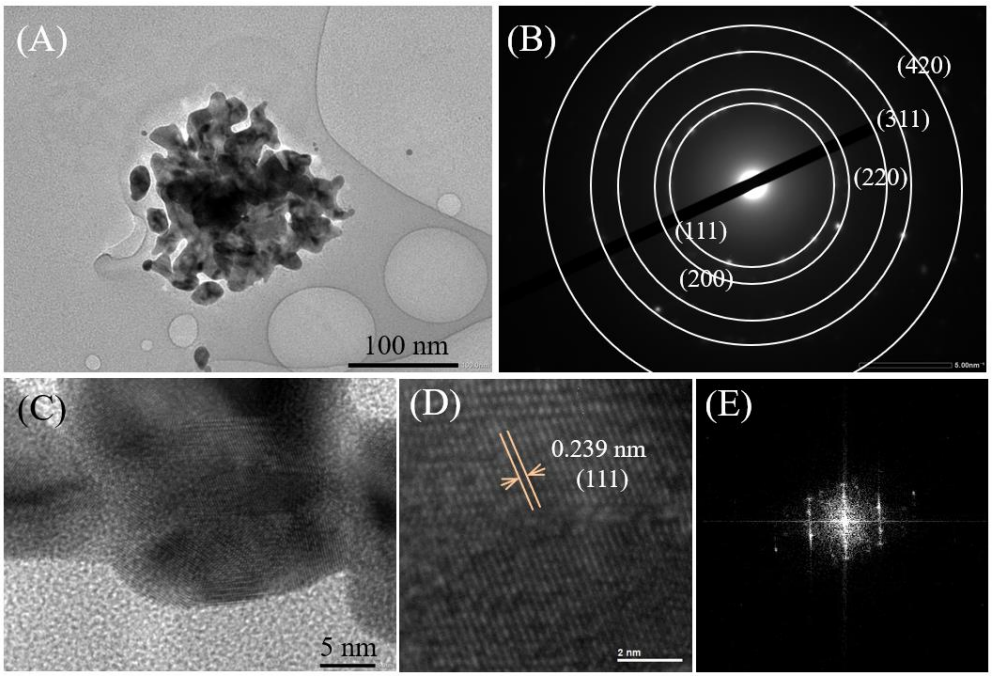

Figure 5.6 TEM analysis for Pd/Au@PIM-EA-TB. (A) Au particles separated by ultrasonication. (B) Selected area electron diffraction (SAED) pattern with Au indexing. (C) Higher magnification of Au particles. (D) High-resolution image showing d-spacing of 0.239 nm indexed to (111) facet of Au. (E) Fast Fourier transform (FFT) diffraction pattern of (D).

Figure 5.7 shows regions where both gold and palladium nanoparticles are present side-by-side. Gold nanoparticles with a typical size of 10 to 35 nm are present, which are larger than the palladium. Some palladium nanoparticles are not attached to or modified by gold which may affect the overall activity of the Pd/Au@PIM-EA-TB catalyst.

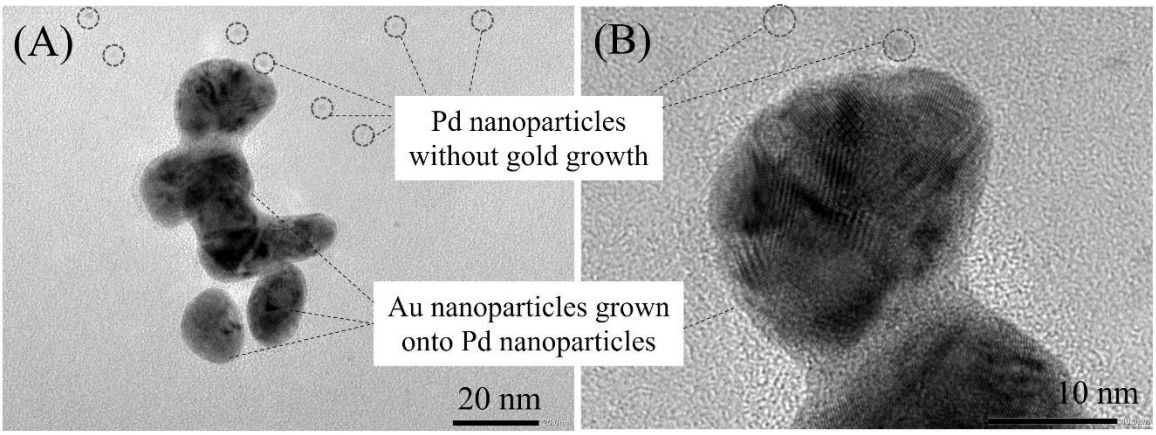

Figure 5.7 TEM images for Pd/Au@PIM-EA-TB: bigger Au particles (with a size of 10 to 35 nm intergrown into bigger aggregates) attached to small Pd nanoparticles (size of approximate 3.2 nm).

5.2.5 Clark Probe Measurements

The consumption of oxygen and generation of hydrogen were monitored in situ by a commercial Clark sensor. The core of the Clark probe is an electrochemical cell inside the cap where Pt acts as the working electrode, Ag/AgCl is the reference and counter electrode, and concentrated KCl solution is the electrolyte (see Figure 5.1A). The Pd@PIM-EA-TB or Pd/Au@PIM-EA-TB coated Nylon disks were fixed onto the Teflon membrane of the probe (by additional Nylon stripes and rubber ring). By immersing the Clark probe in solution, the oxygen transport from the solution (through Teflon membrane) and hydrogen flux formed on the catalyst into the sensor can be detected under different applied potentials. The oxygen was monitored at -0.7 V vs. Ag/AgCl, and the hydrogen flux was performed at + 0.6 V vs. Ag/AgCl [25,32]. The Nylon substrate offers the space for the diffusion of gases and provides a convenient way in terms of reuse and reproducibility.

5.2.6 Quantification Measurements of Hydrogen Peroxide by LC-MS

The quantification of H_2O_2 generated by catalysts was achieved indirectly based on the reaction between *para*-nitrophenylboronic acid and H_2O_2 under alkaline conditions [33]. Instead of using a colourimetric assay often employed in other studies, a more powerful LC-MS technique is applied. The reaction to generate the *para*-nitrophenol product is demonstrated as Equation 5.4.

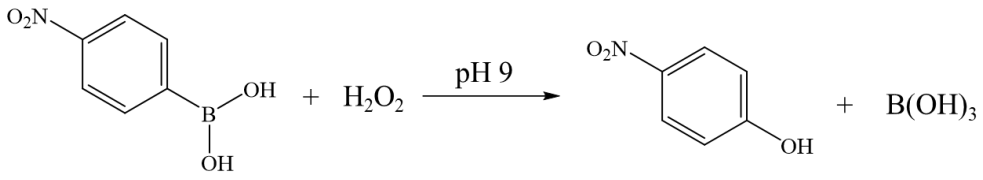

(5.4)

The product of *para*-nitrophenol was separated and quantified by LC-MS analysis. Compared to UV-vis spectrometry, LC-MS technique gives lower detection range (2 µM in this case). The standard calibration curve (see inset of Figure 5.8A) for a range of H_2O_2 concentrations was generated following the procedures: a volume of 100 µL H_2O_2 solution with concentrations ranging from 2 to 500 µM was mixed with 1 mL of 100 µM *para*-nitrophenylboronic acid in 10 mM carbonate buffer solution (pH 9 in 10% DMSO and 90% of water solvent) and kept in the dark for 1 h, followed by dilution to 1/50 of the concentration with 10% DMSO/90% water and submission to LC-MS system. For the detection of H_2O_2 generated by catalysts, the sample solution was pre-adjusted to pH 9 by adding Na_2CO_3 powder before commencing the analysis procedures.

LC-MS analyses were performed on an Automated Agilent QTOF (Walkup) used with HPLC (4 chromatography columns) and variable wavelength detector (Agilent QTOF 6545 with Jetstream electrospray ionisation (ESI) spray source coupled to an Agilent 1260 Infinity II Quat pump HPLC with 1260 autosampler, column oven compartment, and variable wavelength detector). Compound chromatograms (Figure 5.8A) and mass spectrum (Figure 5.8B) of *para*-nitrophenol can be extracted from the analysis results processed in Qual B 07.00 and Quant 10.0 software. The responses of the calibration curve were generated from the peak integration of the chromatograms located at 4.05 min acquisition time.

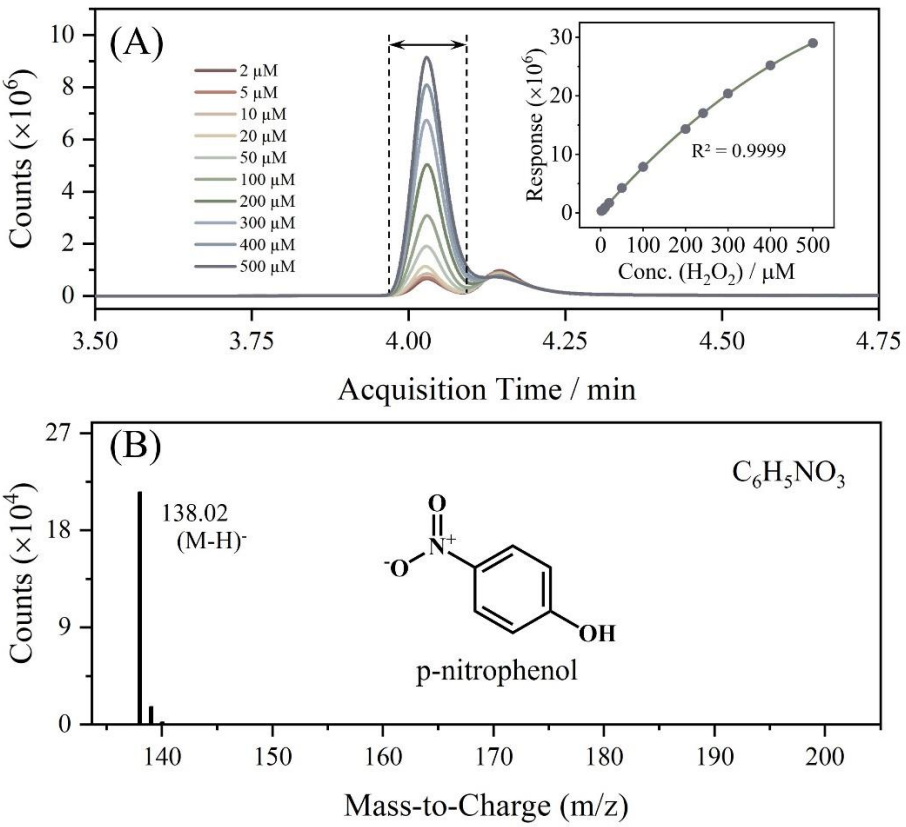

Figure 5.8 Liquid chromatograms (A) and mass spectrum (B) of the product *para*-nitrophenol compound. Inset in (A): calibration curve of H_2O_2 concentration ranging from 2 to 500 µM. The response here is the area under the chromatogram at 4.05 min acquisition time.

5.3 Results and Discussion

5.3.1 Clark Probe Evidence for Oxygen Consumption and Hydrogen Production from Formic Acid at Pd@PIM-EA-TB

By attaching Pd@PIM-EA-TB on Nylon substrate to the Teflon surface of a Clark probe, the detection of oxygen consumption (lowering the flux of oxygen into the Clark sensor) and hydrogen production (inducing the flux of hydrogen into the Clark sensor) can be achieved. Figure 5.9(A) shows the current-time transient results of oxygen detected at -0.7 V vs. Ag/AgCl in different formic acid solutions. Without the addition of formic acid, the Clark probe equilibrates to approximate -0.35 µA after 5 min. This value is consistent with previous reports [27], representing the oxygen flux from the solution through the Nylon mesh and the Teflon sensor membrane to the underlying platinum electrode. Typically, it takes about 2 to 5 min to get the equilibration state (quasi steady state) in this case, despite the fact that additional catalytic reactions might slow the equilibration process. The relation between

oxygen response and formic acid concentration is plotted in Figure 5.9(B). Around half of the oxygen flux is consumed in 2 mM formic acid, whilst almost all oxygen flux is lost locally at the catalyst in 4 mM formic acid.

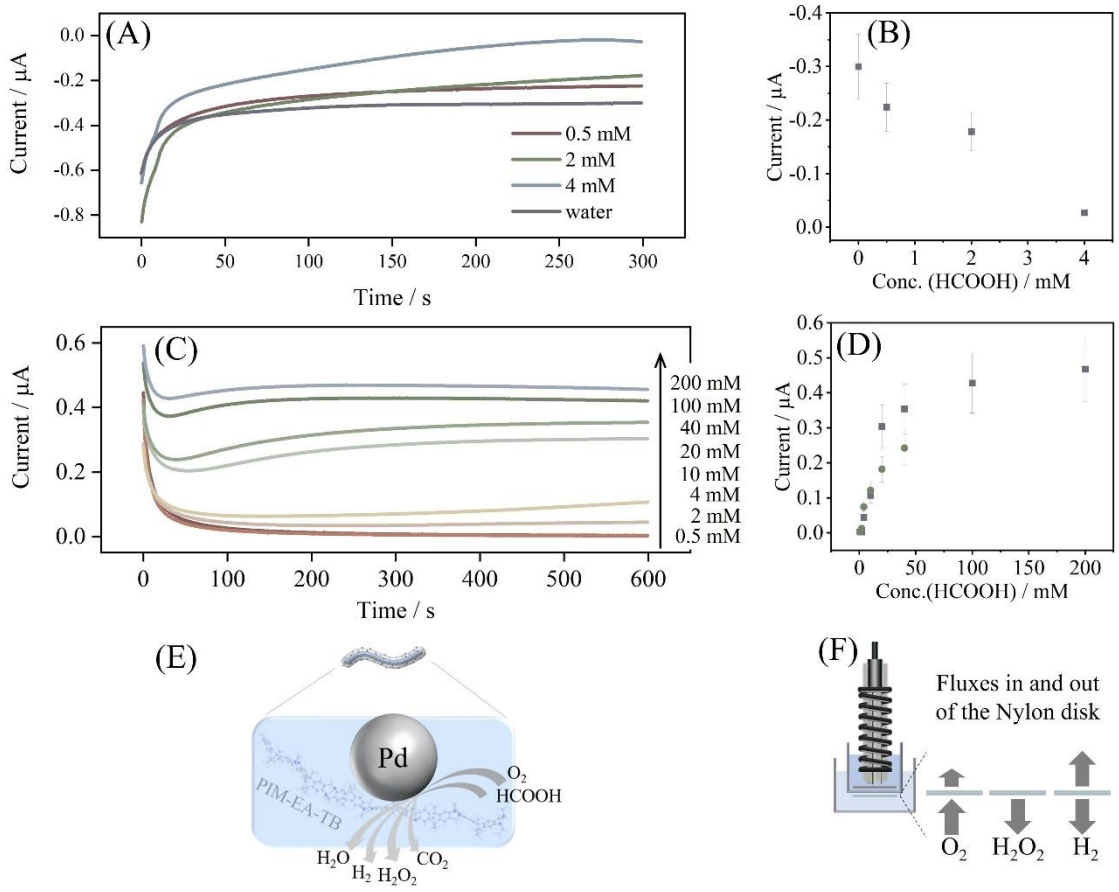

Figure 5.9 Evaluation of oxygen consumption and hydrogen production on Pd@PIM-EA-TB catalyst by a Clark sensor. (A) Clark probe oxygen current-time transients (-0.7 V vs. Ag/AgCl applied voltage) in water, 0.5 mM, 2 mM, and 4 mM HCOOH. (B) A plot of the approximate Clark probe oxygen responses versus HCOOH concentration. (C) Clark probe hydrogen current-time transients (+ 0.6 V vs. Ag/AgCl applied voltage) in 0.5 to 200 mM HCOOH. (D) A plot of the approximate Clark probe hydrogen response versus HCOOH concentration (error bars estimated ± 20%) in ambient condition (grey square plot) and argon (green round plot). (E) Schematic illustration of catalytic reactions at Pd@PIM-EA-TB. (F) Illustration of fluxes to and from the Nylon disk with catalyst.

When exploring the effect of formic acid concentration on hydrogen generation (see Figure 5.9C), a "switch-on" transition is observed at approximately 10 mM formic acid. Higher formic acid contents induce a plateau in the current response, probably linked to saturation of the solution with hydrogen. The Clark sensor current responses generated from high

formic acid concentrations are consistent with the data from hydrogen-saturated solution by intentional gas bubbling [27]. Similar results of hydrogen production are obtained from argon purged formic acid solutions (green plot in Figure 5.9D), which confirms the observation that most oxygen in higher than 2 mM formic acid solution is consumed during the catalytic reaction processes. A reaction scheme is suggested (see Figure 5.9E) as the Pd@PIM-EA-TB catalyst driving the reaction between oxygen and formic acid to produce hydrogen, hydrogen peroxide, and carbon dioxide.

Supplementary experiments with bare Nylon mesh showed no evidence of background catalytic activity. The contrast experiment was carried out on a Pd immobilised Nylon mesh using the same sample preparation procedure without applying PIM-EA-TB material. The experiment with palladium-modified Nylon leads to negligible activity. Therefore, the microporous PIM-EA-TB is essential in binding $PdCl_4^{2-}$ and accommodating guest Pd nanoparticles without impeding the catalytic activity. The microchannels of the host polymer may provide additional effects on reactant and product transport. Fundamentally, the catalytic reactions on the Pd catalyst can be tentatively proposed as oxygen consumption (processes 1 and 2, see Equations 5.1 and 5.2) and hydrogen production (process 3, see Equation 5.3).

To unravel the processes at the catalyst, attention needs to be paid to the fluxes to/from the Nylon disk (see Figure 5.9F). The overall oxygen flux diffused from bulk solution can be dissected into two parts: reactive flux at the catalyst and flux into the Clark sensor. For the reactive oxygen flux density of Process 1 (in mol m^{-2} s^{-1}), an expression rate (Process 1) = $\Phi_{Process\ 1} = k_1$ [HCOOH] [O_2], in which k_1 (in mol^{-1} m^4 s^{-1}) denotes the apparent rate constant for the surface catalytic process within the Pd@PIM-EA-TB catalyst. The oxygen flux density (in the same unit mol m^{-2} s^{-1}) in the quiescent solution can be estimated as $\Phi_{oxygen\ transport} = D_{oxygen}$ [O_2] / δ, where the diffusion coefficient for oxygen is approximately $D_{oxygen} = 3 \times 10^{-9}$ m^2 s^{-1} [34], the bulk concentration of oxygen at room temperature is [O_2] = 0.2 mol m^{-3} [34], and the diffusion layer thickness of natural convection in aqueous media is about δ = 0.5 mm. Therefore, the resulting flux density for the diffusion oxygen is $\Phi_{oxygen\ transport} = 1.2 \times 10^{-6}$ mol m^{-2} s^{-1}. When oxygen is consumed without entering the Clark sensor, in this case [HCOOH] = 4 mM, the flux density of Process 1 ($\Phi_{Process\ 1}$) can be considered the same as the diffusion of oxygen ($\Phi_{oxygen\ transport}$). Thus, the apparent rate constant can be estimated from $\Phi_{oxygen\ transport} \approx \Phi_{Process\ 1} = k_1$ [HCOOH] [O_2] as $k_1 = 1.5 \times 10^{-6}$ mol^{-1} m^4 s^{-1}.

This rate constant describes the consumption of oxygen under the conditions of this experiment for a given Galvani potential.

For hydrogen generation, hydrogen saturation in solution takes place at [HCOOH] = 100 mol m^{-3} (see Figure 5.9C), which can be applied to determine reaction rates. The flux density of Process 3 is formally rate (Process 3) = $\Phi_{Process\ 3} = k_3$ [HCOOH], where k_3 can be estimated at the point of hydrogen saturation (*i.e.* insufficient diffusion of hydrogen away from the Clark sensor). The flux density of hydrogen is $\Phi_{hydrogen\ transport} = D_{hydrogen}$ [H_2] / δ with $D_{hydrogen} = 9 \times 10^{-9}$ m^2 s^{-1} [35], and [H_2] being the saturation concentration of 0.74 mol m^{-3}. Consequently, by connecting flux density for hydrogen and the formal rate of Process 3, $\Phi_{hydrogen\ transport} = \Phi_{Process\ 3} = k_3$ [HCOOH] gives the apparent rate constant $k_3 = 1.3 \times 10^{-7}$ m s^{-1}. The rate for Process 2 needs to be discussed based on H_2O_2 quantification results.

When testing the catalyst durability in high concentration (higher than 0.2 M) formic acid for hydrogen production, reduced performance was observed upon going back to lower concentrations. Deterioration of Pd catalyst in a high concentration of formic acid has been linked to poisoning [36], but no specific mechanism has been allocated.

5.3.2 Clark Probe Evidence for Oxygen Consumption and Hydrogen Evolution from Formic Acid at Pd/Au@PIM-EA-TB

When electrolessly depositing gold on palladium catalyst (denoted Pd/Au@PIM-EA-TB), a new reactivity pattern turns up. The modified Pd is likely to follow a similar pattern when interacting with formic acid to give carbon dioxide, protons, and electrons, whereas the electrons can flow into the larger gold, as illustrated in Figure 5.10E. Gold is known to drive the reduction of oxygen to form hydrogen peroxide under mild conditions [37]. The Pd/Au composition works as a bipolar catalyst.

The typical Clark probe oxygen removal data (at -0.7 V *vs.* Ag/AgCl) generated at Pd/Au@PIM-EA-TB catalyst from different concentrations of formic acid are presented in Figure 5.10A. The plot of the current response against formic acid concentration (Figure 5.10B) demonstrates that about half of the oxygen is consumed at approximate 20 mM formic acid. Total removal of oxygen happens at about 40 mM formic acid. Substitution of [HCOOH] = 40 mM into the flux expression gives a Process 1 rate constant $k_1 \approx 1.5 \times 10^{-}$

^{7} mol^{-1} m^{4} s^{-1}, an order of magnitude lower than that for Pd@PIM-EA-TB catalyst. The drastic decrease in the rate of reactivity is caused by the lower availability of palladium surface and a less negative Galvani potential generating on Pd/Au catalysts.

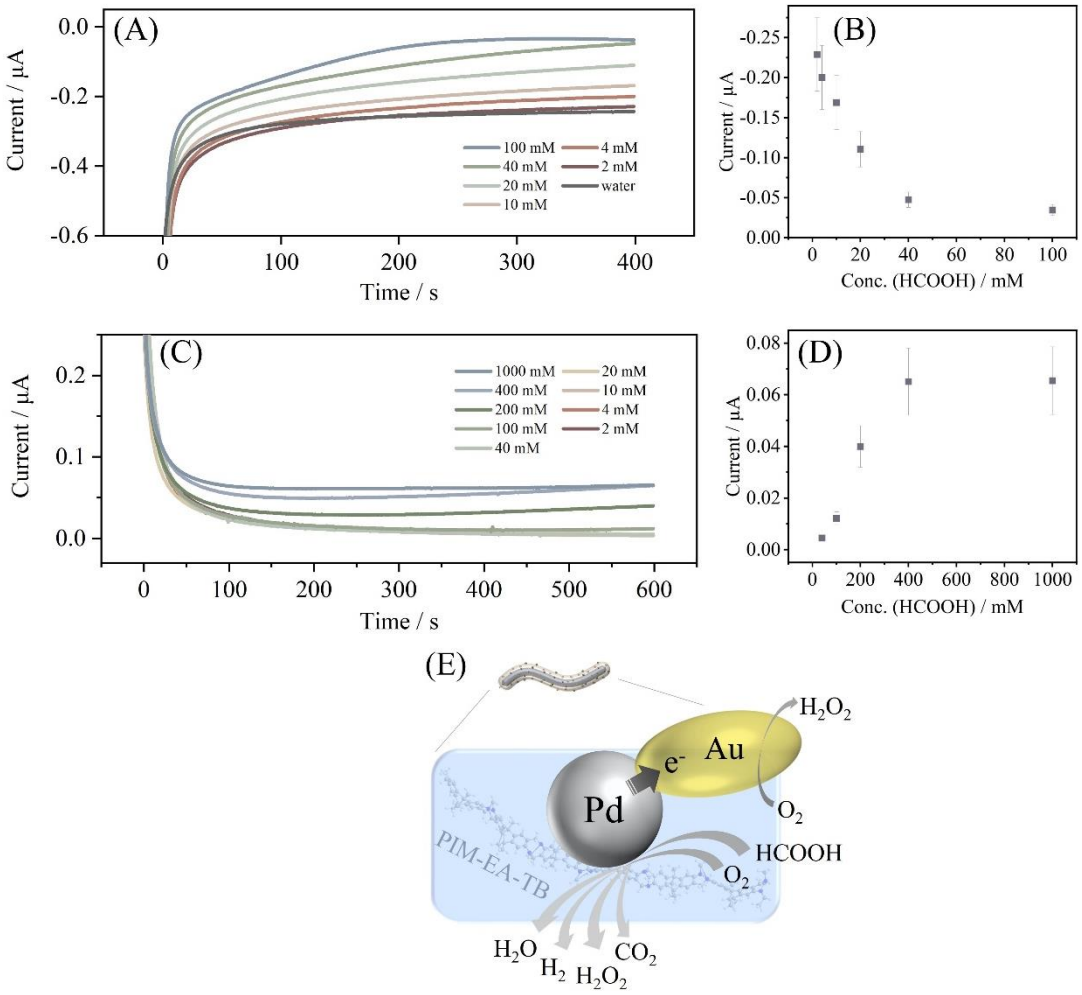

Figure 5.10 Evaluation of oxygen consumption and hydrogen production on Pd/Au@PIM-EA-TB catalyst by a Clark sensor. (A) Clark probe oxygen current time transients in water, 2 mM, 4 mM, 10 mM, 20 mM, 40 mM, and 100 mM HCOOH. (B) A plot of the approximate Clark probe oxygen response versus HCOOH concentration (error bars estimated ± 20%). (C) Clark probe hydrogen current time transients in 2 to 1000 mM HCOOH. (D) A plot of the approximate Clark probe hydrogen response versus HCOOH concentration (error bars estimated ± 20%). (E) Schematic illustration of catalytic reactions at Pd/Au@PIM-EA-TB.

Correspondingly, hydrogen generation is severely suppressed. Hydrogen production data from different formic acid concentrations are shown in Figure 5.10C. Even at a high concentration of 1 M formic acid, the flux or rate of hydrogen generation remains low,

probably due to kinetic restraint. The lowered hydrogen production rate is linked to considerable deactivation of the palladium in Pd/Au@PIM-EA-TB. The overall catalytic efficiency towards hydrogen production at Pd/Au@PIM-EA-TB is suppressed to approximately 1% of that observed without gold. In contrast, one would expect that the production of another key intermediate, H_2O_2, in the reduction of oxygen (see Process 1) is promoted during the whole catalytic process. Thus, the production of H_2O_2 is monitored and discussed next.

5.3.3 Evidence for Hydrogen Peroxide Formation from Oxygen and Formic Acid

The quantification of H_2O_2, the product of the catalytic Process 1, is achieved based on the reaction of *para*-nitrophenylboronic acid to *para*-nitrophenyl (see experimental). The detection of *para*-nitrophenyl by the LC-MS technique indirectly provides a calibration range from 2 to 500 μM H_2O_2. In this case, the bulk concentration of H_2O_2 is probed and further employed to estimate the flux towards the Nylon disk catalyst. Experiments are carried out under stirring, so the rate of mass transport to the Nylon disk could be considered as enhanced approximately by 20 times that of quiescent solutions at the Clark sensor (assuming an order of magnitude increase in mass transport and access to both sides).

Figure 5.11A shows the production of H_2O_2 as a function of reaction time. The catalytic reaction between 2 mM formic acid and approximate 0.2 mM oxygen (in ambient [34]) at Pd@PIM-EA-TB under stirring gives a gradual and approximate linear increase in H_2O_2 production over time. Approximately 20 μM H_2O_2 is produced after 2 h of reaction in a volume of 10 cm^3 stirred solution. The gradual increase trend over time agrees with the gradual transport of H_2O_2 from the Nylon disk to bulk. Figure 5.11B presents the H_2O_2 production at 2 h reaction time versus formic acid concentration (in 2 cm^3 stirred solution). The flux density of H_2O_2 can be determined as $\Phi_{Process\ 1} = [H_2O_2]V/(At)$, where V is the volume of the reaction solution, A is the surface area of the catalyst (8 mm diameter Nylon disk providing 5×10^{-6} m^2), and t is the reaction time. So the point of the highest H_2O_2 production rate with 2 mM formic acid gives the flux density of $\Phi_{Process\ 1} = 1.1 \times 10^{-7}$ mol m^{-2} s^{-1}, which is much lower than the anticipated oxygen flux density of $\Phi_{oxygen\ transport} = 2.4 \times 10^{-5}$ mol m^{-2} s^{-1} under these conditions (assumed 20 times higher of the flux to the Clark sensor). The catalytic reaction of Process 1 must be significantly affected by the degradation of H_2O_2, as depicted in Process 2.

When the formic acid concentration increases to 4 mM, the H_2O_2 yield reduces again, as shown in Figure 5.11B. The reason can be suggested as the ability of Pd nanoparticles to reduce H_2O_2 to H_2O. The oxygen flux towards the Nylon disk is sufficient, whereas locally inside PIM-EA-TB, the increase of formic acid from 2 mM to 4 mM leads to more reduction of H_2O_2 to H_2O.

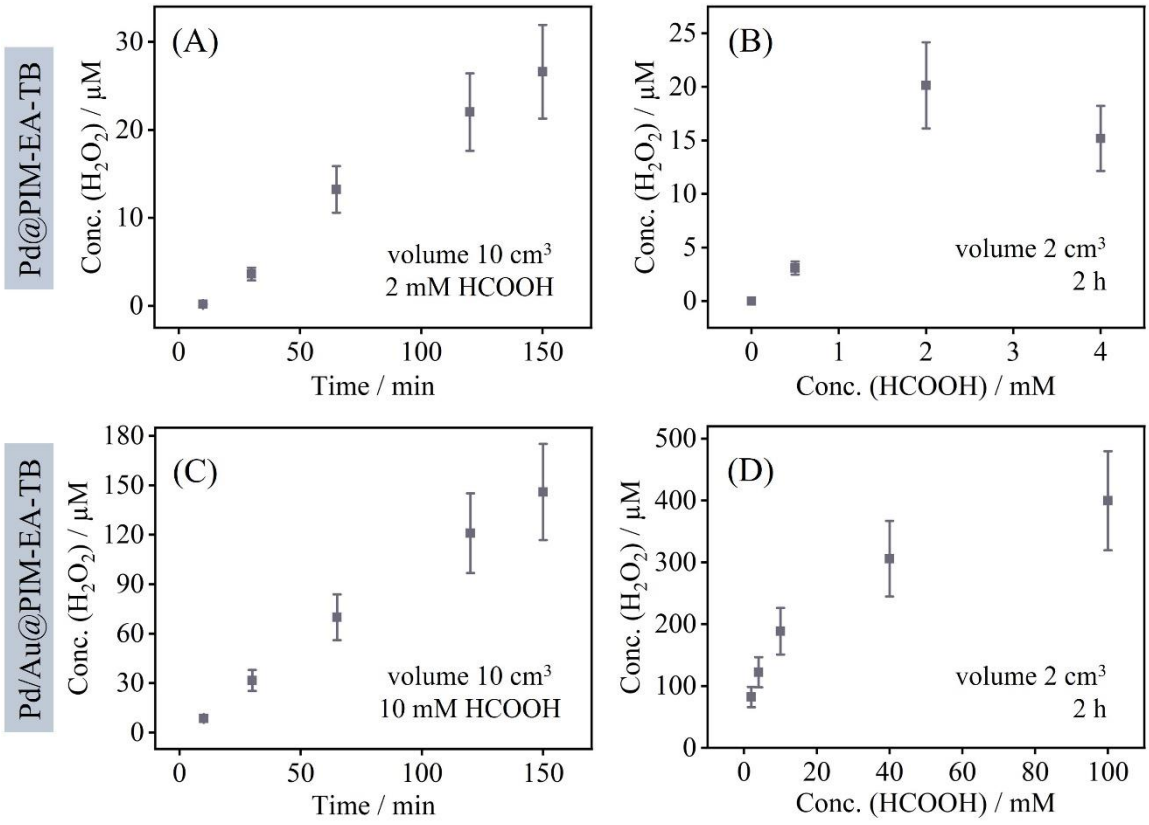

Figure 5.11 Quantification of H_2O_2 produced at Pd@PIM-EA-TB or PdAu@PIM-EA-TB from oxygen and formic acid. (A) A plot of H_2O_2 concentration as a function of time (one Nylon disk modified with Pd@PIM-EA-TB in 10 mL stirred solution) for 2 mM formic acid concentration. (B) A plot of H_2O_2 concentration after 2 h reaction (one nylon disk modified with Pd@PIM-EA-TB in 2 mL stirred solution) as a function of formic acid concentration. (C) A plot of H_2O_2 concentration as a function of time (one Nylon disk modified with Pd/Au@PIM-EA-TB in 10 mL stirred solution) for 10 mM formic acid concentration. (D) A plot of H_2O_2 concentration after 2 h reaction (one Nylon disk modified with Pd/Au@PIM-EA-TB in 2 mL stirred solution) as a function of formic acid concentration (error bars based on variations in catalyst disks and Clark probe responses estimated ± 20%).

Figure 5.11C shows how H_2O_2 is produced as a function of time for Pd/Au@PIM-EA-TB catalyst in 10 mM formic acid. The comparison with data in Figure 5.11A indicates approximately 5 times higher H_2O_2 yield, consistent with 5 times higher amount of formic acid. Figure 5.11D shows the effect of formic acid concentration on H_2O_2 production at 2 h reaction time. An order of magnitude increase in H_2O_2 production is observed with the presence of gold. From the result with 10 mM formic acid, the approximate H_2O_2 flux density at the Nylon disk can be estimated as $\Phi_{Process\ 1} = 1.0 \times 10^{-7}$ mol m^{-2} s^{-1}. The H_2O_2 production further rises with higher formic acid concentration and reaches a plateau with $\Phi_{Process\ 1} = 2.2 \times 10^{-6}$ mol m^{-2} s^{-1}. This value is still low compared to the predicted oxygen flux ($\Phi_{oxygen\ transport} = 2.4 \times 10^{-5}$ mol m^{-2} s^{-1}); thereby, oxygen transport improbably affects H_2O_2 production significantly. A steady state is signified when the formic acid concentration is high, meaning that the process is independent of formic acid concentration. That implies the H_2O_2 generation (see Process 1) and consumption (see Process 2) presenting the same reaction rate. Therefore, a combination of the rate expressions for Process 1 ($\Phi_{Process\ 1} = k_1[HCOOH][O_2]$) and Process 2 ($\Phi_{Process\ 2} = k_2[HCOOH][O_2]$) for the case of high formic acid concentration gives that $k_1/k_2 = [H_2O_2]/[O_2]$. Given that $k_1 = 1.5 \times 10^{-7}$ mol^{-1} m^4 s^{-1} and $[H_2O_2] = 0.4$ mM and $[O_2] = 0.2$ mM, the apparent rate constant is $k_2 = ½\ k_1 = 0.75 \times 10^{-7}$ mol^{-1} m^4 s^{-1} for the case of Pd/Au@PIM-EA-TB. Despite the considerable H_2O_2 generation under these conditions, it could be further enhanced by changing the oxygen content in the solution.

Further investigations were carried out on the reactivity of Pd/Au@PIM-EA-TB for hydrogen peroxide production. Figure 5.12A presents the data for comparing a single Nylon disk with double Nylon disks in a stirred solution. Perhaps surprisingly, the production of H_2O_2 is raised at short times (for low H_2O_2 concentration). However, doubling the catalyst amount seems trivial for reaction times longer than 1 h. A change in the amount of catalyst can alter the apparent rate constants k_1 and k_2, but not the ratio of k_1/k_2, which is the indication of the long-term steady state concentration of H_2O_2. In other words, for a longer reaction time or higher formic acid concentration, the same limiting concentration $[H_2O_2]_{lim}$ is produced independently of the catalyst amount.

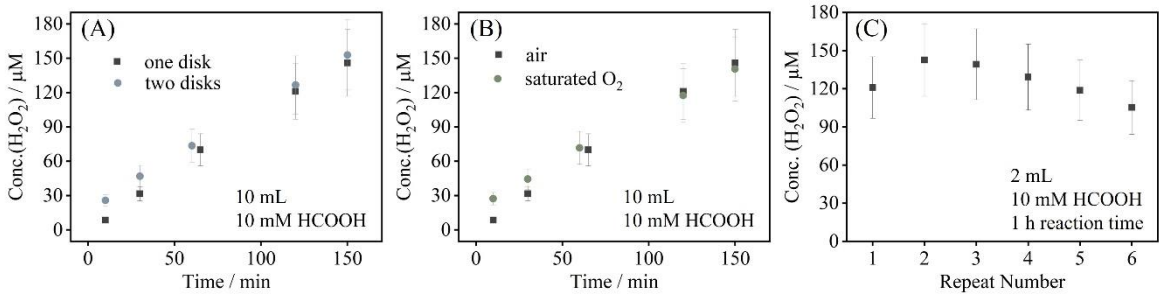

Figure 5.12 Reactivity of Pd/Au@PIM-EA-TB for H_2O_2 production. (A) A plot of H_2O_2 concentration formed at Pd/Au@PIM-EA-TB in the presence of 10 mM formic acid as a function of time. Data sets for one Nylon disk (black) and two Nylon disks (grey) modified with Pd/Au@PIM-EA-TB in a 10 cm^3 stirred solution. (B) A plot of H_2O_2 concentration formed at Pd/Au@PIM-EA-TB in the presence of 10 mM formic acid as a function of time. Data sets for 0.2 mM oxygen (black) and 1 mM oxygen (green) for one Nylon disk modified with Pd/Au@PIM-EA-TB in a 10 cm^3 stirred solution. (C) A plot of H_2O_2 concentration formed at Pd/Au@PIM-EA-TB in the presence of 10 mM formic acid at 1 h reaction time for repeat experiments (one Nylon disk modified with Pd/Au@PIM-EA-TB in 2 cm^3 stirred solution) (error bars based on variations in catalyst disks and Clark probe responses estimated ± 20%).

Figure 5.12B shows the effect of oxygen concentration dissolved in the solution. The data were collected from oxygen in ambient (approximate 0.2 mM) and saturated condition (approximate 1.0 mM). A significant enhancement of H_2O_2 production is observed only during the initial 30 min with values converging against reaction time. The data trend is very similar over a period of 150 min reaction, although the final value of $[H_2O_2]_{lim}$ could be higher with the saturated oxygen case. Finally, Figure 5.12C demonstrates the possibility of reusing the catalyst. Using Nylon disk substrates makes it easy to refresh the catalyst by taking it out from the solution and rinsing it with water. The yield of H_2O_2 remains approximately constant over 6 sequential experiments of repeating the detection from 10 mM formic acid solution for 1 h each.

The catalytic generation of hydrogen peroxide on a bipolar Pd/Au@PIM-EA-TB catalyst can be dissected as individual redox processes presuming Tafel law effects on kinetics connected to the Galvani potential on the nano-catalysts. The apparent rate constants under specific reaction conditions depend on the potential, similar to heterogeneous transfer rate constants. Based on this hypothesis, the scheme for the case of spontaneous oxidation of formic acid on palladium catalyst is illustrated in Figure 5.13A. Specifically, the hydrogen is spontaneously generated on palladium catalyst from formic acid and then oxidised to protons. The rate for this process is Galvani potential dependent followed Tafel law. The

oxidation rate increases with potential as designated as a line. Also presented is the process for the reduction of oxygen to water on palladium. The intersection indicates the operational potential during catalysis under a specific condition (*i.e.* a given concentration of reagents). Figure 5.13B shows the effect of oxygen depletion. As oxygen is consumed, the oxygen reduction slows down, and the intersection point ① moves along the line approaching point ②. Point ② is the intersection of hydrogen oxidation and proton reduction processes, denoting the equilibrium potential for H^+/H_2 at more negative potentials.

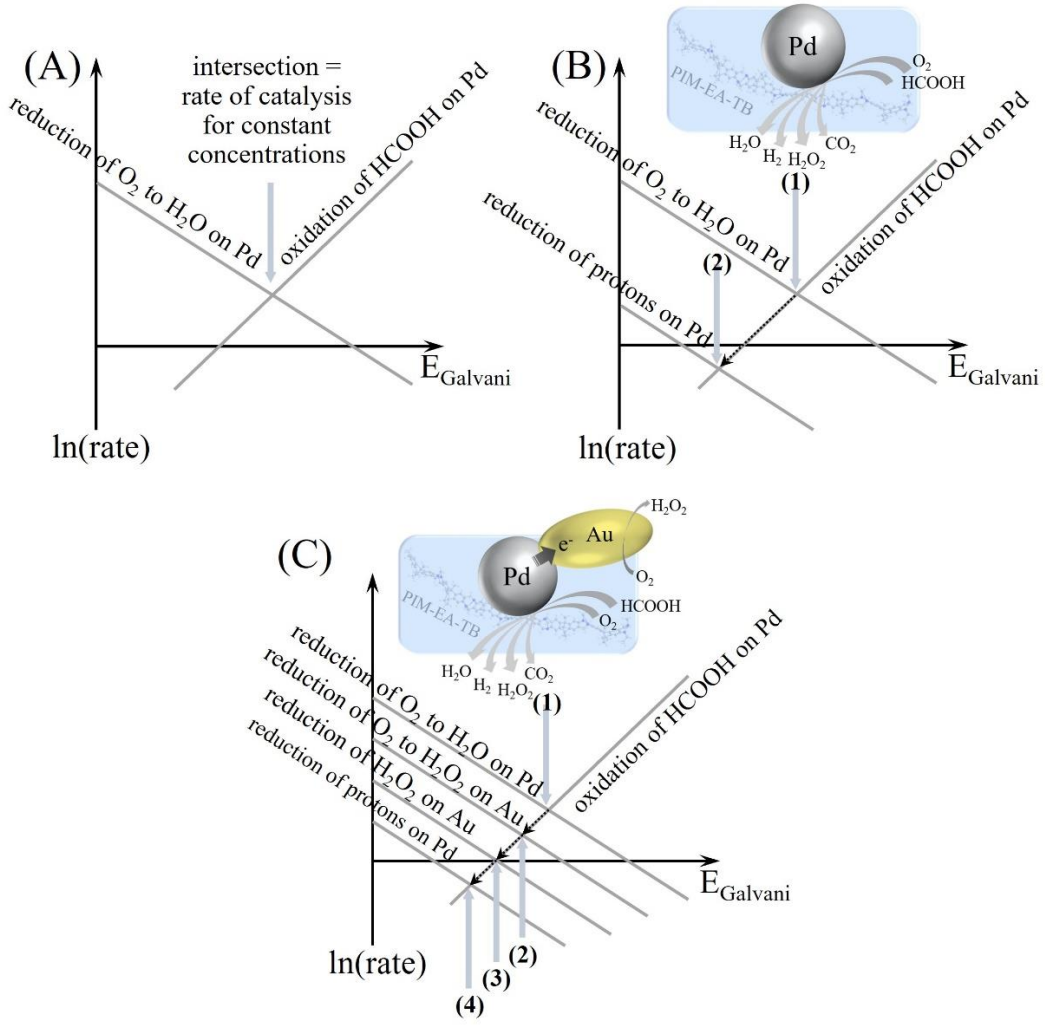

Figure 5.13 Schematic illustration of the effect of the Galvani potential on the reaction rate. (A) Oxidation of formic acid and reduction of oxygen leads to a mixed potential on Pd. (B) On Pd oxidation of formic acid and reduction of oxygen form mixed potential ① and after depletion of oxygen, the potential shifts to ②. (C) On Pd/Au oxidation of formic acid on Pd leads to a mixed potential for reduction of O_2 on Pd ①, then reduction of O_2 to H_2O_2 on Au ②, then reduction of H_2O_2 on Au ③, and, finally, reduction of protons to hydrogen ④.

The processes on the bipolar Pd/Au@PIM-EA-TB nanoparticles are discussed in Figure 5.13C. Initially, the catalyst operates at potential ① where oxygen reduction to water dominates on palladium. As oxygen is depleted, the potential alters to point ② where oxygen reduction to hydrogen peroxide on gold occurs. Point ② represents the optimum operating conditions as further oxygen depletion pushing the Galvani potential more negative where hydrogen peroxide diminishes again at ③. So, for a high hydrogen peroxide yield, the oxygen reduction to water on Pd at point ① should be suppressed by adjusting the ratio of Pd to Au surface area; the hydrogen peroxide production process on Au at point ② needs to be optimised by contributing high Au surface area; the reagent (formic acid) concentration could be chosen to keep the operational potential of Pd/Au@PIM-EA-TB close to point ②.

The rigid micropores in PIM-EA-TB likely play a role in the mass transport of reagents (HCOOH, O_2, H_2O_2) in the case presented here, which could affect the results. A published work demonstrated that up to 56 mM H_2O_2 was produced on a PdAu catalyst directly from hydrogen and oxygen gas. The yields of H_2O_2 presented in this chapter are two orders of magnitude lower and could be promoted with more optimisations.

5.4 Conclusions

Nano-catalysts of Pd and Pd/Au are immobilised in the microporous host PIM-EA-TB. Both catalysts were demonstrated to consume oxygen and produce hydrogen in the presence of formic acid, evidenced by a Clark sensor. The catalyst of Pd nanoparticles is effective in generating hydrogen, whilst Pd/Au is more active in producing H_2O_2. High concentrations of formic acid (> 0.2 M) cause deterioration of the Pd catalyst.

Compared to Pd catalyst, Pd/Au catalyst produces a higher amount of hydrogen peroxide with only a minimal hydrogen generation even at a high formic acid concentration. This could be rationalised as electron transport from Pd to Au, making the Galvani potential on Pd/Au catalyst less negative while operating. The electrons generated on Pd where formic acid reacts are transferred to Au. And oxygen is reduced to make hydrogen peroxide on Au.

The functions of the intrinsically microporous polyamine, PIM-EA-TB, during the catalytic reaction can be summarised as (i) providing the microporous environment (with amine groups) for binding $PdCl_4^{2-}$ and incorporating Pd catalyst; (ii) allowing the deposition of nano-Au attached to Pd seeds; (iii) permeation of reactants and products; (iv) making it

possible to reuse and recover the catalysts. It is worth noting that the tertiary amine functional group in PIM-EA-TB may also affect the catalytic process when permeating reaction intermediates. Further works could be emphasized on modifying the host polymer structure (to enhance the permeation and selectivity towards intermediates) and adjusting Pd to Au ratio (to suppress degradation of H_2O_2) in terms of higher hydrogen peroxide yield.

5.5 References

1 Tao, R., Ma, X., Wei, X., Jin, Y., Qiu, L., & Zhang, W. Porous organic polymer material supported palladium nanoparticles. *Journal of Materials Chemistry A* **8**, 17360-17391 (2020).

2 Felpin, F. X., Ayad, T. & Mitra, S. Pd/C: an old catalyst for new applications-its use for the Suzuki-Miyaura reaction. *European Journal of Organic Chemistry* **2006**, 2679-2690 (2006).

3 Bayguzina, A. & Khusnutdinov, R. Catalytic N-alkylation of anilines. *Russian Journal of General Chemistry* **91**, 305-347 (2021).

4 Saldan, I., Semenyuk, Y., Marchuk, I. & Reshetnyak, O. Chemical synthesis and application of palladium nanoparticles. *Journal of Materials Science* **50**, 2337-2354 (2015).

5 Zhong, H., Iguchi, M., Chatterjee, M., Himeda, Y., Xu, Q., & Kawanami, H. Formic acid-based liquid organic hydrogen carrier system with heterogeneous catalysts. *Advanced Sustainable Systems* **2**, 1700161 (2018).

6 Luo, M., Yang, Y., Sun, Y., Qin, Y., Li, C., Li, Y., Li, M., Zhang, S. & Guo, S. Ultrathin two-dimensional metallic nanocrystals for renewable energy electrocatalysis. *Materials Today* **23**, 45-56 (2019).

7 Menegazzo, F., Signoretto, M., Ghedini, E. & Strukul, G. Looking for the "dream catalyst" for hydrogen peroxide production from hydrogen and oxygen. *Catalysts* **9**, 251 (2019).

8 Dittmeyer, R., Grunwaldt, J.-D. & Pashkova, A. A review of catalyst performance and novel reaction engineering concepts in direct synthesis of hydrogen peroxide. *Catalysis Today* **248**, 149-159 (2015).

9 Dimitratos, N., Lopez-Sanchez, J. A. & Hutchings, G. J. Green catalysis with alternative feedstocks. *Topics in Catalysis* **52**, 258-268 (2009).

10 Zhong, M., Xu, Y., Li, J., Ge, Z. X., Jia, C., Chen, Y., Deng, P. & Tian, X. Engineering PdAu nanowires for highly efficient direct methane conversion to methanol under mild conditions. *The Journal of Physical Chemistry C* **125**, 12713-12720 (2021).

11 Villa, A., Janjic, N., Spontoni, P., Wang, D., Su, D. S. & Prati, L. Au-Pd/AC as catalysts for alcohol oxidation: Effect of reaction parameters on catalytic activity and selectivity. *Applied Catalysis A: General* **364**, 221-228 (2009).

12 Pritchard, J., Kesavan, L., Piccinini, M., He, Q., Tiruvalam, R., Dimitratos, N., Lopez-Sanchez, J. A., Carley, A. F., Edwards, J. K., Kiely, C. J. & Hutchings, G. J. Direct synthesis of hydrogen peroxide and benzyl alcohol oxidation using Au-Pd catalysts prepared by sol immobilization. *Langmuir* **26**, 16568-16577 (2010).

13 Halder, K., Bengtson, G., Filiz, V. & Abetz, V. Catalytically active (Pd) nanoparticles supported by electrospun PIM-1: influence of the sorption capacity of the polymer tested in the reduction of some aromatic nitro compounds. *Applied Catalysis A: General* **555**, 178-188 (2018).

14 Drogui, P., Elmaleh, S., Rumeau, M., Bernard, C. & Rambaud, A. Hydrogen peroxide production by water electrolysis: application to disinfection. *Journal of Applied Electrochemistry* **31**, 877-882 (2001).

15 Dimitratos, N., Lopez-Sanchez, J. A. & Hutchings, G. J. Green catalysis with alternative feedstocks. *Topics in Catalysis* **52**, 258-268 (2009).

16 Vennestrøm, P. N., Christensen, C. H., Pedersen, S., Grunwaldt, J. D. & Woodley, J. M. Next-generation catalysis for renewables: combining enzymatic with inorganic heterogeneous catalysis for bulk chemical production. *ChemCatChem* **2**, 249-258 (2010).

17 Barrington, D. J. & Ghadouani, A. Application of hydrogen peroxide for the removal of toxic cyanobacteria and other phytoplankton from wastewater. *Environmental Science & Technology* **42**, 8916-8921 (2008).

18 Guan, R., Yuan, X., Wu, Z., Jiang, L., Li, Y., & Zeng, G. Principle and application of hydrogen peroxide based advanced oxidation processes in activated sludge treatment: A review. *Chemical Engineering Journal* **339**, 519-530 (2018).

19 Amaeze, N. J., Shareef, M. U., Henriquez, F. L., Williams, C. L., & Mackay, W. G. Influence of delivery system on the efficacy of low concentrations of hydrogen peroxide in the disinfection of common healthcare-associated infection pathogens. *Journal of Hospital Infection* **106**, 189-195 (2020).

20 Dannacber, J., & Schlenker, W. The Mechanism of hydrogen peroxide bleaching. *Textile Chemist & Colorist* **28**, 24-28 (1996).

21 Mistik, S. I., & Yükseloğlu, S. M. Hydrogen peroxide bleaching of cotton in ultrasonic energy. *Ultrasonics* **43**, 811-814 (2005).

22 Zhang, S. D., Zhang, Y. R., Wang, X. L. & Wang, Y. Z. High carbonyl content oxidized starch prepared by hydrogen peroxide and its thermoplastic application. *Starch-Stärke* **61**, 646-655 (2009).

23 Gao, J. & Liu, B. Progress of electrochemical hydrogen peroxide synthesis over single atom catalysts. *ACS Materials Letters* **2**, 1008-1024 (2020).

24 Torres-Pinto, A., Sampaio, M. J., Silva, C. G., Faria, J. L. & MT Silva, A. Recent strategies for hydrogen peroxide production by metal-free carbon nitride photocatalysts. *Catalysts* **9**, 990 (2019).

25 Yalfani, M. S., Contreras, S., Medina, F. & Sueiras, J. Direct generation of hydrogen peroxide from formic acid and O_2 using heterogeneous Pd/γ-Al_2O_3 catalysts. *Chemical communications* 3885-3887 (2008).

26 Comotti, M., Della Pina, C., Falletta, E., & Rossi, M. Aerobic oxidation of glucose with gold catalyst: hydrogen peroxide as intermediate and reagent. *Advanced Synthesis & Catalysis* **348**, 313-316 (2006).

27 Zhao, Y., Malpass-Evans, R., Carta, M., McKeown, N. B., Fletcher, P. J., Kociok-Köhn, G., Lednitzky, D. & Marken, F. Size-Selective photoelectrochemical reactions in microporous environments: Clark probe investigation of Pt@g-C_3N_4 embedded into intrinsically microporous polymer (PIM-1). *ChemElectroChem* **8**, 3499-3505 (2021).

28 Carta, M., Malpass-Evans, R., Croad, M., Rogan, Y., Jansen, J. C., Bernardo, P., Bazzarelli, F. & McKeown, N. B. An efficient polymer molecular sieve for membrane gas separations. *Science* **339**, 303-307 (2013).

29 Xia, F., Pan, M., Mu, S., Malpass-Evans, R., Carta, M., McKeown, N. B., Attard, G. A., Brew, A., Morgan, D. J. & Marken, F. Polymers of intrinsic microporosity in electrocatalysis: novel pore rigidity effects and lamella palladium growth. *Electrochimica Acta* **128**, 3-9 (2014).

30 Pourbaix, M. Atlas of electrochemical equilibria in aqueous solution. *NACE* **307** (1974).

31 Kanyanee, T., Fletcher, P. J., Madrid, E. & Marken, F. Indirect (hydrogen-driven) electrodeposition of porous silver onto a palladium membrane. *Journal of Solid State Electrochemistry* **24**, 2789-2796 (2020).

32 Mišlov, D., Cifrek, M., Krois, I. & Džapo, H. in *2015 IEEE Sensors Applications Symposium (SAS)*. 1-5 (IEEE).

33 Lu, C.-P., Lin, C.-T., Chang, C.-M., Wu, S.-H. & Lo, L.-C. Nitrophenylboronic acids as highly chemoselective probes to detect hydrogen peroxide in foods and agricultural products. *Journal of Agricultural and Food Chemistry* **59**, 11403-11406 (2011).

34 Weber, J., Wain, A. J. & Marken, F. Microwire chronoamperometric determination of concentration, diffusivity, and salinity for simultaneous oxygen and proton reduction. *Electroanalysis* **27**, 1829-1835 (2015).

35 Crozier, T. E. & Yamamoto, S. Solubility of hydrogen in water, sea water, and sodium chloride solutions. *Journal of Chemical and Engineering Data* **19**, 242-244 (1974).

36 Madrid, E., Harabajiu, C., Hill, R. S., Black, K., Torrente-Murciano, L., Dickinson, A. J., Fletcher, P. J., Ozoemena, K. I., Ipadeola, A. K., Oguzie, E., Akalezi, C. O. & Marken, F. Indirect formic acid fuel cell based on a palladium or palladium-alloy film separating the fuel reaction and electricity generation. *ChemElectroChem* **8**, 378-385 (2021).

37 Das, S., Mishra, A. & Ghangrekar, M. Production of hydrogen peroxide using various metal-based catalysts in electrochemical and bioelectrochemical systems: mini review. *Journal of Hazardous, Toxic, and Radioactive Waste* **24**, 06020001 (2020).

Chapter 6 Formate Oxidase Reactivity with Nano-Palladium Embedded in Intrinsically Microporous Polyamine (Pd@PIM-EA-TB) Driving the H_2O_2 – 3,5,3',5'-Tetramethylbenzidine (TMB) Colour Reaction

---

Contents

Chapter Abstract

Palladium nano-catalysts with a typical size of 3 nm in diameter are embedded in a polymer of intrinsic microporosity PIM-EA-TB (denoted as Pd@PIM-EA-TB). These catalysts are revealed to indirectly drive the colour reaction of a visualising reagent 3,5,3',5'-tetramethylbenzidine (TMB) in the presence of formic acid. Exploration shows that the overall catalytic reaction can be dissected into two processes: oxygen reduction on the palladium catalyst to yield H_2O_2, followed by homogeneous TMB oxidation. The H_2O_2 formation is a first-order process with optimised conditions at approximately pH 3 to 4. Therefore, the H_2O_2 production from formic acid is investigated individually as a nanozyme-like catalytic process analogous to formate oxidase reactivity. The molecularly rigid and microporous PIM-EA-TB host (structured with tertiary amine sites) enhances both (i) 2-electron formate oxidation and (ii) 2-electron oxygen reduction to H_2O_2. The favourable effect of perchlorate anions indirectly proves the activity of amine sites. A computational DFT model for the formate oxidase reactivity of Pd@PIM-EA-TB is exploited to demonstrate and support the hypothesis of the host PIM-EA-TB as an active catalyst element.

Graphical Abstract

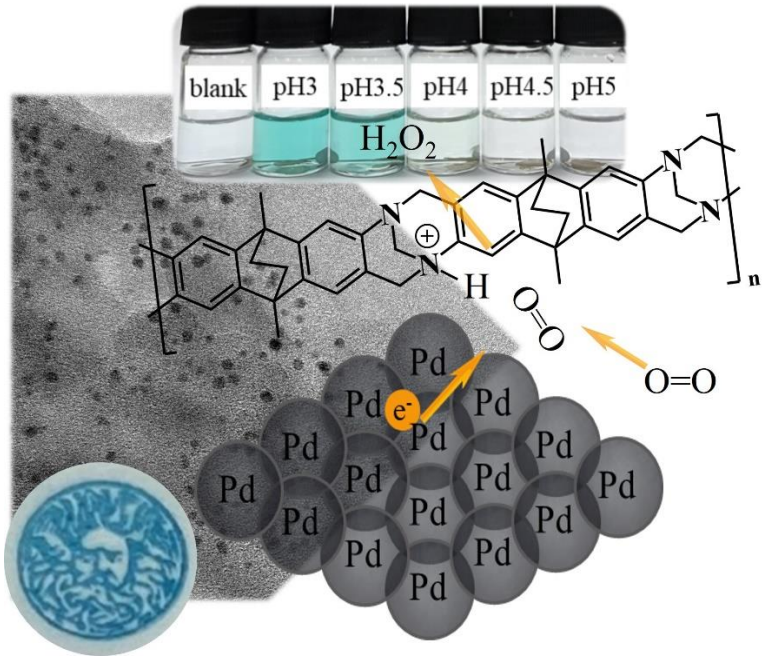

Publications associated with this chapter

Wang, L., Carta, M., Malpass-Evans, R., McKeown, N. B., Fletcher, P. J., Estrela, P., Roldan, A. & Marken, F. Artificial Formate Oxidase Reactivity with Nano-palladium Embedded in Intrinsically Microporous Polyamine (Pd@PIM-EA-TB) Driving the H_2O_2–3, 5, 3′, 5′-tetramethylbenzidine (TMB) Colour Reaction. *Journal of Catalysis*, **416**, 253-266 (2022).

Credit Statement

The candidate performed the immobilisation of palladium in PIM-EA-TB, quantification of hydrogen peroxide based on LC-MS, electrochemical experiments based on a Clark probe, TMB colour reaction, data curation, and interpretation of the results. Neil B. McKeown provided the PIM-EA-TB material. Philip J. Fletcher carried out the SEM and TEM characterisation in this work. Alberto Roldan designed and improved the DFT calculation model, carried out all the computational simulations, provided all the activation energy and reaction energy data during each reaction step, and helped explain the computational results. Mariolino Carta, Richard Malpass-Evans, Neil B. McKeown, Philip J. Fletcher, Pedro Estrela and Alberto Roldan gave valuable comments and input to the draft. Frank Marken supervised the candidate throughout the whole project, gave critical and valuable comments to the results, aided the candidate in the discussion of computational simulation with Alberto, and helped with the reviewing and editing of the original draft.

Special Acknowledgements

Thanks to Prof. Neil McKeown and his research group from the University of Edinburgh for collaborating and providing PIM-EA-TB material. A sincere acknowledgement to Dr Alberto Roldan from Cardiff University who carried out the DFT calculations detailed in this chapter. Thanks also to Dr Philip Fletcher for help with SEM, EDX, and TEM characterisation for this chapter.

6.1 Introduction

Enzyme mimic modelling the reactivity of natural enzyme has drawn attention in electroanalysis [1,2], and biosensing [3]. Formate oxidase, extracted from the formaldehyde-resistant fungi Aspergillus nomius [4], can oxidise formate to carbon dioxide with molecular oxygen as an electron acceptor [5,6]. The ability of formate detoxification is of considerable importance in nature during microbial degradation [7]. The reactivity of formate oxidase is associated with hydrogen peroxide (H_2O_2) production *via* formate oxidation [4] (Equations 6.1 and 6.2), in which the hydrogen carrying cofactor is FAD/$FADH_2$. This type of peroxide generating enzymes or nanozymes [8] is of great interest since H_2O_2 applications vary in disinfection [9], biomass breakdown [10], and pollution treatment [11].

$$HCOOH \rightleftharpoons CO_2 + H_2(\text{cofactor}) \tag{6.1}$$

$$O_2 + H_2(\text{cofactor}) \rightleftharpoons H_2O_2 \tag{6.2}$$

Formate oxidase reactivity in nature [12] has been discovered as a FAD (chemically modified) cofactor dependent process [13]. It is worth noting that a more common formate dehydrogenase depends on NAD^+/NADH [14] or a cytochrome to serve as an electron acceptor [5]. Studies on the catalytic generation of H_2O_2 have been illustrated to be applicable in a wide range of synthetically oxidation chemistry [15]. Mimicking the formate oxidase reactivity with a chemically robust catalyst is worth exploring. Here, the reactivity of palladium nanoparticles embedded in a microporous polymer host is studied towards formic acid oxidation.

By exploring the enzyme-like reactivities of a chemically robust catalyst, palladium, the drawbacks of a natural enzyme, including temperature instability, difficulty in extraction, and high cost, can be improved. Here, palladium nanoparticles are immobilised in PIM-EA-TB (see molecular structure in Figure 6.1) and assessed for a catalytic reaction in formic acid solutions. Evaluation of the catalytic reactions in terms of oxygen and hydrogen levels in the aqueous solutions is carried out by a Clark sensor.

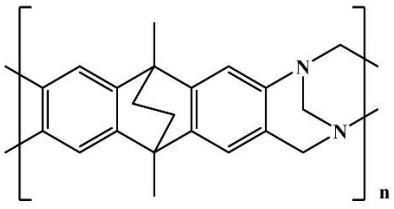

PIM-EA-TB

Figure 6.1 Molecular structure for PIM-EA-TB.

Palladium nanoparticles are embedded in PIM-EA-TB (or Pd@PIM-EA-TB) by absorbing $PdCl_4^{2-}$ [16] followed by borohydride reduction (detailed in Chapter 5). The Pd@PIM-EA-TB shows the ability to generate H_2O_2 at low formic acid concentrations and produce H_2 at high formic acid concentrations. The rate of H_2O_2 production is sensitive to reaction conditions. Here, the effect of the PIM-EA-TB host on catalytic reactions is explored more closely. Nanozyme reactivity (mimicking formate oxidase) is demonstrated with the PIM-EA-TB providing cavities to accommodate palladium and being an active component with tertiary amine functional groups adjacent to the palladium surface.

Nanomaterial-based artificial enzymes (or nanozymes [3,17]) can effectively mimic catalytic sites of natural enzymes [18,19]. Nanozymes have captured massive attention due to their tunable catalytic activities, high stability, biocompatibility, and low cost [20,21]. Applications of nanozymes in biosensing [22,23], point-of-care diagnostics [22], food safety [24], and environmental analysis [25] have been achieved. Nanozymes have been reported to drive the 3,5,3',5'-tetramethylbenzidine (TMB) colour response [26]. A nanozyme as an alternative to glucose oxidase has been employed with TMB colour reaction [27,28]. Palladium has been reported as peroxidase mimetics for TMB colourimetric sensing and evaluation of antioxidants in fruit juices [29].

In this chapter, palladium nanoparticles are immobilised in the molecularly rigid microporous polyamine (PIM-EA-TB). The Pd@PIM-EA-TB catalyst is shown to react with oxygen and formic acid to yield hydrogen peroxide by a single process. The catalytic process shows optimum reactivity at a pH range of 3 to 4. A computational DFT model is developed to rationalise the hydrogen peroxide process at the Pd@PIM-EA-TB catalyst and to consolidate the hypothesis of PIM-EA-TB as an active component during the catalytic reaction. The H_2O_2 production can be combined with processes such as the oxidative colour reaction of TMB. The whole reaction is optimised to accumulate oxidised coloured dye into a Nafion-coated substrate which could be an initial step for future applications of immune-assay and colourimetric sensing.

6.2 Experimental

6.2.1 Reagents

Palladium(II) chloride ($PdCl_2$, 99%), hydrochloric acid (HCl, ACS reagent, 37%), sodium borohydride ($NaBH_4$, powder, 98%), formic acid (HCOOH, 96%, ACS Reagent), 3,3',5,5'-Tetramethylbenzidine (TMB, ≥99%), phosphoric acid (H_3PO_4, 85 wt.% solution, ACS Reagent), monosodium phosphate (NaH_2PO_4, 99%), sodium formate (NaCOOH, ACS reagent, ≥99.0%), *p*-nitrophenylboronic acid (≥95.0%), sodium carbonate (Na_2CO_3, powder, ≥ 99.5%, ACS Reagent), Nafion (5% solution), 1-butanol (ACS reagent, ≥99.4%), and Whatman® nitrocellulose membrane filters (gridded white, pore size 0.45 μm) were purchased from Sigma-Aldrich. Acetic acid (CH_3COOH, >99%) was the product of Fisher Scientific. Hydrogen peroxide (H_2O_2, ACS Reagent, 30 wt.% in H_2O) and dimethyl sulfoxide (DMSO, for HPLC, ≥99.7%) were products from Honeywell. Sodium bicarbonate ($NaHCO_3$, ≥99.7%) was bought from Fluka. PIM-EA-TB was synthesised following a previous method [30]. Nylon mesh from 75 μm diameter Nylon was purchased from Amazon.com (Therpin reusable Nylon fine mesh food strainer bag, 75 μm threads, woven, with approximate 130 μm × 130 μm open holes). A Fisherbrand universal indicator pH paper (pH 1-14) was employed to roughly monitor the acidity of test solutions for the H_2O_2 quantification experiments. Filter paper (Whatman™, pore size < 2 μm) was ordered from GE Healthcare Life Sciences. The stamp was customised online (www.getstamped.co.uk.).

6.2.2 Instrumentation

Ultra-pure water (resistivity not less than 18.2 MΩ cm at 20 °C) was taken from a Thermo Scientific water purification system. A pH meter (Jenway 3505) was used to monitor the pH of solutions. The Clark probe (HI76407) and concentrated KCl solution (HI7041S) were purchased from HANNA Instruments Ltd., UK. The current responses of hydrogen production and oxygen consumption were recorded by chronoamperometry on a potentiostat (Metrohm mAutolab II). A field emission scanning electron microscope (FESEM, JEOL JSM-7900F), a scanning electron microscope (SEM, Hitachi SU3900) and an attached energy dispersive X-ray analyser (170 mm^2 Ultim Max EDX) were employed to characterise the morphologies and elemental distribution of samples. Closer magnified details of samples were performed on a transmission electron microscope (TEM, JEOL JEM-2100PLUS). The

quantification of the H_2O_2 product was carried out by a liquid chromatography - mass spectroscopy (LC-MS) technique (Agilent 6545 Accurate-Mass Q-TOF LC/MS system).

6.2.3 Nylon disk substrates for catalysts

The preparation of the Pd@PIM-EA-TB catalyst on a Nylon mesh is the same as in Chapter 5 (see section 5.2.3 for details).

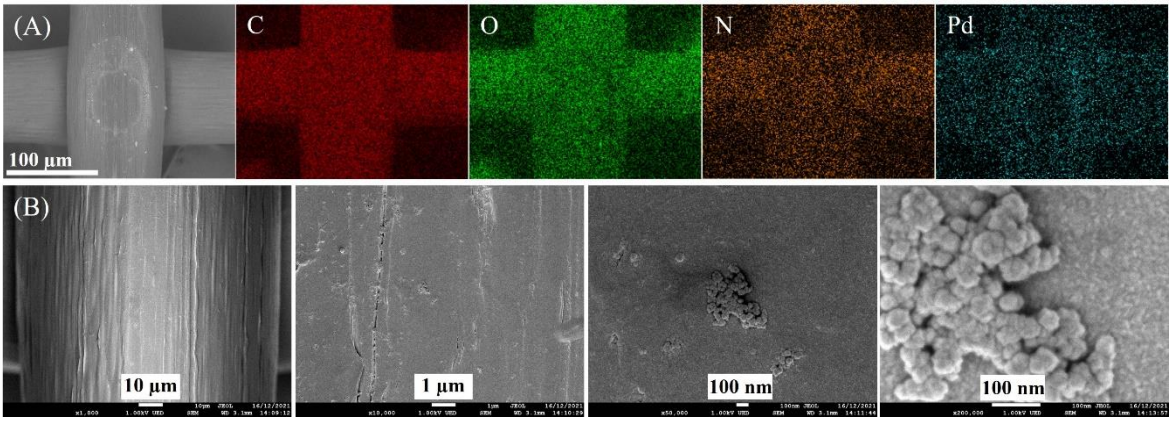

Figure 6.2 (A) Scanning electron microscopy image (SEM, back scatter mode) and EDX mapping for C, O, N, and Pd. (B) Field emission scanning electron microscopy (FESEM) images of the Pd@PIM-EA-TB coated Nylon fibre with 5 nm sputter coated chromium to suppress charging.

Figure 6.2A represents the SEM images and corresponding EDX elemental distribution for the sample of Pd@PIM-EA-TB coated Nylon. Comparison between the location of Nylon mesh and nitrogen distribution shows consistency, meaning PIM-EA-TB film uniformly coated on the Nylon substrate. Also presented is Pd distributed where PIM-EA-TB appears, revealing uniformly distribution of nanoparticles immobilised in PIM-EA-TB. The morphology results from FESEM are shown in Figure 6.2B. The film on the Nylon substrate is assembled by some small particles (tens of nanometres), which are likely to be the aggregation of polymer during coating.

The size and distribution of Pd nanoparticles in the polymer film are measured by TEM. Samples were sonicated in isopropanol in order to isolate Pd@PIM-EA-TB from the Nylon substrate. Results in Figure 6.3 show that the mean particle size of Pd is approximately 3.0 ± 0.1 nm. Nanoparticles are uniformly embedded in the polymer host.

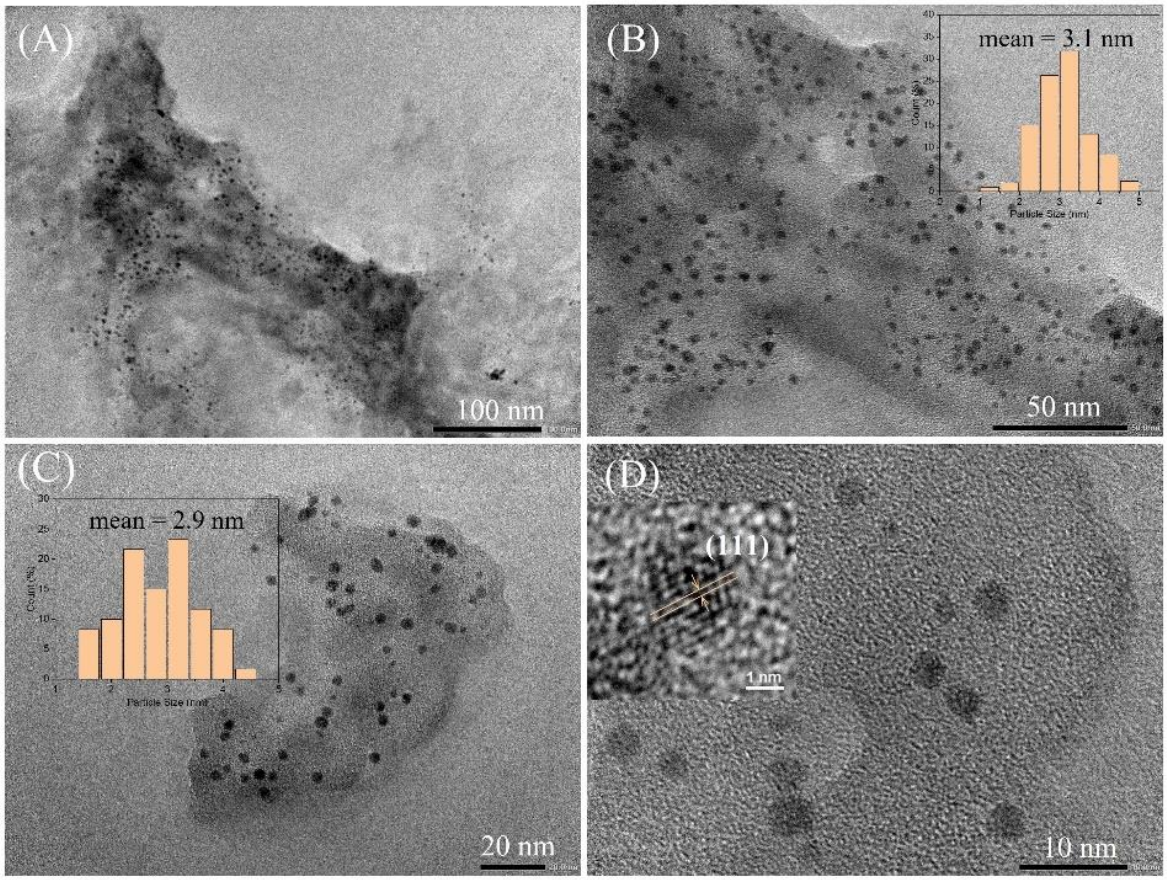

Figure 6.3 Transmission electron microscopy (TEM) images for Pd@PIM-EA-TB. (A) Pd nanoparticles distributed in PIM-EA-TB. (B, C) Higher magnification images show particles with a mean size of 3.0 ± 0.1 nm (insets: size distribution of Pd nanoparticles). (D) High-resolution image showing d-spacing of 0.22 nm indicating the (111) crystal facet of Pd.

6.2.4 Hydrogen Peroxide Detection

The hydrogen peroxide quantification method is the same as the process described in Chapter 5. Briefly, the stoichiometric reaction of H_2O_2 with *p*-nitrophenol boronic acid in alkaline conditions produces *p*-nitrophenol. By quantifying the product of *p*-nitrophenol in the LC-MS system, the concentration of H_2O_2 can be indirectly worked out.

6.2.5 Colorimetric Assay Based on TMB

All colourimetric assays base on TMB were performed in the dark at room temperature. The reagents (TMB, HCOOH/HCOONa, HCl, $HClO_4$, Pd@PIM-EA-TB coated Nylon catalyst) were placed in glass vials (typically 10 mM HCOOH, pH 3.75, 580 μM TMB, 33% DMSO,

with a solution volume of 3 mL in total). Reaction solutions were only put under light for quick photographs at a specific reaction time.

The TMB colour response was amplified by accumulation onto a Nafion-coated filter paper strip. Specifically, the filter paper was cut into a strip (7×1.8 cm^2). The Nafion coating was achieved by stamping a solution of 100 µL with a mixture of 80 wt% Nafion and 20 wt% 1-butanol.

6.2.6 Computational details

A spin-polarised density functional theory (DFT) calculation was developed using the Vienna Ab initio Software Package (VASP [31]) to study the HCOOH decomposition and H_2O_2 formation on Pd particles in the presence and absence of PIM-EA-TB. In order to get an optimum trade-off between an accurate physical model and computational costs, the model considers the most stable palladium surface, Pd(111), and an active PIM-EA-TB fragment based on a monomeric unit. The exchange-correlation contributions were calculated using the generalized gradient approximation (GGA) with the revised functional of Perdew-Burke-Ernzerhof (RPBE [32]). The core electrons were described using the Projected Augmented Wave (PAW) formalism [33], and a kinetic energy cut-off of 450 eV was chosen for the valence electron plane-wave basis set. The Brillouin zone was sampled with a k-spacing of 0.2 $Å^{-1}$. The convergence criteria were set to -0.03 eV $Å^{-1}$ for the ionic and 10^{-5} eV for the electronic threshold. The zero-damping Grimme's empirical correction (D3) accounted for the long-range dispersion interactions. [34] Appropriate dipole corrections were used perpendicular to the surfaces upon molecular adsorptions. The solvent effect of water was calculated by an implicit polarised continuum model (PCM), which describes the interaction between a solvent and a solute in plane-wave DFT [35,36] without adding explicit water molecules to the model.

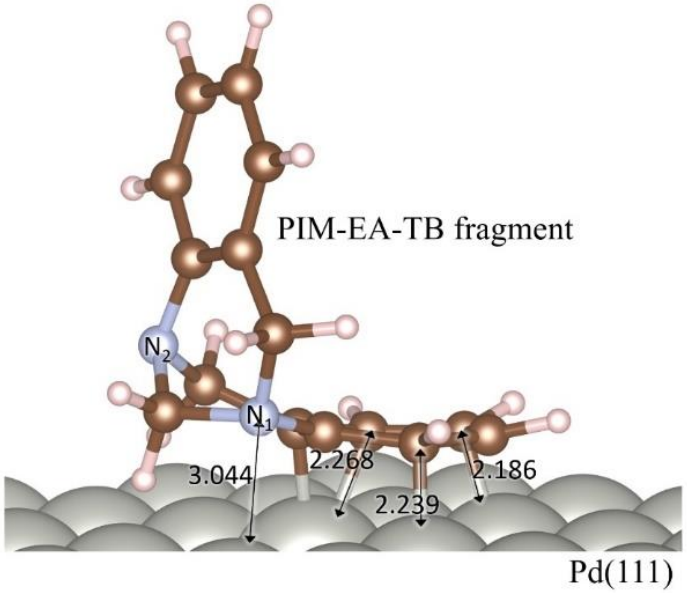

Figure 6.4 Schematic representation of the PIM-EA-TB fragment on its most favourable adsorption configuration on a *p(5×5)* Pd(111) supercell. Distances are given in Å. Grey, brown, pale blue, and white balls indicate Pd, C, N and H atoms, respectively.

A slab model is applied to indicate the Pd surface with a thickness of 5 atomic layers, the bottom 3 layers frozen at the optimised solid lattice, and the top 2 layers free to relax in any direction. For the case of absorbed PIM-EA-TB fragment, the Pd supercell dimension of *p(5×5)* is used, whilst a *p(3×3)* is applied for the case of bare Pd. A vacuum of 15 Å perpendicular to the surface was added to eliminate the interaction between periodic images. Two configurations of PIM-EA-TB fragment absorption on Pd(111) with the ring parallel and perpendicular to the Pd surface have been tested (see Figure 6.5). The configuration with the ring parallel to the Pd surface (Figure 6.4) appears to be an interaction of 0.61 eV, more stable than the perpendicular one. Additionally, isolated molecules are placed in an asymmetric position far enough to cause any spurious interaction with periodic images.

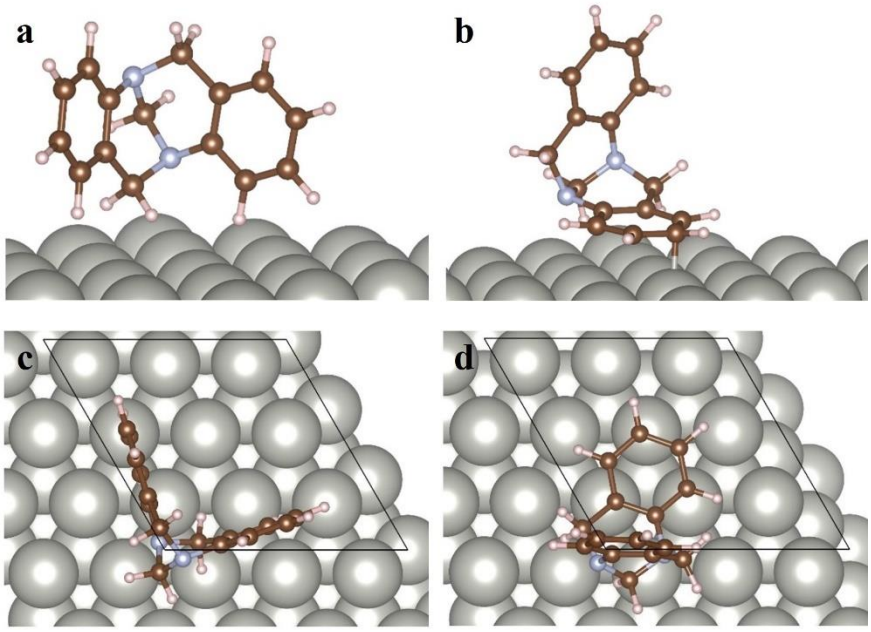

Figure 6.5 Schematic representation of the PIM-EA-TB fragment adsorbed on Pd(111). **a** and **b** show side view of the two configurations tested in a *p(3×3)*. **c** and **d** show the top view of **a** and **b** including the simulation unit cell as the black frame. Grey, brown, pale blue and white balls indicate Pd, C, N and H atoms respectively.

The adsorption energies (E_{ads}) are calculated based on Equation 6.3, where E_{system} is the energy of the adsorbate on the slab, E_{slab} and $E_{molecule}$ are the energy of the clean surface (without PIM-EA-TB) and the energy of the isolated adsorbate.

$$E_{\mathrm{ads}} = E_{\mathrm{system}} - (E_{\mathrm{slab}} + E_{\mathrm{molecule}}) \tag{6.3}$$

The reaction energy of each reaction step (E_R) is defined as the difference between the final and the initial state energies. The climbing-image nudged elastic band (CI−NEB [37,38]) is combined with the improved dimer method to find the saddle points of the transition states (TS) structures, linking the minima across the reaction profile. [39] All states have been characterized using vibrational analysis and confirmed that only TS have a single imaginary frequency. The activation barrier (E_A) is given by the energy difference between the initial and the transition state energies. All energies reported are corrected with the vibrational contribution at zero Kelvin, *i.e.*, at the zero-point energy.

6.3 Results and Discussion

6.3.1 Pd@PIM-EA-TB Reactivity I.: Colorimetric Evidence for Hydrogen Peroxide Production from Formic Acid and Oxygen

Colourimetric assays based on TMB reactivity are usually applied in H_2O_2 sensing. [40] The fundamental mechanism of TMB reactivity has been reported [41] and can be illustrated in a reaction scheme [42] in Figure 6.6A. The oxidation of TMB undergoes two sequential one-electron processes. Colourless TMB is oxidised to the $TMB^{+\bullet}$ radical, which is considered to equilibrate and dimerise (with loss of a proton) into a blue charge transfer complex. The further oxidation step yields a yellow product of the diimine. The yellow product is commonly used to quantify the reaction after the addition of a strong acidic stop solution. Green colour can be observed when both the charge transfer complex and the diamine exist.

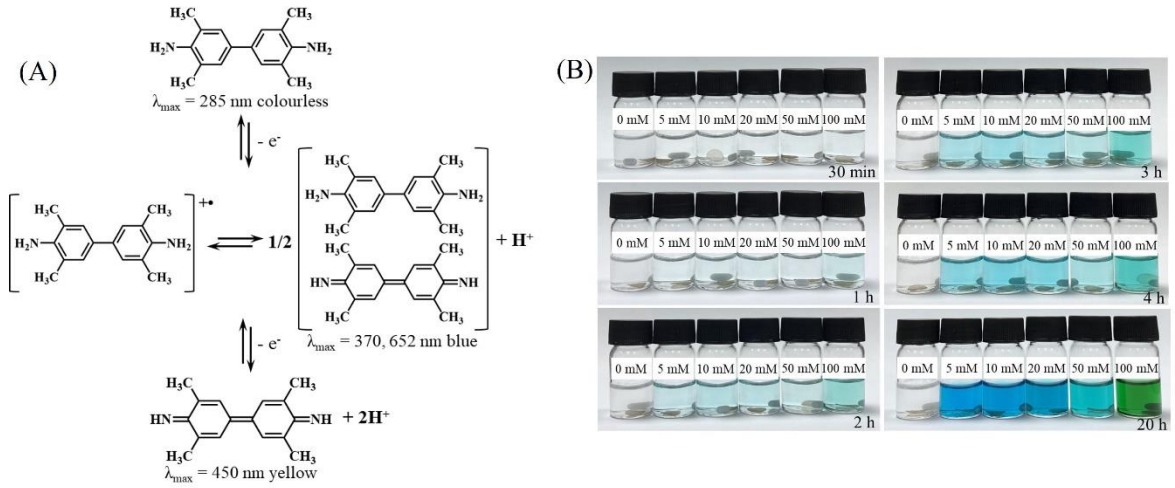

Figure 6.6 (A) Reaction scheme for the TMB colour reaction induced by oxidation. [29] (B) Effect of formic acid concentration on TMB reactivity in the presence of Pd@PIM-EA-TB. Photographs are shown of vials with 580 µM TMB in different concentrations of formic acid ranging from 0 to 100 mM (stirred in the dark, 16 % DMSO to aid solubility) as a function of reaction time.

Figure 6.6B shows the formic acid concentration effect on the TMB colour development over time. Note here that the function of DMSO is to dissolve TMB. The colour response indicates H_2O_2 production at the Pd@PIM-EA-TB catalyst since TMB concentration stays constant. Both formic acid concentration and pH can affect the reaction process. A strong blue colour response occurs at approximately 10 mM formic acid concentration. The Pd catalyst may play a role in several of the reaction steps. There are reports about Pd [43] or other

catalysts [44] presenting peroxidase reactivity towards the reaction of TMB with H_2O_2. However, the molecular size of TMB is considerable relative to the micropores of PIM-EA-TB. Therefore, the permeation of TMB and relative products into the microchannels of PIM-EA-TB seems remarkably difficult. In fact, the Pd catalysis effect for TMB oxidation can be excluded by the following experiments.

The effect of solution pH has been explored (see Figure 6.7A) by employing solutions of 10 mM HCOOH/HCOONa with varied pH values. A significant blue colour response occurs at pH 3 and 3.5. This result verifies that both formic acid concentration and pH influence the overall catalytic reaction. An acidic condition with a pH value between 3 and 4 is most effective.

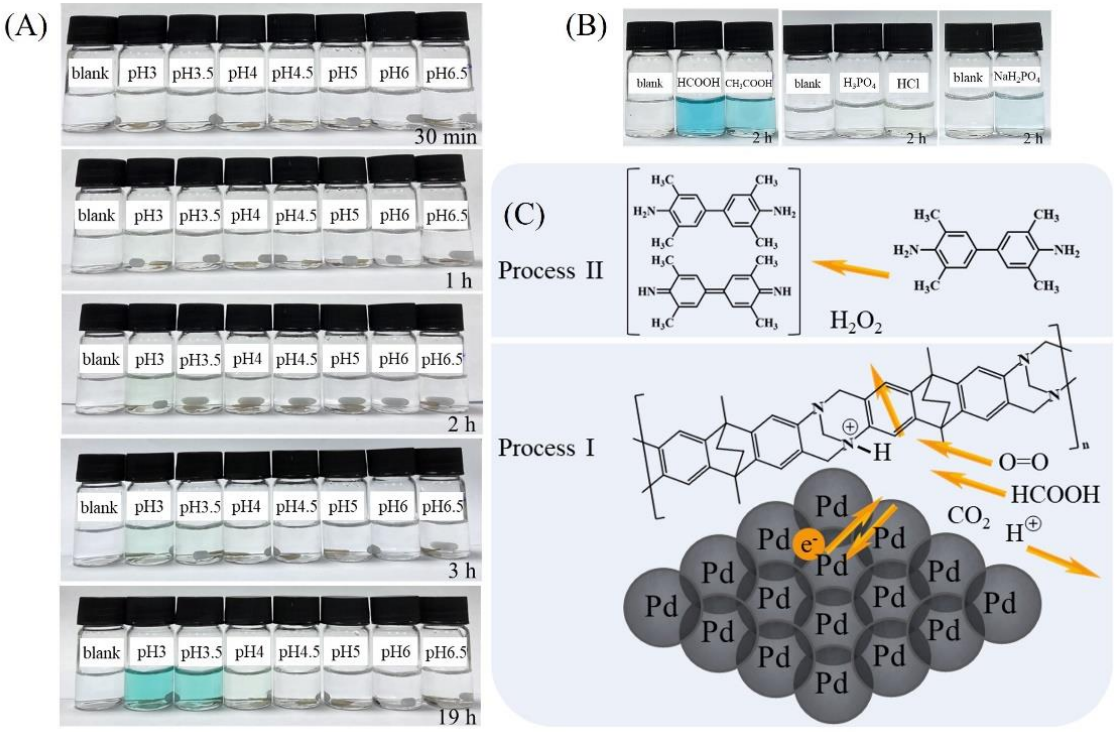

Figure 6.7 (A) Effect of pH values on TMB reactivity. Photographs of 580 µM TMB in 10 mM HCOOH/HCOONa with a pH value ranging from 3 to 6.5 in the presence of Pd@PIM-EA-TB (stirred in the dark, 16% DMSO) as a function of reaction time. (B) Effect of acids on H_2O_2 catalysis for TMB. Photographs of 580 µM TMB in 10 mM H_2O_2 in the presence of 10 mM formic, acetic, perchloric, phosphoric, hydrochloric acid, and 10 mM NaH_2PO_4 (reaction time 2 h, no catalyst, 16% DMSO to aid solubility). (C) Illustration of the TMB oxidation process in the presence of Pd@PIM-EA-TB and HCOOH: Pd catalysed formation of H_2O_2 (Process I) followed by homogeneous oxidation of TMB (Process II).

Next, the effect of different acids on the oxidation of TMB by H_2O_2 is studied without the Pd@PIM-EA-TB catalyst. Figure 6.7B shows clear reactivity for TMB and H_2O_2 in formic acid and acetic acid solution, possibly due to the formation of peroxoformate or peroxoacetate. Peroxoformic acid for epoxidation reaction is generated by combining HCOOH and H_2O_2 in an equilibrium. [45,46] The oxidation reactivity of TMB by H_2O_2 is less obvious in perchloric, hydrochloric, or phosphoric acid. Although there is a weak colour response in NaH_2PO_4 (pH 4.5), the mechanism details stay unclear. These tests result proposes that TMB does not have to permeate through micropores to interact with the Pd@PIM-EA-TB catalyst to give a colour reaction. Therefore, the overall reaction can be dissected as two separated processes (Figure 6.7C): (**Process I**) the generation of H_2O_2 driven by the catalyst Pd@PIM-EA-TB, and (**Process II**) homogeneous oxidation of TMB by H_2O_2. Next, the **Process I** is studied individually for the formate oxidase reactivity of Pd@PIM-EA-TB in the absence of TMB.

6.3.2 Pd@PIM-EA-TB Reactivity II.: Formate Oxidase Reactivity

The H_2O_2 production from formic acid on Pd@PIM-EA-TB is systematically investigated. Figure 6.8A shows that the generation of H_2O_2 on Pd catalyst in 20 mM HCOOH is adequate, and the reaction rate is constant within 3 h under stirring. The formic acid concentration effect (Figure 6.8B) demonstrates a "switch-on" effect at about 10 mM HCOOH, with the H_2O_2 production rate approaching a plateau at higher formic acid concentrations. Here, the H_2O_2 production reaching a plateau could be related to (i) a kinetic limit in Pd@PIM-EA-TB due to Michaelis-Menten effects or mass transport in micropores; or (ii) the pH effect in the solution. Accordingly, the effect of formic acid concentration at fixed pH of 3.75 is explored. Data in Figure 6.8C illustrates that the H_2O_2 production is a first-order reaction which is not limited at constant pH. Consequently, the plateau in Figure 6.8B must be linked to the pH effect instead of kinetic. The catalytic process for H_2O_2 production is likely to be associated with the protonation of PIM-EA-TB ($pKA \approx 4$ [17]) triggers the enhancement of the catalytic reaction.

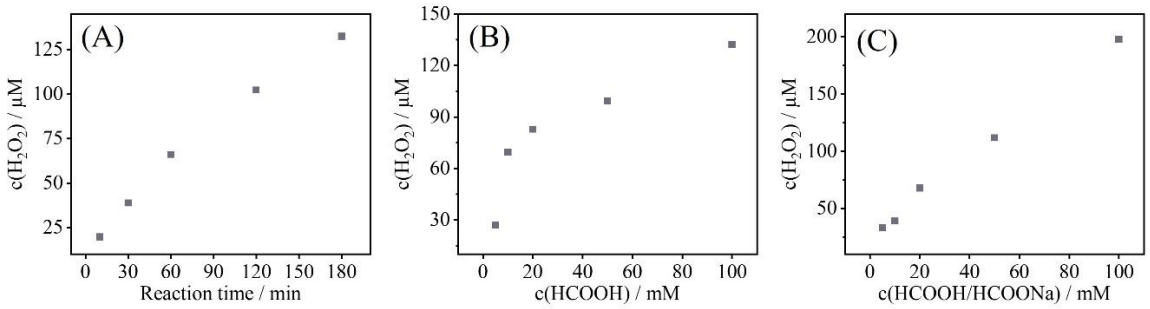

Figure 6.8 (A) Plot of H_2O_2 concentration as a function of time (one Nylon disk modified with Pd@PIM-EA-TB in 10 mL stirred solution) for 20 mM formic acid concentration. (B) A plot of H_2O_2 concentration after 2 h reaction (one Nylon disk modified with Pd@PIM-EA-TB in 2 mL stirred solution) as a function of formic acid concentration. (C) A plot of H_2O_2 concentration after 2 h reaction (one Nylon disk modified with Pd@PIM-EA-TB in 2 mL stirred solution) as a function of formic acid concentration at fixed pH of 3.75.

The data verifies that the Pd@PIM-EA-TB catalyst can drive H_2O_2 production from the formic acid solution, and the pH plays a considerable role in the reaction rate. The important processes that happen at the confined Pd catalyst here are (i) the consumption of O_2, (ii) the production of H_2O_2, (iii) the formation of H_2O, and (iv) the generation of H_2 and CO_2 from HCOOH (see Figure 6.9A). Both O_2 consumption and H_2 production can be monitored with a Clark sensor. [19] The configuration of a commercial Clark probe is illustrated in Figure 6.1A, where the catalyst coated Nylon disk is attached to the Teflon membrane outer surface. By applying different potentials, oxygen (-0.7 V *vs*. Ag/AgCl) and hydrogen (+0.6 V *vs*. Ag/AgCl) detection is achieved.

Figure 6.9B shows data for oxygen consumption (negative, grey current data) and hydrogen production (positive, green current data). When testing the formate/formic acid concentration effect at a fixed pH of 3.75, a transition at a concentration of approximately 10 mM is observed for both oxygen consumption (with reaching a plateau at higher concentrations) and hydrogen production (with enhanced production at higher concentrations). Oxygen is not fully consumed by the Pd@PIM-EA-TB catalyst when hydrogen is observed. Considering the processes at the catalyst, there probably be a balance of H_2O_2, H_2O, and H_2 production. In contrast to the catalysis process happening under stirring when the catalyst disk is floating in the solution, at the Clark sensor, the solution is stagnant, which means slower oxygen transport. Therefore, hydrogen production is more likely happening at the Clark probe instead of in the stirred solution. When detecting H_2O_2

in a stirred solution, it should ultimately cease at higher formic acid concentrations beyond the range (higher than 100 mM) shown in Figure 6.8C.

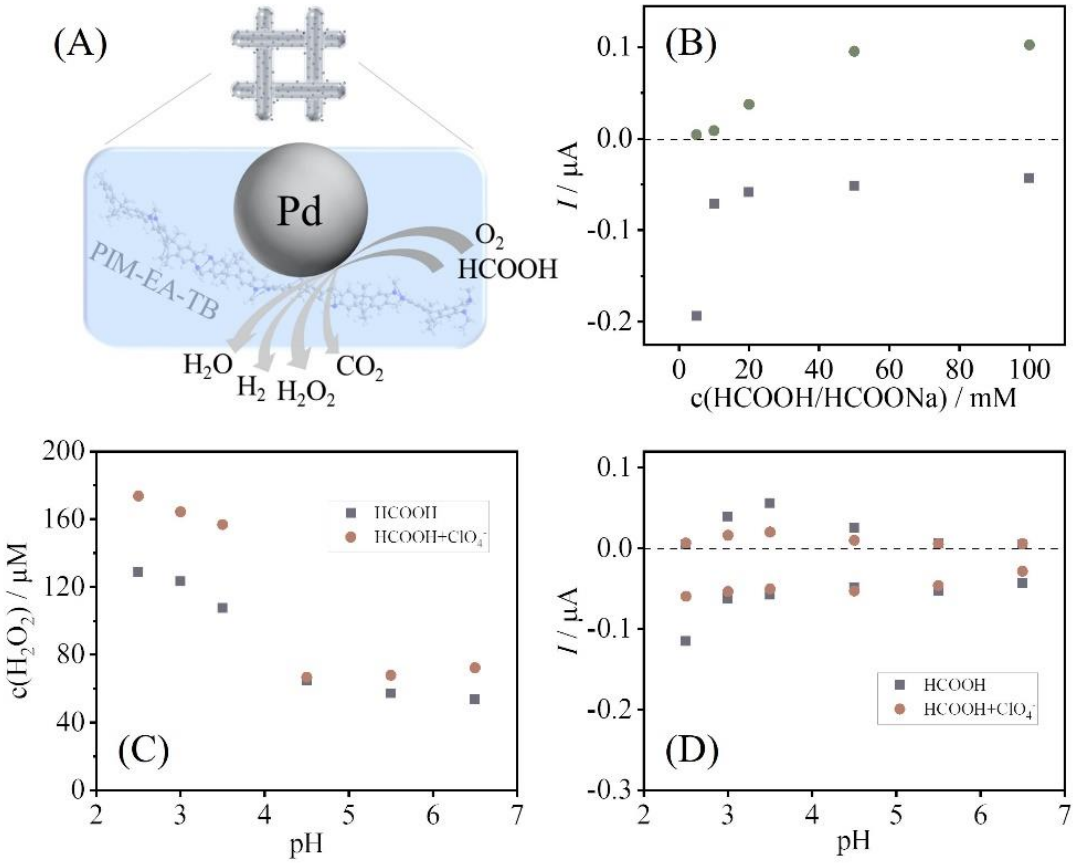

Figure 6.9 (A) Schematic reactions at Pd nanoparticles. (B) Effect of concentration of HCOOH at a fixed pH of 3.5 on H_2 and O_2 levels. A plot of approximate Clark probe H_2 response (green) and O_2 consumption response (grey) *versus* formic acid concentration at pH of 3.75. (C) A plot of H_2O_2 concentration formed at Pd@PIM-EA-TB in the presence of 50 mM HCOOH (or HCOONa) with/without 50 mM $HClO_4$ (or $NaClO_4$) as a function of pH. Data sets for 2 mL stirred solution without ClO_4^- (grey), with ClO_4^- (red) after 2 h reaction time. (D) A plot of Clark probe H_2 and O_2 responses in the presence of 50 mM HCOOH (or HCOONa) with (red) or without (grey) 50 mM ClO_4^- as a function of pH.

Next, the Clark probe data for the pH effect from 50 mM formate/formic acid are presented in Figure 6.9D. The oxygen consumption stays relatively constant over the pH range of 2.5 to 6.5. However, hydrogen production reaches the maximum between pH 3 and pH 4. That is, moderate acidity is favourable to hydrogen generation, but the solution with a pH less than 3 can suppress hydrogen formation. The overall occasion is complex but could be considered as the effect of microporous PIM-EA-TB confining the space around the

palladium nanoparticles. Specifically, oxygen reduction is favoured by the protonation of PIM-EA-TB, providing a catalytic reaction site in the vicinity of the proton. However, the reaction of formic acid requires binding to the amine site of PIM-EA-TB and accepting a proton to produce hydrogen and carbon dioxide. The presence of other anions such as perchlorate could affect the binding ability of PIM-EA-TB towards proton and/or formic acid. So, perchlorate is added to the reaction solution to probe the catalytic "cavity effects" of Pd@PIM-EA-TB.

The addition of perchlorate is employed as a probe to explore the effects of the PIM-EA-TB protonation on catalytic formate oxidase reactivity. Perchlorate is reported to be readily incorporated into PIM-EA-TB during the protonation of amine sites. [47] Therefore, one would expect that the protonation of PIM-EA-TB will be enhanced by perchlorate, whilst the binding of formic acid will be suppressed. Figure 6.9C shows the effect of perchlorate on H_2O_2 production from formate/formic acid solutions with varied pH. A significant enhancement of H_2O_2 production by perchlorate occurs at pH $\leq$ 4, whereas a minimal difference is observed when the pH of the solution is greater than 4. These results are consistent with the fact that protonation of PIM-EA-TB occurs at pH $\leq$ 4. The presence of perchlorate results in a higher population of protonated amine sites without coordination of formate ions. Accordingly, the positive charge on protonated amines can promote the oxygen reduction into H_2O_2, while less bound formate leads to lower hydrogen production, as evidenced in Figures 6.9C and D.

When diving into more details in the Clark probe data of hydrogen production (positive data in Figure 6.9D), the presence of perchlorate clearly causes suppressed hydrogen production in the pH range of 3 to 4. This effect of perchlorate could be a further verification of protonated amines in PIM-EA-TB contributing to the catalytic mechanism. Since it is difficult to determine the conditions in the micropores of the catalyst experimentally, a DFT "cavity model" analysis is employed to envisage better the catalytic reactions of H_2O_2 and H_2 formation in the Pd@PIM-EA-TB catalyst.

6.3.3 Pd@PIM-EA-TB Reactivity III.: Nanozyme Cavity Effects probed by DFT

A computational DFT mechanistic study is developed at the PIM-EA-TB/Pd(111) interface to unravel further kinetic aspects for the H_2O_2 production and dehydrogenation of formate/formic acid. A model of the PIM-EA-TB fragment with the Pd(111) surface was

selected (Figure 6.4). The interaction between the PIM-EA-TB fragment and Pd surface shown here is discovered to be the most stable configuration with an adsorption energy of -2.09 eV in the p(5×5) supercell. Even though both nitrogen atoms in the PIM-EA-TB fragment structure can be protonated, N_1 (see Figure 6.4) protonation/hydrogenation is more favourable with protonation energy of -0.51 eV compared to that of N_2 (0.16 eV more difficult). Note that in the DFT model, protonation is equivalent to hydrogenation with the electron going into the Pd slab. In fact, the formation of N_1H^+ is as favourable as hydrogenating the pristine Pd(111) surface (E_{ads} = -0.51 eV). Therefore, the N_1 is considered as the active amine site for both catalytic O_2 hydrogenation and HCOOH dehydrogenation reactions.

Oxygen Reduction to H_2O_2. The protonated amine site in the PIM-EA-TB fragment (see Figure 6.10**a**) is applied as the starting point of the simulation for the co-adsorption of molecular O_2 on the Pd(111) surface. The molecular O_2 adsorption is energetically favourable with E_{ads} = -0.67 eV. As the O_2 molecule reaches the protonated N1, the adsorption process becomes more exothermic with E_{ads} = -0.80 eV at 2.637 Å from N1H (Figure 6.10**b**). The O-O stretching mode (ν_{O-O}) alters from 1563.4 cm^{-1} in the gas phase to 918.9 cm^{-1} when O_2 is co-adsorbed at 3.061 Å from N_1H and finally gets to 865.9 cm^{-1} in intermediate **b**. The first hydrogenation of adsorbed O_2 (Figure 6.10**c**) occurred after overcoming activation energy of 0.15 eV (E_R = -0.09 eV), lowering the ν_{O-O} to 532.5 cm^{-1}. The moderate acidic solution (pH 3 to 4) regenerates N_1H (Figure 6.10**d**) upon taking activation energy of 0.11 eV. A slightly endothermic second hydrogenation generates H_2O_2. The adsorbed H_2O_2 (Figure 6.10**e**) shows a stretching frequency of 718.1 cm^{-1} and is located at -1.37 eV below the energy reference (*i.e.*, PIM-EA-TB fragment, molecular hydrogen, and molecular oxygen). H_2O_2 requires energy of +0.72 eV to desorb from the PIM-EA-TB fragment/Pd(111) surface. The gas phase H_2O_2 displays an O-O distance of 1.492 Å with O-O stretching of 890.6 cm^{-1}, which is consistent with the benchmark (1.475 Å and 877 cm^{-1}).[48,49]

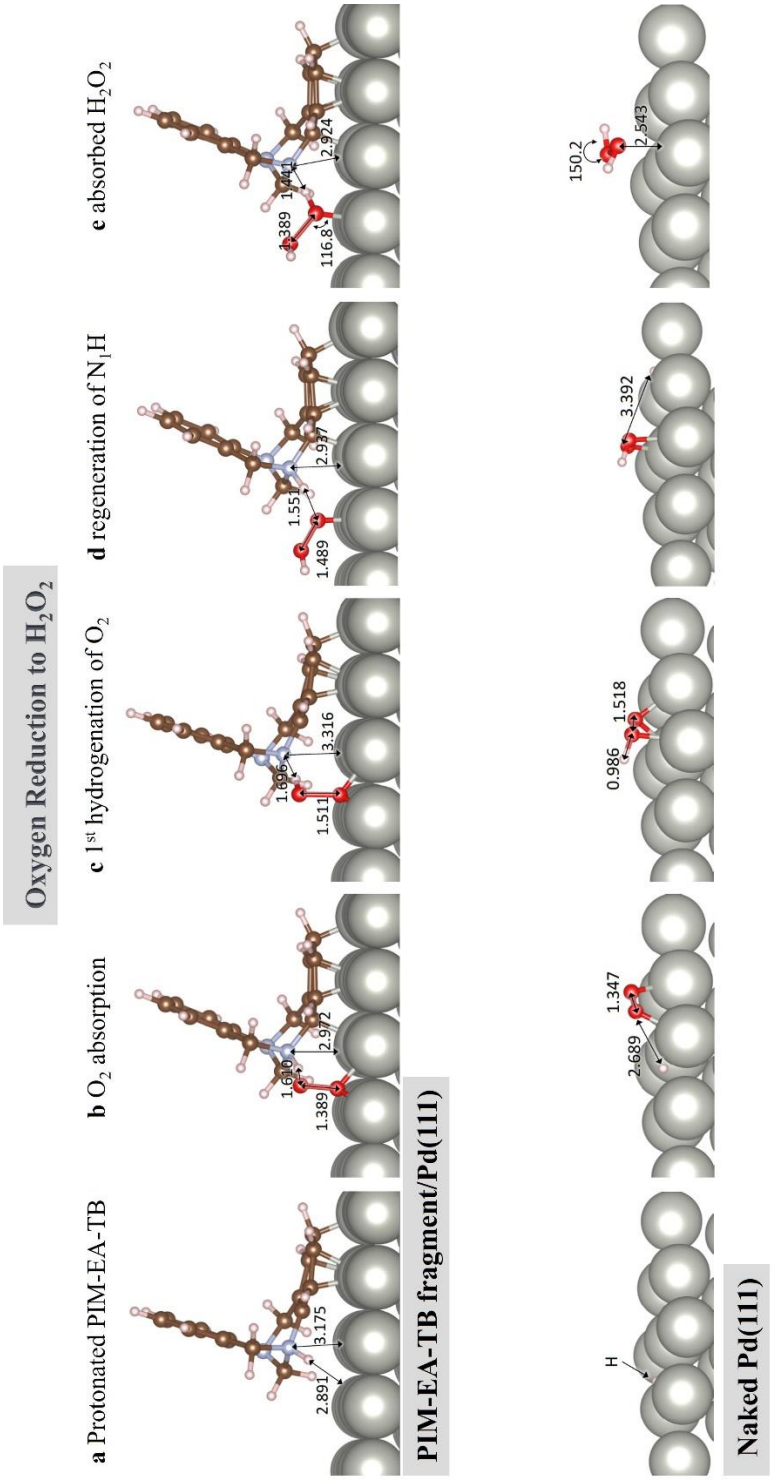

Figure 6.10 Schematic representation of the key structures along the H_2O_2 formation (left) assisted by the PIM-EA-TB fragment/Pd(111) and (right) on naked Pd(111). Inset distances and angles are in Angstroms and degrees respectively. Grey, brown, pale blue and white balls indicate Pd, C, N and H atoms respectively.

The computational model emphasizes on the function of PIM-EA-TB in the catalytic process; therefore, the case of catalysis formation of H_2O_2 on pristine Pd(111) has been calculated

using the same computational method. The optimised structures are depicted in Figure 6.10, labelled with critical interatomic distances and angels. The results agree well with previous computational reports taking into account the differences in functional and long-range energy contributions. [50] Table 6.1 lists and compares the energies along the reaction pathway with or without the presence of PIM-EA-TB. Figure 6.11 shows the energy profile of the O_2 adsorption and hydrogenation to form H_2O_2.

Table 6.1 DFT data for activation (E_A) and reaction (E_R) energies for the H_2O_2 formation on PIM-EA-TB fragment/Pd(111) and on pristine Pd(111). Note that "*" indicates bound species.

	PIM$_f$/Pd(111)		**Pd(111)**	
	E_A /eV	E_R /eV	E_A /eV	E_R /eV
$O_2(g) \rightarrow O_2^*$	--	-0.80	--	-0.56
$O_2^* + H^* \rightarrow HOO^*$	0.15	-0.09	0.66	-0.26
$HOO^* \rightarrow HOOH^*$	0.11	0.04	0.75	-0.11
$HOOH^* \rightarrow H_2O_2(g)$	--	+0.72	--	+0.35

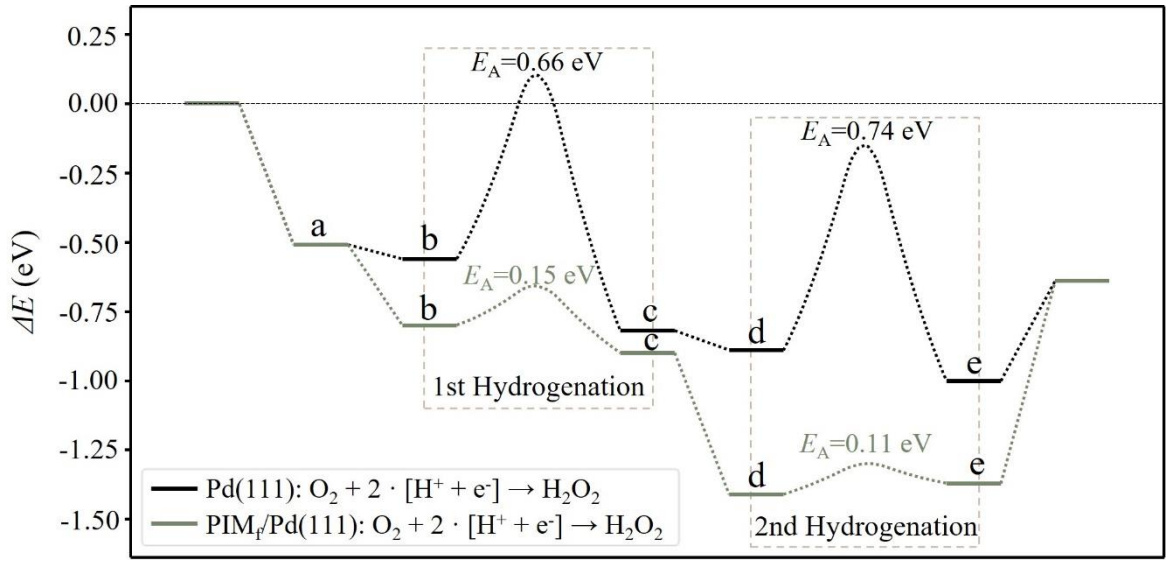

Figure 6.11 Energy profile for the formation of H_2O_2 from O_2 on pristine Pd(111) and PIM-EA-TB fragment/Pd(111). Inset values indicate the activation energies (E_A) of elementary steps. Letters **a-e** represent the surface intermediates as depicted in Figure 6.10. The last step indicates the H_2O_2 energy in the gas phase relative to reactants.

The presence of PIM-EA-TB on the Pd surface significantly stabilises the co-adsorption of molecular oxygen (**b**), the HOO intermediates (**c** and **d**), and H_2O_2 (**e**), leading to lower hydrogenation energy barriers compared to those on pristine Pd(111) by > 0.5 eV as summarised in Figure 6.11. The DFT calculation results suggest that the immobilisation and dispersion of Pd nano-catalysts in the microporous PIM-EA-TB facilitates the production of H_2O_2. The side reactions of H_2O_2 decomposition, which may also be affected by the presence of PIM-EA-TB, are not included in the calculation.

Formic acid Dehydrogenation to CO_2. Computational DFT calculations are carried out to reveal the role of PIM-EA-TB on formic acid decomposition. Similarly, the protonation of N_1 in the PIM-EA-TB fragment is considered for further mechanism study on the formic acid dehydrogenation on Pd. The HCOOH decomposition on Pd catalyst is commonly believed to take two different pathways generating either CO_2 (Pathway 1, Equation 6.4) or CO (Pathway 2, Equation 6.5). [51-53]

$$Pathway\ 1: \quad HCOOH \rightarrow CO_2 + H_2 \quad \Delta G = -48.4\ kJ\ mol^{-1} \tag{6.4}$$

$$Pathway\ 2: \quad HCOOH \rightarrow CO + H_2O \quad \Delta G = -28.5\ kJ\ mol^{-1} \tag{6.5}$$

The acidic form of HCOOH (see Figure 6.12**a**) is employed as the starting point of the formic acid decomposition process, even though the behaviour of formic acid can be different as pH varies. The HCOOH molecule transfers a proton exothermically to the amine group (N_1) of the co-adsorbed PIM-EA-TB fragment (E_R = -0.52 eV) or the pristine Pd (111) surface (E_R = -0.11 eV) for the case in the absence of PIM-EA-TB. As a result, formate (HCOO*) is left on the Pd surface (Figure 6.12**b**). In fact, there could be two ways for HCOOH to lose a proton: breaking from the O-H bond leading to HCOO* and delivering the proton from the H-C bond resulting in carboxylic surface species (COOH*, Figure 6.12**c**). Both intermediates are investigated in terms of their formation and decomposition. Table 6.2 summarises the activation and reaction energies of the formic acid dehydrogenation processes. The atomic representation of key structures along the HCOOH decomposition process is illustrated in Figure 6.12.

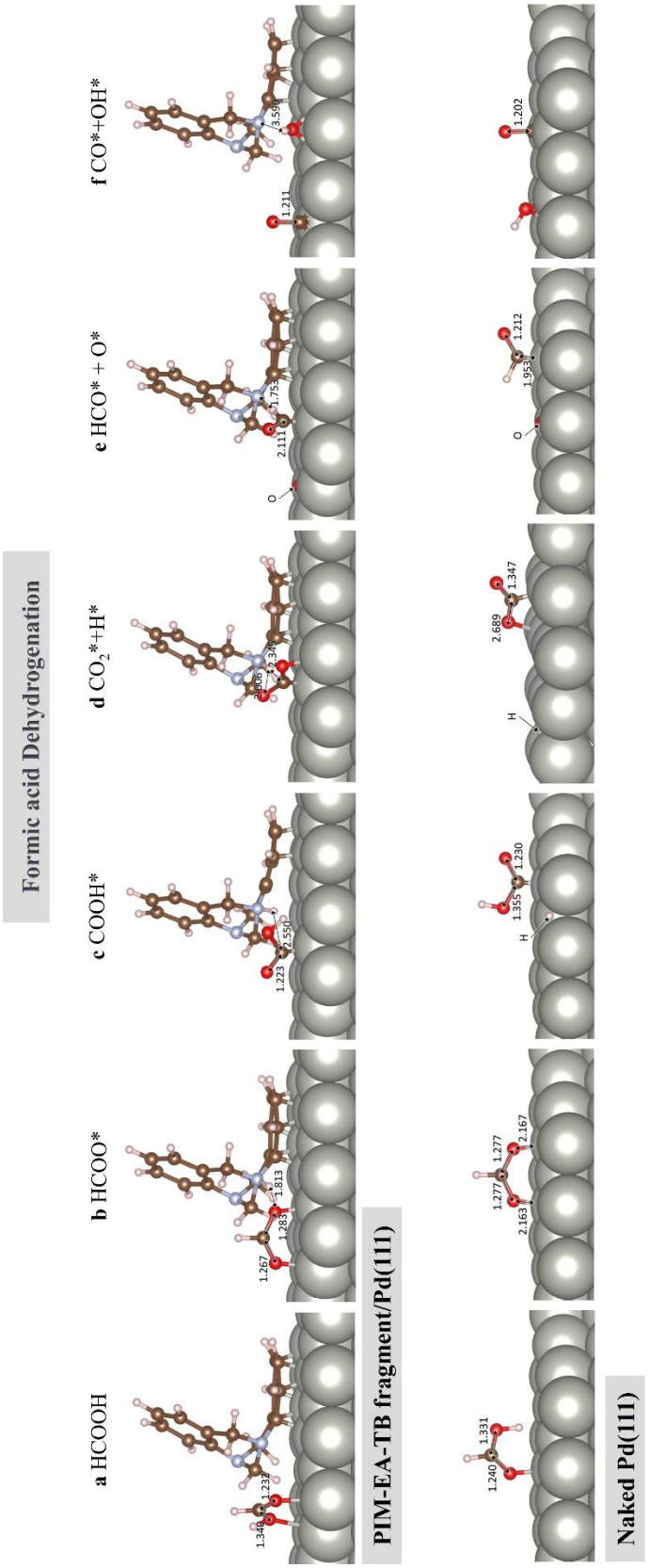

Figure 6.12 Schematic representation of the key structures along the HCOOH decomposition process (left) assisted by the PIM-EA-TB fragment/Pd(111) and (right) on naked Pd(111). Inset distances are in Angstroms. Grey, brown, pale blue and white balls indicate Pd, C, N and H atoms respectively.

Table 6.2 Summary of DFT data for activation (E_A) and reaction (E_R) energies for the HCOOH decomposition on PIM-EA-TB fragment/Pd(111) and pristine Pd(111). The ‡ subscript indicates that the H transferred to the Pd(111) surface or the PIM-N_1. Note that "*" indicates bound species.

	PIM-EA-TB fragment/Pd(111)		**Pd(111)**	
	E_A /eV	E_R /eV	E_A /eV	E_R /eV
$HCOOH(g) \rightarrow HCOOH^*$	--	-0.35	--	-0.41
$HCOOH^* \rightarrow HCOO^* + H^{*‡}$	0.02	-0.52	0.23	-0.11
$HCOO^* \rightarrow CO_2^* + H^{*‡}$	0.42	-0.65	0.75	-0.45
$HCOO^* \rightarrow HCO^* + O^*$	1.65	+0.79	1.67	+1.05
$HCOOH^* \rightarrow COOH^* + H^{*‡}$	0.76	-0.44	0.61	-0.25
$COOH^* \rightarrow CO_2^* + H^{*‡}$	0.19	-0.15	0.73	+0.02
$COOH^* \rightarrow CO^* + OH^*$	0.88	-0.25	0.83	-0.26

The intermediate HCOO* (**b**) decomposes into adsorbed CO_2* + H* (**d**) in the presence of the PIM-EA-TB fragment by overcoming activation energy of 0.42 eV (E_R = -0.65 eV). It is unlikely that **b** dissociates to HCO* + O* (**e**) because of higher activation energy and endothermic property; further dehydrogenation of **e** would result in CO*. Similarly, the carboxylic surface species COOH* (**c**) is likely to overcome activation energy of 0.19 eV and generate **d** rather than CO* + OH* (**f**), which requires energy of 0.88 eV. The formation of **f** is kinetically unfavourable even though it shows slightly more exothermic than the formation of **d**.

For the catalytic process that occurs on the naked Pd(111) surface, the decomposition pathways of HCOO* (**b**) and COOH* (**c**) are the same as those on the PIM-EA-TB fragment/Pd(111). Formate (**b**) leads to CO_2* + H* (**d**) because HCO* + O* (**e**) is energetically inhibited (Figure 6.14). However, the CO* formation from **c** shows a higher energy barrier of only 0.01 eV but slightly endothermic formation energy exothermic compared to the formation of **f**. So, these two processes compete with each other. Figures 6.13A and B depict the energy differences of the reaction processes with or without the presence of PIM-EA-TB. The overall reaction pathway of formic acid dehydrogenation in

the presence of PIM-EA-TB is likely to be O-H dehydrogenation followed by C-H dehydrogenation.

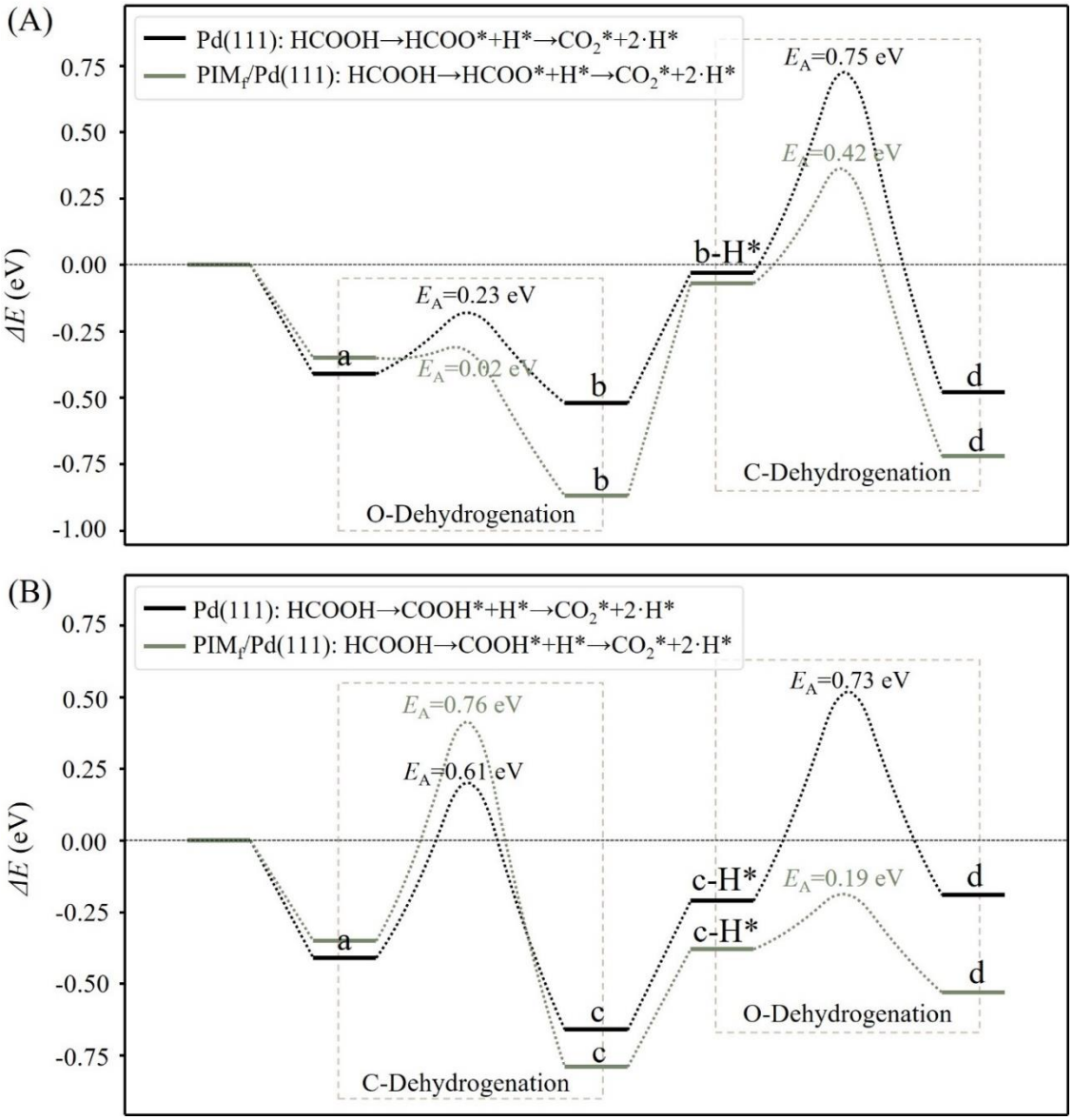

Figure 6.13 Energy profiles for HCOOH decomposition to CO_2* and 2·H* on pristine Pd(111) and on PIM-EA-TB fragment/Pd(111). (A) Energy profiles for C-H dehydrogenation followed by O-H dehydrogenation. (B) Energy profiles for O-H dehydrogenation followed by C-H dehydrogenation. Inset values indicate the activation energies (E_A) of elementary steps. Letter **a-d** represents the surface intermediates as depicted in Figure 6.12. Note that "*" indicates bound species.

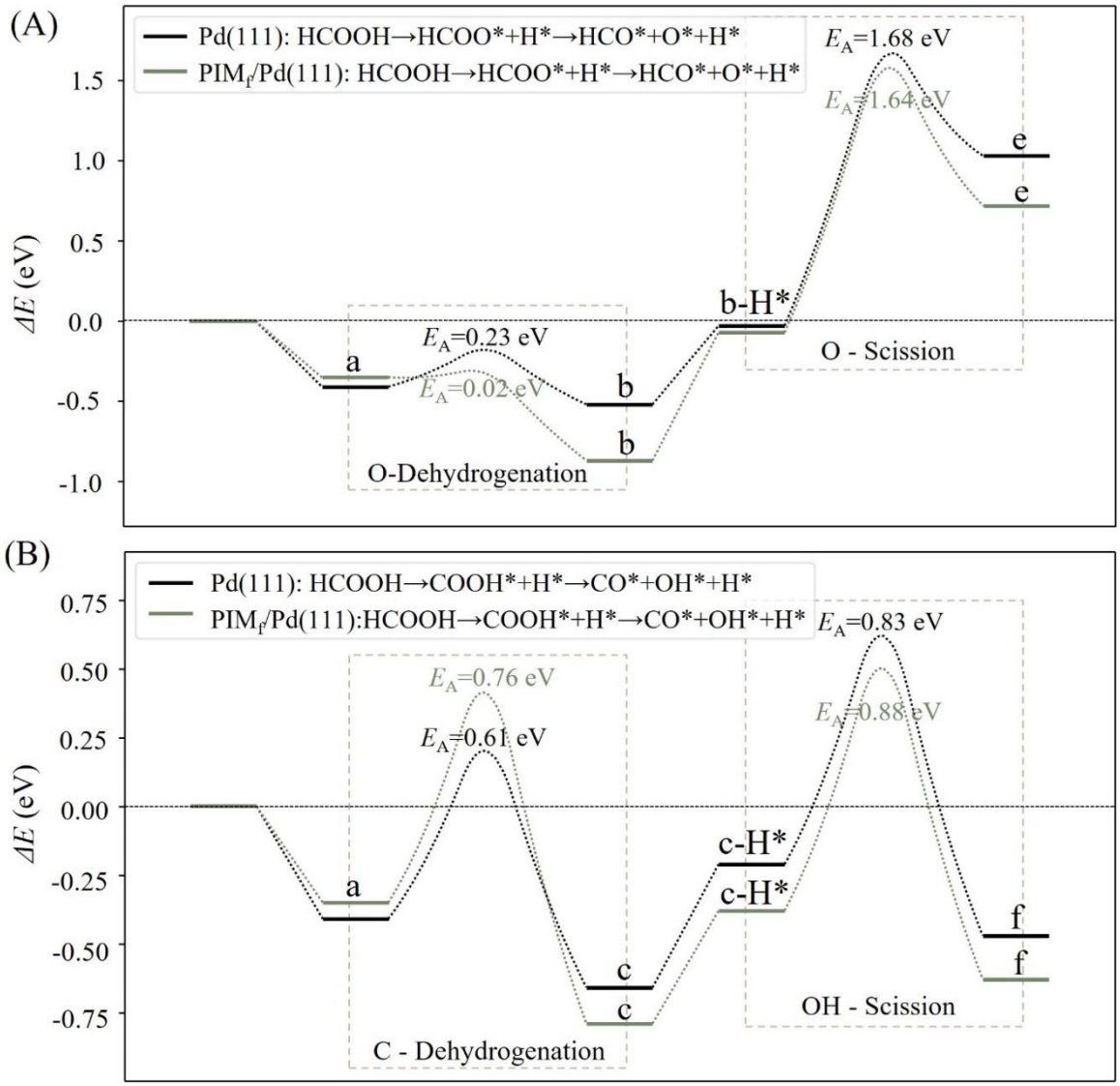

Figure 6.14 Energy profile for HCOOH decomposition on pristine Pd(111) and PIM-EA-TB fragment/Pd(111), a model of Pd particles intercalated in the PIM microporous structure. Pathway (A) goes through the COOH* intermediate while (B) goes through HCOO* one. Inset values indicate the activation energies (E_A) of each elementary step. Letter **a-f** represents the surface intermediates depicted in Figure 6.12.

The absorbed CO on the palladium catalyst surface shows a notorious poison effect causing deactivation of the catalyst. However, no deterioration is observed in the experiments studied here with Pd@PIM-EA-TB. The calculation data demonstrate that the microporous structure created by PIM-EA-TB surrounding Pd nano-catalysts (i) enhances the HCOOH decomposition to H_2 and CO_2, and (ii) promotes the mechanistic reaction generating CO_2 (Pathway 1) and suppresses the formation of CO (Pathway 2).

6.3.4 Pd@PIM-EA-TB Reactivity IV.: TMB Oxidation in the Presence of Perchlorate

Having studied **Process I** and **Process II** (see Figure 6.7C) individually, the next step is to re-inspect the TMB colourimetric reactivity driven by H_2O_2 generation. Figure 6.15 shows data of comparison for TMB reaction with intentionally added H_2O_2 in the absence of catalyst or with generated H_2O_2 by Pd@PIM-EA-TB catalyst. For the case without the catalyst, H_2O_2 is added at a level to mimic the catalytic reaction (Figure 6.15A). The evident TMB blue colour is observed in formate/formic acid solution at concentrations higher than 10 mM at a pH of 3.75. The same reaction in the presence of Pd@PIM-EA-TB (Figure 6.15B) gives a similar colour pattern at formate/formic acid concentration of less than 20 mM, but a loss of TMB oxidation when going to higher concentrations of 50 or 100 mM. The production of H_2O_2 should still be going under these conditions, but the negative Galvani potential of Pd catalyst and a possible trace of Pd^{2+} in the solution could affect the oxidation of TMB at higher formate/formic acid concentrations.

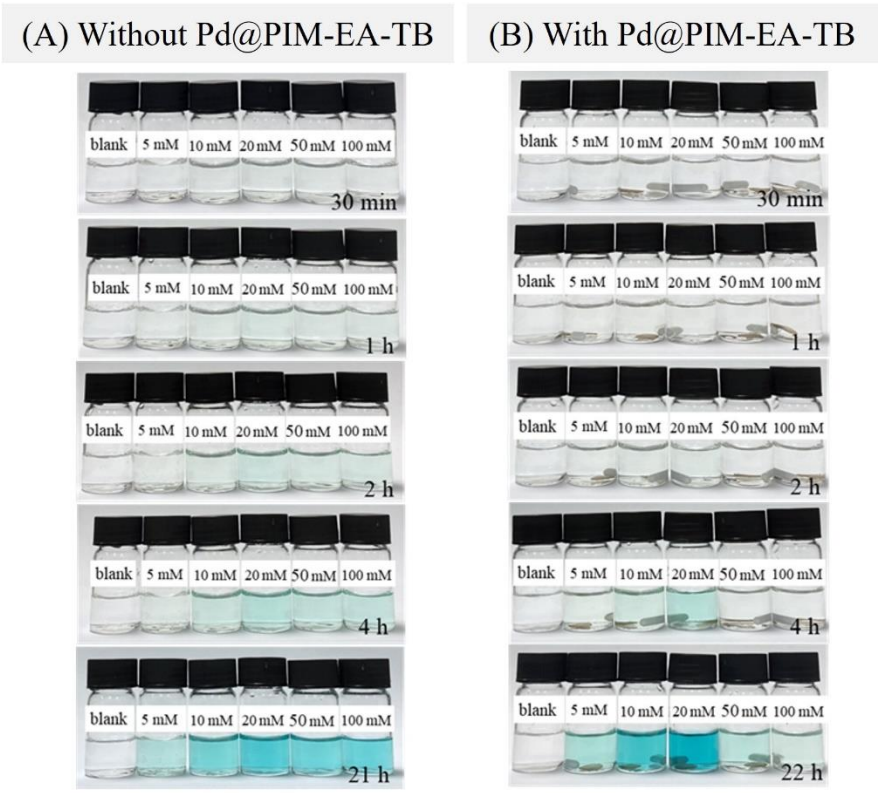

Figure 6.15 (A) Effect of HCOOH/HCOONa concentration at pH 3.75 on TMB reactivity. Photographs of 580 µM TMB in the absence of Pd@PIM-EA-TB (stirred in the dark, 33% DMSO) as a function of reaction time. H_2O_2 was added to reflect reactivity as in data presented in Figure 6.8C: blank: no H_2O_2, 5 mM: 33 µM, 10 mM: 41 µM, 20 mM: 59 µM, 50 mM: 111 µM, 100 mM: 198 µM H_2O_2. (B) Photographs of 580 µM TMB in the presence of Pd@PIM-EA-TB (stirred in the dark, 33% DMSO) as a function of reaction time. H_2O_2 was generated *in situ*.

The TMB reaction as a function of pH is also examined in the presence of Pd@PIM-EA-TB. Figure 6.16B illustrates the blue-green colour (combination of blue mono- and yellow di-oxidised TMB) when the solution pH is between 2.5 and 3.5. Less acidic solutions yield a relatively small amount of H_2O_2; thus, the colour is not shown. In the presence of perchlorate, a similar pattern of TMB oxidation reactivity appears (Figure 6.16A). The blue colour is clearer with some precipitate existing, which is likely to be the blue colour TMB dimer salt containing perchlorate.

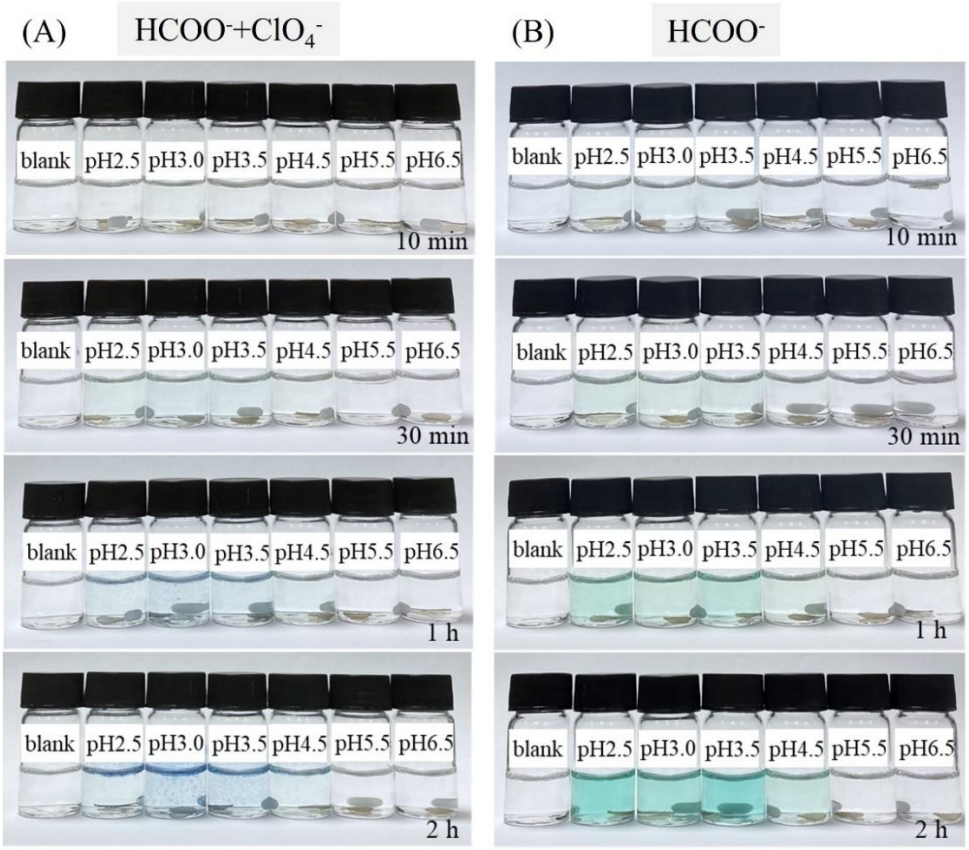

Figure 6.16 Effect of 50 mM ClO_4^- for 50 mM HCOOH/HCOONa concentration at pH 3.75 on TMB reactivity. Photographs of 580 µM TMB (A) in the presence and (B) in the absence of ClO_4^- with Pd@PIM-EA-TB (stirred in the dark, 33% DMSO) as a function of time.

Even though the presence of perchlorate is proved to enhance the H_2O_2 production (see Figure 6.9A) from formate/formic acid, the effect on the TMB colour reaction is not substantial. The colour scales of TMB oxidation are similar in the presence and absence of perchlorate. However, a deeper blue colour is observed in the presence of perchlorate

compared to the blue-green colour without perchlorate. In fact, the colour reaction is different because of the precipitation of the product when perchlorate is involved. In terms of actual application, precipitation or accumulation of the coloured products appears to be beneficial to reproducibility and sensor-effective read-out. From this perspective, an optimisation investigation on accumulated blue colour product into an indicator strip is carried out next.

6.3.5 Pd@PIM-EA-TB Reactivity V.: Optimized TMB Colour Reaction

The blue precipitate product from TMB oxidation in the presence of ClO_4^- implies a cationic characteristic (see the mechanism in Figure 6.4). For the purpose of collecting the blue product and delivering a stronger colour change, a negatively charged Nafion ionomer can be used. Here, the Nafion solution is stamped onto a filter paper (Figure 6.17).

Figure 6.17 Effects of Nafion ionomer printed on a filter paper on the TMB colour response with/without 50 mM ClO_4^- for 10 mM HCOOH/HCOONa concentration at pH 3.75. Photographs of 580 µM TMB (A) without catalyst, (B) without Nafion, (C) in the absence of ClO_4^-, and (D) with ClO_4^- (stirred in the dark, 33% DMSO, 11 cm^3) as a function of reaction time.

The collection of blue-coloured TMB products is carried out under optimised conditions (10 mM HCOOH/HCOONa, pH 3.75). A blue colouration gradually appears due to Pd@PIM-EA-TB producing H_2O_2. A weak pattern is observed in the absence of catalyst, probably derived from a slow aerial background TMB reaction. In the presence of Pd@PIM-EA-TB catalyst, a distinct blue pattern emerges on a Nafion ionomer printed filter paper. An advantageous effect of ClO_4^- is shown at 4 to 5 h reaction time. However, for a more prolonged time, the difference between with and without the addition of perchlorate is less noticeable. These results verify the catalytically generated H_2O_2 resulting in TMB oxidation and colour response. Nafion ionomer printed onto a filter paper substrate is effective in showing distinct blue colour contrast due to accumulation of the TMB oxidation product.

6.4 Conclusions

Investigations show that palladium nanoparticles immobilised in PIM-EA-TB display formate oxidase reactivity, which drives hydrogen peroxide production from formic acid. Molecularly rigid PIM-EA-TB, as a host, creates "cavities" surrounding palladium nano-catalysts, presenting catalytic reactivity due to the presence of tertiary amines in the vicinity of the palladium surface. A computational DFT model is developed to study the catalyst cavity effect. The key results are:

(i) The Pd@PIM-EA-TB drives the catalytic conversion of formic acid to hydrogen peroxide in the presence of oxygen (*i.e.* nanozyme mimicking formate oxidase).

(ii) The interaction of microporous PIM-EA-TB (providing tertiary amines) with palladium surface creates numerous active catalytic sites.

(iii) The hydrogen peroxide production is enhanced at pH < 4, which is related to the protonation of PIM-EA-TB.

(iv) Hydrogen generation in competition to hydrogen peroxide formation is only major at pH close to 4 but less important in more acidic or alkaline solutions, especially under stirring.

(v) Perchlorate enhances peroxide production in acidic solutions due to its ability to provide more ammonium active sites.

(vi) A DFT model simulates the possible reaction pathways in "cavities" of Pd@PIM-EA-TB, which shows enhanced reactivity of both oxygen hydrogenation and formic acid dehydrogenation.

(vii) The colourimetric homogeneous oxidation of TMB is employed to visualise hydrogen peroxide formation.

(viii) Nafion ionomer is employed to enhance the TMB colour change by accumulating the blue cationic species.

The involvement of intrinsically microporous polymers (PIMs) in a catalytic reaction is intriguing and needs more explorations for catalyst development. In the future, modifications of PIMs to produce more cavities and the use of different types of PIMs provide potential applications in selective catalytic reactions. Although only one specific DFT model does not represent a variety of cases of catalytic conditions on catalysts based on PIMs structure, it can provide powerful complementary information and could be used to predict catalytic reactivities at various types of catalysts surfaces.

6.5 References

1 Rao, H., Li, J., Luo, M., Zhang, K., Gou, H., Liu, H., & Xue, Z. A label-free and modification-free ratiometric electrochemical strategy for enhanced natural enzyme detection using a bare electrode and nanozymes system. *Analytical and Bioanalytical Chemistry* **414**, 2991-3003 (2022).

2 Białas, K., Moschou, D., Marken, F. & Estrela, P. Electrochemical sensors based on metal nanoparticles with biocatalytic activity. *Microchimica Acta* **189**, 1-20 (2022).

3 Stasyuk, N., Smutok, O., Demkiv, O., Prokopiv, T., Gayda, G., Nisnevitch, M., & Gonchar, M. Synthesis, catalytic properties and application in biosensorics of nanozymes and electronanocatalysts: A review. *Sensors* **20**, 4509 (2020).

4 Tieves, F., Willot, S. J. P., van Schie, M. M. C. H., Rauch, M. C. R., Younes, S. H. H., Zhang, W., Dong, J., Santos, P. G., Robbins, J. M., Bommarius, B., Alcalde, M., Bommarius, A. S. & Hollmann, F. Formate oxidase (FOx) from Aspergillus oryzae: one catalyst enables diverse H_2O_2-dependent biocatalytic oxidation reactions. *Angewandte Chemie International Edition* **58**, 7873-7877 (2019).

5 Robbins, J. M., Bommarius, A. S. & Gadda, G. Mechanistic studies of formate oxidase from Aspergillus oryzae: A novel member of the glucose-methanol-choline oxidoreductase enzyme superfamily that oxidizes carbon acids. *Archives of Biochemistry and Biophysics* **643**, 24-31 (2018).

6 Doubayashi, D., Ootake, T., Maeda, Y., Oki, M., Tokunaga, Y., Sakurai, A., Nagaosa, Y., Mikami, B. & Uchida, H. Formate oxidase, an enzyme of the glucose-methanol-choline oxidoreductase family, has a His-Arg pair and 8-formyl-FAD at the catalytic site. *Bioscience, Biotechnology, and Biochemistry* **75**, 1662-1667 (2011).

7 Maeda, Y., Oki, M., Fujii, Y., Hatanaka, A., Hojo, M., Hirano, K., & Uchida, H. Cloning and expression of three formate oxidase genes from Debaryomyces vanrijiae MH201. *Bioscience, Biotechnology, and Biochemistry*, **72**, 0807040967-0807040967 (2008).

8 Li-Zeng, G. & Xi-Yun, Y. Discovery and current application of nanozyme. *Progress in Biochemistry and Biophysics* **40**, 892-902 (2013).

9 Liu, Y., Zeng, X., Hu, X., Xia, Y. & Zhang, X. Solar-driven photocatalytic disinfection over 2D semiconductors: The generation and effects of reactive oxygen species. *Solar Rrl* **5**, 2000594 (2021).

10 Vennestrøm, P. N., Christensen, C. H., Pedersen, S., Grunwaldt, J. D. & Woodley, J. M. Next-generation catalysis for renewables: combining enzymatic with inorganic heterogeneous catalysis for bulk chemical production. *ChemCatChem* **2**, 249-258 (2010).

11 Hu, J., Zhang, P., An, W., Liu, L., Liang, Y., & Cui, W. In-situ Fe-doped g-C_3N_4 heterogeneous catalyst via photocatalysis-Fenton reaction with enriched photocatalytic performance for removal of complex wastewater. *Applied Catalysis B: Environmental* **245**, 130-142 (2019).

12 Robbins, J. M., Geng, J., Barry, B. A., Gadda, G. & Bommarius, A. S. Photoirradiation generates an ultrastable 8-formyl FAD semiquinone radical with unusual properties in formate oxidase. *Biochemistry* **57**, 5818-5826 (2018).

13 Maeda, Y., Doubayashi, D., Oki, M., Nose, H., Sakurai, A., Isa, K., Fujii, Y. & Uchida, H. Expression in Escherichia coli of an unnamed protein gene from Aspergillus oryzae RIB40 and cofactor analyses of the gene product as formate oxidase. *Bioscience, Biotechnology, and Biochemistry* **73**, 2645-2649 (2009).

14 Popov, V. O. & Lamzin, V. S. NAD (+)-dependent formate dehydrogenase. *Biochemical Journal* **301**, 625 (1994).

15 Mehri, A. & Kochkar, H. In situ generated H_2O_2 over supported Pd-Au clusters in hybrid titania nanocrystallites. *Chemistry Letters* **43**, 1046-1048 (2014).

16 Xia, F., Pan, M., Mu, S., Malpass-Evans, R., Carta, M., McKeown, N. B., Attard, G. A., Brew, A., Morgan, D. J. & Marken, F. Polymers of intrinsic microporosity in electrocatalysis: Novel pore rigidity effects and lamella palladium growth. *Electrochimica Acta* **128**, 3-9 (2014).

17 Wang, H., Wan, K. & Shi, X. Recent advances in nanozyme research. *Advanced Materials* **31**, 1805368 (2019).

18 Liang, M. & Yan, X. Nanozymes: from new concepts, mechanisms, and standards to applications. *Accounts of Chemical Research* **52**, 2190-2200 (2019).

19 Wang, P., Wang, T., Hong, J., Yan, X. & Liang, M. Nanozymes: a new disease imaging strategy. *Frontiers in Bioengineering and Biotechnology* **8**, 15 (2020).

20 Ren, X., Chen, D., Wang, Y., Li, H., Zhang, Y., Chen, H., Li, X. & Huo, M. Nanozymes-recent development and biomedical applications. *Journal of Nanobiotechnology* **20**, 1-18 (2022).

21 Jiang, D., Ni, D., Rosenkrans, Z. T., Huang, P., Yan, X., & Cai, W. Nanozyme: new horizons for responsive biomedical applications. *Chemical Society Reviews* **48**, 3683-3704 (2019).

22 Das, B., Franco, J. L., Logan, N., Balasubramanian, P., Kim, M. I., & Cao, C. Nanozymes in point-of-care diagnosis: An emerging futuristic approach for biosensing. *Nano-Micro Letters* **13**, 1-51 (2021).

23 Komkova, M. A., Vetoshev, K. R., Andreev, E. A. & Karyakin, A. A. Flow-electrochemical synthesis of Prussian Blue based nanozyme 'artificial peroxidase'. *Dalton Transactions* **50**, 11385-11389 (2021).

24 Wu, L., Zhou, S., Wang, G., Yun, Y., Liu, G., & Zhang, W. Nanozyme applications: A glimpse of insight in food safety. *Frontiers in Bioengineering and Biotechnology*, **9**, 727886 (2021).

25 Li, X., Wang, L., Du, D., Ni, L., Pan, J., & Niu, X. Emerging applications of nanozymes in environmental analysis: Opportunities and trends. *TrAC Trends in Analytical Chemistry* **120**, 115653 (2019).

26 Xie, X., Tan, L., Liu, S., Wen, X., Li, T., & Yang, M. High-sensitive photometric microplate assay for tumor necrosis factor-alpha based on Fe@BC nanozyme. *Journal of Immunological Methods* **499**, 113167 (2021).

27 Swaidan, A., Addad, A., Tahon, J. F., Barras, A., Toufaily, J., Hamieh, T., Szunerits, S. & Boukherroub, R. Ultrasmall CuS-BSA-$Cu_3(PO_4)_2$ nanozyme for highly efficient

colorimetric sensing of H_2O_2 and glucose in contact lens care solutions and human serum. *Analytica Chimica Acta* **1109**, 78-89 (2020).

28 Cui, F., Deng, Q. & Sun, L. Prussian blue modified metal-organic framework MIL-101 (Fe) with intrinsic peroxidase-like catalytic activity as a colorimetric biosensing platform. *RSC Advances* **5**, 98215-98221 (2015).

29 Borah, N. & Tamuly, C. Ultrasensitive Pd nano catalyst as peroxidase mimetics for colorimetric sensing and evaluation of antioxidants and total polyphenols in beverages and fruit juices. *Talanta* **238**, 123000 (2022).

30 Carta, M., Malpass-Evans, R., Croad, M., Rogan, Y., Jansen, J. C., Bernardo, P., Bazzarelli, F. & McKeown, N. B. An efficient polymer molecular sieve for membrane gas separations. *Science* **339**, 303-307 (2013).

31 Kresse, G. & Furthmüller, J. Efficiency of ab-initio total energy calculations for metals and semiconductors using a plane-wave basis set. *Computational Materials Science* **6**, 15-50 (1996).

32 Hammer, B., Hansen, L. B. & Nørskov, J. K. Improved adsorption energetics within density-functional theory using revised Perdew-Burke-Ernzerhof functionals. *Physical Review B* **59**, 7413 (1999).

33 Blöchl, P. E. Projector augmented-wave method. *Physical Review B* **50**, 17953 (1994).

34 Grimme, S., Ehrlich, S. & Goerigk, L. J. Effect of the damping function in dispersion corrected density functional theory. *Journal of Computational Chemistry* **32**, 1456-1465 (2011).

35 Mathew, K., Kolluru, V. C., Mula, S., Steinmann, S. N. & Hennig, R. G. Implicit self-consistent electrolyte model in plane-wave density-functional theory. *Journal of Chemical Physics* **151**, 234101 (2019).

36 Mathew, K., Sundararaman, R., Letchworth-Weaver, K., Arias, T. & Hennig, R. G. Implicit solvation model for density-functional study of nanocrystal surfaces and reaction pathways. *The Journal of Chemical Physics* **140**, 084106 (2014).

37 Henkelman, G. & Jónsson, H. Improved tangent estimate in the nudged elastic band method for finding minimum energy paths and saddle points. *The Journal of Chemical Physics* **113**, 9978-9985 (2000).

38 Henkelman, G., Uberuaga, B. P. & Jónsson, H. A climbing image nudged elastic band method for finding saddle points and minimum energy paths. *The Journal of Chemical Physics* **113**, 9901-9904 (2000).

39 Henkelman, G. & Jónsson, H. A dimer method for finding saddle points on high dimensional potential surfaces using only first derivatives. *The Journal of Chemical Physics* **111**, 7010-7022 (1999).

40 Liu, D.-M., Xu, B. & Dong, C. Recent advances in colorimetric strategies for acetylcholinesterase assay and their applications. *TrAC Trends in Analytical Chemistry* **142**, 116320 (2021).

41 Josephy, P. D., Eling, T. & Mason, R. P. The horseradish peroxidase-catalyzed oxidation of 3, 5, 3', 5'-tetramethylbenzidine. Free radical and charge-transfer complex intermediates. *Journal of Biological Chemistry* **257**, 3669-3675 (1982).

42 Zhang, X., Yang, Q., Lang, Y., Jiang, X. & Wu, P. Rationale of 3, 3′, 5, 5′-tetramethylbenzidine as the chromogenic substrate in colorimetric analysis. *Analytical Chemistry* **92**, 12400-12406 (2020).

43 Zhuo, S., Fang, J., Zhu, C., Du, J. Preparation of palladium/carbon dot composites as efficient peroxidase mimics for H_2O_2 and glucose assay. *Analytical and Bioanalytical Chemistry* **412**, 963-972 (2020).

44 Mu, J., Wang, Y., Zhao, M. & Zhang, L. Intrinsic peroxidase-like activity and catalase-like activity of Co_3O_4 nanoparticles. *Chemical Communications* **48**, 2540-2542 (2012).

45 Swern, D. Epoxidation and hydroxylation of ethylenic compounds with organic peracids. *Organic Reactions* **7**, 378-434 (2004).

46 Swern, D., Billen, G. N., Findley, T. W. & Scanlan, J. T. Hydroxylation of monounsaturated fatty materials with hydrogen peroxide. *Journal of the American Chemical Society* **67**, 1786-1789 (1945).

47 Rong, Y., Kolodziej, A., Madrid, E., Carta, M., Malpass-Evans, R., McKeown, N. B., & Marken, F. Polymers of intrinsic microporosity in electrochemistry: Anion uptake and transport effects in thin film electrodes and in free-standing ionic diode membranes. *Journal of Electroanalytical Chemistry* **779**, 241-249 (2016).

48 Shimaouchi, T. Tables of Molecular Vibrational Frequencies Consolidated Volume 1, NBS NSRDS 39, National Bureau of Standards, Washington D.C. 1972.

49 Redington, R. L., Olson, W. B., & Cross, P. C. Studies of hydrogen peroxide: The infrared spectrum and the internal rotation problem. *The Journal of Chemical Physics* **36**, 1311-1326 (1962).

50 Ford, D. C., Nilekar, A. U., Xu, Y. & Mavrikakis, M. Partial and complete reduction of O_2 by hydrogen on transition metal surfaces. *Surface Science* **604**, 1565-1575 (2010).

51 Sanchez, F., Alotaibi, M. H., Motta, D., Chan-Thaw, C. E., Rakotomahevitra, A., Tabanelli, T.,Roldan, A., Hammond, C., He, Q., Davis, T., Villa, A. & Dimitratos, N. Hydrogen production from formic acid decomposition in the liquid phase using Pd nanoparticles supported on CNFs with different surface properties. *Sustainable Energy & Fuels* **2**, 2705-2716 (2018).

52 Barlocco, I., Bellomi, S., Delgado, J. J., Chen, X., Prati, L., Dimitratos, N., Roldan, A. & Villa, A. Enhancing activity, selectivity and stability of palladium catalysts in formic acid decomposition: Effect of support functionalization. *Catalysis Today* **382**, 61-70 (2021).

53 Barlocco, I., Capelli, S., Lu, X., Bellomi, S., Huang, X., Wang, D., Prati, L., Dimitratos, N., Roldan, A. & Villa, A. Disclosing the role of gold on palladium-gold alloyed supported catalysts in formic acid decomposition. *ChemCatChem* **13**, 4210-4222 (2021).

Chapter 7 Polymer-Enhanced Hydrogen Peroxide Generation from Oxygen and Formic Acid: One-Step Formation of Nanocatalysts (Pd, Au, or a PdAu Mixture) Confined into Intrinsically Microporous Polymers (PIM-EA-TB or PIM-1)

Contents

Chapter Abstract

Nanoparticles of Pd, Au, or PdAu mixtures are immobilised in polymers of intrinsic microporosity hosts (PIM-EA-TB and PIM-1) and evaluated and compared as catalysts for the reactivity towards formic acid oxidation and oxygen reduction during H_2O_2 production. Microporous catalyst composites are prepared in a single-step process by casting polymer, Pd(II)(acetate)$_2$, or/and Au(I)Cl(triethylphosphine) together from a chloroform solution, followed by borohydride reduction. Nano-catalysts with typically 3 nm diameter of Pd, Au, and PdAu mixtures are assessed in formic acid solutions, which suggest PdAu@PIM-EA-TB is the most active catalyst for H_2O_2 production. A colourimetric assay based on 3,5,3',5'-tetramethylbenzidine (TMB) sensor dye verifies the pattern of H_2O_2 generation reactivity. In contrast to PIM-1, PIM-EA-TB is suggested to be directly contributing to the catalytic process by creating rigid surface cavities with (i) amine sites as proton acceptors (for formate oxidation) and (ii) ammonium sites as proton donors (for oxygen reduction).

Graphical Abstract

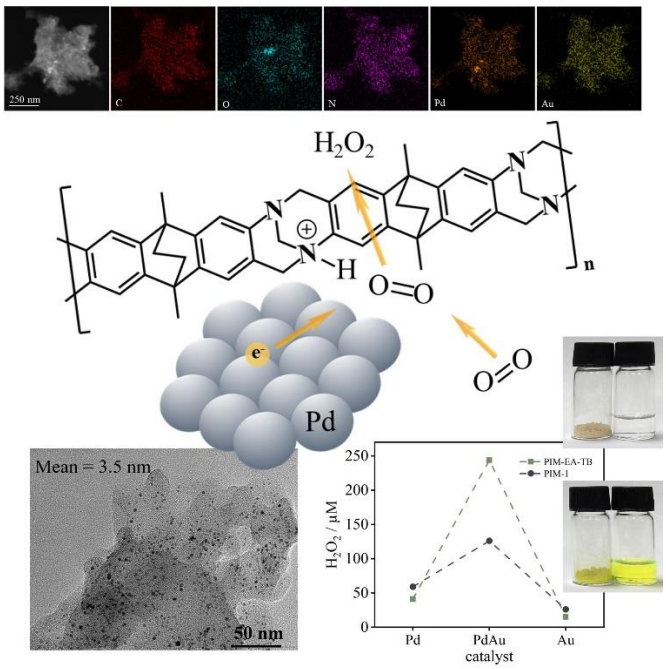

Credit Statement

The candidate developed the immobilisation methods of palladium, gold, and palladium/gold mixtures in PIM-EA-TB, and performed the quantification of hydrogen peroxide based on LC-MS, electrochemical experiments based on a Clark probe, TMB colour reaction, data curation, and interpretation of the results. Neil Mckeown provided the PIM-EA-TB and PIM-1 material. Philip Fletcher performed the SEM and TEM characterisation in Figures 7.3 to 7.14. Shik Chi Tsang and Ping-Luen Baron Ho helped collect the TEM images in Figure 7.15. Mariolino Carta, Richard Malpass-Evans, Neil B. McKeown, Philip J. Fletcher, Shik Chi Tsang and Ping-Luen Baron Ho input valuable comments to the draft. Frank Marken supervised the candidate, gave critical and valuable guidance to this work, and helped review and edit the original draft.

Special Acknowledgements

Thanks to Prof. Neil Mckeown and his research group from the University of Edinburgh for collaborating and providing PIM-EA-TB and PIM-1 material in the following study. Special thanks go to Dr Philip Fletcher for your support in SEM, TEM, and EDX analysis listed in Figures 7.3 to 7.14. Thanks also to Prof. Shik Chi Tsang and Ping-Luen Baron Ho from the University of Oxford for helping with the TEM images presented in Figure 7.15.

7.1 Introduction

Catalytic reactions in microporous environments have drawn significant attention for the comparable reactive cavities to natural enzymes [1,2]. A particular interesting system is based on polymers of intrinsic microporosity (PIMs). The open cavities in PIMs can be generated at the surface of heterogeneous catalysts [3], for example, to be beneficial to (i) creating micro reactive space without capping the catalyst surface, [4] (ii) affecting solvent structure at the catalyst surface, and (iii) creating additional reaction sites (based on functional groups) close to the catalyst surface. The polyamine PIM-EA-TB (see molecular structure in Figure 7.1A) at the surface of the nano palladium catalyst has been verified to participate in the catalytic reactions experimentally and theoretically (see Chapter 6). It was suggested that the tertiary amines in PIM-EA-TB could pick up a proton during formic acid oxidation. Then the ammonium site could donate this proton in the oxygen reduction process. In this chapter, a similar system is studied by comparing the reactivity of Pd, Au, and PdAu mixtures immobilised in the hosts of PIM-EA-TB or PIM-1 (see molecular structure in Figure 7.1B).

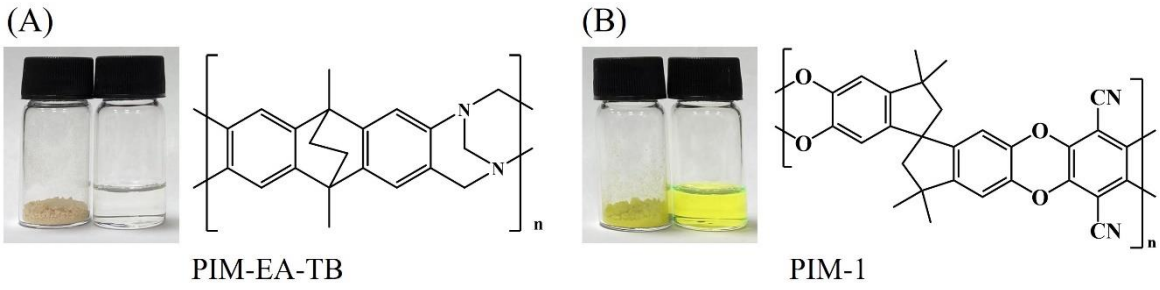

Figure 7.1 (A) Photograph of PIM-EA-TB powder and solution in chloroform (1 mg/mL) and molecular structure of PIM-EA-TB; (B) Photograph of PIM-1 powder and solution in chloroform (1 mg/mL), and molecular structure of PIM-1.

In practice, PIMs with nanocavities could confine catalysts and avoid aggregation during catalyst synthesis. Differences in cavities, functional groups, and wettability of PIMs could be critical factors causing variable activities in catalytic reactions. Microporous composites with embedded nano-catalysts lead to highly reactive systems with accessible nanoparticle catalysts in a reaction environment defined by a microporous host, for example, PIMs. Here, reactivity comparison between PIM-EA-TB and hydrophobic PIM-1 [5] composites with immobilised Pd, Au, and PdAu mixtures during the catalytic hydrogen peroxide formation process are investigated.

Bimetallic PdAu nanoparticles have been reported to significantly enhance catalytic reactivity and selectivity in many reactions compared to their monometallic counterparts [6]. Applications have been addressed in nitrite reduction [7], selective oxidation of the primary C-H bonds in toluene [8], selective oxidation of saturated hydrocarbons [9], oxygen reduction in electrocatalysis [10], electrooxidation of formic acid [11], hydrogen evolution from formic acid [12], enzymatic biosensing [13], selective detection of acetone in clinical application [14], and other reactions [15-17]. Interests in PdAu rely on (i) Pd and Au can form solid solutions in the whole range of Pd/Au atomic ratio [6,7]; and (ii) the presence of the second element alters the electronic property of the primary metal nanoparticles with the formation of alloy and/or core-shell configurations [18]. Here, performance of H_2O_2 production from oxygen and formic acid are assessed on PdAu mixture nano-catalysts in comparison to monometallic Pd or Au nanoparticles.

The only reports directly explored enhanced catalytic processes in PIMs are increased oxygen reduction catalysis in PIM-1 [19], the accumulation of hydrophobic substrates effects [20,21], and enhanced generation of hydrogen peroxide on Pd (Chapter 6). In this Chapter, more direct evidence for catalytic processes being affected by PIMs is shown by pH-dependent investigation. One-step formation of nano Pd, Au, and PdAu mixtures catalysts embedded in PIM-EA-TB and PIM-1 is achieved by co-deposition of chloroform soluble metal precursors with PIMs followed by reduction. Coupled processes of formic acid oxidation and oxygen reduction to generate H_2O_2 are evaluated based on a Clark-type sensor, mass spectroscopy, and colourimetric assay based on 3,5,3',5'-tetramethylbenzidine (TMB) dye.

7.2 Experimental

7.2.1 Reagents

Chloro(triethylphosphine)gold(I) ($[(C_6H_5)_3P]AuCl$, ≥99.9), palladium (II) acetate ($[Pd(OAc)_2]_3$, reagent grade, 98%), Sodium borohydride ($NaBH_4$, powder, 98%), formic acid (HCOOH, 96%, ACS Reagent), sodium carbonate (Na_2CO_3, powder, ≥ 99.5%, ACS Reagent), p-nitrophenylboronic acid (≥ 95.0%), Nafion® 117 solution (~5% in a mixture of lower aliphatic alcohols and water), chloroform (≥ 99.8%), sodium formate (NaCOOH, ACS reagent, ≥99.0%), 3,3',5,5'-Tetramethylbenzidine (TMB, ≥99%) were purchased from Sigma-Aldrich. Dimethyl sulfoxide (DMSO, for HPLC, ≥ 99.7%) and hydrogen peroxide

(H_2O_2, ACS Reagent, 30 wt.% in H_2O) were products of Honeywell. Sodium bicarbonate ($NaHCO_3$, ≥ 99.7%) and sodium hydroxide (NaOH, pellets, laboratory reagent grade) were obtained from Fluka. The synthesis procedures of PIM-EA-TB [22] and PIM-1 [23] were the same as the literature. The Whatman™ brand filter paper (602H, pore size < 2 μm) was ordered from GE Healthcare Life Sciences. The Jovitec universal pH test paper (pH full range 1-14) was used in H_2O_2 detection. The Nylon mesh purchased from Amazon (Nut milk bag 200 Micron) was applied as the catalyst substrate.

7.2.2 Instrumentation

Consumption of oxygen and production of hydrogen were monitored by a commercial Clark-type polarographic dissolved oxygen probe (HI76407) from Hanna Instruments Ltd. A concentrated KCl solution (HI7041S) was employed as a fill electrolyte inside the probe. The current responses were recorded as chronoamperometry by a potentiostat (Metrohm microAutolab II). Ultra-pure water (resistivity not less than 18.2 MΩ cm at 20 °C) was purified from a Thermo Scientific water purification system. A pH meter (Jenway 3505) was applied to monitor the acidity of the testing solutions. The morphologies of samples were imaged by a field emission scanning electron microscope (FESEM, JEOL JSM-7900F) and a transmission electron microscope (TEM, JEOL JEM-2100PLUS). An energy dispersive X-ray analyser (170 mm^2 Ultim Max EDX) equipped to the FESEM system and an Oxford Instruments large area EDX detector attached to TEM were to carry out the elemental detection. An aberration-corrected JEOL ARM300 CF microscope operated at 300 kV in STEM mode was used for imaging the microstructures of PdAu@PIM-EA-TB and PdAu@PIM-1 samples (Figure 7.15). The quantification of H_2O_2 was performed on an Agilent 6545 Accurate-Mass Q-TOF liquid chromatography-mass spectroscopy (LC-MS) equipment.

7.2.3 Preparation of metal@PIM-EA-TB and metal@PIM-1

Stock solutions of 4 mM $Pd(OAc)_2$ (m.w. 224.51 g/mol), 4 mM $[(C_6H_5)_3P]AuCl$ (m.w. 494.71 g/mol), 1 mg/mL PIM-EA-TB (monomer weight 300 g/mol; m.w. approx. 70 kD; typically 3.3 mmol monomer in solution), and 1 mg/mL PIM-1 (monomer weight 460 g/mol; m.w. approx. 90 kD; typically 2.2 mmol monomer in solution) in chloroform were prepared

at the first step. Typically, for the preparation of Pd@PIM-EA-TB, a mixture of $Pd(OAc)_2$ and PIM-EA-TB solutions (volume ratio 1 to 1) was cast deposited (40 µL) on a Nylon mesh disk (8 mm in diameter) followed by a reduction process in a freshly made 5 mg/mL $NaBH_4$ solution at 4 °C in a fridge for 20 h. After rinsing with water, the sample was ready to be assessed. The preparation of other samples employed the same method but used a different mixture of chloroform solutions (see more details in Figure 7.2 and Table 7.1). Note that the mixing of solutions needs to be freshly done as precipitation was observed in long-term stocked mixture solutions.

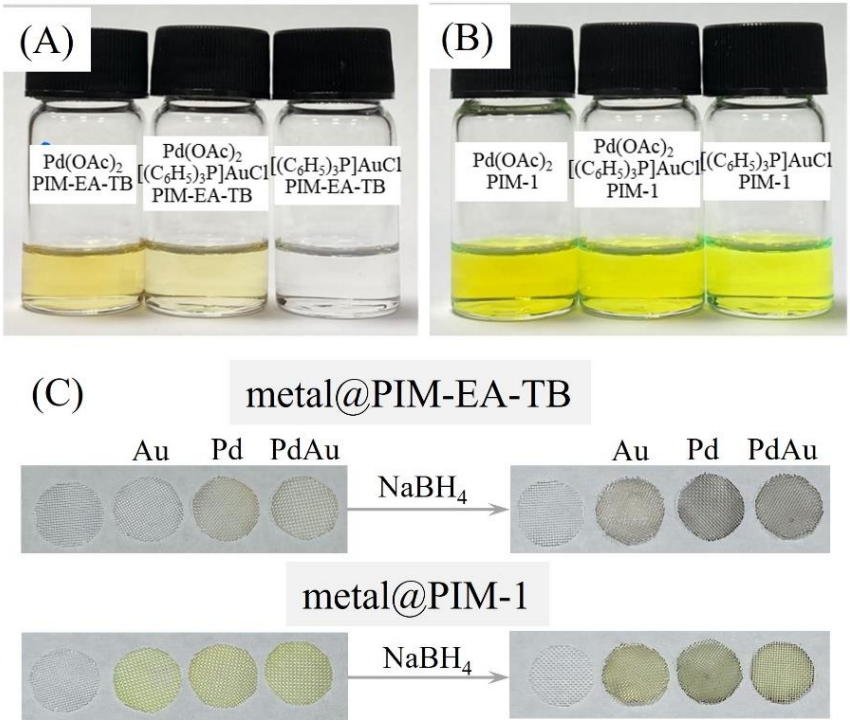

Figure 7.2 (A, B) (Photographs of different solutions containing $Pd(OAc)_2$, $[(C_6H_5)_3P]AuCl$, or both with PIM-EA-TB or with PIM-1. (C) Photographs of the Nylon disks and the coated Nylon disks before and after $NaBH_4$ reduction to embedded nanoparticles.

Table 7.1 Pre-mixed solutions and their corresponding products. The theoretical ratios of metal to polymer monomer unit (in PIM-AE-TB or PIM-1) are shown.

Solution Mixture	Final Product	Metal : Monomer Ratio
2 mM $Pd(OAc)_2$, 0.5 mg/mL PIM-EA-TB	Pd@PIM-EA-TB	4.0 : 3.3
1 mM $Pd(OAc)_2$, 1 mM $[(C_6H_5)_3P]AuCl$, 0.5 mg/mL PIM-EA-TB	PdAu@PIM-EA-TB	2.0 : 2.0 : 3.3
2 mM $[(C_6H_5)_3P]AuCl$, 0.5 mg/mL PIM-EA-TB	Au@PIM-EA-TB	4.0 : 3.3
2 mM $Pd(OAc)_2$, 0.5 mg/mL PIM-1	Pd@PIM-1	4.0 : 2.2
1 mM $Pd(OAc)_2$, 1 mM $[(C_6H_5)_3P]AuCl$, 0.5 mg/mL PIM-1	PdAu@PIM-1	2.0 : 2.0 : 2.2
2 mM $[(C_6H_5)_3P]AuCl$, 0.5 mg/mL PIM-1	Au@PIM-1	4.0 : 2.2

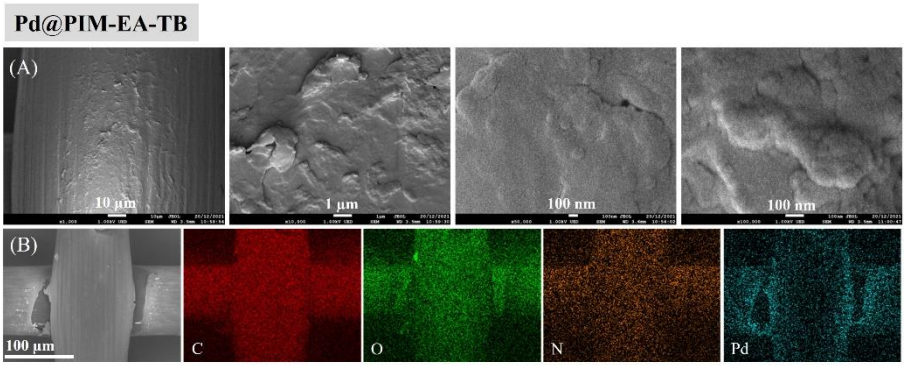

Figure 7.3 (A) Field emission scanning electron microscopy (FESEM) and (B) scanning electron microscopy (SEM) image and energy dispersive X-ray elemental analysis mapping for Pd@PIM-EA-TB.

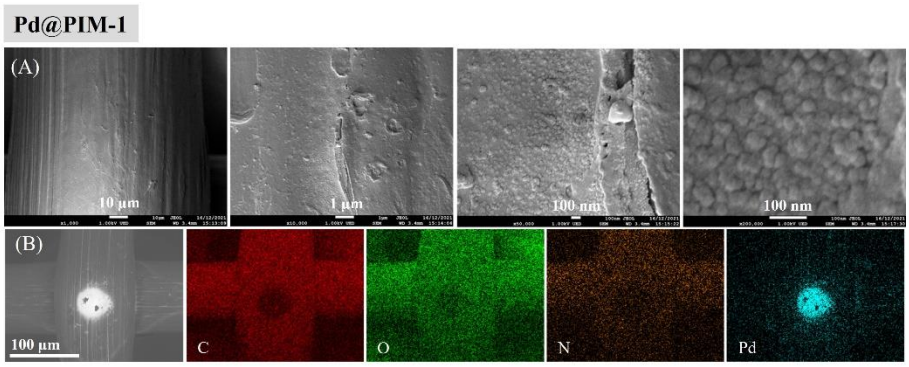

Figure 7.4 (A) Field emission scanning electron microscopy (FESEM) and (B) scanning electron microscopy (SEM) image and energy dispersive X-ray elemental analysis mapping for Pd@PIM-1.

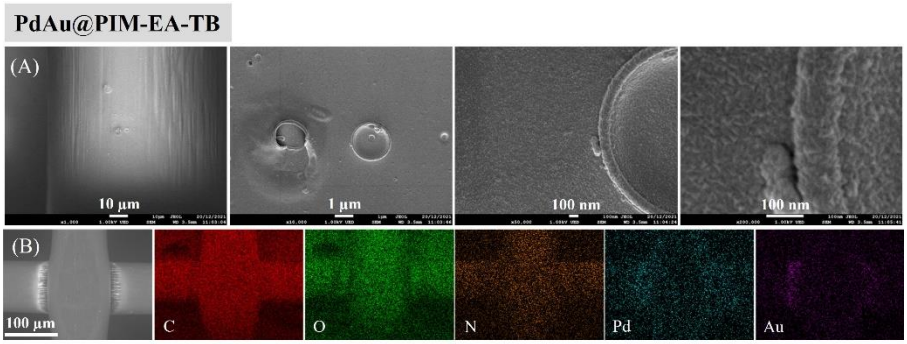

Figure 7.5 (A) Field emission scanning electron microscopy (FESEM) and (B) scanning electron microscopy (SEM) image and energy dispersive X-ray elemental analysis mapping for PdAu@PIM-EA-TB.

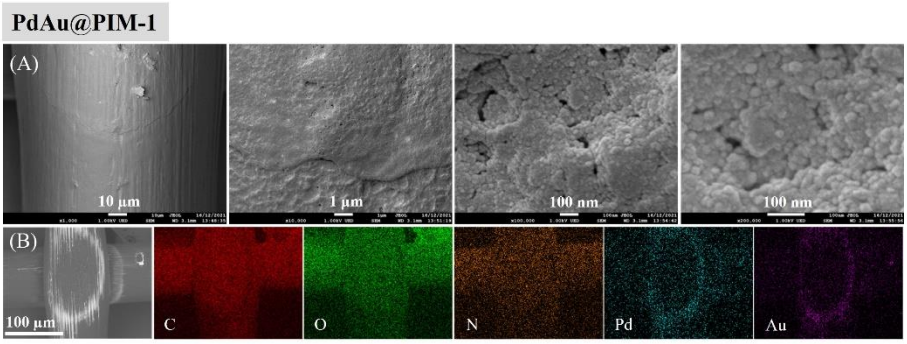

Figure 7.6 (A) Field emission scanning electron microscopy (FESEM) and (B) scanning electron microscopy (SEM) image and energy dispersive X-ray elemental analysis mapping for PdAu@PIM-1.

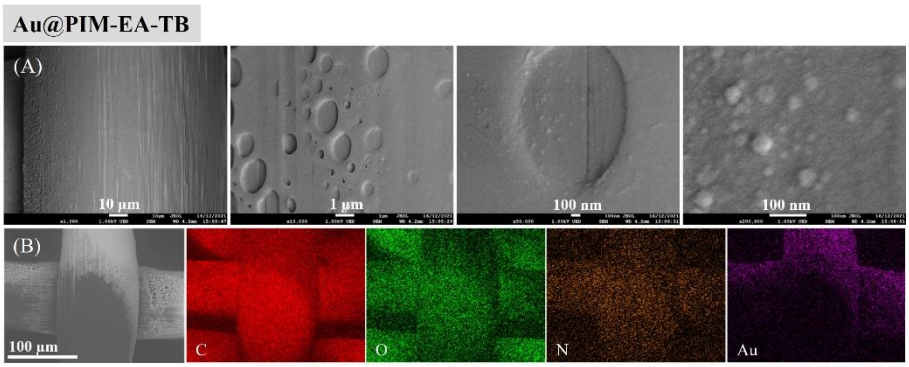

Figure 7.7 (A) Field emission scanning electron microscopy (FESEM) and (B) scanning electron microscopy (SEM) image and energy dispersive X-ray elemental analysis mapping for Au@PIM-EA-TB.

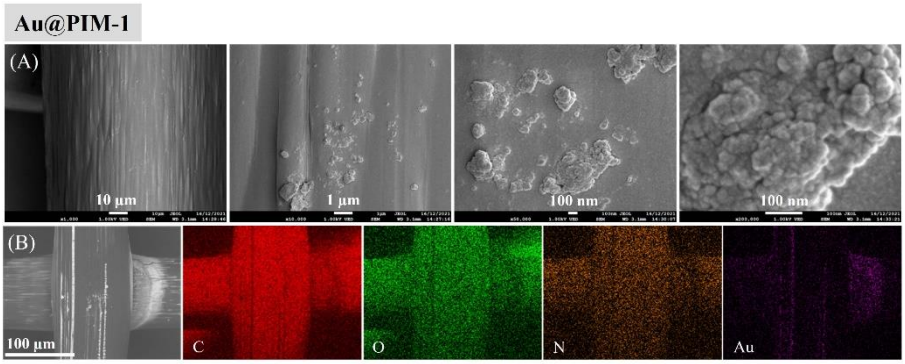

Figure 7.8 (A) Field emission scanning electron microscopy (FESEM) and (B) scanning electron microscopy (SEM) image and energy dispersive X-ray elemental analysis mapping for Au@PIM-1.

7.2.4 Evaluation of O_2 consumption and H_2 production by Clark probe

Detection of oxygen consumption and hydrogen production was performed on a Clark probe by attaching the catalyst disk to the Teflon membrane cap (same as the method demonstrated in Chapters 5 and 6). Chronoamperometry data were monitored on a potentiostat by applying different potentials. For the case of oxygen detection, the potential was fixed at -0.7 V *vs* Ag/AgCl, and hydrogen detection at 0.6 V *vs* Ag/AgCl [24].

7.2.5 Quantification of H_2O_2 by LC-MS

Quantification of H_2O_2 followed the same method as illustrated in Chapters 5 and 6. Briefly, H_2O_2 reacts with *para*-nitrophenylboronic acid stoichiometrically in alkaline conditions to

give *para*-nitrophenol. The product was separated and detected by the LC-MS technique so that the amount of H_2O_2 could be calculated accordingly.

7.2.6 Colorimetric Assay Based on TMB

The colourimetric assay followed the same procedure as proposed in Chapter 6. Colourless 3,3',5,5'-Tetramethylbenzidine (TMB) can be homogeneously oxidised by H_2O_2 in the presence of formic acid and give a blue colour product (as exemplified in Chapter 6). The visibility of the reaction solution colour change is a powerful and convenient tool to reveal the presence of H_2O_2. Typically, a 3 mL solution of 580 μM TMB, 10 mM HCOOH/HCOONa and 33% DMSO to aid solubility at pH 3.75 was placed in a small glass vial. For comparison, different catalysts prepared here were individually immersed into the solution and kept in the dark under stirring. To make a stronger colour contrast, a filter stripe (0.5×4 cm^2) coated with 10 μL Nafion solution was dipped into the reaction solution to accumulate the blue product.

7.3 Results and Discussion

7.3.1 Synthesis and Characterisation

In order to screen catalyst performance, a Nylon disk (8 mm diameter, 75 μm diameter threads, 200 μm pitch) was employed as a substrate to support and coat the polymer composite deposits. The Nylon is coated with either PIM-EA-TB or PIM-1 together with the desired Pd and/or Au precursors. Preconditions of a single-step cast deposition are that the metal precursors need to be dissolved in chloroform together with PIMs and can be reduced to metal nanoparticles. This catalyst preparation strategy aims to simplify and improve the procedures based on $PdCl_4^{2-}$ absorption demonstrated in Chapter 6. The commercially available metal complexes $Pd(OAc)_2$ and $[(C_6H_5)_3P]AuCl$ are soluble in chloroform and therefore chosen for the synthesis. The component molar ratio of the resulting catalyst could be calculated from the mass and molecular weight of the deposits. Following the experiment, this should yield approximately one metal atom per polymer monomer unit for the PIM-EA-TB case (see Table 7.1), comparable to previous studies from Chapter 6.

The colour of the metal complexes and PIMs in chloroform solutions are visible (see Figures 7.2A and B). Figure 7.2C shows the colour change before and after the $NaBH_4$ reduction process with the darkening observed for the metal nanoparticle formation. Scanning electron microscopy characterisation reveals the morphology of Pd@PIM-EA-TB (see Figure 7.3), Pd@PIM-1 (Figure 7.4), PdAu@PIM-EA-TB (Figure 7.5), PdAu@PIM-1 (Figure 7.6), Au@PIM-EA-TB (Figure 7.7), and Au@PIM-1 (Figure 7.8). EDX elemental mapping confirms that the PIM-EA-TB and PIM-1 films composed of aggregation polymer particles are uniformly coated over the Nylon mesh. The metal elements distribute on the location of PIMs. TEM data (see Figures 7.9 to 7.14 and 7.15) suggest a population of nanoparticles mainly in the range of 2.5 to 5 nm in diameter. In the samples containing Au, bigger particles from 18 to 25 nm are present. Given the preparation method, it is unlikely that a uniform alloy has been obtained for PdAu mixtures. More likely, a distribution of metals/alloys has been produced in different regions of the host polymers. Data in Figure 7.11 and PdAu@PIM-1 Figure 7.12 samples show a clear difference in Pd and Au distribution.

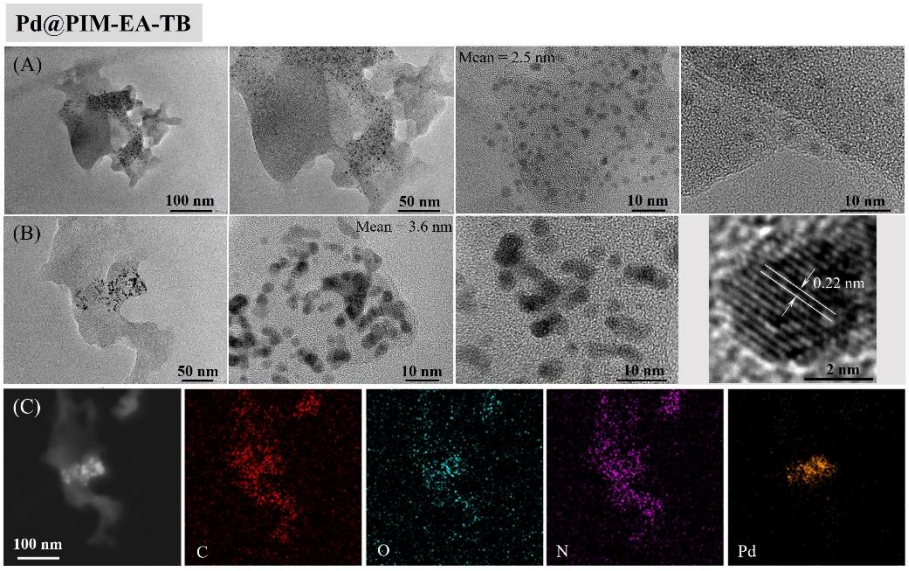

Figure 7.9 (A, B) Transmission electron microscopy (TEM) and (C) energy dispersive X-ray elemental analysis mapping for Pd@PIM-EA-TB.

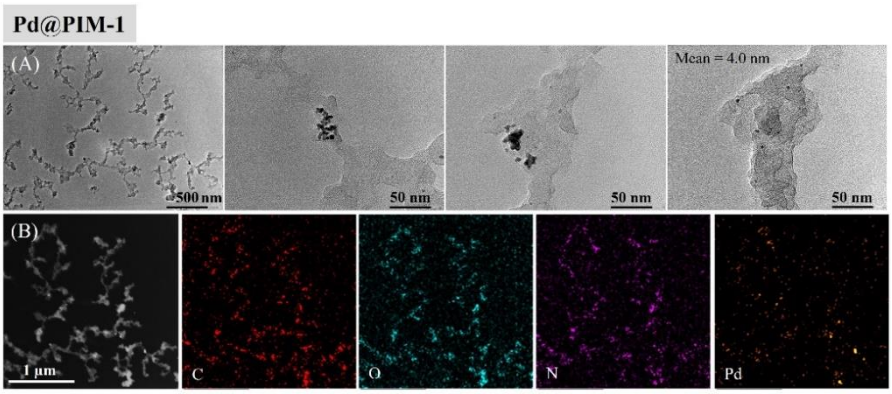

Figure 7.10 (A) Transmission electron microscopy (TEM) and (B) energy dispersive X-ray elemental analysis mapping for Pd@PIM-1.

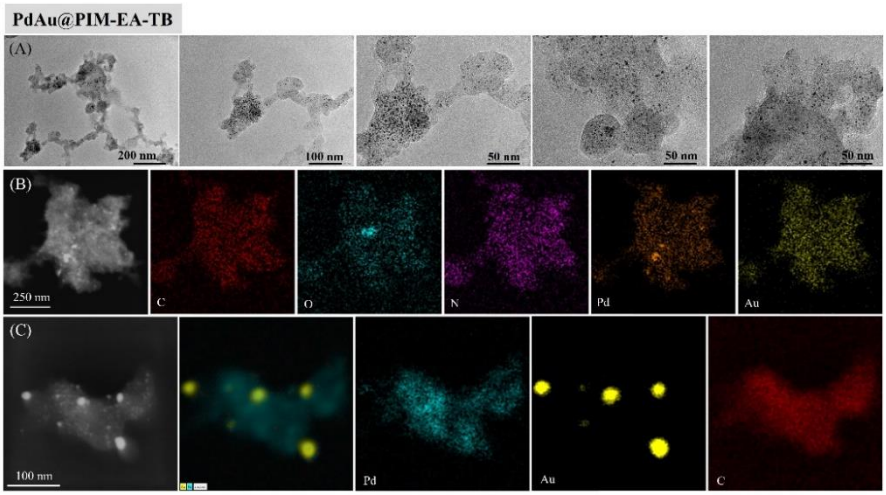

Figure 7.11 (A) Transmission electron microscopy (TEM) and (B, C) energy dispersive X-ray elemental analysis mapping for PdAu@PIM-EA-TB.

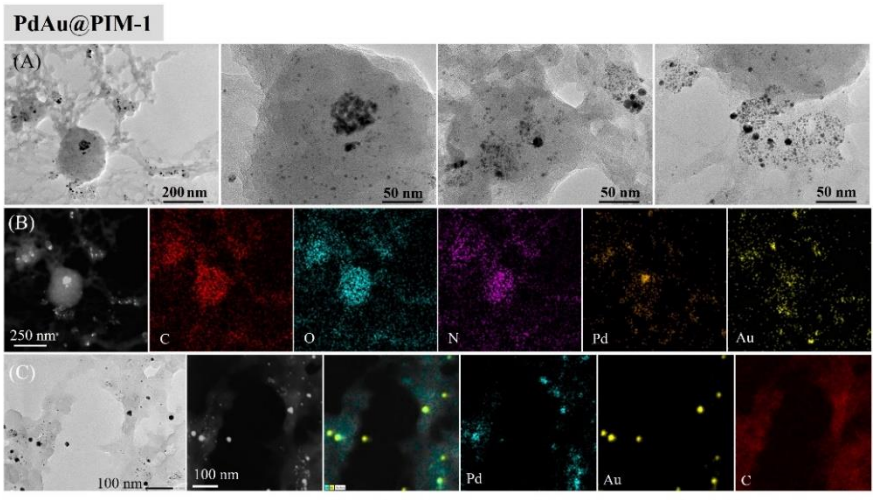

Figure 7.12 (A) Transmission electron microscopy (TEM) and (B, C) energy dispersive X-ray elemental analysis mapping for PdAu@PIM-1.

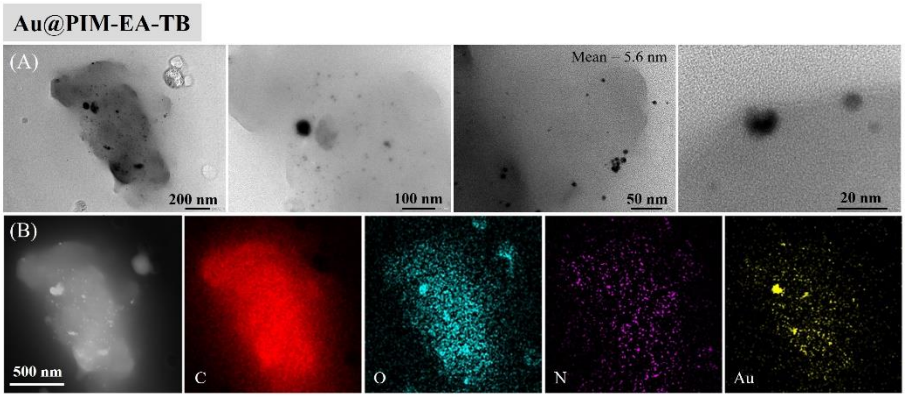

Figure 7.13 (A) Transmission electron microscopy (TEM) and (B) energy dispersive X-ray elemental analysis mapping for Au@PIM-EA-TB.

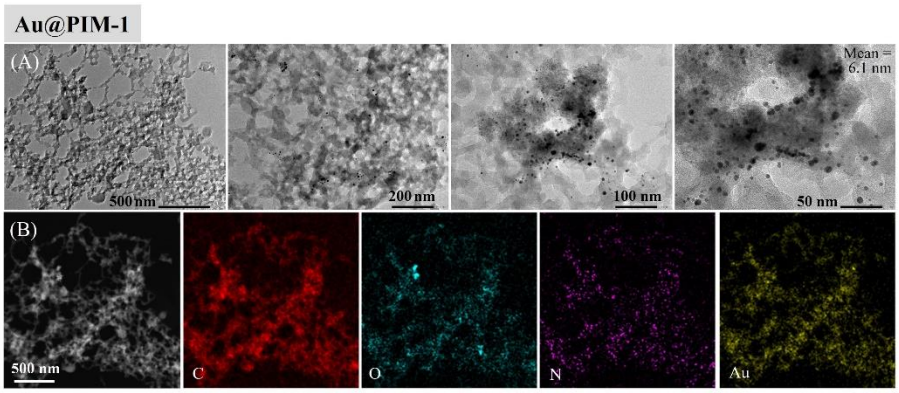

Figure 7.14 (A) Transmission electron microscopy (TEM) and (B) energy dispersive X-ray elemental analysis mapping for Au@PIM-1.

Figure 7.15 presents further evidence from scanning transmission electron microscopy (STEM) images for the distribution of nanoparticles. High-resolution images of both PdAu@PIM-EA-TB and PdAu@PIM-1 samples show fringe patterns being consistent with either Au (ICSD: 53763, cell 4.09 Å [25]) or Pd (ICSD: 64920, cell 3.908 Å [26]) or alloys (with intermediate cell parameter). Nanoparticles are shown with a similar distribution pattern in both polymer matrixes.

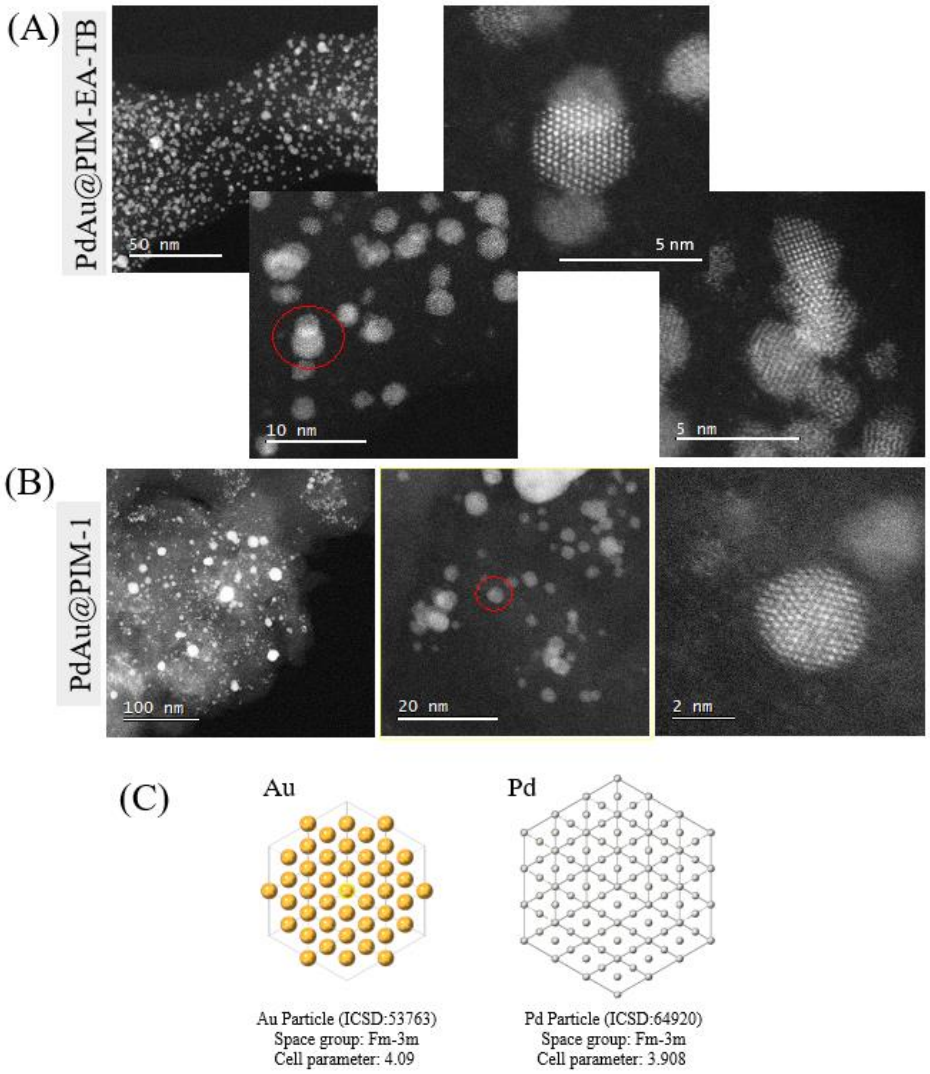

Figure 7.15 High-angle annular dark-field scanning transmission electron microscopy (HAADF-STEM) images of (A) PdAu@PIM-EA-TB and (B) PdAu@PIM-1. (C) Published crystal structure data of Au and Pd.

7.3.2 Hydrogen Peroxide Formation Reactivity I: Clark Probe Screening

Initially, the catalytic performance of three types of metals, Pd, Au, and PdAu, immobilised in host PIM-EA-TB and PIM-1, are compared for reactivity towards formic acid. The Nylon disk is fixed to the surface of a Teflon membrane of the Clark sensor to enable screening for O_2 consumption (at -0.7 V vs. Ag/AgCl) and H_2 generation (at +0.6 V vs. Ag/AgCl).

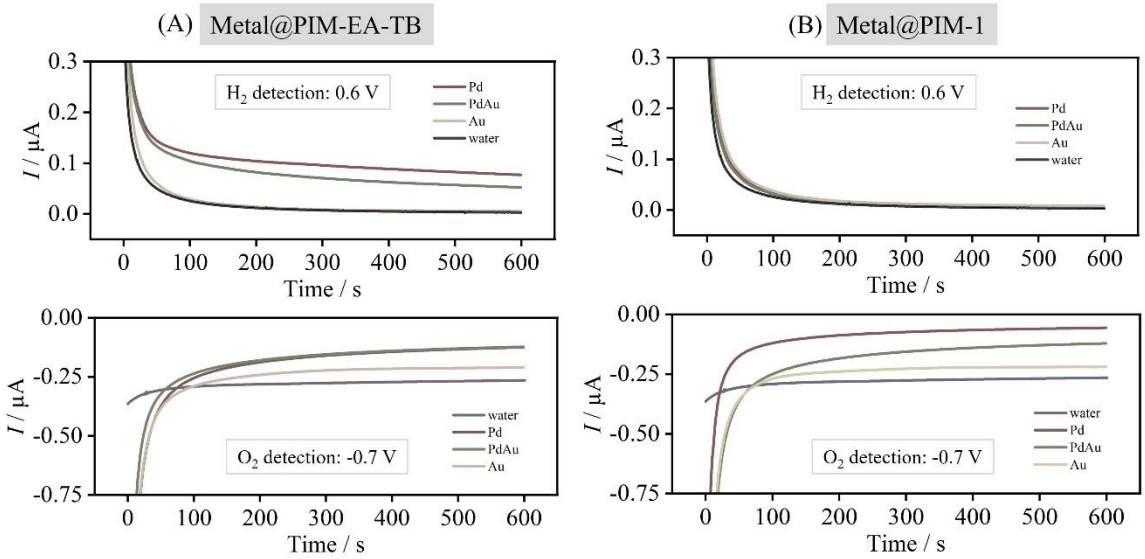

Figure 7.16 Clark probe responses for (A) Metal@PIM-EA-TB materials and (B) Metal@PIM-1 materials immersed in aqueous 0.1 M HCOOH. Each experiment was repeated more than three times to avoid isolated results.

The comparison data among three different catalysts, Pd, Au, and PdAu immobilised in PIM-EA-TB are tested in 0.1 M formic acid and shown in Figures 7.16A and 7.17A. Oxygen is consumed by all three catalysts, with Au@PIM-EA-TB showing the lowest consumption ability. Hydrogen generation is observed for both Pd and PdAu cases, but oxygen is not depleted. Here, oxygen depletion is not achieved while hydrogen is produced. This means that the processes of oxygen consumption and hydrogen evolution occur at the same time and are not necessarily related to each other. A deeper understanding of the relationship between these reactions needs further exploration. Although the oxygen consumption levels are the same for Pd and PdAu samples, the Pd@PIM-EA-TB shows the highest hydrogen-producing reactivity. The result is consistent with palladium being known to produce hydrogen from formic acid [27-29]. Lower ability in hydrogen production on PdAu@PIM-EA-TB catalyst could be because of a lower amount of Pd presence in the composite (half Pd of that in the Pd@PIM-EA-TB case), or because of the presence of Au affecting the performance of Pd. Note that the hydrogen production on Pd catalyst here (approximately 0.1 µA) is much lower than that for the previous data (0.4 µA) [30], where Pd catalyst was prepared by absorbing the $PdCl_4^{2-}$ method. Since the molar ratios between Pd and PIM-EA-TB host monomer unit are approximately similar (1 to 1) in these two samples prepared by different methods, the reactivity difference towards hydrogen production could result from

varied locations (whether or not in the vicinity of amine sites) of Pd nanoparticles in the host. No hydrogen production is observed on the Au@PIM-EA-TB catalyst.

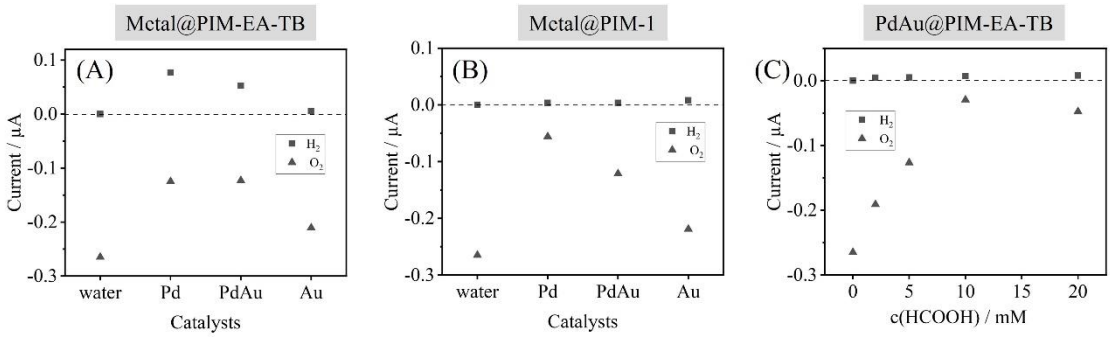

Figure 7.17 Clark probe data for (A) Current responses of three types of catalysts, Pd, PdAu, and Au, immobilised PIM-EA-TB for hydrogen production (positive data, squared) and oxygen consumption (negative data, triangled) in 0.1 M formic acid. (B) Same as in (A) but for catalysts of Pd, PdAu, and Au immobilised PIM-1. (C) Current responses of PdAu@PIM-EA-TB catalyst for hydrogen production (positive data, squared) and oxygen consumption (negative data, triangled) in 0, 2, 5, 10, and 20 mM formic acid.

When exploring PIM-1 composites, the Pd@PIM-1 and PdAu@PIM-1 are most effective in consuming oxygen (see Figures 7.16B and 7.17B). However, there is no evidence for hydrogen generation for all PIM-1 based composites. This reactivity pattern may be associated with both the rate of hydrogen generation and the ability of both liquid and gas phases to coexist in the microporous host. PIM-1 has been suggested to bind hydrogen gas [31], which could influence H_2 production.

The PdAu@PIM-EA-TB catalyst is of interest in oxygen consumption and hydrogen production, thus being explored further for lower formic acid effects (Figure 7.17C). More oxygen consumption appears when formic acid concentration goes from 0 to 10 mM, followed by a slight decrease at 20 mM. Hydrogen evolution is not detected under these conditions. The fact of scarce hydrogen being generated whereas a considerable amount of oxygen being consumed suggests that oxygen is likely reduced into H_2O_2 (in competition to H_2O generation) during this process (with further proof needed).

Similar experiments based on a Clark probe screening for oxygen consumption and hydrogen evolution were also performed in 10% (volume percentage) formaldehyde and 10% (volume percentage) methanol aqueous solution (not shown here). There was very low oxygen consumption of oxygen for the formaldehyde case, but no hydrogen was detected.

No reaction was observed in the methanol solution. Based on these, formic acid or formate continued to be explored.

7.3.3 Hydrogen Peroxide Formation Reactivity II: Hydrogen Peroxide Production

In order to get direct evidence of the reaction product, quantification of hydrogen peroxide is investigated to compare the role of PIM-EA-TB and PIM-1 in the catalytic process. Data in Figure 7.18A shows the formic acid effects on H_2O_2 generation at PdAu@PIM-EA-TB and PdAu@PIM-1 under stirring. Production of H_2O_2 is clearly observed in all the cases. The PdAu@PIM-EA-TB catalyst produces approximately double the amount of H_2O_2 (660 µM in 100 mM HCOOH) in comparison to PdAu@PIM-1 (approximately 330 µM in 100 mM HCOOH) over 2 hours reaction. Given that the sample reactor (small glass vial) is unsealed during the H_2O_2 generation reaction under stirring, oxygen is supplied continuously from the air, so it is illogical to calculate the oxygen conversion percentage. Though, if the reaction follows Equation 5.1, one mole of formic acid being converted into one mole of H_2O_2, then for the case of PdAu@PIM-EA-TB in 100 mM HCOOH, 0.66% of HCOOH has been converted into H_2O_2 over 2 hours. More specifically, H_2O_2 production increased as a function of formic acid concentration with a "switch-on" effect at 10 mM HCOOH observed. A similar trend appears for the PdAu@PIM-1 case with a plateau at a high concentration of 100 mM formic acid. These results could be related solely to formic acid content but could also be linked to the pH of the solutions. Presumably, the localised pH inside the PIMs structure changes during the catalysis. But it is a considerable challenge to monitor it on a nanometre scale.

Next, the same formate/formic acid dependence experiments are carried out at fixed pH of 3.75 (see Figure 7.18B). A similar trend with PdAu@PIM-EA-TB exhibiting higher catalytic reactivity is observed when compared to the data observed in Figure 7.18A. The plots suggest first-order behaviour up to 20 mM formate with non-linearity beyond this point. This could be linked to some decomposition of H_2O_2. The effect of pH control under these conditions needs further systematic investigations.

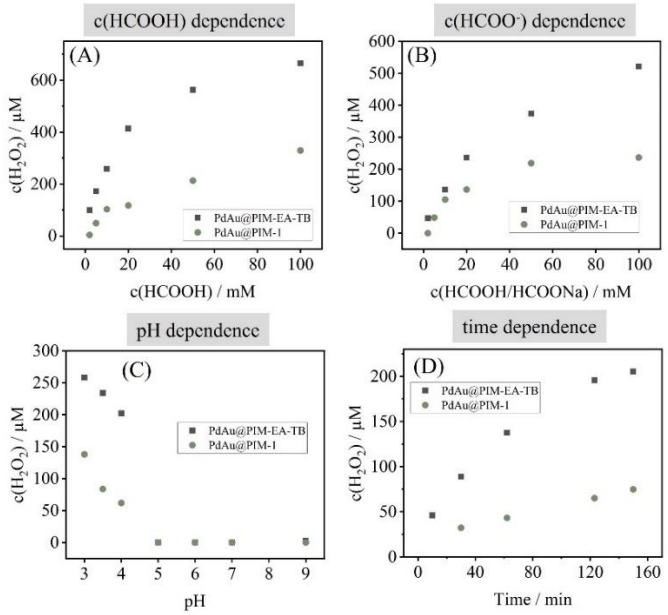

Figure 7.18 Hydrogen peroxide quantification. (A) Production of H_2O_2 on a PdAu@PIM-EA-TB or PdAu@PIM-1 catalysts coated Nylon disk in 2, 5, 10, 20, 50, and 100 mM formic acid (2 mL reaction solution, under stirring for 2 h). (B) As in (A), but in formate/formic acid reaction solution at fixed pH of 3.75. (C) As in (A), but for 10 mM formate/formic acid at pHs of 3, 3.5, 4, 5, 6, and 9. (D) Production of H_2O_2 on a PdAu@PIM-EA-TB or PdAu@PIM-1 catalysts coated Nylon disk in 20 mM formic acid solution under stirring for 10, 30, 60, 120, and 150 min (10 mL reaction solution).

Figure 7.18C shows data for H_2O_2 production from 10 mM HCOOH/HCOONa solutions with pH ranging from acidic to neutral and then alkaline. The production of H_2O_2 is only active when pH ≤ 4 and decreases when going to less acidic for both PdAu@PIM-EA-TB and PdAu@PIM-1 cases. The PdAu@PIM-EA-TB catalyst shows significant higher reactivity (more than doubles at pH 4) relative to that for the PdAu@PIM-1 case, which is consistent with results in Figures 7.18A and B. This substantial enhanced catalytic performance could be linked to the protonation of PIM-EA-TB ($pK_A \approx 4$ [32]). Perhaps surprisingly, no H_2O_2 is produced when pH > 4 for both cases. Figure 7.18D shows the time dependence of H_2O_2 production data on PdAu@PIM-EA-TB or PdAu@PIM-1. Evidently, both PIMs are effective, but PIM-EA-TB does produce more H_2O_2. For both catalysts in 20 mM formic acid, an approximately linear increase of H_2O_2 concentration with time in the first hour is shown.

Catalyst activity screening is performed in 10 mM formic acid solution (see Figure 7.19A). For both hosts of PIM-EA-TB and PIM-1, the PdAu catalyst shows a significantly higher ability to generate H_2O_2 compared to those for Pd or Au samples (in agreement with a

previous report on the effect of Au deposition on Pd nanoparticles [30]). Note that the amount of Pd or Au atoms in the bimetallic PdAu catalyst is half that in the monometallic catalysts. When comparing PdAu catalysts performance, PdAu@PIM-EA-TB exhibit considerable higher catalytic reactivity with approximately double the amount of H_2O_2 production relative to PdAu@PIM-1. The exact role of Au in this process is not clear, but a bifunctional process with Pd catalysing formate oxidation and Au catalysing oxygen reduction is possible.

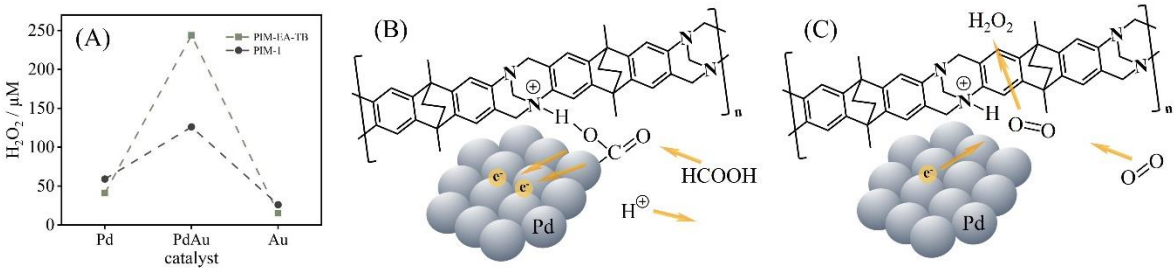

Figure 7.19 (A)Hydrogen peroxide production of Pd, PdAu, and Au nanoparticles embedded in PIM-EA-TB or PIM-1 catalysts in 10 mM HCOOH stirred for 2 h (2 mL reaction solution). (B) Schematic illustration of the 2 electron – 2 proton formic acid oxidation. (C) Schematic illustration of the 2 electron – 2 proton oxygen reduction. PIM-EA-TB provides a protonation site at the tertiary amine.

The beneficial effects of the protonation of tertiary amines in PIM-EA-TB being confirmed by DFT computational modelling (see Chapter 6) have been demonstrated in Figures 7.19B and 7.19C. Both PIMs hosts here supply rigid cavities to accommodate catalysts for catalytic reactions and give pathways for the reagent to permeate (and for products to diffuse out). However, the amine sites in PIM-EA-TB stabilise the transition state for formate oxidation (a 2 electron – 2 proton process). And the protonated amine, in turn, lowers the energy barrier for oxygen reduction (a 2 electron – 2 proton process). Overall, the catalytic process is balanced in protons and in electrons.

Meanwhile, the protonation of the amine also helps keeping the local proton concentration balanced. Considering the small size of the reactive cavity, an excess of protons generated at the surface may lead to the loss of a proton into the next cavity. Thus, it takes time for the following reaction step to happen if the proton is required. The boosted generation of hydrogen peroxide can be verified and visualised in a colour reaction.

7.3.4 Hydrogen Peroxide Formation Reactivity III: Visualisation with TMB Colour Reaction

Visibility for hydrogen peroxide formation could be achieved by employing TMB sensor dye. Colourless TMB can be oxidised by H_2O_2 to form cationic blue colour in the presence of formic acid (as detailed in Chapter 6). In order to better reveal the reactivity of different catalysts, an anionic Nafion ionomer is coated on filter paper and immersed in the TMB reaction solution to accumulate the blue colour product.

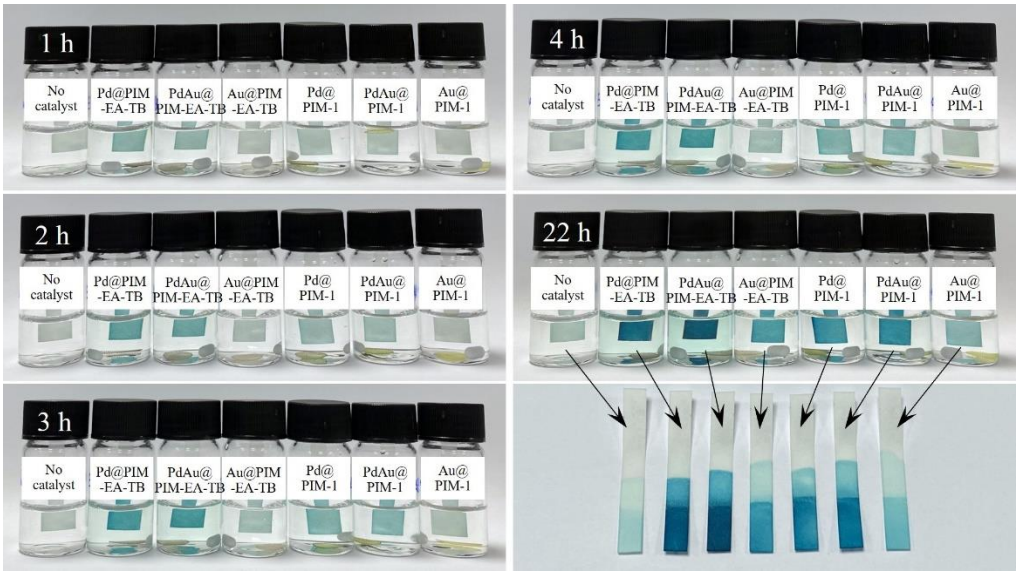

Figure 7.20 TMB colourimetric assay for H_2O_2 production. Photographs of 580 µM 3,3',5,5'-Tetramethylbenzidine (TMB) in 10 mM HCOOH/HCOONa at pH 3.75 in the presence of Pd@PIM-EA-TB, PdAu@PIM-EA-TB, Au@PIM-EA-TB, Pd@PIM-1, PdAu@PIM-1, and Au@PIM-1 catalyst disk (stirred in the dark, 33% DMSO, 3 mL) as a function of reaction time. TMB blue colour product accumulates in Nafion ionomer (10 µL) coated on a filter paper (0.5×4 cm^2).

Figure 7.20 shows the colour comparison among different catalyst disks as a function of reaction time. Blue colour responses gradually occur along with reaction time for all the cases. The weak colour observed in the absence of catalyst is likely due to a slow aerial background TMB reaction. The strongest colour response is observed in the presence of PdAu@PIM-EA-TB catalyst (followed by Pd@PIM-EA-TB), which suggests the highest activity towards H_2O_2 production from formic acid production. This is consistent with the H_2O_2 LC-MS quantification results (see Figure 7.19A). A similar trend is observed for PIM-

1 catalyst-containing experiments, with PdAu exhibiting the best activity compared to those of Pd@PIM-1 and Au@PIM-1. The Colour responses trend being consistent with the H_2O_2 quantification data suggests that TMB is an effective and powerful tool to assess hydrogen peroxide production.

7.4 Conclusions

It has been shown that a PdAu mixture embedded in polymers of intrinsic microporosity, for example, PIM-EA-TB and PIM-1, has been synthesised by a one-step method. Compared to the monometallic counterparts (Pd or Au), the bimetallic PdAu immobilised polymer shows significantly higher activity towards hydrogen peroxide production from formic acid and oxygen. Among all the microporous catalyst composites studied in this chapter, PdAu@PIM-EA-TB is the most active catalyst for H_2O_2 production. The key results are:

(i) Nano Pd, Au, and PdAu mixtures immobilised PIM-EA-TB, or PIM-1 microporous composites, are prepared by a single-step reduction of Pd and/or Au precursor co-deposits together with the host polymer.

(ii) The Clark probe current responses suggest oxygen removal yet minimal hydrogen generation ability for PdAu@PIM-EA-TB or PdAu@PIM-1 catalyst from formic acid aqueous solutions under stagnant conditions.

(iii) Hydrogen peroxide production on both PdAu@PIM-EA-TB and PdAu@PIM-1 catalysts is significantly affected by pH, which is likely to be linked to the protonation/deprotonation of formate/formic acid during the catalytic process.

(iv) A significant enhancement in activity for PdAu@PIM-EA-TB observed at pH 4 is due to the tertiary amines in PIM-EA-TB.

(v) Reactivity screening in aqueous formic acid suggests that PdAu@PIM-EA-TB is the most active catalyst for H_2O_2 production. This could relate to PIM-EA-TB directly contributing to the catalytic process, with amine sites accepting protons for formic acid oxidation and ammonium sites donating protons for oxygen reduction.

(vi) A colourimetric assay based on TMB gives the same result of PdAu@PIM-EA-TB being the most reactive catalyst for hydrogen peroxide generation.

The Pd/Au ratio in the alloy/mixture has a significant impact on its catalytic performance. [33] An atomic-level understanding of bimetallic mixtures remains challenging yet needs further

exploration. The colourimetric assay based on TMB colour change upon chemical reaction provides another perspective for sensing application. The fact that the PIM-EA-TB host directly contributes to the catalytic process paves the way for other further PIMs material to be explicitly investigated to boost catalytic reactions.

7.5 References

1 Fuentes, K. M., Onna, D., Rioual, T., Huvelle, M. A. L., Britto, F., Simian, M., Sánchez-Domínguez, M., Soler-Illia, G. J.A.A. & Bilmes, S. A. Copper upcycling by hierarchical porous silica spheres functionalized with branched polyethylenimine: Antimicrobial and catalytic applications. *Microporous and Mesoporous Materials* **327**, 111391 (2021).

2 Tapia, L., Alfonso, I. & Solà, J. Molecular cages for biological applications. *Organic & Biomolecular Chemistry* **19**, 9527-9540 (2021).

3 McKeown, N. B., Budd, P. M., Msayib, K. J., Ghanem, B. S., Kingston, H. J., Tattershall, C. E., Makhseed, S., Reynolds, K. J. & Fritsch, D. Polymers of intrinsic microporosity (PIMs): bridging the void between microporous and polymeric materials. *Chemistry–A European Journal* **11**, 2610-2620 (2005).

4 He, D., He, D. S., Yang, J., Low, Z. X., Malpass-Evans, R., Carta, M., McKeown, N. B. & Marken, F. Molecularly rigid microporous polyamine captures and stabilizes conducting platinum nanoparticle networks. *ACS Applied Materials & Interfaces* **8**, 22425-22430 (2016).

5 Zhang, C., Li, P., & Cao, B. Electrospun microfibrous membranes based on PIM-1/POSS with high oil wettability for separation of oil–water mixtures and cleanup of oil soluble contaminants. *Industrial & Engineering Chemistry Research* **54**, 8772-8781 (2015).

6 Tofighi, G., Yu, X., Lichtenberg, H., Doronkin, D. E., Wang, W., Wöll, C., Wang, Y. & Grunwaldt, J. D. Chemical nature of microfluidically synthesized AuPd nanoalloys supported on TiO_2. *ACS Catalysis* **9**, 5462-5473 (2019).

7 Seraj, S., Kunal, P., Li, H., Henkelman, G., Humphrey, S. M., & Werth, C. J. PdAu alloy nanoparticle catalysts: effective candidates for nitrite reduction in water. *ACS Catalysis* **7**, 3268-3276 (2017).

8 Ghosh Chaudhuri, R. & Paria, S. Core/shell nanoparticles: classes, properties, synthesis mechanisms, characterization, and applications. *Chemical Reviews* **112**, 2373-2433 (2012).

9 Long, J., Liu, H., Wu, S., Liao, S. & Li, Y. Selective oxidation of saturated hydrocarbons using Au-Pd alloy nanoparticles supported on metal–organic frameworks. *ACS Catalysis* **3**, 647-654 (2013).

10 Liu, S., Ren, H., Yin, S., Zhang, H., Wang, Z., Xu, Y., Li, X., Wang, L & Wang, H. Defect-rich ultrathin AuPd nanowires with Boerdijk–Coxeter structure for oxygen reduction electrocatalysis. *Chemical Engineering Journal* **435**, 134823 (2022).

11 Chai, J., Li, F., Hu, Y., Zhang, Q., Han, D., & Niu, L. Hollow flower-like AuPd alloy nanoparticles: One step synthesis, self-assembly on ionic liquid-functionalized graphene, and electrooxidation of formic acid. *Journal of Materials Chemistry* **21**, 17922-17929 (2011).

12 Zhang, S., Li, M., Zhao, J., Wang, H., Zhu, X., Han, J., & Liu, X. Plasmonic AuPd-based Mott-Schottky photocatalyst for synergistically enhanced hydrogen evolution from formic acid and aldehyde. *Applied Catalysis B: Environmental* **252**, 24-32 (2019).

13 Yang, J., Deng, S., Lei, J., Ju, H., & Gunasekaran, S. Electrochemical synthesis of reduced graphene sheet–AuPd alloy nanoparticle composites for enzymatic biosensing. *Biosensors and Bioelectronics* **29**, 159-166 (2011).

14 Zheng, F., Zhang, L., Li, Y. Y., Liu, Q., Li, Z., & Yao, H. C. Bimetallic AuPd alloy nanoparticles decorated on macroporous WO_3 supports for selective detection of acetone. *ACS Applied Nano Materials* **4**, 2713-2720 (2021).

15 Wissing, M. & Studer, A. Tuning the selectivity of AuPd nanoalloys towards selective dehydrogenative alkyne silylation. *Chemistry–A European Journal* **25**, 5870-5874 (2019).

16 Zhao, G., Wu, G., Liu, Y., He, Y., Feng, J., & Li, D. Preparation of AuPd/ZnO–CuO for the directional oxidation of glycerol to DHA. *Catalysis Science & Technology* **10**, 6223-6234 (2020).

17 Rangasamy, R., Lakshmi, K. & Selvaraj, M. Synthesis of ultrafine AuPd bimetallic nanoparticles using a magnetite-cored poly (propyleneimine) dendrimer template and its sustainable catalysis of the Suzuki coupling reaction. *New Journal of Chemistry* **45**, 14227-14235 (2021).

18 Villa, A., Dimitratos, N., Chan-Thaw, C. E., Hammond, C., Veith, G. M., Wang, D., Manzoli, M., Prati, L. & Hutchings, G. J. Characterisation of gold catalysts. *Chemical Society Reviews* **45**, 4953-4994 (2016).

19 Madrid, E., Lowe, J. P., Msayib, K. J., McKeown, N. B., Song, Q., Attard, G. A., Düren, T. & Marken, F. Triphasic nature of polymers of intrinsic microporosity induces storage and catalysis effects in hydrogen and oxygen reactivity at electrode surfaces. *ChemElectroChem* **6**, 252-259 (2019).

20 Zhao, Y., Wang, L., Malpass-Evans, R., McKeown, N. B., Carta, M., Lowe, J. P., Lyall, C. L., Castaing, R., Fletcher, P. J., Kociok-Köhn, G., Wenk, J., Guo, Z. & Marken, F. Effects of g-C_3N_4 Heterogenization into intrinsically microporous polymers on the photocatalytic generation of hydrogen peroxide. *ACS Applied Materials & Interfaces* **14**, 19938-48 (2022).

21 Ahn, S. D., Kolodziej, A., Malpass-Evans, R., Carta, M., McKeown, N. B., Bull, S. D., Buchard, A. & Marken, F. Polymer of intrinsic microporosity induces host-guest substrate selectivity in heterogeneous 4-benzoyloxy-TEMPO–catalysed alcohol oxidations. *Electrocatalysis* **7**, 70-78 (2016).

22 Carta, M., Malpass-Evans, R., Croad, M., Rogan, Y., Jansen, J. C., Bernardo, P., Bazzarelli, F. & McKeown, N. B. An efficient polymer molecular sieve for membrane gas separations. Science 339, 303-307 (2013).

23 Budd, P. M., Elabas, E. S., Ghanem, B. S., Makhseed, S., McKeown, N. B., Msayib, K. J., Tattershall, C. E. & Wang, D. Solution-processed, organophilic membrane derived from a polymer of intrinsic microporosity. *Advanced Materials* **16**, 456-459 (2004).

24 Zhao, Y., Malpass-Evans, R., Carta, M., McKeown, N. B., Fletcher, P. J., Kociok-Köhn, G., Lednitzky, D. & Marken, F. Size-Selective photoelectrochemical reactions in microporous environments: Clark probe investigation of Pt@g-C_3N_4 embedded into intrinsically microporous polymer (PIM-1). *ChemElectroChem* **8**, 3499-3505 (2021).

25 Vegard, L. LV. Results of crystal analysis.—III. *The London, Edinburgh, and Dublin Philosophical Magazine and Journal of Science* **32**, 505-518 (1916).

26 McKeehan, L. W. The crystal structures of the system palladium-hydrogen. *Physical Review* **21**, 334 (1923).

27 Hu, C., Pulleri, J. K., Ting, S. W., & Chan, K. Y. Activity of Pd/C for hydrogen generation in aqueous formic acid solution. *International Journal of Hydrogen Energy* **39**, 381-390 (2014).

28 Kim, Y., Lee, H., Yang, S., Lee, J., Kim, H., Hwang, S., Jeon, S. W. & Kim, D. H. Ultrafine Pd nanoparticles on amine-functionalized carbon nanotubes for hydrogen production from formic acid. *Journal of Catalysis* **404**, 324-333 (2021).

29 Liu, T., Zhang, Z., Yan, L., Zhang, Z., Zhang, Y., & Yin, Y. Pd nanoparticles immobilized on aniline-functionalized MXene as an effective catalyst for hydrogen production from formic acid. *International Journal of Hydrogen Energy* **46**, 33098-33106 (2021).

30 Wang, L., Carta, M., Malpass-Evans, R., McKeown, N. B., Fletcher, P. J., Lednitzky, D., & Marken, F. Hydrogen peroxide versus hydrogen generation at bipolar Pd/Au nano-catalysts grown into an intrinsically microporous polyamine (PIM-EA-TB). *Electrocatalysis* **12**, 771-784 (2021).

31 Zhao, Y., Al Abass, N. A., Malpass-Evans, R., Carta, M., Mckeown, N. B., Madrid, E., Fletcher, P. J. & Marken, F. Photoelectrochemistry of immobilised Pt@g-C_3N_4 mediated by hydrogen and enhanced by a polymer of intrinsic microporosity PIM-1. *Electrochemistry Communications* **103**, 1-6 (2019).

32 Madrid, E., Rong, Y., Carta, M., McKeown, N. B., Malpass-Evans, R., Attard, G. A., Clarke, T. J., Taylor, S. H., Long. Y.-T. & Marken, F. Metastable ionic diodes derived from an amine-based polymer of intrinsic microporosity. *Angewandte Chemie* **126**, 10927-10930 (2014).

33 Miura, H. & Shishido, T. Concerted catalysis of Pd and Au on alloy nanoparticles for efficient heterogeneous molecular transformations. *Chemistry Letters* **50**, 346-352 (2021).

Chapter 8 Conclusions and Future Work

Contents

8.1 Conclusions

In this thesis, the application of intrinsically microporous polymers (PIMs), for example, PIM-EA-TB and PIM-1, in heterogeneous redoxcatalysis has been explored. The molecularly rigid PIMs have been proven to provide nanocavities for binding/immobilising species of anionic complexes ($Fe(CN)_6^{3-/4-}$ and $PdCl_4^{2-}$), molecules (catechin and quercetin), and metal nanoparticles (Pd, bipolar Pd/Au, and PdAu mixture). The active species embedded polymer complexes have been employed as heterogeneous catalysts for redox catalytic aqueous systems and as nanozymes to mimic enzyme-like activities. In addition, PIM-EA-TB has been shown to have direct catalytic effects on acidity-related redox reactions both experimentally and theoretically.

To explore the immobilisation and reactivity of anionic species in PIMs, a typical reversible redox couple $Fe(CN)_6^{3-/4-}$ was embedded in an intrinsically microporous polyamine PIM-EA-TB to give a thin layer of redox film. When investigated by cyclic voltammetry, the reactivity of PIM-EA-TB/$Fe(CN)_6^{3-/4-}$-coated electrodes has been shown to be sensitive to parameters of $Fe(CN)_6^{3-/4-}$ concentration, film thickness, and pH (linked to $pK_{A,\ PIM\text{-}EA\text{-}TB} \approx 4$) of the solutions during immobilisation and voltammetry. The interaction between $Fe(CN)_6^{3-/4-}$ and protons inside the PIM-EA-TB host is suggested to be responsible for the uptake, retention, and relatively slow leaching processes. Electrocatalytic oxidation of ascorbic acid has been achieved by the PIM-EA-TB/$Fe(CN)_6^{3-/4-}$ film.

Two *ortho*-quinol molecules, catechin and quercetin, were studied as guest species immobilised in the PIM-EA-TB host. Hydrogen bonding was suggested to be critical to bridge catechin (or quercetin) and tertiary amine sites in PIM-EA-TB. The binding capacity has been demonstrated to be typically one guest molecule binding to each monomer of PIM-EA-TB. Cyclic voltammetric data suggested apparent Langmuirian binding behaviour of the *ortho*-quinols, which undergo 2-electron 2-proton redox conversion to the corresponding quinones in a mono-layer PIM-EA-TB film. When investigating release behaviours, water-soluble catechin spontaneously leached into solutions, whilst the release of quercetin with low water solubility requires electrochemical stimuli to locally create alkaline conditions.

The anionic complex binding ability of polyamine has inspired a new strategy of synthesizing metal nanoparticles where $PdCl_4^{2-}$ was accumulated in PIM-EA-TB followed by borohydride reduction to form Pd@PIM-EA-TB. The Pd nanoparticles with an approximate 3 nm diameter could catalyse the spontaneous reaction between formic acid and

oxygen to competingly yield H_2O_2 (at low formic acid concentrations in the air), water, and H_2 (at higher formic acid concentration or under argon). Combined with a following spontaneous electroless Au deposition process, the Pd/Au@PIM-EA-TB product gave an order of magnitude increased H_2O_2 yield even at higher concentrations of formic acid with suppressed hydrogen production. Evaluation of oxygen consumption and hydrogen production was carried out on a Clark-type sensor, while H_2O_2 quantification was completed indirectly based on a liquid chromatography - mass spectroscopy method. Pd and Au work hand-in-hand as bipolar electrocatalysts.

Further application possibilities of catalyst-immobilised polymer complexes include natural enzymes mimics as nanozymes. The Pd@PIM-EA-TB complex exhibited formate oxidase reactivity, which was revealed to indirectly drive the colour reaction of a sensor dye 3,5,3',5'-tetramethylbenzidine (TMB) in the presence of formic acid. The whole catalytic reaction has been dissected and investigated as two processes: oxygen reduction on the Pd@PIM-EA-TB catalyst to produce H_2O_2 (first order process showing formate oxidase reactivity), followed by homogeneous TMB oxidation. The favourable effect of perchlorate anions and the computational DFT model verified that PIM-EA-TB as an active component (providing ammonium sites) had enhanced both formate oxidation and oxygen reduction in H_2O_2 processes.

Finally, Pd, Au, and PdAu mixture were embedded in two different microporous polymers, PIM-EA-TB and PIM-1, by a single-step process and evaluated as catalysts for the reactivity towards formic acid oxidation and oxygen reduction during H_2O_2 production. During the preparation processes, the Pd and/or Au precursors were cast from chloroform solution together with the polymer, followed by borohydride reduction. Reactivity screening in aqueous formic acid suggested that PdAu@PIM-EA-TB is the most active catalyst for H_2O_2 production. Colour reactions based on TMB visualising reagent verified the same reactivity pattern. It was proposed that, in contrast to PIM-1, PIM-EA-TB directly contributes to the catalytic process with amine sites as proton acceptors (for formate oxidation) and ammonium sites as proton donors (for oxygen reduction). The difference in roles of two host polymers during the catalytic process has validated the key role played by functional groups.

Overall, work in this thesis has shown that PIMs, as a building block of the heterogeneous catalysts, directly or indirectly contribute to the catalytic processes. The actual conditions inside the micropores of the polymer composites catalysts could be complicated and

challenging to probe. However, the functions of PIMs discovered in this thesis are (i) providing “nanocavities” for redox reaction to happen; (ii) binding and incorporating active species like ions, molecules, and nanoparticles; (iii) creating a considerable number of active catalytic sites *via* host-guest interactions; (iv) restricting the nanoparticle size into nanoscale; (v) allowing permeation of reactants and products; (vi) making the catalyst to be easily reused and recovered; (vii) directly being an active catalyst component. Furthermore, mechanisms for catalytic processes like the conversion of formic acid and oxygen to hydrogen and CO_2 has been proposed. Analytical methods for oxygen consumption and hydrogen production based on a Clark-type sensor and for indirect quantification of hydrogen peroxide based on liquid chromatography coupled with mass spectroscopy (LC-MS) have been developed.

Overall, catalysts can be immobilised in PIMs and used for biomass conversion. The PIM structures can assist the catalysis processes similar to natural enzyme activities. However, the small pore sizes of PIMs would limit many processes. Therefore, biomass with small molecules can react instead of bigger molecules. Catalysts immobilised in PIMs can be reused and recovered, which is beneficial to certain types of processes. Biomass conversion into hydrogen peroxide has been shown for formic acid. Biomass conversion to hydrogen is feasible but difficult for molecules beyond formic acid.

8.2 Future Work

Since two PIMs examples have been investigated in redoxcatalysis and investigation methods have been provided, it may be interesting to extend the research area to other types of microporous polymers or modified PIMs in order to get a deeper understanding of the mechanisms during catalytic processes. For example, cyanide groups in PIM-1 can be chemically modified into carboxyl groups, which could lead to different behaviours of the host polymer. Cross-linking could alter the microporosity and solubility of PIMs, which is critical, if controlled, to systematic studies on the role of PIMs in the catalytic processes.

The exploratory methods presented in this thesis are limited. Due to the complex nature of the polymer composites, the real environments inside the micropores remains unsolved. Therefore, other powerful technologies and strategies may be required to get detailed information. For example, gas adsorption analysis could be employed to investigate the pore size distribution change of polymers before and after the immobilisation of species. In addition, inductive coupled plasma (or ICP) analysis could be used to identify trace amounts of the elements inside the polymer composites.

Specific to the PdAu mixture demonstrated in Chapter 7, only one ratio of Pd to Au was investigated for hydrogen peroxide production activity. If one were to take this work forward, it would be intriguing to see how other Pd/Au ratios affect the mixture components and catalytic efficiency. It could also be interesting to apply this catalyst to other catalytic reactions, for example, in the oxidation of alcohols and carbohydrates, or CO_2 reduction.

More generally, PIMs could be applied as hosts for catalysis in a much wider range of applications. Nano particulate catalysts in PIMs are easily applied and recovered without complicated separation processes. Sensors or industrial catalytic processes could be improved.

8.3 Publications

(1) **Wang, L.**, Zhao, Y., Fan, B., Carta, M., Malpass-Evans, R., McKeown, N. B., & Marken, F. Polymer of intrinsic microporosity (PIM) films and membranes in electrochemical energy storage and conversion: a mini-review. *Electrochemistry Communications* **118**, 106798, (2020).

(2) **Wang, L.**, Malpass-Evans, R., Carta, M., McKeown, N. B., & Marken, F. The immobilisation and reactivity of $Fe(CN)_6^{3-/4-}$ in an intrinsically microporous polyamine (PIM-EA-TB). *Journal of Solid State Electrochemistry* **24**, 2797-2806, (2020).

(3) **Wang, L.**, Malpass-Evans, R., Carta, M., McKeown, N. B., Reeksting, S. B., & Marken, F. Catechin or quercetin guests in an intrinsically microporous polyamine (PIM-EA-TB) host: accumulation, reactivity, and release. *RSC Advances* **11**, 27432-27442, (2021).

(4) Li, Z., **Wang, L.**, Malpass-Evans, R., Carta, M., McKeown, N. B., Mathwig, K., Fletcher, P. J. & Marken, F. Ionic diode and molecular pump phenomena associated with caffeic acid accumulated into an intrinsically microporous polyamine (PIM-EA-TB). *ChemElectroChem* **8**, 2044-2051, (2021).

(5) **Wang, L.**, Carta, M., Malpass-Evans, R., McKeown, N. B., Fletcher, P. J., Lednitzky, D., & Marken, F. Hydrogen peroxide versus hydrogen generation at bipolar Pd/Au Nano-catalysts grown into an intrinsically microporous polyamine (PIM-EA-TB). *Electrocatalysis* **12**, 771-784, (2021).

(6) Marken, F., **Wang, L.**, Zhao, Y., Li, Z., Amiri, M., & Imanzadeh, H. Polymers of intrinsic microporosity (PIMs) in sensing and in electroanalysis. *Current Opinion in Chemical Engineering* **35**, 100765, (2022).

(7) Zhao, Y., **Wang, L.**, Malpass-Evans, R., McKeown, N. B., Carta, M., Lowe, J. P., Lyall, C. L., Castaing, R., Fletcher, P. J., Kociok-Köhn, G., Wenk, J., Guo, Z. & Marken, F. Effects of g-C_3N_4 Heterogenization into Intrinsically Microporous Polymers on the Photocatalytic Generation of Hydrogen Peroxide. *ACS Applied Materials & Interfaces* **14**, 19938-48 (2022).

(8) **Wang, L.**, Carta, M., Malpass-Evans, R., McKeown, N. B., Fletcher, P. J., Estrela, P., Roldan, A. & Marken, F. Artificial Formate Oxidase Reactivity with Nano-palladium Embedded in Intrinsically Microporous Polyamine (Pd@PIM-EA-TB) Driving the H_2O_2–3, 5, 3′, 5′-tetramethylbenzidine (TMB) Colour Reaction. *Journal of Catalysis*, **416**, 253-266 (2022).

(9) **Wang, L.**, Carta, M., Malpass-Evans, R., McKeown, N. B., Fletcher, P. J., Ho, P.-L. B., Tsang, S. C. & Marken, F. Polymer-Enhanced Hydrogen Peroxide Generation from Oxygen and Formic Acid: One-Step Formation of Nanocatalysts (Pd, Au, or a PdAu Mixture) Confined into Intrinsically Microporous Polymers (PIM-EA-TB or PIM-1). Publication in preparation.